UNIVERSITY OF CAPE TOWN

Department of Mechanical Engineering

RONDEBOSCH, CAPE TOWN
SOUTH AFRICA

2022

Influence of post-weld heat treatment (PWHT) on the tensile behaviour of P91 weldments

Tinashe Jambo
(JMBTIN001)

SUPERVISOR:
Prof R. Knutsen

Plagiarism Declaration

Declaration:

1. I know that plagiarism is wrong. Plagiarism is to use another's work and pretend that it is one's own.
2. I have used the IEEE 2006 convention for citation and referencing. Each significant contribution to, and quotation in, this report from the work(s) of other people has been attributed and has been cited and referenced.
3. This report/project is my own work.
4. I have not allowed and will not allow anyone to copy my work with the intention of passing it off as his or her own work.

Signature

Signed by candidate

Abstract

A key factor for successful installation of Grade 91 steel for high pressure-high temperature applications in power plant is optimised welding and post weld heat treatment (PWHT) which restores homogeneous mechanical properties after welding. Although optimum PWHT is prescribed in standards, deviations in the field practices can potentially lead to accelerated component degradation and failure. Consequently, a full understanding of cross-weld behaviour as a function of deviations in PWHT is required. This study investigates the influence of PWHT on the occurrence of strain localisation in cross-weld tensile specimens tested at temperatures up to typical power plant service temperature. Localised strain maps were obtained during high temperature tensile deformation. These assist in understanding the influence of PWHT on the overall performance of the cross-weld, and the identification of the location most susceptible to failure in the welded specimens.

Specimens used in this work were extracted from as-welded new Grade 91 pipe material. Wire cut EDM was used to extract rectangular blocks with the weld in the centre which were machined to required geometry. Specimens for as-welded (AW) tests were not subjected to PWHT. The recommended PWHT for P91 steel is tempering at 760°C for 2 hours. Post weld heat treatments that were performed on specimens included soaking at 720°C, 760°C and 800°C for 2 hours respectively, as well as so-called excursion heat treatments that included extended treatment at 760°C for up to 6 hours. In addition, excursion heat treatments also included over-heating up to 840°C followed by soaking for 2 hours at 760°C. A Gleeble 3800D thermomechanical simulator was used for high temperature tensile testing at a strain rate of 10^3 s^{-1}. High temperature tensile tests were performed at 300°C and 535°C. Three-dimensional (3D) digital image correlation (DIC) was used for non-contact strain measurement (i.e., application of virtual strain gauges) to accurately map the occurrence of strain localisation. DANTEC Istra 3D DIC software was used for capturing and post processing the DIC data for strain analysis across the weldment. Specimen subjected to PWHT exhibited reduced resistance to deformation at room temperature having a lower yield strength (YS) and ultimate tensile strength (UTS) compared to the AW condition, indicating that PWHT lowers the materials resistance to the onset of plastic deformation. Despite an overall reduction of UTS at elevated temperatures, this observation was extended to tensile strength at elevated test temperatures. Over tempering resulted in diminished tensile properties as observed in specimens tempered at 800°C for 2 hours. A comparison of specimens subjected to excursions and extended heat treatments shows that excursions resulted in poor tensile properties, exhibiting very low yield strength and ultimate tensile strength compared to the recommended PWHT. Specimens subjected to excursions and over tempering in PWHT exhibited diminished tensile properties compared to the recommended PWHT. The change of tensile behaviour across weldments as a function of PWHT contributes to understanding the metallurgical risk associated with deviations in PWHT field practices. Localised strain maps showed that the weld metal has high resistance to deformation at room temperature which decreases as test temperature increases. At room temperature the peak localised strain occurred in the base metal (BM) for all PWHT conditions. The peak localised strain migrated further into the BM with increased PWHT temperature, while it occurred in a hot zone at elevated test temperatures.

Based on experimental results obtained at room temperature, strain localisation was established as a function of heat treatment condition. The non-uniform temperature profile remains a challenge to reliably conclude the extent to which strain localisation is influenced by heat treatment and material property.

Acknowledgements

First and foremost, I would like to thank God for the gift of life within which I pursued this MSc. To achieve something like this is by no means of personal effort but a collective effort of different individuals who played critical roles in my study. I would like to extend my gratitude to all those individuals.

I would like to extend my most sincere gratitude to my supervisor, Professor Robert Knutsen for affording me the opportunity to do this MSc project. I would also like to thank him for his support, patience, guidance and supervision. Following his expertise in material science we managed to steer through this project and in the process, I acquired invaluable knowledge. I would also like to thank Professor Thorsten Becker for his support and invaluable input that transformed the quality of this work.

I would like to thank CME staff Penny Louw, Soraya Von Willingh and Maxwell Vos for assistance with the CME machinery and support throughout my MSc. In addition, I would like to thank the workshop staff for machining my specimen. Recognition is directed towards Mr Pierre Smith , Dylon Jacobs and Grant Springle.

This MSc project would not have been possible without funding from the Eskom Power Plant Engineering Institute (EPPEI). I am grateful for the funding and conferences that contributed towards my personal growth. I would also like to thank the UCT mechanical engineering department for granting me opportunities to tutor.

In closing I would like to extend my gratitude to my research colleagues especially Graham and Andrew, close friends and my mom for their unwavering support, encouragement and inspiration that they provided. I am forever grateful.

Table of Contents

Table of Figures

List of Tables

Abbreviations and Acronyms

Hrs _____h (hours)
Hr _____h (hours)
CSEF_____Chrome Strength enhanced ferritic steel
SAW_____Submerged Arc Welding
SMAW_____Shielded Metal Arc Welding
GTAW -TIG ___Gas Tungsten Arc Welding
GMAW–MIG___Gas Metal Arc Welding
FCAW_____Flux-Cored Arc Welding
PWHT _____ Post Weld Heat Treatment
AW _____As-welded
DIC_____Digital Image Correlation
OBM _____ Over tempered base metal
HAZ _____ Heat affected zone
BM _____ Base metal
FL1_____Fusion line 1
FL2_____Fusion line 2

1. Introduction

The tensile behaviour of a material is defined by mechanical properties such as Yield Strength (YS-σ_o), Ultimate Tensile Strength (UTS-σ_u), Percentage elongation at fracture, Strain hardening ratio: UTS/Yield and Tensile toughness (area under graph until fracture) [1].

Table *1.1* shows material properties obtainable from mechanical tests. The influence of post weld heat treatments (PWHT) on the tensile behaviour of P91 weldments can be analysed in reference to some of these material properties.

Table 1.1: Material properties obtainable from tension tests [1]

Category	Engineering Property	True Stress–Strain Property
Elastic constants	Elastic modulus, E, E_t Poisson's ratio, ν	—
Strength	Proportional limit, σ_p Yield strength, σ_o Ultimate tensile strength, σ_u Engineering fracture strength, σ_f	True fracture strength, $\tilde{\sigma}_{fB}$ Strength coefficient, H
Ductility	Percent elongation, $100\varepsilon_f$ Reduction in area, $\%RA$	True fracture strain, $\tilde{\varepsilon}_f$
Energy capacity	Tensile toughness, u_f	True toughness, $\tilde{u}_f$
Strain hardening	Strain hardening ratio, σ_u/σ_o	Strain hardening exponent, n

In this work, a robust experimental technique was developed and applied to specimens subjected to different heat treatment conditions. The experimental technique utilised hardness tests to locate different sections of the weldments i.e., weld metal (WM), fusion line (FL), heat affected zone (HAZ) in specimens and measure the HAZ width. Microhardness tests were used to locate weld zones in the HAZ. Three-dimensional Digital Image Correlation (3D DIC) is used for non-contact strain measurement.

A robust technique was used to optimise the acquisition and interpretation of tensile data for accurate strain localization measurement in composite cross-weld specimens. The technique involved using a physical reference point on the specimen to aid 3D DIC evaluation. Room temperature and elevated temperature tensile tests were conducted on a Gleeble 3800D thermomechanical simulator. Experimental data obtained from the experiments was analysed to extract specimen material properties. The experimental data were analysed to understand the influence of PWHT on mechanical behaviour of P91 weldments.

1.1. Background

The need of emission reduction has led to design of new advanced power plants with higher efficiency resulting in increased operational temperature and pressures. The modern supercritical and ultra-super-critical power plants operate more efficiently by accessing the elevated operating conditions [2].

Material suitability is the major problem associated with increasing the operating temperature and pressure of plants. For super critical/ultra-supercritical power plant, reported operating temperature and pressure can exceed 600 °C and 30 MPa, respectively. At such high temperatures components undergo microstructural changes over time. P91 steel, which belongs to 9–12 wt% Cr ferritic creep resisting steel group, was developed for elevated temperature service for nuclear and fossil energy applications, it is a modified Cr-Mo (9 wt% Cr-1 wt% Mo) creep resisting steel that provides significantly higher design strength [3]. Over the last few decades, the development of creep strength enhanced ferritic steels (CSEF) started from P9, P91, and P92. The CSEF steels were developed for the fabrication of thin and thick-walled components for use in power plants in the mid-1960s. The operating temperatures that these components were subjected to in power plants was 565°C. The creep strength of 12 wt% Cr steels was derived from the solid solution strengthening and precipitate hardening. The common cause of material failure in long-term exposure for most of 12 wt% Cr steels was the unexpected precipitation of Z-phase (Cr, V, Nb) [4]. Pandey et al. [4] reported that recent investigations have demonstrated that Z-phase precipitation is strongly accelerated by the high Cr content. These phases coarsen over time leading to formation of cavities which affects the creep rupture life of components in service leading to common type IV cracking observed in most failed welds [2].

The Cr percentage was brought down to 9 wt%, to enhance the creep strength of 12 wt% Cr steels. The Oak Ridge National Laboratory (ORNL) was first to develop 9 wt% Cr CSEF steel, under the designation P9 (9 wt% Cr- 1wt% Mo) [4]. The addition of strong carbide and nitride forming elements such as V and Nb with controlled amount of N has resulted in improvements in CSEF 9 wt% Cr- 1 wt%. Mo steel. Addition of these elements resulted in a modified steel. The modified steel was designated as Grade 91(X10CrMoVNb 9-1) steel, also known as modified 9Cr-1Mo-V. It is designated as P91 for pipe, T91 for tube, and ASTM A335 for plate.

The P91 steel is used for pipes in the superheater section of the boilers and joining of the pipes is inevitable [5]. A typical weldment can be differentiated into three different zones, the weld fusion zone (FZ), heat affected zone (HAZ) and the over-tempered base metal (OBM) exhibiting heterogeneous topology of microstructure and mechanical properties. Hence, homogeneous microstructure across the weldments is a primary requirement of the welded joint to achieve the desired strength. As a result, Cr-Mo P91 welds are subjected to post weld heat treatment (PWHT) to attain desirable microstructure and mechanical properties.

Weld related failures in P91 steel applications in power plants have caused concern [6]. The Cr-Mo P91 steels require strict adherence to appropriate welding procedures for acceptable weld quality mechanical properties such as adequate weld strength and impact toughness [2]. This has led to achievement of optimum weld metal properties for P91 steel in its application in power plants. Solidification of Cr-Mo P91 steel leads to the formation of martensitic microstructure. Further heat treatment is required to achieve adequate mechanical properties in the weld heat affected zones (HAZs). As a result, Cr-Mo P91 welds undergo post weld heat treatment (PWHT) to attain desirable microstructure and mechanical properties [2]. Most weld failure occurs in the HAZ which has distinct zones of microstructure with varying mechanical properties i.e., coarse grained heat affected zone (CGHAZ), fine grained heat affected zone (FGHAZ), inter critical heat affected zone (ICHAZ). FGHAZ and ICHAZ have been identified as the most preferential location of failure [2].

Although optimum PWHT is prescribed, deviations in the field practices can potentially lead to accelerated component degradation and failure. Hence, a comprehensive comprehension of

cross weld behaviours concerning deviations in post-weld heat treatment (PWHT) becomes essential. Research on as-welded P91 microstructures reveals the complete dissolution of precipitates in the heat-affected zone (HAZ), leading to elevated hardness [2]. These precipitates play a crucial role in pinning the grain boundaries, thereby affecting the overall performance. PWHT leads to coarsening of precipitates and finer precipitates reducing hardness and increasing ductility. Post-weld normalising and tempering (PWNT) is another heat treatment process after welding to improve the mechanical properties and microstructure of the welded joints. Normalising involves heating the welded joint to a temperature above its critical temperature, and then allowing it to cool in still air. This process refines the grain structure and improves the tensile strength, toughness, and dimensional stability of the welded joint. Tempering involves heating the welded joint to a temperature below its critical temperature and holding it at this temperature for a certain period. This process reduces the brittleness of the welded joint, improves its toughness, and enhances its resistance to impact and fatigue. Pandey et al. [2] reported that size of precipitates measured in the PWNT condition was higher than the PWHT, this influences the mechanical properties of the weldment.

Reduction in mechanical properties at high temperature is the primary problem affecting performance of P91 steel at high temperature. In the present work, the effect of PWHT on mechanical properties and strain localisation in P91 weldments was studied in detail. Mechanical properties investigated included yield strength (YS), ultimate tensile strength (UTS), toughness, ductility and hardness. Digital image correlation, a non-contact method for measuring strain deformation was employed. Elevated temperature tensile tests were conducted on a Gleeble 3800D thermomechanical simulator.

1.2. Project Objectives

A key factor for successful installation of Grade 91 is optimised welding and correct post weld heat treatment (PWHT). Welds may not achieve specified mechanical properties and high temperature performance when PWHT is omitted, or specifications not followed.

This project reported on the sensitivity of tensile strength (across the composite weldment) to the microstructural state that evolves during different PWHT practices. Attention was directed to the behavior of the different zones within the cross-weld specimens and assessing the degree to which strain localization is affected by PWHT and tensile test temperature.

In addition to the investigation of the metal behavior, the project also sought to evaluate the test technique to optimise the acquisition and interpretation of tensile data for accurate strain localization (a function of temperature) measurement in composite cross-weld specimens.

2. Literature Review

2.1. Introduction to P91 steel

2.1.1. P91 chemical composition

The properties of Grade 91 steel are mainly due to its chemical composition and microstructure [4].The ideal chemical composition for achieving the best properties of Grade 91 steel was established through detailed metallurgy studies. Following reviews by code committees, some relaxation from the optimal recommendation was adopted for practical reasons. Even with this relaxation, the specification is deemed tighter than with traditional low alloy steels.

The tighter compositional requirements are aimed at ensuring that a fully tempered martensite microstructure is developed. Achieving a homogeneous microstructure requires proper control of both composition and heat treatment and these effects are, in many cases, interrelated[7]. The enhanced creep strength for Grade 91 is based on:

- A relatively high density of dislocations which introduce a high internal stress in the steel.
- Second phase precipitates which provide precipitate hardening.
- Solid solution strengthening due to alloying elements.
- The precipitation of vanadium/Niobium rich carbonitrides of type MX (where M = Nb or V and X=C or N or CN) at defect sites and lath boundaries in the martensitic base structure [7].

The chromium in P91 steel reacts with oxygen at high temperatures preventing oxidation and nitrogen acts as a creep resistance enhancer [3]. It was assumed that the chemical composition of the steel used in this study is the same as the standard specification ASME SA335 P91 shown in Table *2.1* [8].

The addition of titanium allows for levels of niobium to be taken slightly lower [9]. Titanium serves as an effective replacement for niobium. However its level should not exceed 0.010 wt%. This is because titanium has a tendency of combining with nitrogen reducing the efficiency of nitrogen as creep strength enhancer at high temperatures.

Control of aluminium levels, keeping them at a minimum is important as it ensures that there is adequate nitrogen to form carbo-nitrides precipitates that support the long-term creep strength of P91 [7]. This is achieved by reducing the other oxidisers such that most of the aluminium in the molten metal combines with oxygen. Table *2.1* shows the ASME SA 335 composition of P91 steel.

Table 2.1 P91 Composition specification [7] :

Element	**ASME SA 335**
	Pipe (wt%)
Carbon	0.08– 0.12
Manganese	0.30 – 0.60
Phosphorus	0.020 (max.)
Sulphur	0.010 (max.)
Silicon	0.20–0.50
Chromium	8.0–9.50
Molybdenum	0.85–1.05
Vanadium	0.18–0.25
Niobium	0.06–0.10
Nitrogen	0.030–0.070
Nickel	0.40 (max.)
Aluminium	0.02 (max.)
Titanium	0.01(max)
Zirconium	0.01 (max)

2.1.2 P91 Microstructure

It is important to study the microstructure of P91 to understand the evolution of the microstructure and the impacts of welding and heat treatment. This also allows tracking of changes as the microstructure evolves during tensile testing at high temperatures.

The EPRI G91 steel handbook [7] also shows that the desired microstructure for Grade 91 components is tempered martensite with a fully developed network of $M_{23}C_6$carbides (where M: Fe, Cr, Mo) and MX-type carbo-nitrides MX (where M = Cb or V and X=C or N) that precipitate on lath boundaries and other defect sites in the sub-structure.

Transmission Electron Microscopy (TEM) and optical micrographs of virgin P91 by Li and Mitchell [3] steel have shown that the microstructure of the P91 base metal consists of fully tempered martensite. Figure 2.1 [10] shows an optical micrograph of virgin P91 steel with a martensitic structure. Grain and lathe boundaries were decorated by tiny $M_{23}C_6$ precipitates. Quantitative metallography studies revealed an average lath size ranging from 0.25 to 0.5 μm.

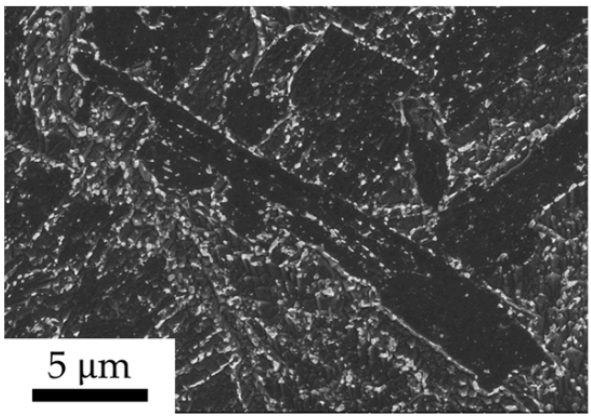

Figure 2.1: Optical micrograph showing the tempered martensitic structure[10]

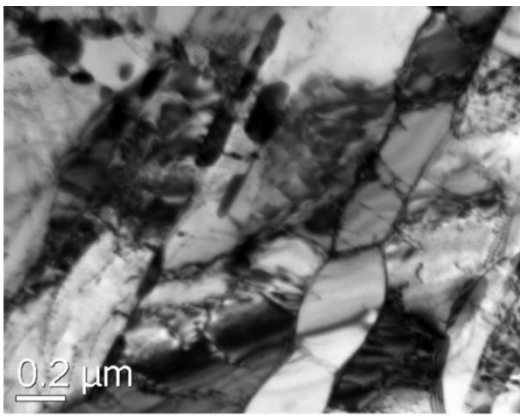

Figure 2.2: TEM Virgin P91 steel. Thin foil showing a detail of the lath structure showing Cr-rich elongated carbides mainly on the lath boundaries[3]

Transmission electron microscopy (TEM) of the virgin P91 (Figure 2.*2*) shows the lath martensitic structure, as well as the coarse carbide precipitates embedded along the lath boundaries as shown in Figure 2.2, which are possibly of the $M_{23}C_6$ type [7] [1]. Where M is a mixture of Fe and Cr [1]. The mechanism of enhanced creep strength enhancement for Grade 91 is precipitate hardening from vanadium/niobium rich carbonitrides at defect sites and $M_{23}C_6$ precipitates at grain boundaries in the martensitic base structure [7]. This method of strengthening is commonly known as precipitate hardening.

Steel goes through microstructural changes during welding. Evolution of the microstructure can be observed by analysing microstructural changes in weldments of P91 steel specimens subjected to different post weld heat treatments comparing to the microstructure of the virgin material [4][4].

As reported in the EPRI P91 handbook technical report [7], P91 steel undergoes microstructure degradation in service and as a result, loses creep strength. The following microstructure degradation effects appear to be primarily responsible for the loss of long-term creep strength:

- Dissolution of fine M_2X and MX carbonitrides (where M=Nb or V and X=C or N or CN) due to formation of new phases.
- Overall reduction of dislocation density as a result or recovery of dislocation substructure (increase in subgrain size). This initiates because of preferential recovery of microstructure in the close proximity to prior austenite grain boundaries (PAGBs).
- Loss of creep ductility because of development of creep voids
- Reduction in the fine M_2X and MXs and or $M_{23}C_6$ precipitates as a result of precipitation of Z phase, M_6X carbonitrides and laves during creep causes a loss of creep strength.

Relatively coarse Z phase, a complex nitride of the form Cr(Nb,V)N has been observed in P91 steel after exposure at 600 °C and 650°C. The fraction of Z-phase is low even after long term

exposure, therefore the formation of the Z-phase does not affect the long term mechanical properties of Grade 91 steel significantly [7].

Grade 91 steel experiences significant recovery of the dislocation substructure during creep [7]. Creep strain effects greatly influence the recovery of the dislocation substructure. Research has shown that holding Grade 91 steel for long periods at high temperature in the absence of stress, i.e., aging, has minimal effect on the dislocations.

Contrary to this observation, a significant increase in subgrain size during creep was observed. It has long been established that strain localization effects, especially at grain boundaries, are important during creep of engineering steels [7].

The loss of creep rupture strength in P91 steel is associated with preferential recovery of the microstructure in the vicinity of PAGBs. The preferential recovery promotes an acceleration of the local creep rate and the additional strain leads to further recovery [7]. Hence, the process once started is self-sustaining and leads to premature rupture.

Low strength, precipitate free zones adjacent to the boundaries form as a result of coarsening of grain boundary precipitates. The formation of intermetallic Laves phase $(Fe, Cr)_2 (Mo,W)$ has also been reported, this can influence creep behaviour in two ways [7]:

- It appears that relatively large amounts of Mo and, in Grade 92 steel W, are incorporated in the intermetallic Laves phase. The depletion of these elements from solid solution will therefore cause a reduction of the overall creep resistance.
- The Laves phase appears to nucleate mostly on sub-grain boundaries and on prior austenite grain boundaries. This phase will coarsen during creep at temperatures up to about 650°C. Since Laves is relatively hard it can provide preferred sites for nucleation of creep voids.

2.1.3 P91 Post Weld Heat Treatment (PWHT)

Steels undergo post weld heat treatment (PWHT) to achieve desired mechanical properties. P91 Pipe PWHT is normally done in the field using ceramic blankets. It is often difficult to achieve accurate temperature control in the field. Walker [11] conducted work on heat transfer analysis of Localised heat treatment for Grade 91 steel. A forward calculation model was developed that can be used to inform the user about the maximum and minimum temperatures the pipe will experience during heat treatment. This includes the maximum temperature that the heat blanket will reach in order to achieve the desired pipe temperature, and the time that it takes to reach the PWHT temperature. The forward model requires user inputs: minimum required temperature of the coldest part of the pipe (inner pipe surface), pipe diameter, pipe thickness, and ambient temperature. The model will accurately predict the temperature profile with changes in PWHT temperatures, pipe diameter and thickness. This approach is practical because it assists in achieving more accurate heat treatments.

The chemical composition and heat treatment history determines the microstructure of P91 steel[7]. A diffusion-controlled process controls the transformation during heating. The onset of transformation on heating is delayed by some increment of temperature that is directly proportional to a specific rate of heating. On cooling, the beginning of transformation is also

delayed by some increment of temperature that is directly proportional to a specific rate of cooling.

Tempering heat treatment is essential for Grade 91 material, it to improves the ductility of the material and reduces residual stresses present before service installation because virgin P91 martensite is relatively hard and brittle [7]. Stabilization of Grade 91 material during high temperature service is due to the temper-resistant carbides and carbo-nitrides that are formed during tempering heat treatment [7].

In application, P91 steel is usually welded. Post weld heat treatments need to be conducted to remove weld effects on material properties. As a result of weld thermal cycles, welds have heterogeneous microstructures which typically result in a variation in mechanical properties across the weld. Normal Post Weld Heat Treatment (PWHT) is aimed at reducing welding residual stresses and tempering the microstructure to achieve a homogeneous microstructure. In study by Pandey et al. [4] PWHT of P91 steel was performed in the temperature range of 760°C-788 °C for a tempering time which ranges from 0.5 h – 3 h. This results homogeneous distribution of carbides inside a fully tempered martensitic structure. As the material undergoes PWHT, $M_{23}C_6$ carbides precipitate at lath boundaries, along with MX precipitates (where M=Nb or V and X=C or N or CN).

In some applications, a full post weld renormalization heat treatment is recommended after welding (PWNT). In this case, the weld and heat affected zone microstructures will be modified with the final microstructure formed being dependent on the normalization (austenitising) time and temperature and the subsequent cooling rate. Even with a renormalising heat treatment there will still be some microstructural variation as the weld metal has certain key differences from the base metal. One of the most important of these differences is that the weld metal typically contains a notable density of inclusions. These are not normally modified by the renormalising process. In Grade 91 type alloys typically slower cooling rates (which are near to equilibrium) result in the formation of ferrite, with martensite formed under more rapid cooling conditions.

Table 2.*2* shows the transformation temperatures for P91 steel [4]. An essential aspect of heat treatment is to carefully observe the temperature ranges at which a material undergoes transformation. Knowing the martensite start and finish (M_s and M_f) temperatures during welding is useful for selecting optimised minimum preheat and maximum interpass temperatures and being aware when retained austenite might be present after welding and before PWHT [12].

Table 2.2: Typical transformation temperatures for P91 steel [4]

Phase transformation	**Temperature**
Lower critical temperature (A_{c1})	810-825 °C
Upper critical temperature (A_{c3})	912-930 °C
Martensitic formation start temperature (M_s)	390-400 °C
Martensitic formation finish temperature (M_f)	200-230 °C

It is also important to ensure that the PWHT soaking temperature level is set at sufficient margins below the lower mixed austenite – ferrite domain boundary temperature (A_{c1}) in order to avoid fresh/un-tempered martensite to be present in the weld after PWHT when cooling to ambient temperature. Figure 2.3 shows results from dilatometry tests performed by Doubell et

al. [12]. For weld metal and base metal Doubell et al. [12] gives measured transformation temperatures. Dilatometry is a powerful analytical technique to determine the dimensional changes in a material as a function of temperature. These changes are then correlated to the different phases of a material at different temperatures.

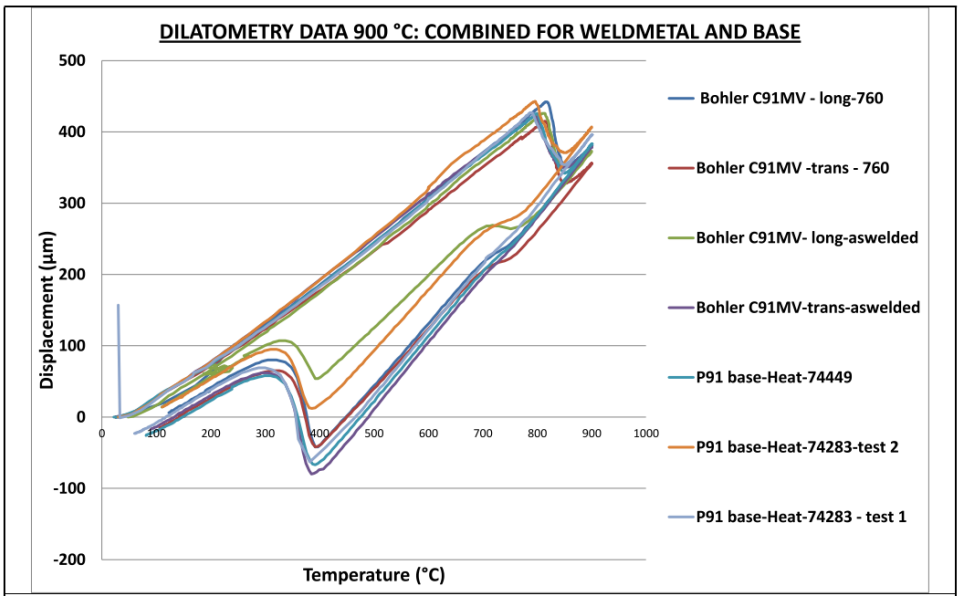

Figure 2.3: Superimposed dilatometer results for P91 BM and WM [12]

Table 2.3 shows the measured transformation temperatures for two P91 base metals and different weld consumable materials. These values were extracted from results in Figure 2.3. The table shows transformation temperatures for filler material and P91 base metal.

Table 2.3: Measured transformation temperatures [12]

Heat #	**Sample ID**	**Temperature** (degrees °C)			
		Ac3	**Ac1**	**Ms**	**Mf**
WG H74283	900-P91H74283-test1	848-853	787-791	382	288-300
WG H74449	900-P91H74449-test1	852-855	799-800	392	299-310
V&M171290	900-3-test2-PD	854	795	395	330-345
Bohler C9MV-IG	900-P91-WM-AW-long	848-858	810-815	392-397	326-337
Bohler C9MV-IG	900-P91-WM-760-trans	851-854	813-815	392	310-326
Bohler C9MV-IG	900-P91-WM-760-Long-	852-855	815-818	392-397	305-321

Table 2.4 shows the measured transformation temperatures for P91 base metal as reported by Doubell et al. [12]. These values differ from values reported in Table 2.2, this could be due to different experimental approaches. There is no experimental approach reported for values in Table 2.2.

Table 2.4: Measured transformation temperatures for P91 Base metal [13]

Phase transformation	**Temperature °C**
Lower critical temperature (A_{c1})	787-800°C
Upper critical temperature (A_{c3})	848-855°C
Martensitic formation starts temperature (M_s)	382-392°C
Martensitic formation finish temperature (M_f)	288-310°C

Time-Temperature-Transformation (TTT) diagrams can be used to design heat treatments for P91 steel [7]. The microstructure formed can be estimated using TTT diagrams that show the possible microstructure state for different temperatures and cooling times. The normalising of P91 steel above A_{c1} temperature results in transformation of austenite (FCC) into lath martensite (BCT) on rapid cooling. The 100% total transformation of austenite into martensite is necessary for optimal material strength. If the transformation of austenite is incomplete, there will be retained austenite in the microstructure and the material will have poor strength before tempering.

Wright and Lesica [13] conducted work on effects of PWHT on creep rupture properties of P91 steel. They recommend that the post-weld heat treatment of any Grade 91 steel should be conducted by first determining the A_1 temperatures of all involved materials, including the filler metals and base metals. The upper bound temperature for PWHT should not be higher than the lowest A_1 temperature of all materials. The lower bound temperature for PWHT should be sufficient for restoring toughness to prevent brittle fracture as a result of residual stresses.

A schematic diagram showing evolution of precipitates during the normalising and tempering treatment is shown in Figure 2.4 [4]. This shows that the solid-state phase transformations occurring in P91 steel during heat treatment. Therefore, different heat treatments should result in different solid-state transformations.

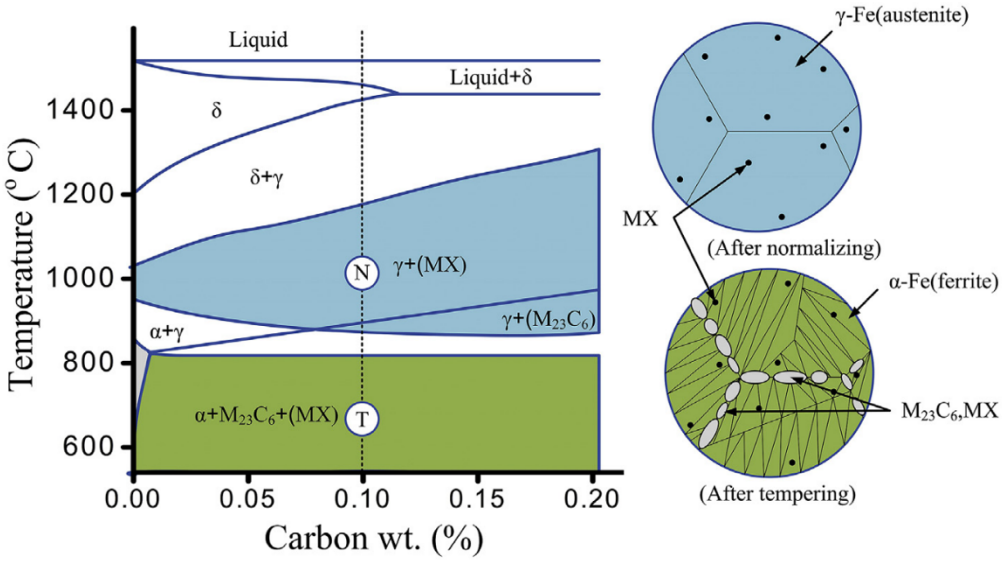

Figure 2.4: Schematic diagram of evolution of MX and $M_{23}C_6$ precipitates during normalising and tempering [4]

By controlling the applied thermal cycles for a number of different manufacturing processes, Continuous Cooling Transformation (CCT) curves can be used to develop required microstructures [7]. Figure 2.5 shows the CCT diagram of P91 steel. The solid phase composition and resulting microstructures expected following cooling from a given temperature can thus be estimated from the CCT diagram based on rate of cooling. In this study, the CCT diagram was used as a guide to design heat treatments based the expected solid-state composition for each heat treatment.

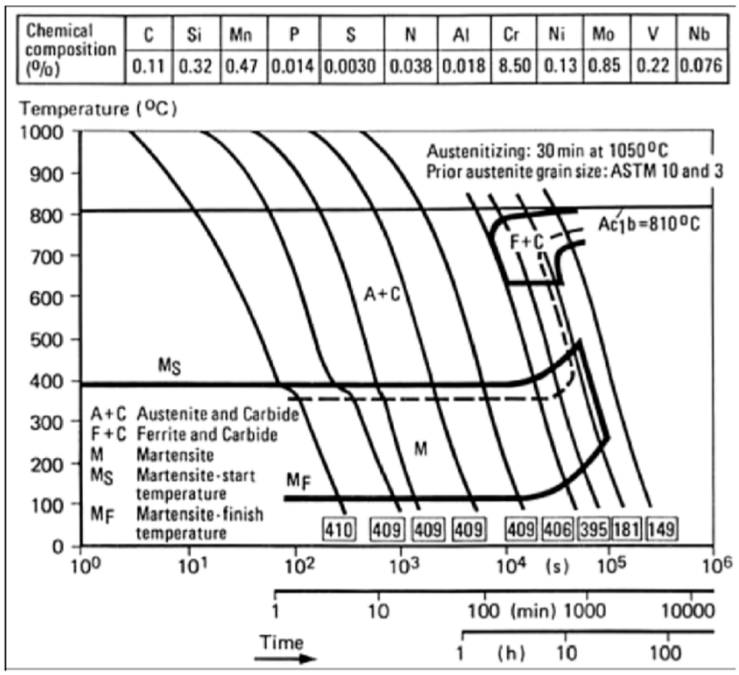

Figure 2.5:Typical continuous cooling diagram for Grade 91 steel [7]

Experiments conducted by Pandey et al. [2] investigated the effect of post-weld heat treatments on the microstructure evolution and type IV cracking behaviour of P91 steel welds.

2.1.4 Type IV Cracking in Weldments

Type IV cracking is creep cracking which occurs at the parent material/heat affected zone (HAZ) interface in ferritic steel weldments. Thus, it occurs at the edge of the HAZ in the over-tempered, intercritical or refined region of the HAZ. It was first detected in the HAZ of girth welds in 0.5wt% CrMoV steel steam pipework operating at temperatures around 550 to 570°C [14]. It has since been detected in most low alloy ferritic steels which rely on dispersion strengthening for creep strength, e.g., 1-1.25 wt% CrMo, 2.25 wt% CrMo, 9 wt% CrMoVNb. This form of cracking is found in elevated temperature pipeline girth welds and seam welds, pressure vessel end-cap welds, pressure vessel nozzle intersections, pipe branch connections, etc [14].

Figure 2.*6* shows a schematic diagram of evolution of cracks in P91 weldments. Pandey et al. [4] observed that in P91 welded joints, when subjected to long-term creep exposure, Localised creep cavitations in the HAZ led to intergranular fracture. This type of cracking is termed Type

IV cracking. The study shows that the type IV cracking mainly nucleates from the HAZ present in weldments. However, it is difficult to clearly distinguish the location of HAZ.

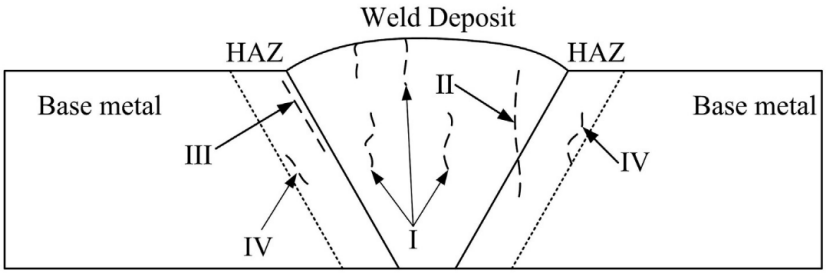

Figure 2.6: Schematic diagram of evolution of cracks in P91 weldments[4]

Type IV cracking initiates from localised formation and growth of creep voids in the 'Type IV zone'. A significant feature of the subsequent cracking is that it can be relatively rapid. The crack can be regarded as an 'unzipping' of an already creep-damaged zone. For pipe girth welds, the phenomenon usually leads to a leak-before-break situation. However, for pipe seam welds or end-cap welds, failures have often been catastrophic ruptures [14]. Type IV cracking is detectable by ultrasonic non-destructive testing (NDT).

2.2 P91 Steel Welding

A typical weldment can be differentiated into three different zones i.e., the weld fusion zone, HAZ and the over tempered base metal. These different zones exhibit distinct topology of microstructure and mechanical properties [15]. The weld zones forms due to thermal weld cycles. Failure of P91 steel has been observed in different areas across the weldments depending on heat treatment on the material.

There are many suppliers for P91 base materials and welding consumables for fabrication. Issues have been noted in the fabrication of thick-section components and in field fabrication. These issues are typically related to improper or inadequate heat treating and bending operations. It has been reported that improper heat treatment has resulted in the formation of “soft spots” in piping and other thick- section components [15].

According to the EPRI welding guide for P91 [15], well manufactured welds should outperform the heat affected zone. Differences have been observed in hardness between the base metal, weld metal and HAZ for a Grade 91 steel weldment. The commonly exhibited “soft zone” in the HAZ exists in all CSEF steels and corresponds to the fine grained (FGHAZ) and intercritical region of the HAZ (ICHAZ). Figure 2.7 shows different fracture modes characteristic of thick-section failures (as in headers and/or piping possible in P91 welds.

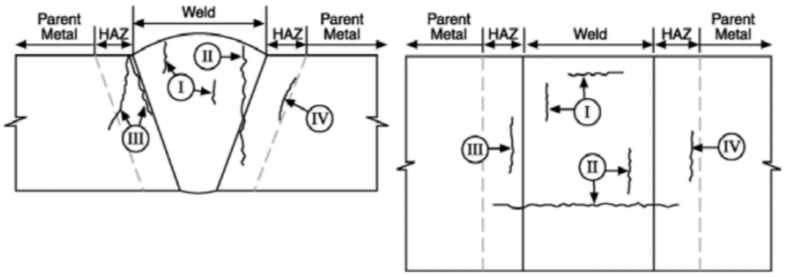

Figure 2.7:Typical Fracture Modes in Cr-Mo and CSEF Steel Weldments [15]

As previously indicated in Section 2.1.4 on Type IV cracking in weldments, the common type of failure in P91 weldments is known as "Type IV" cracking. Dislocation substructure, precipitate coarsening, refined grain size, and other factors influence high temperature creep properties in the HAZ region. In application if a weld is required, In the case that similar chrome strength enhanced ferritic (CSEF) weld metal (as is most often the case) is used, the weld metal and base metal are usually stronger than the either FGHAZ or HAZ in general [15]. As a result, damage accumulates in the Type IV region in the form of creep voids, and the linking of these voids will cause eventual cracking.

The only way to avoid premature failure in the HAZ is to subject the weldment to a normalise and temper (N+T) heat treatment, which will eliminate the HAZ [2]. Such a heat treatment is only possible if the appropriate weld metal is used and evaluated to ensure adequate properties following a N+T heat treatment. Typically, such a heat treatment is not practical or feasible for many complex components and cannot be done in field conditions because adjacent material outside the heated band will be subjected to an intercritical temperature excursion.

2.2.1 Welding processes

The EPRI P91 welding guide gives guidelines on welding procedures for P91 Steel [15]. According to this guide, welding of CSEF steels is accomplished with the common arc processes i.e., Submerged Arc Welding (SAW), Shielded Metal Arc Welding (SMAW), Gas Tungsten Arc Welding (GTAW -TIG), Gas Metal Arc Welding (GMAW - MIG) and Flux-Cored Arc Welding (FCAW). Filler metals have been formulated to complement a given CSEF base metal. During production, these consumables require refinement to achieve low levels of residual elements [15]. Weld metal deposited with TIG typically exhibits far greater toughness than weld metal deposited by processes using flux and slag systems (for example, FCAW, SMAW or SAW). This variation is explained by a significant difference in weld metal oxygen content and the decrease in the populations of non-metallic inclusions. As a result, the TIG (GTAW) process is commonly required for pipe roots and other small diameter or thin wall pipe. Although much slower than other processes, the GTAW process still provides weld deposits with the highest integrity.

The SMAW / SAW process is commonly preferred for very thick section welds that can be rotated or manipulated into the flat position for the weld [15]. Regardless of welding process, component or consumable, low hydrogen controls must be implemented and maintained during fabrication. Such controls are equally important in the procurement, use, and storage of welding consumables. Manufacturer's recommendations for storage and reconditioning must be observed such as keeping electrodes in dry storage. Other precautions such as purging of inert

gas, weld positions and recommendations on bead profile and sequence should be followed to achieve optimal welds, as these have significant effect on toughness.

2.2.2 Filler material

The American Welding Society has material specifications for P91 filler material and as part of ongoing research EPRI has provided some guidelines for filler material selection shown in Table 2.5 [15].

Table 2.5: EPRI Filler material recommendations[15]

Elements (wt. %)	ASME SFA 5.5:2010 E901X-B9	ASME SFA 5.28:2010 ER90S-B9	ASME SFA 5.23:2011 EB91	ASME SFA 5.29:2010 E9XT1-B9	EPRI Recommendations[3]
C	0.08 – 0.13	0.07 – 0.13	0.07 – 0.13	0.08 – 0.13	
Mn	1.20	1.20	1.25	1.20	0.70 – 1.20
Si	0.30	0.15 – 0.50	0.50	0.50	
P	0.010	0.010	0.010	0.020	0.010[2]
S	0.010	0.010	0.010	0.015	
Ni	0.80	0.80	1.00	0.80	
Cr	8.0 – 10.5	8.0 – 10.5	8.5 – 10.5	8.0 – 10.5	8.5 – 9.5
Mo	0.85 – 1.20	0.85 – 1.20	0.85 – 1.15	0.85 – 1.20	
V	0.15 – 0.30	0.15 – 0.30	0.15 – 0.25	0.15 – 0.30	
Cu	0.25	0.20	0.10	0.25	
Al	0.040	0.040	0.040	0.040	0.020
Cb	0.020 – 0.10	0.020 – 0.10	0.020 – 0.10	0.020 – 0.10	
N	0.020 –	0.030 – 0.070	0.030 – 0.070	0.020 – 0.070	0.040 – 0.070
Ni+Mn	1.50	1.50	1.50	1.50	1.0
As					0.010
Sn					0.0050
Sb					0.0030

In general, when welding identical CSEF steels together, it is suggested to utilise nominally matching filler metal (that is, when welding Grade 91 to Grade 91, a – B91 consumable would be utilised). Finite Element Analysis (FEA) modelling studies conducted to show whether undermatching or overmatched filler materials are more suitable have shown that the overmatched weld metal imposed a constraint on the CGHAZ and in turn, the CGHAZ and base material concentrated stress in the FGHAZ [15]. EPRI research studies suggest using a less strong filler material to decrease stress concentration in the fine-grained heat-affected zone (FGHAZ) and using a matching filler metal is more advantageous than undermatching or overmatching fillers [15].

2.2.3 Preheating

The use of preheat when welding CSEF steels minimises the susceptibility to hydrogen induced cracking (HIC) [15]. To a lesser extent, preheat reduces cooling rates during welding and can therefore (at least theoretically) reduce the hardness level, especially in the HAZ. Preheating of weld joints is achieved through use of electric induction. Though not new, the use of electrical induction for preheat and PWHT is gaining favour because equipment has become smaller, more portable and more user friendly. Preheating can also be conducted in furnace or electrical resistance methods.

Tests performed on Grade 91 have revealed that a 175°C - 200°C minimum preheat is required to completely avoid cracking [16]. EPRI research [15] has indicated that the use of elevated preheat in Grade 91 weldments (specifically an increase from 250 to 350°C) may increase the creep strength of the weldment by a considerable amount. Work done at EPRI through a

supplemental project on Grade 91[15], indicated that the use of elevated preheat had no effect on the creep strength of the weldment. Table 2.6 [15] shows the recommended preheat and interpass temperatures for different welding processes.

Table 2.6 : Recommended preheat and interpass temperatures [15]

Process	Application	Min Pre-heat °C	Max interpass °C
GTAW	Any	150	350
SMAW, SAW, FCAW, GMAW	Tubing	150	350

The typical interpass maximum for CSEF steels is 315°C. The interpass maximum helps to control the bead shape and subsequently prevent the possibility of hot cracking due to the silicon and niobium content of the weld metal [15]. Furthermore, imposing an interpass maximum allows the weldment to cool to below the martensitic start temperature [M_S is typically in the range of 370 to 427°C, and therefore promotes tempering of the transformed martensitic microstructure]. The preheat temperature applied to material used in this work is 193.2°C and an interpass temperature of 225.2°C. These values are within acceptable range and speak to proper heat treatment practice.

Exceeding maximum interpass is difficult to avoid in thin welds. It is therefore recommended [15] that should thin tubing be welded in any CSEF steel, it is advisable to use thin beads, less filler metal and a lower heat input to avoid exceeding the suggested interpass requirements .Original equipment manufacturers specify posted weld cooling requirements for supplied P91.

A post weld bake may be of critical importance, especially for heavy sections or where flux-type processes are used [15]. This involves maintaining the preheat/interpass window for an extended period of time either during or following completion of the weld. This post weld bake provides additional time for the diffusion of hydrogen in the weldment and thereby preventing trapped hydrogen from causing cracking and also reduce the risk of stress corrosion cracking (SCC).

If the consumable or procedure is not accurately documented, a post weld bake is always recommended to be implemented to ensure that the risk to hydrogen induced cracking (HIC) is minimised. The suggested procedure for a post weld bake involves holding in the temperature range of 260 to 400°C for a minimum time of 1 hour for thicknesses of 1 inch or less and two hours if the thicknesses is greater than 1 inch [15].

2.2.4 P91 Weldment Microstructure

Heterogeneous mechanical properties such as toughness and hardness across HAZs can lead to the initiation of the defects in the weakest zone. Such variation of microstructural and mechanical properties in HAZs can be very severe in high strength steel such as Cr-Mo steels [2].

Chen and Yamashita [17] conducted experiments on effects of PWHT temperature on mechanical properties of high chromoim ferritic heat-resistant steel weld metals. Some samples were subjected to post weld heat treatment at 760 °C for 2h and air cooled. As-welded and

PWHT specimens showed the Type IV mode of failure. The fracture reportedly occurred in soft fine-grained heat affected zone/inter-critical heat affected zone (FGHAZ/ICHAZ).

Other samples were normalised at 1040°C for 60 min, air cooled and tempered at 760°C for 2 h, then air cooled. In these samples, a shift in fracture location was observed from FGHAZ/ICHAZ to over tempered base metal zone [2]. The results indicated a great influence of heat treatment conditions on the fracture location and microstructure evolution of the P91 welded joint.

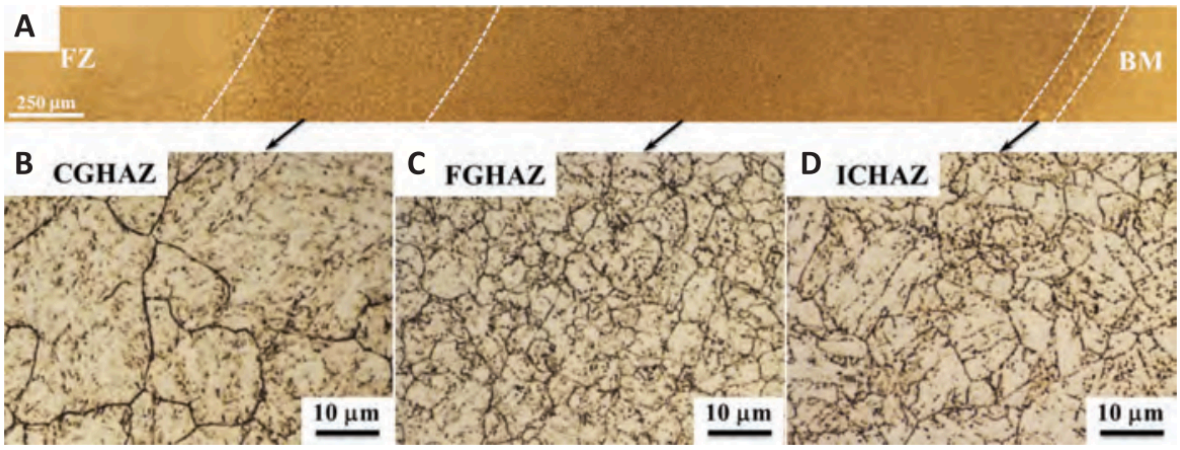

Figure 2.8: Microstructure of HAZ in as-welded P91 Specimen [13]

Figure 2.9 shows typical heat-affected zone regions in a 25mm thick P91 pipe joint [13]. The weldment was fusion welded using a matching flux-cored wire. The microstructure of the ICHAZ in Figure 2.8 d, shows a heterogeneous mixture of finer grains which were formed during thermal welding cycles and coarser grains retained from the base metal. Figure 2.9 shows a schematic diagram of the HAZ in relation to the equilibrium phase diagram of P91 weldments.

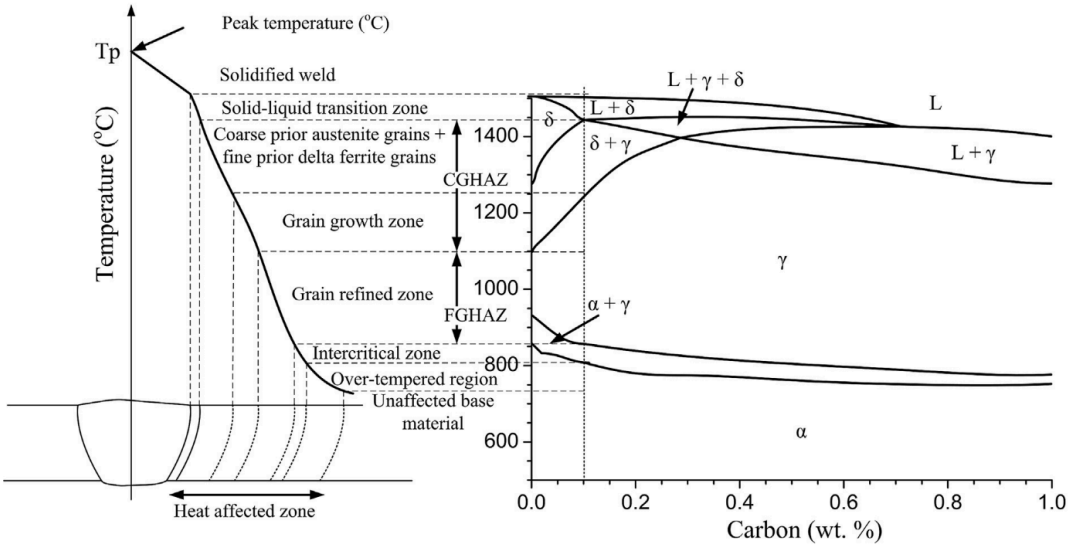

Figure 2.9: Schematic diagram of the sub-zones of the HAZ and relation to the calculated equilibrium phase diagram of P91 weldments[4]

Work by Wang and Li [18] on the evolution of microstructure of the weldment of P91 steel showed that the as-welded FGHAZ has a microstructure of martensite laths within fine prior austenite grains. The undissolved, Cr-rich $M_{23}C_6$ carbides are distributed on the PAGBs and some lath boundaries. Fine $M_{23}C_6$ carbides nucleate on the PAGBs and internal martensite laths. PWHT tempering produces fine equiaxed ferrite grains and coarsened precipitates. Elevated temperature tensile tests further temper the martensite, and promotes the grain growth with an increased HAGB/LAGB ratio. The paper also states that coarsening and segregation of Cr-rich $M_{23}C_6$ carbides in specific grains causes a higher local strain during creep.

The main mechanism of the intergranular fracture of P91 welds during creep is because of the nucleation and growth of cavities in the FGHAZ/ICHAZ [18]. The nucleation of initial cavities during creep in the FGHAZ and ICHAZ is promoted by the creep strain mismatch between the un-recrystallised grains that seem to contain precipitates and fully recrystallised grains that seem to be precipitate-free [18]. This is because the welding thermal cycles in the ICHAZ and outer edge of the FGHAZ do not have high enough peak temperatures to promote the formation of grains with uniformly distributed precipitates [18]. Instead, the lower peak temperature experienced in the ICHAZ and HAZ tends to retain the variations in precipitate distribution in the base metal microstructure. The non-uniform distribution of carbides is further enhanced by recrystallization during PWHT i.e. the formation of precipitate-rich and precipitate-free grains [18].

Wright and Lesica [13] conducted experiments where they assessed the mechanical properties of the different weld zones in as-welded and PWHT specimen. PWHT temperature affects microstructure, material hardness and tempers the microstructure, with decomposition of tempered martensite to ferrite. PWHT at temperatures above Ac_1, results in a higher hardness and formation of fresh martensite. Wright and Lesica [13] conducted PWHT at 600°C and temperatures between 760 C to 820°C. Based on this work, the as-welded P91 microstructure is a mixture of tempered martensite and some untempered martensite, with a 475 HV hardness.

PWHT at 600°C starts to temper the microstructure and the hardness decreases slightly. PWHT at 760°C to 820°C significantly tempers the microstructure, with decomposition of tempered martensite to ferrite [13]. The hardness decreases even more to 390 HV. PWHT at 840°C, however, increases the hardness, because the heating temperature is above the Ac_1 temperature. The HAZ microstructure showed that the coarse grain zone has seen martensite tempering, refinement of coarse grains through recrystallization, and the fine grain zone has seen grain growth

Reduced hardness with increased PWHT temperatures; martensite decomposes to ferrite. Stress relaxation tests conducted at 650°C with 1.5 % total strain, shorter times. Higher heat treating temperatures produce increased strain rates with no benefit in prolonging PWHT time. Figure 2.10 shows the hardness of the different regions of the HAZ at different PWHT temperatures by Silwal et al. [19].

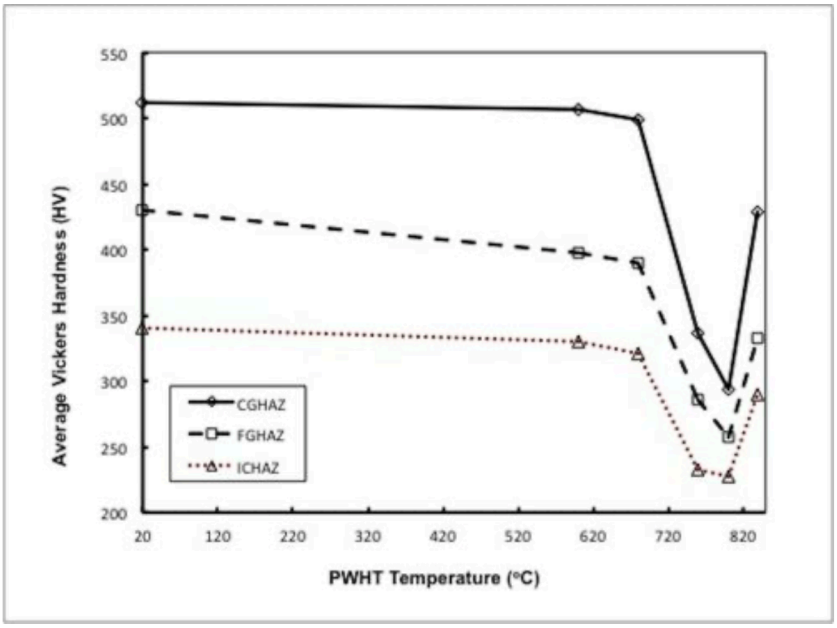

Figure 2.10: Vickers hardness values of different HAZ zones after post-weld heat treating at various temperature [19]

Figure 2.10 shows that in the as-welded HAZ, the hardest region is the CGHAZ, where the microstructure is fresh and tempered martensite. The second hardest is the FGHAZ, the microstructure is fine-grained tempered martensite [19]. The ICHAZ is the softest, the microstructure is a mixture of ferrite from the base metal and tempered martensite.

In PWHT coarse grains form through recrystallization, and the fine grain zone has seen grain growth. CGHAZ at 600°C PWHT is similar to as-welded with tempered martensite, PWHT at 800°C [19] shows tempering of martensite to ferrite, with associated carbide precipitation, new ferrite subgrains. PWHT at 840°C refines the grains, coarsens carbides and forms new martensite resulting in increased hardness compared to 800°C.

In the work by Silwal et al. [19], uniaxial tensile tests were also conducted on a Gleeble 3800D thermal-mechanical simulator. The uniaxial tensile tests were done to determine the temperature-dependent mechanical properties of Grade 91 steel weldments. Young's modulus of different weld regions following a 760°C-2h PWHT, values were measured from high-temperature tensile tests at 650°C.

2.3 Recommended PWHT for P91 Steel

Pandey et al. [2] had P91 weld joint samples undergo PWHT at 760°C for 2 h, followed by air cooling and PWNT re-austenitising at 1040°C for 60 min/air cooling then tempering at 760 °C for 2 h, followed by air cooling. The samples were tested for creep under 150 and 200 MPa applied stress. Pandey et al. [2] observed that PWHT resulted in a notable increase in creep rupture life as compared to as-welded condition for the high level of applied stress of 200 MPa. The maximum creep exposure life was measured for the PWNT condition in low stress of 150 MPa.

Homogeneous microstructure and hardness were reported across the welded joint of P91 steel PWNT condition. After the PWNT treatment, the fracture location was observed to have shifted from the soft FGHAZ (Type IV) to over tempered base zone (Type V) due to homogeneity across the weldments [2]. This further shows how heat treatment can improve the weld mechanical properties of P91 by improving microstructural homogeneity.

The EPRI Creep Strength Enhanced Ferritic steel guide [15], provides guidelines on PWHT of P91 steel and times. The guidelines are drawn based on data obtained from various experiments on P91 steel. It recommends PWHT of sections under 13 mm, to be conducted at recommended temperatures and time. The recommended temperature is 760°C for 0.5 h. Thicker, 28 mm sections can undergo PWHT at 760°C for 1-5 h. Wright and Lesica [13] conducted experiments on effects of PWHT on creep rupture properties of Grade 91 Steel heavy section welds. After PWHT samples were subjected to side bend tests. Figure 2.11 shows the results from the bend tests. The results show curves best fit on experimental results. Suitable PWHT temperature and times will be within the ductile range. The EPRI recommended temperature of 760°C for 1-2 h falls within this range.

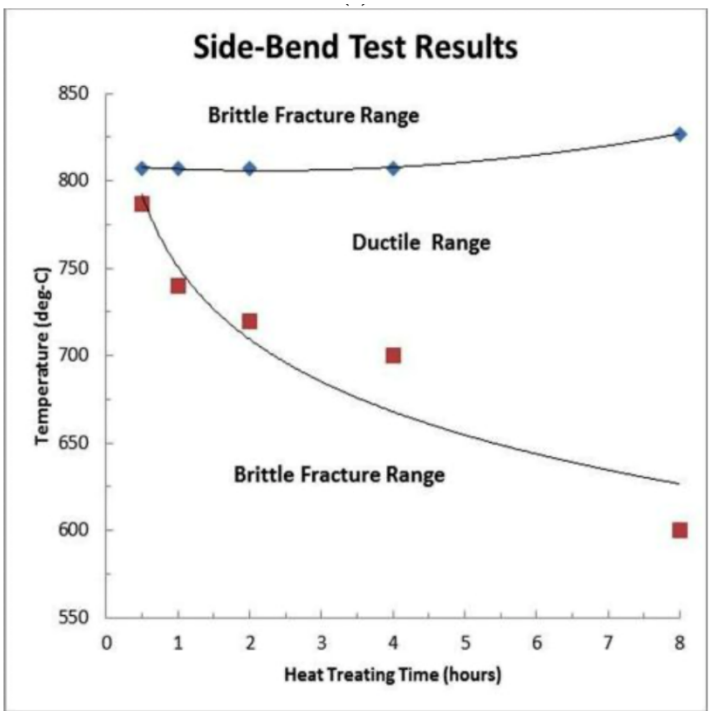

Figure 2.11: Plot of ductility range for various heat treating temperatures and times [13]

Wright and Lesica [13] recommend PWHT at 720°C-770°C for 2h for pipes less than 30 mm because PWHT at this temperature has the highest recovery of impact energy. Figure 2.12 a, shows the impact energy of P91 base metal after heat treatment at 760 °C for 2 h. Figure 2.12 b, shows the impact energy of different weld zones at different PWHT temperatures, comparing to Figure *2.12* a, it can be seen that the highest recovery of impact energy is between PWHT at 720°C -770°C. Experimental results shown in Figure 2.13 also show that the total creep strain at 720°C 2h is lower than at 600°C 2h, which suggests an improvement in mechanical properties as a result of heat treatment. The higher impact energy recovery for PWHT at 720°C -770°C and low creep strain rate, suggests improved mechanical properties compared to PWHT at temperatures outside this range. For PWHT at temperatures above the 820°C, the creep strain

rate and creep ductility significantly increase, failure location was observed to switch to the weld fusion zone, resulting in Type I failure. There may not be any significant effect realised from increasing heat treating time because of insignificant differences between strain rates for PWHT at 760°C for 2 and 8h as shown in Figure 2.13.

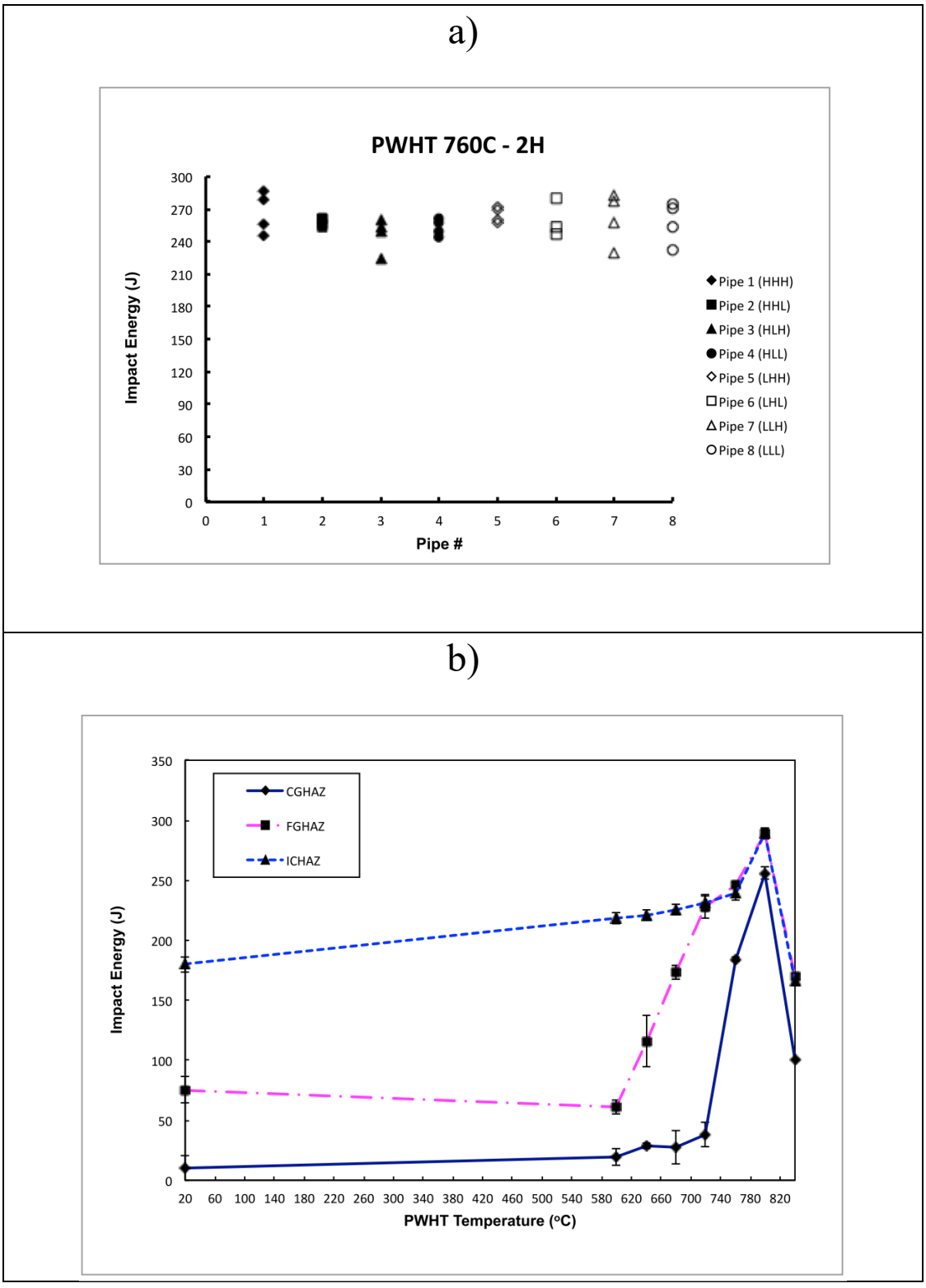

Figure 2.12:As-welded impact energy and impact energy results of different HAZ zones [13]

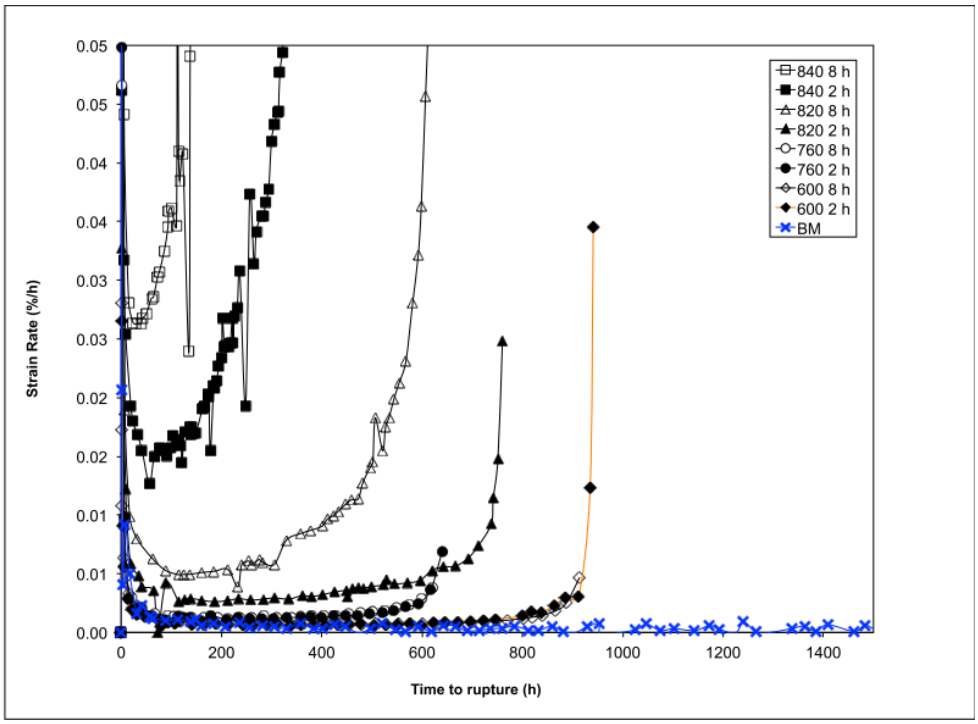

Figure 2.13: Creep strain rate as a function of time for Grade 91 pipe welds of various post-weld heat treating conditions [13]

Figure 2.14 and Figure 2.*15* show recommended post weld heat treatment processes for different thickness sections for P91 [9].

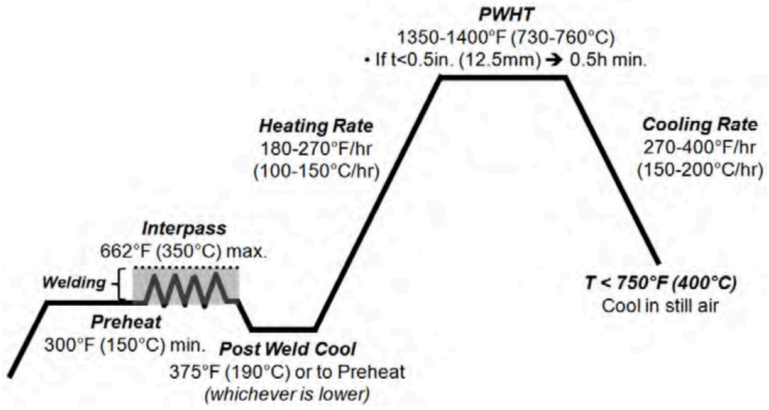

Figure 2.14: Typical PWHT Schedule for Thin-section Grades 91 [9]

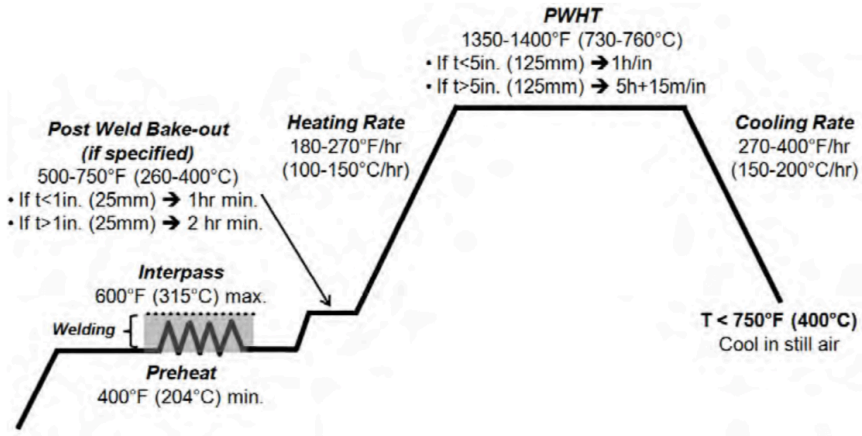

Figure 2.15:Typical PWHT Schedule for thick-section Grades 91/92 [9]

PWHT should follow welding as soon as possible to avoid delayed cracking or more important, stress corrosion cracking. However, if the weld region can be kept dry, PWHT can be delayed. Standards codes do not offer rules or guidance about elapsed time between completion of welding and PWHT [15]. This time is not a technical concern for many materials. CSEF materials in the as-welded condition prior to PWHT are typically very strong, exhibit high hardness with little ductility and could be especially susceptible to stress corrosion cracking.

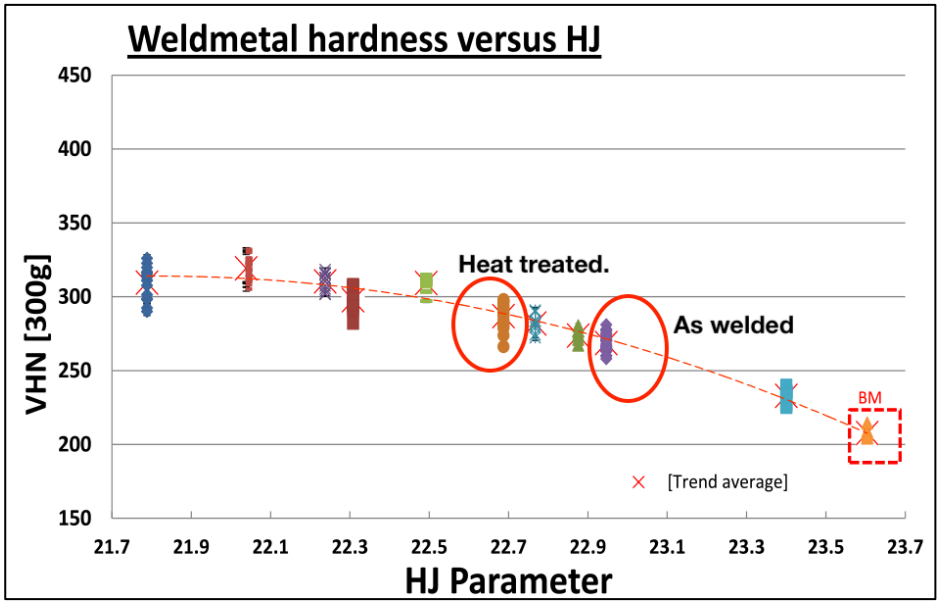

Figure 2.16:Weld hardness plot vs HJ (As- welded conditions not visible on this HJ scale [12]

Figure 2.16 shows results from hardness tests conducted by Doubell et al. [12] on P91 weldments by Hollomon-Jaffe (HJ) parameter. The Hollomon-Jaffe parameter, HJ, is used to compare the response of a steel to a tempering treatment [20], e.g. post-weld heat treatment (PWHT), by describing an equivalence of time and temperature for thermally activated processes. The results show that the weldment in as-welded samples prior to heat treatment are relatively strong with a higher hardness compared to base metal. PWHT further improves material impact toughness.

2.3.1 Application of HJ Parameter to Assess tempering response

Doubell et al. [12] used an Hollomon-Jaffe (HJ) parameter to present mechanical test results. Therefore, the necessary time required to use an alternative PWHT temperature can be calculated to see if it is a viable alternative to a current treatment.

The parameter has a general form:

$$H = \frac{T(C+\log t)}{1000} \quad \text{.....2-1}$$

where H is the Hollomon-Jaffe parameter, T is the temperature in Kelvin (°C + 273.15), C is a constant and t is the time in hours for an isothermal condition (temper time).

The HJ equation [12] was applied for presenting mechanical test results. The equation also takes into account the tempering that occurs when a component is heating to and cooled from the set soaking temper temperature.

According to Doubell et al. [12], for PWHT, the hardness of P91 weld metal is a function of the HJ parameter and the function is not influenced by the welding process (TIG and MMAW). Doubell et al.[12] applied a modified version of the HJ parameter that also considers the tempering that occurs when a component is heating to and cooled from the set soaking temper temperature. The modified HJ equation is shown below:

$$H = \frac{T(C+log(\tau))}{1000} \quad \text{.....2-2}$$

where τ is the effective temper time taking into account tempering during heating and cooling given by:

$$\tau = t + \frac{T}{(2.3(k_1)(20-log(k_1)))} + \frac{T}{(2.3(k_2)(20-log(k_2)))} \quad \text{.....2-3}$$

where:

k_1 = heating rate in K/h
k_2 = cooling rate in K/h
t = selected temper time
T = Temperature in Kelvin

Hence the HJ parameter is a useful tool that can be used to prescribe to site personnel the minimum PWHT temper-time parameters to obtain the required critical mechanical properties and for and investigators of anomalies/failures to screen welds for conforming the specifications [12]. The HJ parameter can be used in designing heat treatments for a specific hardness. Heat treatment parameters can be used to determine HJ parameters and subsequently estimate mechanical properties such as yield strength, impact energy and hardness for different PWHT temperatures.

Hardness vs HJ parameter of weld metal can be used per welding process to prescribe hardness ranges to be used in Quality Control (QC) pertaining to soaking time and temperature (confirm suitability of PWHT to reach required mechanical properties) [12].

2.4 Tensile Testing

The ASME B&PV Code Section I allows an operational temperature limit of 649 °C for grade 91 steel [21]. This was determined based on microstructural stability and creep strength [21]. The elevated temperature tensile tests followed the EPRI recommended service temperature below 560 °C, 80 MPa stress. The service temperature is recommended to avoid exfoliation due to oxidation in service for 150,000 hours [21].

The results of these tensile tests can be considered as only a comparative measure of the strength and ductility for service times of many hours. Therefore, the principal usefulness of the elevated-temperature tensile test was to assure that the tested material was similar to reference material when other measures such as chemical composition and microstructure also showed the two materials were similar [22].

The standard for elevated temperature tests, ASTM E21 [22] recommends that testing apparatus should provide temperature control and heating by means of electrical resistance or radiation with the specimen in atmospheric pressure. A Gleeble 3800D thermomechanical machine was used for elevated temperature tensile tests. It can heat the specimen and simultaneously apply stress.

The Gleeble heats the specimen through direct electrical resistance heating with an alternating current of 50 Hz. The resistance heating technique can maintain equilibrium temperatures within ± 1°C. This machine can heat the samples at very fast speeds up to 10,000°C per second and is combined with a force of 20 tons in compression or 10 tons in tension.

Experiments conducted by Van Rooyen et al. [23] and Curry et al. [24] showed that the specimen geometry is important in achieving repeatable stress strain results within the test specimen. The specimen geometry influences temperature and stress distribution within the specimen.

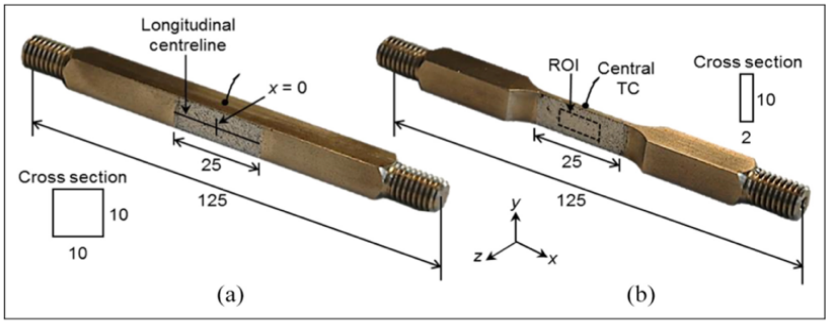

Figure 2.17: Gleeble specimen [23]

Figure 2.17 shows the standard Gleeble specimen with a square 10x10 mm cross section and the modified specimen with a 10x2 mm gauge region in work done by Van Rooyen et al. [23].

Figure 2.18 shows specimens temperature profiles. Square and flat specimens had different temperature gradients across the specimen.

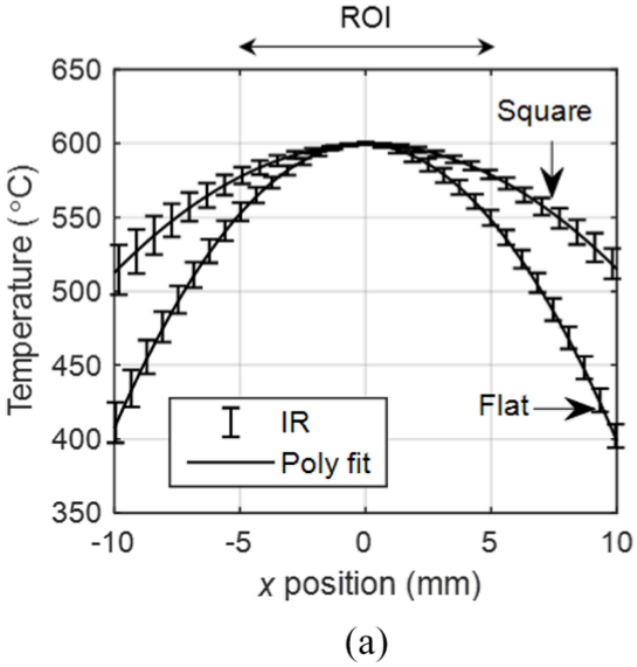

Figure 2.18: Specimen temperature gradient [23]

The temperature gradient symbolises thermal symmetry about centre of specimen. Thermal distribution at centre of plane can be represented by a second order polynomial equation:

$$\frac{dT(\frac{L}{2},t)}{dx} = 0 \quad \text{.....2-4} \quad [23]$$

where T is temperature, L is the length, t is the thickness and x is the incremental distance [25]. Van Rooyen and Becker [26] created an FEM Model to investigate the effect of thermal profile on stress distribution. Figure 2.*19* shows a non-uniform stress region observed in the gauge region resulting from variable expansion effects of a non-uniform thermal profile Expansion results in compressive stress that reduces the applied stress to lower values especially in gauge centre. The results from the FEM model are shown in Figure 2.*19*. A narrow region of uniform stress was also observed to develop across the gauge area. Square specimens have a more gradual temperature gradient, and therefore larger tensile stresses develop within the specimen.

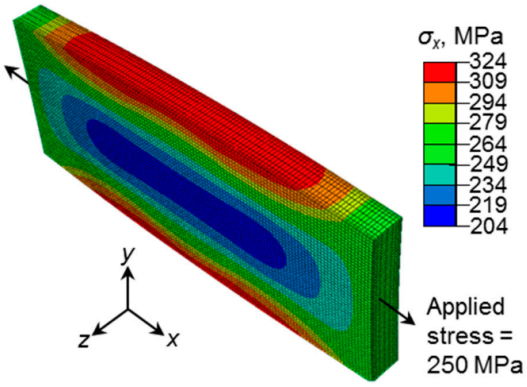

Figure 2.19: FEM Model for gauge region [23]

Curry et al. [24] also indicated that optimising temperature improves the length of the hot zone at the centre of the specimen. He further stated that the hot zone can be improved by:

- Inserting blind holes in specimen ends, 6 mm improves thermal gradient.
- Making use of stainless-steel grips increasing resistance of the specimen.
- Using stainless steel wedges to replace copper wedges on the Gleeble machine.

The experimental optimization resulted in a temperature variation of 10 °C variation over a central region of 8 mm incorporating the HAZ [24]. Wright and Lesica [13] conducted uniaxial tensile testing on a Gleeble thermomechanical machine to determine the temperature dependent mechanical properties of Grade 91 steel weldment. The specimen used had been subjected to PWHT at 760°C for 2h. The testing was done at 650°C and 70 MPa stress. Table 2.7 shows results from these tests. The results show that the ICHAZ and weld metal had the lowest young modulus. This coupled with the low hardness makes the ICHAZ a favourable location for failure. The values indicate a decrease in the Young's modulus of P91 steel at high temperature comparable to reported Youngs modulus values of P91 steel from spherical nano-indentation tests at varying temperatures, where the P91 Young's Modulus at room temperature was reported to be ~167GPa and 21GPa at 600°C [27]. The difference suggests that PWHT and elevated temperatures lead to a change in mechanical properties of P91 steel.

Table 2.7: Young modulus for different weld zones [13]

Constituents	Young's Modulus (MPa)
CGHAZ	26,615
FGHAZ	25,394
IGHAZ	9,491
Weld Metal	7,040
Base Metal	89,643

Ideally the HAZ was placed in the centre of the specimen where the temperature is the highest. The positioning of the HAZ in the hot zone helps establish the influence of temperature and post weld heat treatment on strain localization.

In this work the approaches and methodologies discussed were employed to examine the behaviour of Grade 91 steel under elevated temperature conditions. To ensure precise and repeatable results, elevated-temperature tensile tests were carried out following the EPRI recommended service temperature and stress conditions, with a particular focus on service times of extended durations.

The testing apparatus, as recommended by ASTM E21, will provide exact temperature control through electrical resistance heating, and a Gleeble 3800D thermomechanical machine was utilised. This machine's capabilities, including rapid heating rates and the application of controlled stress, will enable a thorough investigation into the material's behaviour at elevated temperatures. The impact of specimen geometry on stress and temperature distribution within the material was considered, as demonstrated by Van Rooyen et al. [23]. The study will employ specimen designs, such as the modified specimen with a 10x4 mm gauge region, to evaluate the effects of temperature gradients across the specimen and their influence on stress distribution.

The optimisation techniques outlined by Curry et al. [24], such as the use of blind holes, stainless-steel grips, and stainless steel wedges, were explored to enhance temperature uniformity within the specimen. This optimisation crucial in ensuring accurate and consistent results during testing. The positioning of the heat-affected zone (HAZ) within the specimen, as discussed by Wright and Lesica [13], was carefully considered to align with the region of highest temperature. This strategic placement of the HAZ will enable the investigation of temperature and post weld heat treatment effects on strain localisation. The techniques and insights gathered from the literature review were applied in the forthcoming work to conduct rigorous elevated-temperature testing of Grade 91 steel, with a focus on understanding its effect of PWHT on P91 weldments.

2.5 Digital Image Correlation

Digital Image Correlation (DIC) is a non-contact technique which can measure the strain using optical methods. According to Zheng et al. [28] digital image correlation was first proposed in 1980s. The method has recently been widely used for tracking deformation such as elastic-plastic strain distribution, evolution of plastic zone of steels, the true stress-strain curve over a large strain range, thermal expansion of films, and forming limit of metals in both macro and micro ranges. Zheng et al. [28] used the method for evaluation of large plastic deformation in metals. Figure 2.20 a shows the recorded DIC strain distribution at a 3mm stroke specimen deformation. Figure 2.20 b shows the resultant strain curve profile of the strain distribution across the specimen.

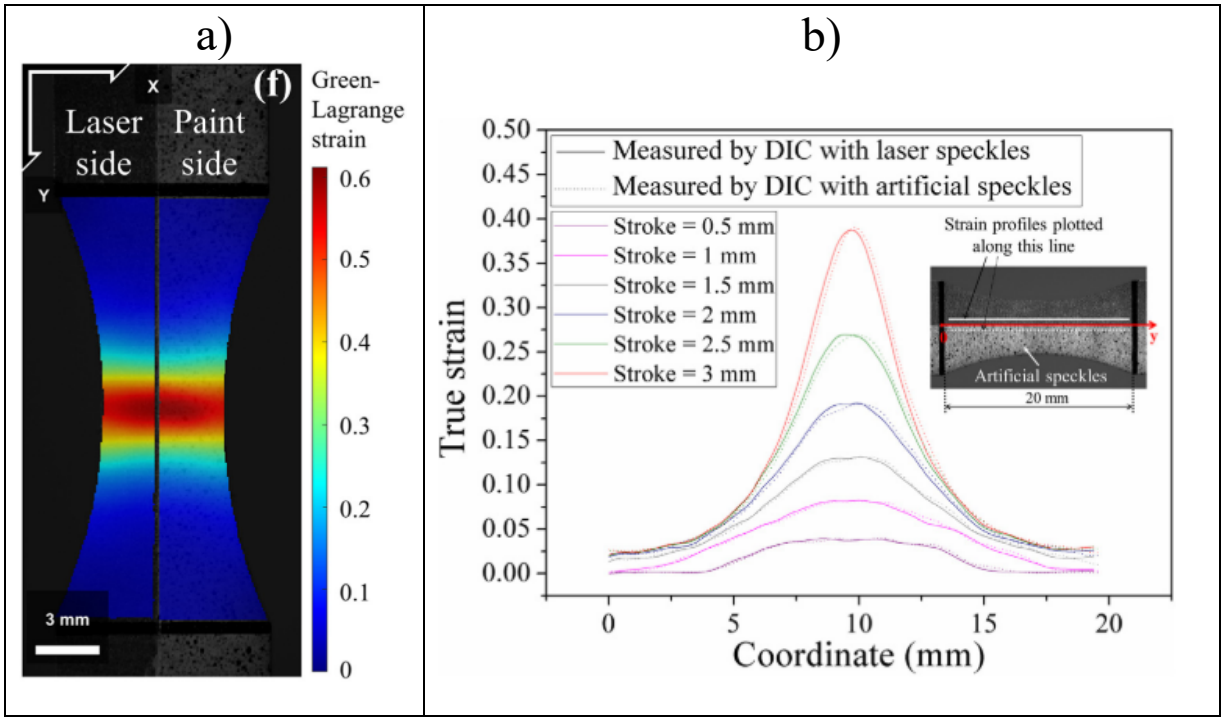

Figure 2.20: a) Strain distribution for laser and paint speckles and b) Specimen strain profiles [28]

A typical DIC system consists of light sources, digital cameras, and software programs for postprocessing the captured pictures. There are two DIC parameters that are critical to ensuring accurate DIC measurements, namely speckle pattern quality and facet size [29]. These parameters are discussed in detail in Section 2.4.2 on speckle patterns and Section 2.4.3 on facet size.

DIC has been adopted over the past 35 years. Since then, the hardware system and the correlation algorithm has been well developed. Figure .2.21 shows a DIC set-up in experiments done by Curry et al. [24] ; a similar set-up was used in this work.

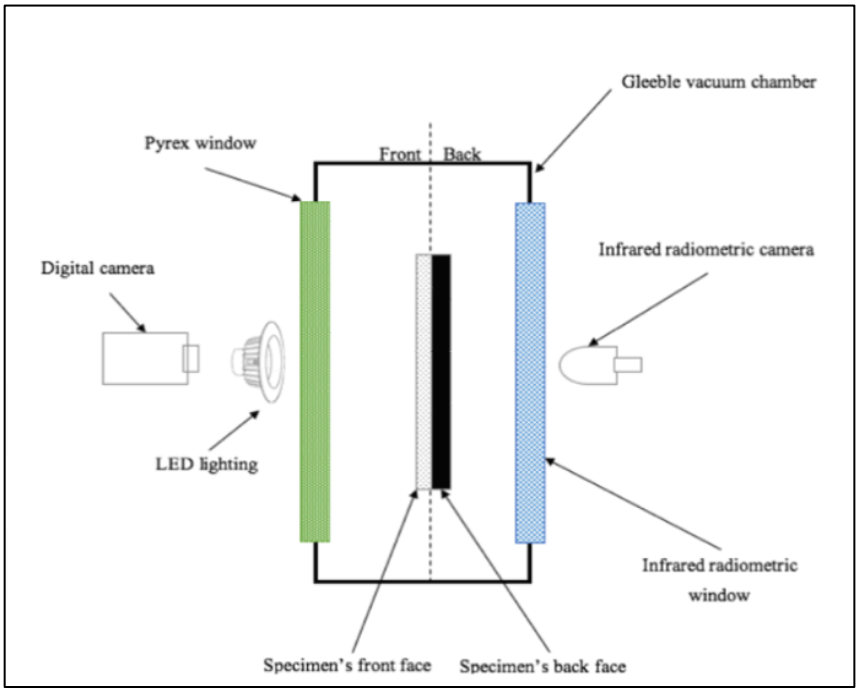

Figure 2.21:Illustration of experimental set-up of test specimen inside of a Gleeble chamber [24]

DIC employs advanced image processing techniques to measure displacement and strain fields in a region of interest (ROI) of an object which is deformed in real time. The ROI consists of many subsets (facets), which are tracked to determine the displacement of a deformed object. In a conventional DIC method, the movement of a point located at the centre of a reference subset (e.g., point P as shown in Figure 2.22) is tracked and the Newton-Raphson method is used to calculate its displacement. The displacement calculation starts from the upper left point of ROI to the remaining along each row or column.

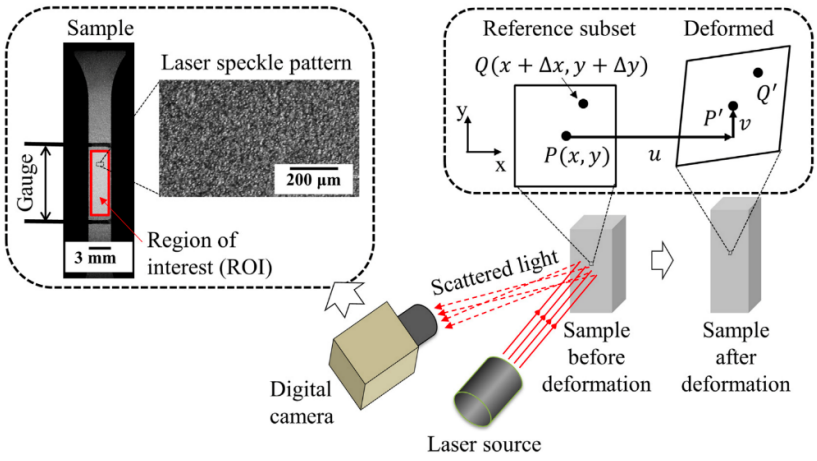

Figure 2.22: Schematic diagram of Illustration of DIC facet tracking between reference and deformed image[28]

To facilitate quick processes, pixels are grouped together into clusters called facet size or reference subset as shown in Figure 2.22. Image correlation is based on obtaining maximum correlation between facets using even spaced grid points called grid spacing to track

deformations [29]. Thus, the facet size and grid spacing are important parameters in DIC accuracy [29].

To save the computing time, the obtained displacement of the current point is used as the initial guess of the reference point in the next step. Thus, the accurate determination of initial guess is important for the convergence in the calculation. However, when it comes to a large deformation, the tracking of the point may fail.

Zheng et al. [28] report that the Reliability-guided DIC (RG-DIC) method is an effective approach to accurately calculate the displacement with less computing time. According to Zheng et al. [28] this method is efficient and robust because only a seed/tracking point is used as an initial guess, and the neighboring points with the highest zero-mean normalised cross correlation coefficient are computed earlier to continue correlation analysis. RG-DIC can be extended to multithread DIC where more than one tracking point is used. The DANTEC Systems DIC software used in this work was similar to the RG-DIC reported by Zheng et al. [28] where tracking points are used as initial guesses within a region of interest.

There are some other approaches, such as Moiré interferometry and Electronic Speckle Pattern Interferometry (ESPI). However, DIC has an advantage of simpler experimental set-up and high accuracy as a result the technique has received much attention in full field displacement and strain measurement [28].

2.4.1 2D and 3D DIC

2D DIC measures in-plane deformation where there is no movement between specimen and camera. The camera is positioned perpendicular to the specimen. 3D DIC measures deformation in 3D space using stereo cameras. 3D surface measurements can be achieved. Local derivative calculations give the strain tensors across the entire surface. Figure 2.24 shows an illustration of 2D and 3D DIC techniques.

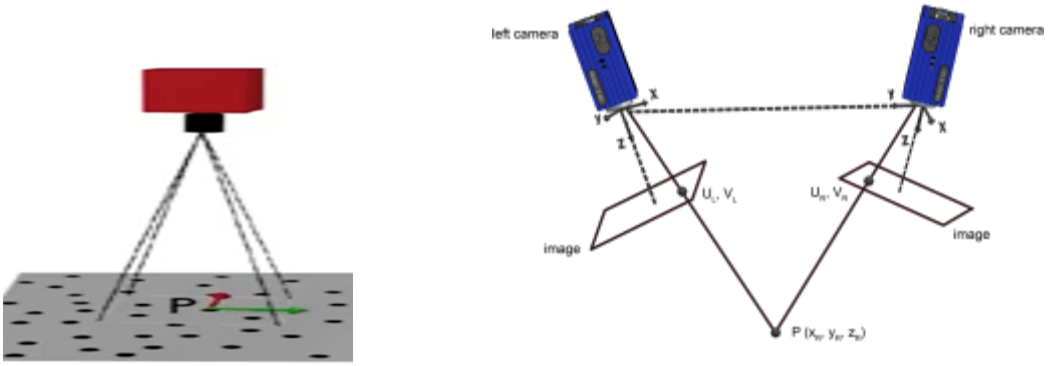

Figure 2.23: 2D (left) and 3D (right) DIC technique [30]

In 3D stereoscopic DIC systems two cameras view the surface of the specimen. The camera system is calibrated such that the relationship between raw and world space is known. By

matching the pattern between cameras and using the calibration model, the height and z-displacement of the surface can be calculated. The 3D DIC system requires precise location of cameras.

Strain measurements in this work were done using a 3D DIC system. The strain was expected to be planar during deformation along the length of the specimen until the onset of necking. Yang et al. [31] assessed the accuracy of DIC compared to data obtained from an extensometer on a tensile specimen. The results from the experiment are shown in Figure 2.24. The DIC data were observed to overlap the stress strain curve plotted using the tensile test machine with extensometer data.

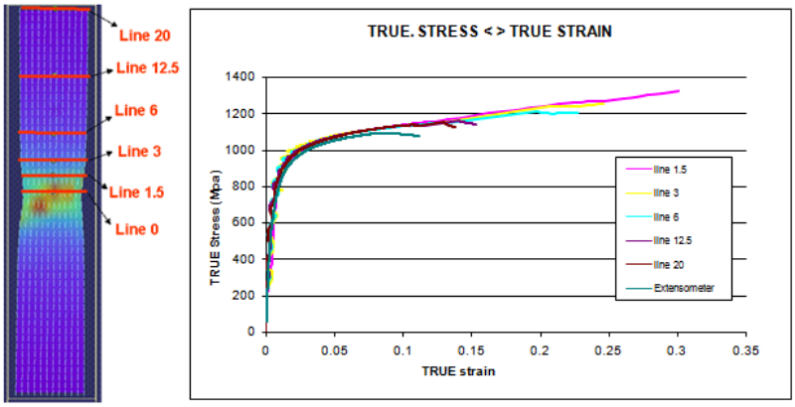

Figure 2.24: DIC data and extensometer data plot [31]

This proved that the data acquired from DIC is highly accurate and reliable [31]. To further prove the reliability of the DIC system, a repeatability study with four samples was done. The results from the repeatability study are shown in Figure 2.25. All curves are very close which demonstrate that the measurements have good repeatability.

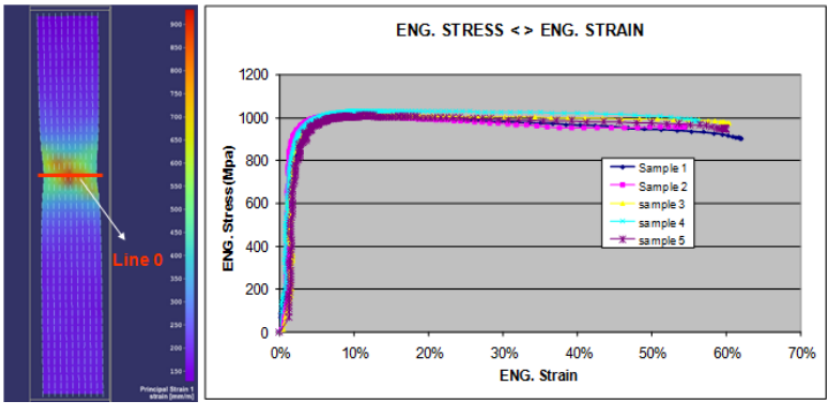

Figure 2.25: Repeatability measurements[31]

Singh [29] developed a technique for measuring influence of temperature on mechanical properties of welds. DIC was used to obtain localised strain measurements. To use DIC for strain measurements it was necessary to correlate the measurements to the mechanical

measuring system used in the experiments. A Gleeble thermomechanical machine was used to heat and deform the specimen.

Singh [29] compared strain values obtained from a Gleeble machine with strain values obtained from the DIC system by placing a virtual strain gauge in the center of the specimen. Gleeble strain measurements were determined by the relative movement of the stroke, whilst the global strain from the DIC system was found by tracking the movement of defined points positioned on either end of the gauge length. Figure 2.26 illustrates the global machine strain across the specimen from both Gleeble and DIC systems.

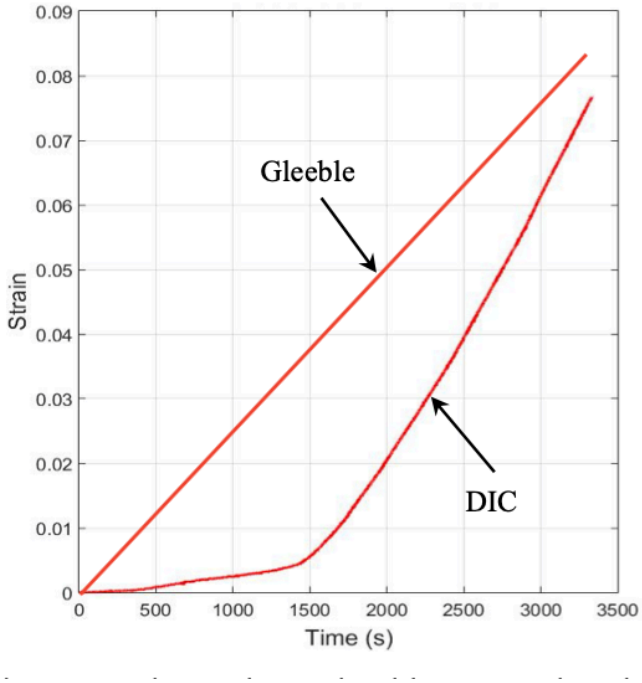

Figure 2.26: Comparison of DIC strain to Gleeble strain [29]

The fundamental difference between the strain-time graphs for both the Gleeble and DIC is due to machine compliance. Machine compliance is defined as the nonlinear displacement within the loading system which arises from the nonlinearity associated with the many connections and/or linkages present within the loading system [32]. The strain-time curve shows that the DIC is measuring the strain accurately, however the Gleeble machine stroke which is used to calculate the strain on the Gleeble also takes into account movement in the crosshead and at the grips before the specimen begins to deform. The DIC only records strain when the specimen starts to deform, that is when the tracked points are displaced.

2.4.2 Speckle Patterns

Random speckle patterns were prepared on the surface of a specimen before testing to correlate between two captured images. Artificial speckle patterns are the most common type and are prepared by spraying high temperature paints on the specimen surface. Figure 2.*27* shows a speckle pattern applied on a tensile test dummy specimen with an average speckle average speckle diameter was 0.09 millimetres (assuming circular speckles) [29] .

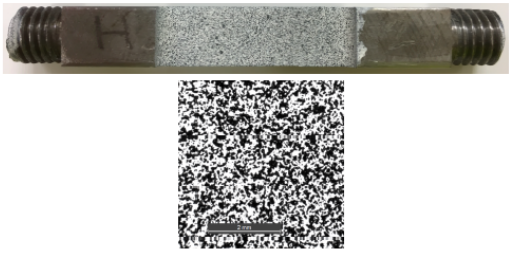

Figure 2.27: Photograph of speckle pattern along gauge length [29]

It has been observed that paints may peel off from the sample after necking, especially at high temperatures, which would result in failure to obtain the material deformation data when the strain localizations become severe [29]. In addition to that an inaccurate measurement of the true strains for thin specimens may occur because of the thickness of the paints.

Zheng et al. [28] proposed that laser speckle patterns without spraying may be required as they overcome the challenges posed by painting specimens citing that laser speckled patterns are more ideal [28] compared to artificial paint speckles. Laser speckle patterns simplify the DIC process by eliminating the need to artificially paint specimen and are versatile in application at high temperatures and thin metal foils [28]. The specimen was divided into two with one half speckled with laser and another with paint as shown in Figure 2.28.

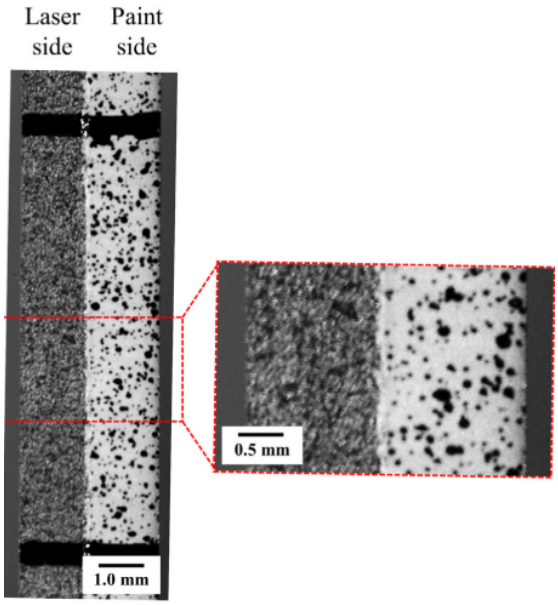

Figure 2.28: Laser and paint speckled specimen [28]

The recorded DIC strain of both sides shown in Figure 2.20 a which illustrates the same distribution, indicating the reliable strain measurement by DIC with laser speckles and paint speckles. Specimens were spray painted with high temperature paint as testing temperatures may not be too high to damage the speckle pattern. Use of both a white and black heat resistant ceramic paint to create a speckle pattern, has been observed to allow testing temperature up to 1100 °C [29].

Speckle patterns can be created by white paint on a black background or black paint on a white background. The intensity variation between black speckles on a white background is higher which subsequently assisted the correlation process and displacement accuracy [29]. To ensure maximum bonding of the speckle pattern paint the specimen surface can be abraded a fine grit sandpaper before applying the speckle pattern. By doing this strain rates can be increased without the paint debonding [29].

According to Singh [29], in tensile testing, maximum paint ductility was achieved when the gauge length was adequately roughened and a thin layer of paint is applied and when the speckling is done 30 minutes before a test. Singh used a Struers 80 grit waterproof silicon carbide paper to abrade the specimen along the gauge length. This was followed by applying a thin layer of paint using (704 – 1093°C) VHT ® FlameProof white paint. A VHT black paint was then used to apply a speckle pattern after the white paint. The paint curing heat treatment process recommended by the manufacturer was not followed as it resulted in flacking off of paint during testing [29].

2.4.3 Facet Size

Facet size and grid spacing selection is critical in ensuring accurate DIC Measurements. The Facet size is the group of pixels that will be used by the correlation algorithm to track the displacements. Larger facets contain a more unique and distinctive speckle pattern in comparison to other facet sizes. On the other hand, the smaller facet sizes allow for more accurate displacement measurements [29].

Singh [29] determined the facet size and grid spacing size based on the strain resolution required to detect pixel displacements. Initially a facet and grid spacing size of 29 (~ 0.6 millimetres) and 19 (~ 0.3 6 millimetres) pixels was used then subsequently evaluating and refining to 19 (~0.3 6 millimetres) and 9 (~0.2 6 millimetres) pixels respectively. With a smaller grid spacing, the tracked facets overlap. Overlap in facets ensure accurate displacement data by countering the influences of background noise by spatial resolution [29].

2.4.4 Hardware

DIC requires use of an led light to illuminate the specimen, camera to capture deformation and filters to eliminate unwanted light from the specimen. Filters are used in high temperature DIC tests where there is radiation from the specimen.

The machine vision system of a DIC set-up requires one or two cameras. In a DIC experiment conducted by Van Rooyen and Becker [26] digital images of the sample surface were captured using two LaVision Imager E-lite 5M cameras with a 2456 x 2058 pixel, 12-bit charge-coupled device (CCD) chip. Macro lenses were used to adjust the field view and a field of view of about 47 x 60 mm was achieved with TECHSPEC 75 mm Double Gauss macro lenses, resulting in a pixel size of about 19 μm. Post-processing was done using LaVision DaVis software that correlates image subsets using the zero-normalised Newton Raphson algorithm [23]. The DIC evaluation was done with subset sizes of 60 x 60 pixels with a step size of 20 pixels Post processing in this work was done using DANTEC Dynamics DIC software.

As the surface temperature of the specimen reaches 600°C, the intensity of the emitted short wavelength light (less than 600 nm) increases. Image saturation occurs when the radiated light

over-intensifies the speckle pattern. Van Rooyen and Becker [26] minimised emitted light by illuminating the surface with two white 20W LaVision LEDs with a high correlated colour temperature of 6500 K, giving it a high blue (440 nm) component within the spectral response of the Sony ICX625 camera sensor. A Hoya B-440 colour filter was used to bracket the emitted and reflected light within the LED wavelength band. It was observed that using a green filter and a blue filter significantly reduced the emitted radiation. It was further recommended that for improved results, a blue LED is required [26].

Singh [29] used a Basler 5-megapixel camera with a resolution of 2 592 x 1 944 pixels, equipped with an adjustable macro lens secured onto a stable tripod and positioned approximately 1.5 m away from the Gleeble chamber. To eliminate interruptions from surrounding light, a 10W LED light was secured onto a separate tripod and was used to illuminate the specimen. To reduce the effects of surface radiation, and to further maximise the signal to noise ratio at elevated temperatures, a blue Hoya B-440 lens filter with a wavelength range of 395 - 480 nm was fitted onto the camera lens during the initial dummy testing. Subsequently, it was found that the radiation emitted from the specimen at this temperature was minimal, and the use of the blue filters was in fact decreasing the signal to noise ratio. Therefore, for subsequent experiments the use of the lens filter was discontinued.

2.4.5 Localised Strain Maps

In work done by Curry et al. [24], an in depth analysis of strain distribution across welded specimen was undertaken shedding light on the significance of localised strain maps in understanding material behaviour. Strain distribution was assessed at three points i.e. just after yielding (YS), at the ultimate tensile stress (UTS), and at the end of the experiment. These points were selected to gain a more holistic view of the influence of temperature on the material and mechanical properties of the weld.

Figure 2.*29* shows localised strain maps from DIC data, and the strain distribution changed increasing from the fusion line towards the FGHAZ. The location of peak strain also changed with increase in temperature with the peak strain moving away from the FGHAZ into the weld metal at 535°C.

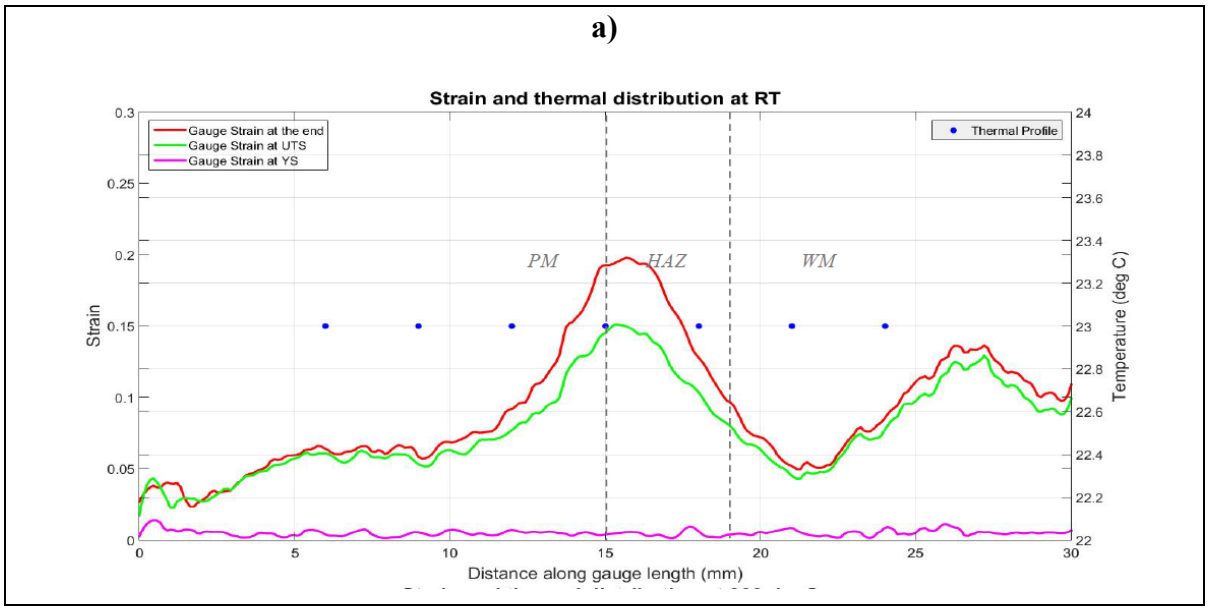

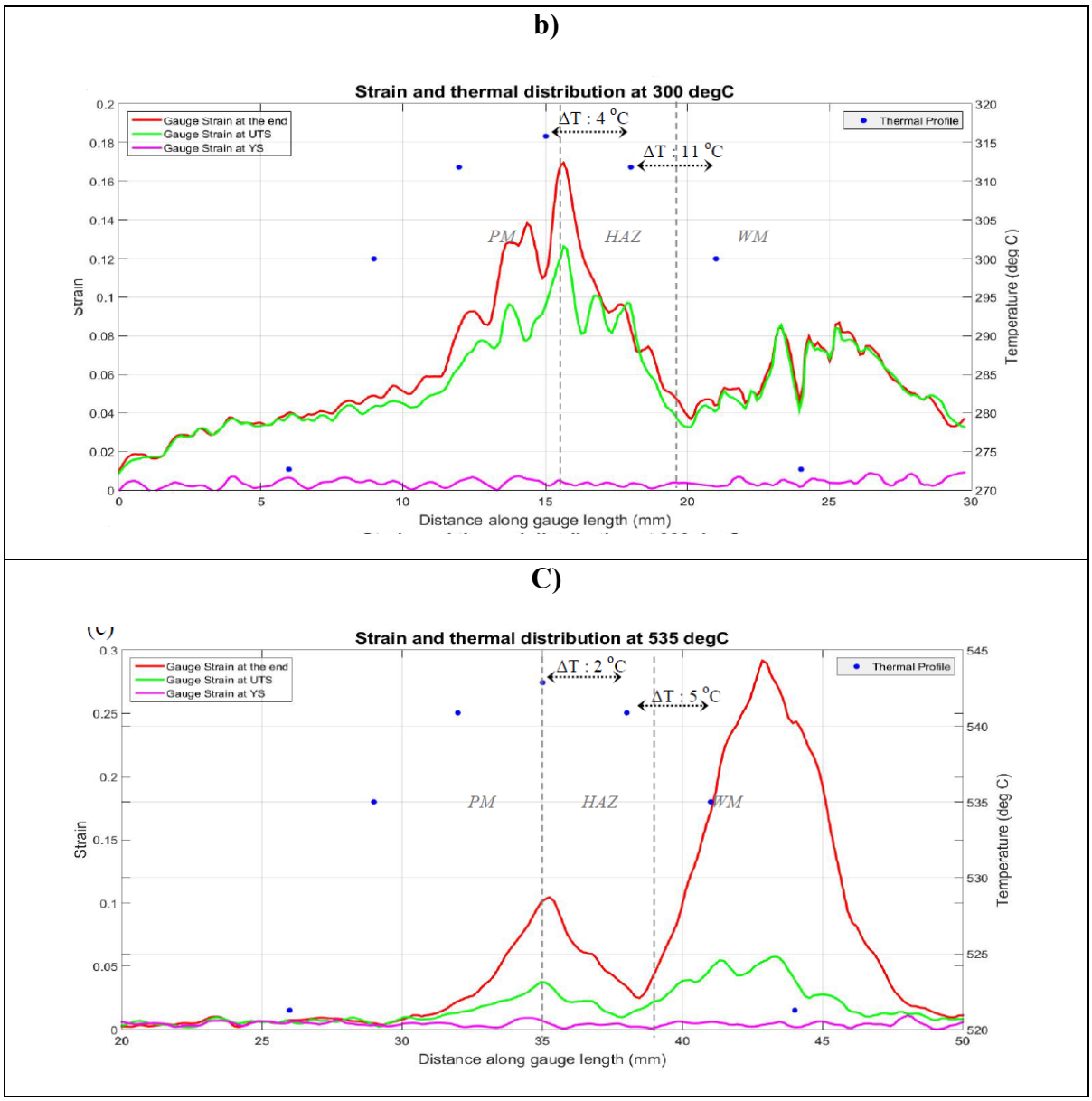

Figure 2.29: Strain distribution across a weldment at (a) RT, (b) 300 °C and (c) 535 °C [24]

Incremental stress strain curves can also assist in gaining more insight into material response. Curry et al. [24] obtained incremental stress strain curves a weldment by utilising incremental gauge lines placed at 1 mm increments from the fusion line shown in Figure 2.30.

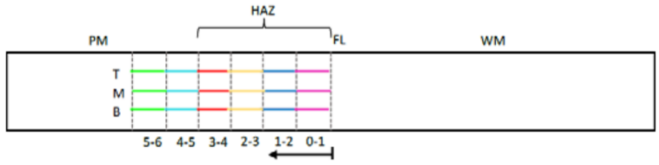

Figure 2.30: Incremental strain illustrated from the fusion line in 1mm increments.

The results showed that strain accumulation from the FL (first incremental gauge line) towards the FGHAZ (fourth incremental gauge line) was once again observed.

Figure 2.*31* shows the results obtained from incremental strain measurements. The 3-4 mm line shows the highest strain in all instances corresponding with the peak shown in Figure 2.29.

a)

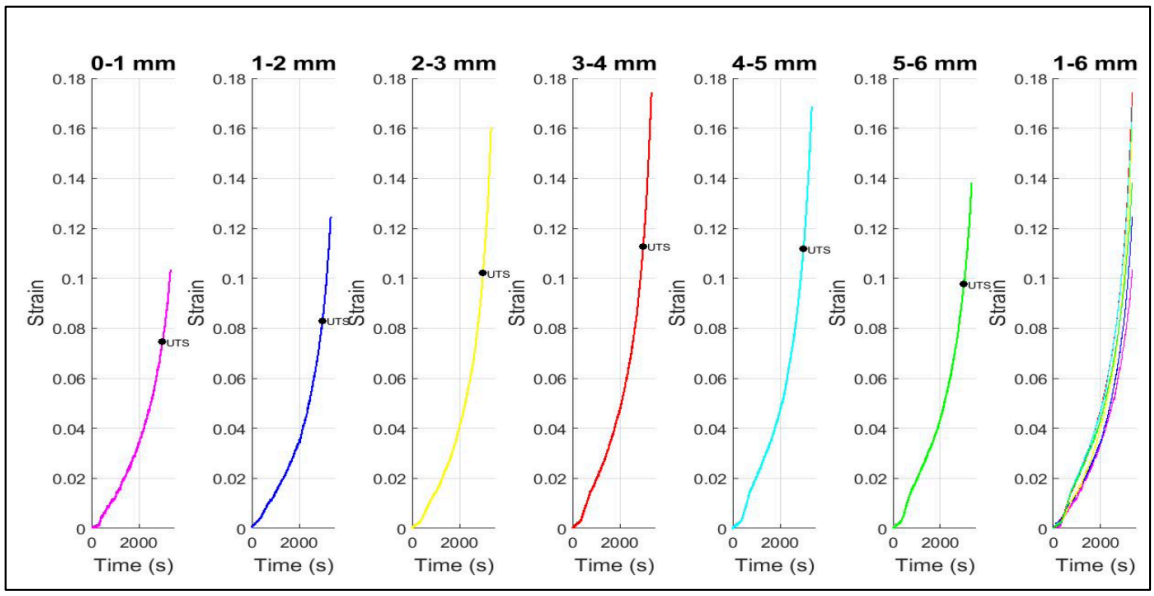

b)

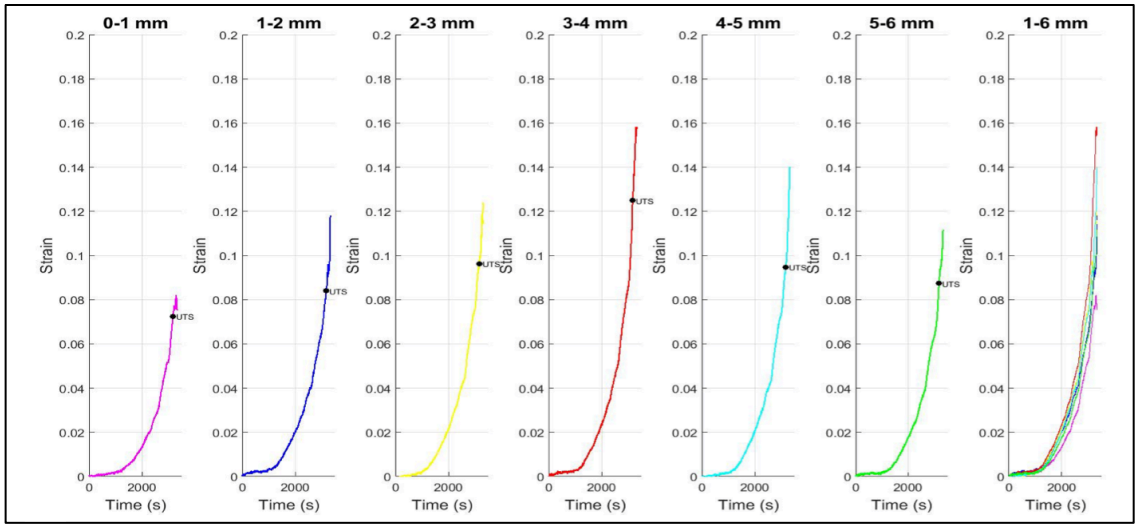

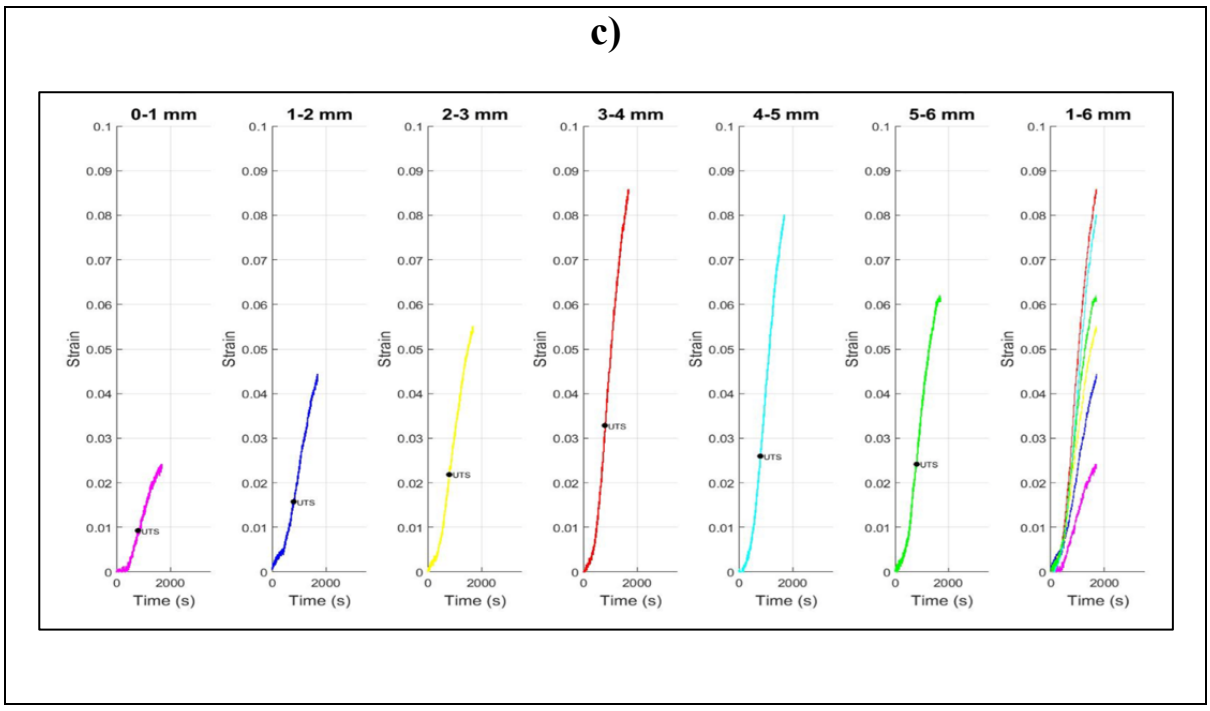

Figure 2.31: Incremental temporal strain across the weld zone at (a) RT°C , (b) 300 °C and 535 °C [29]

2.6 Hardness tests

Hardness tests provide information about the resistance of a material to plastic deformation therefore they play a crucial role in the examination of localised strain and tensile behaviour of materials. Hardness tests can be conducted at specific points or regions within a material, enabling the detection of local variations in hardness. These variations may signify differences in material composition, microstructure, or processing, which can directly impact localised strain and tensile behaviour. Figure 2.32 shows the micro hardness profile across a weldment of ex-service turbine housing material dissimilar welds.

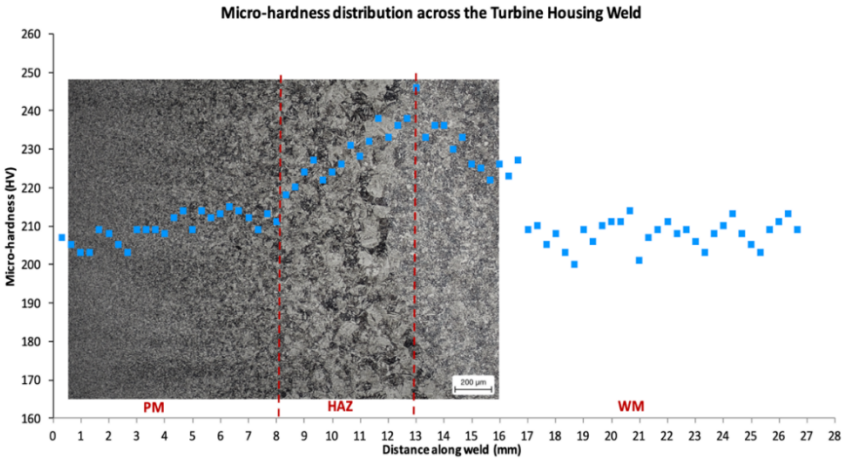

Figure 2.32: Micro-hardness distribution along the transverse direction of the turbine housing weld [29]

The profile in Figure 2.32: Micro-hardness distribution along the transverse direction of the turbine housing weld shows three distinct regions i.e., HAZ, PM, and WM with the fusion line between the weld metal and HAZ. The hardness increase linearly and peaks in the region of the fusion line. The abrupt decrease of hardness value near the FL was related to the existence of delta ferrite in the parent material making the material softer [29]. Figure 2.33 shows a consolidated weld hardness profile from work done by Doubell et al. [12] on investigating effects of different PWHT practices on mechanical properties of P91 steel. In Figure 2.33, the legend shows the heat treatment temperatures and times on the far right as well as the line representing each heat treatment condition.

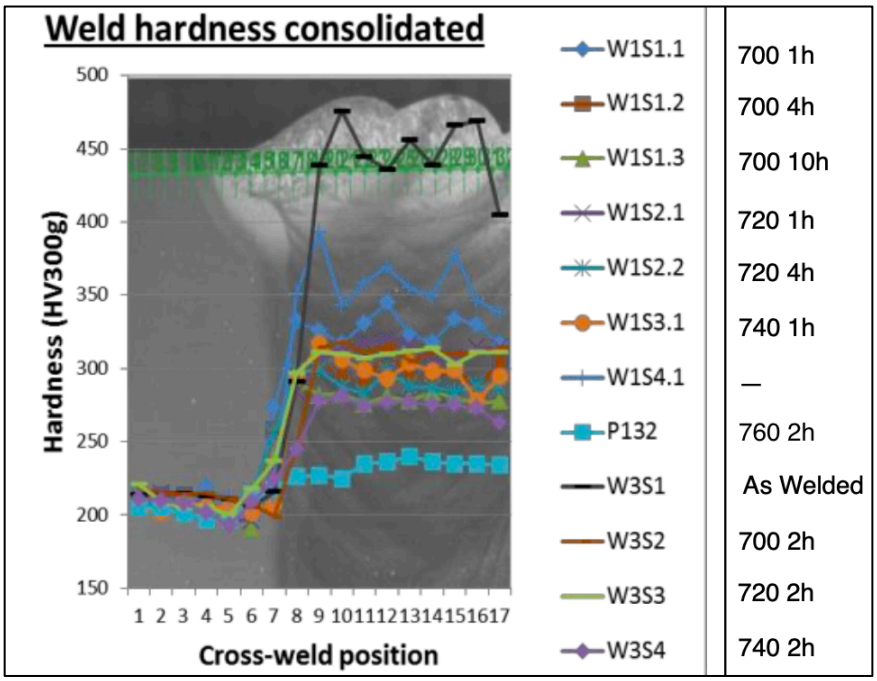

Figure 2.33: P91 Weldment hardness profiles [12]

The as-welded specimen shows increased hardness in the weld metal compared to heat treated specimen. Unlike Figure 2.32 the weldment in Figure 2.33 had similar materials and the selected welding filament was selected close enough to the chemical composition of the parent material. It demonstrated that heat treatment resulted in reduced hardness. The hardness of the weld metal can be seen to decrease at higher heat treatment temperatures for same heat treatment times. Increasing the PWHT time also resulted in further decreasing the hardness of the weld metal. An additional heat treatment in this work was done at 800°C for 2h; this was expected to result in more homogeneous hardness across the specimen.

2.7 Conclusion

This literature review has offered valuable insights into several key aspects concerning the evaluation of materials, particularly in the context of localised strain, tensile behaviour, and hardness testing. The following key takeaways can be summarised: the importance of understanding localised strain and tensile behaviour in assessing materials' performance; Digital Image Correlation (DIC) emerges as a powerful non-contact technique for measuring strain with the capability to track deformation patterns, elastic-plastic strain distributions, and stress-strain curves; the significance of appropriate speckle patterns, facet sizes, and grid spacings in DIC accuracy; the importance of well-designed hardware and calibration; the utility of localised strain maps in revealing material behaviour; and the fundamental role of hardness testing in assessing a material's resistance to plastic deformation. These insights have practical implications for power plants, where the accurate assessment of materials is critical for ensuring optimal performance.

3. Experimental Methods

To evaluate the effect of various PWHT on the mechanical properties of P91 weldments, specimens subjected to different types of heat treatments were studied. The specimens used in this work were cut out from a pipe. The pipe material used in the study was sourced from Wyman-Gordon (USA) and came from a power station's steam pipework replacement project. The material was in the form of a limited number of short offcuts measuring 275 mm in internal diameter and had a wall thickness of 28 mm.

Chemistry of the base material is the most important variable that cannot be readily manipulated during welding and PWHT. The pipe had a root layer deposited by TIG welding with ER90S-B9 filler material followed by filling with SMAW process with filler material ER90S-B9. The welding was performed at a preheat temperature of 193.2 °C and maximum inter-pass temperature of 219.4°C. No intermediate heat treatment was performed. The temperatures are within the acceptable standard for welding of thick sections of P91 which recommends a maximum inter-pass temperature of 350°C [15].

Cross-weld tensile tests at room temperature and elevated temperatures approaching the actual power plant service temperature were performed on specimens. Four thermal test conditions were established i.e., As-welded (AW) and three (3) post-weld heat treatment temperatures (PWHT). Light microscopy and Vickers hardness tests [33] were carried out on the weldments of all test conditions as additional experiments. The experimental approach in this work followed the technique proposed by Singh [29], to measure the influence of temperature on mechanical properties of weldments. Localised strain maps of specimens subjected to different post-weld heat treatments (PWHT) were studied, and a correlation was made with the experimental results from tensile tests.

3.1. Specimen extraction and geometry

Figure 3.1 shows an illustration of the orientation for specimen extraction. Wire-cut EDM was employed to extract rectangular blocks from the pipe section with the weld in the centre. Figure 3.1 (b) shows the pipe section after rectangular cut-outs are extracted. The rectangular blocks were later machined to required specimen geometry. The gauge length of the specimen was surface ground to achieve 0.4 µm surface finish.

Figure 3.1 d shows the specimen geometry. Specimen configurations were made according to the standard Gleeble thermomechanical machine specimen geometry which measures 125 mm with a 10 mm x10 mm cross sectional area. The specimen geometry was modified as recommended by Van Rooyen and Becker [26] who recommended a thinner gauge area and 6 mm holes at the ends of the specimen which was observed to improve the temperature profile on the specimen. The specimens used in this work had a gauge length of 70 mm with a 10 mm x 4mm cross section and overall length of 124 mm.

a)

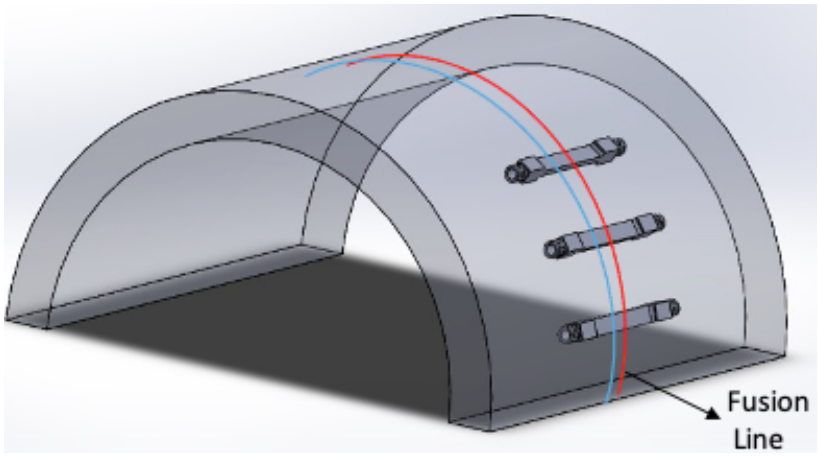

b)

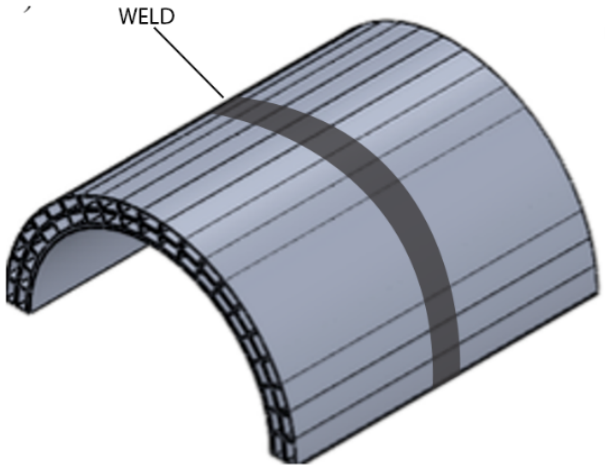

c)

Dimensions:
mm

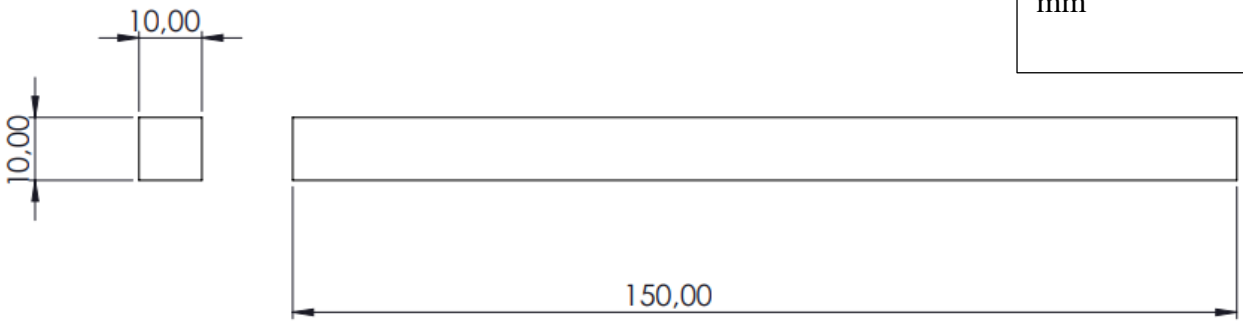

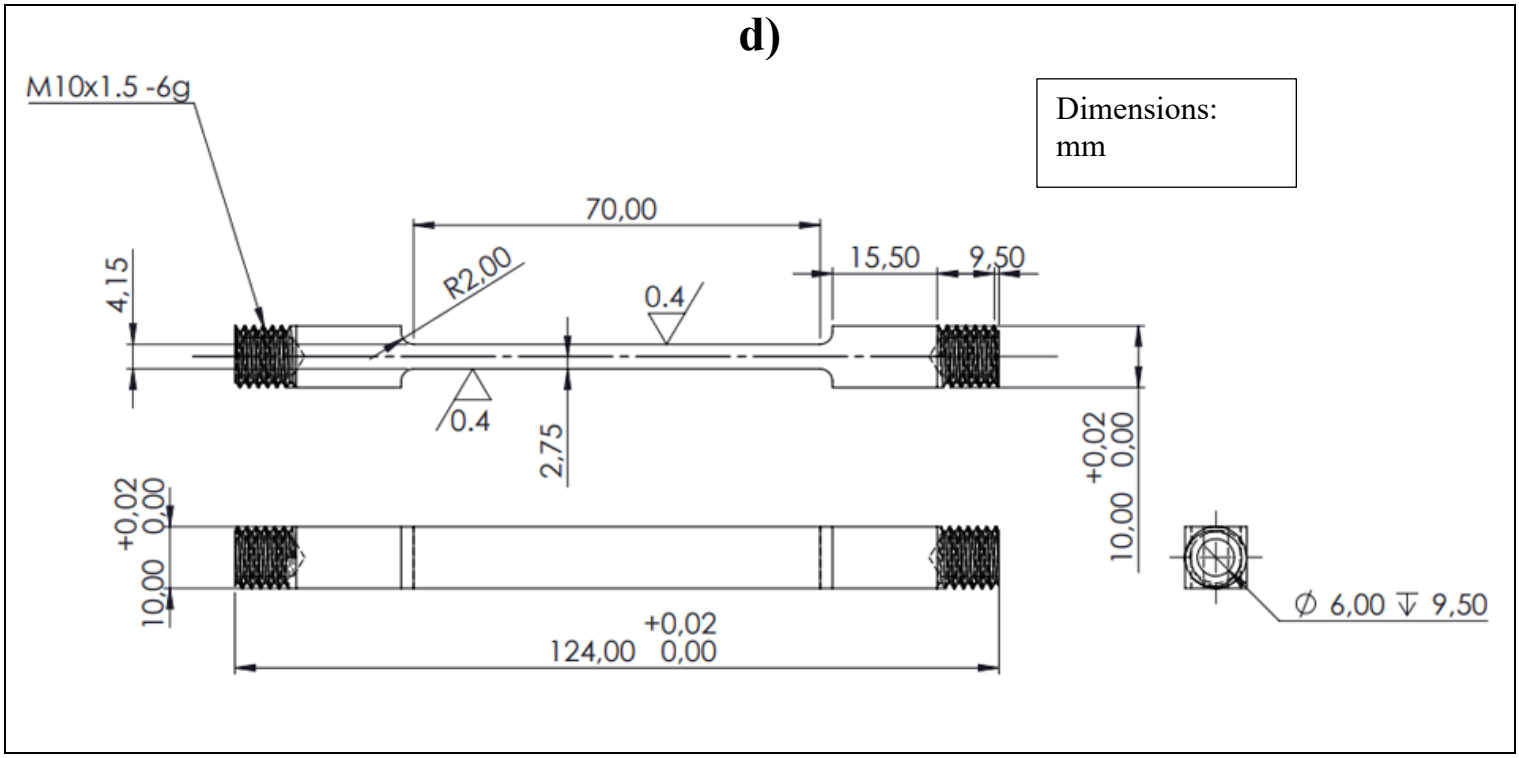

Figure 3.1: Illustration of a) Specimen extraction illustration b) Pipe after extracting cut-outs c) Cut-out geometry, d) machined specimen geometry

3.2. Post Weld Heat Treatment

Specimens were be subjected to different heat treatment temperatures and comparisons were made. Temperatures of 720°C, 760°C and 800°C were proposed temperatures for heat treatment [15]. These PWHT temperatures fall within recommended range according to ASTM A335 [8] standard for specifications for steel for high temperature service which is PWHT at 730 – 800°C and 1040 – 1080°C for PWNT. Table 3.*1* shows the heat treatment specifications for specimen used in this work.

Table 3.1: Heat Treatment Matrix 1

Temperature	Time(h)	Number of specimens
As-Welded	0	3
720°C	2	3
760°C	2	3
800°C	2	3

3.2.1 Vacuum furnace temperature profile

Heat treatments were conducted in a vertical vacuum furnace. Prior to heat treatment, temperature measurements were taken in the vacuum furnace to determine the temperature profile to ensure that heat treatments were done at correct temperatures. A K-type rod thermocouple was used to take temperature measurements over a height of 200 mm. Temperature readings were taken on every 10 mm mark on the thermocouple in 5-minute intervals.

Initially, temperature measurements were conducted at four distinct levels: 1000°C, 800°C, 760°C, and 720°C. The furnace's upper operational limit stands at 1200°C. Within this range, the intended temperatures for heat treatment are 800°C, 760°C, and 720°C. Figure 3.2 shows the temperature profiles obtained for the different temperatures. The measured temperature varied with the height of the vertical furnace. The measured temperature at all furnace temperatures was lower than the indicated furnace temperature and the target temperature for heat treatment.

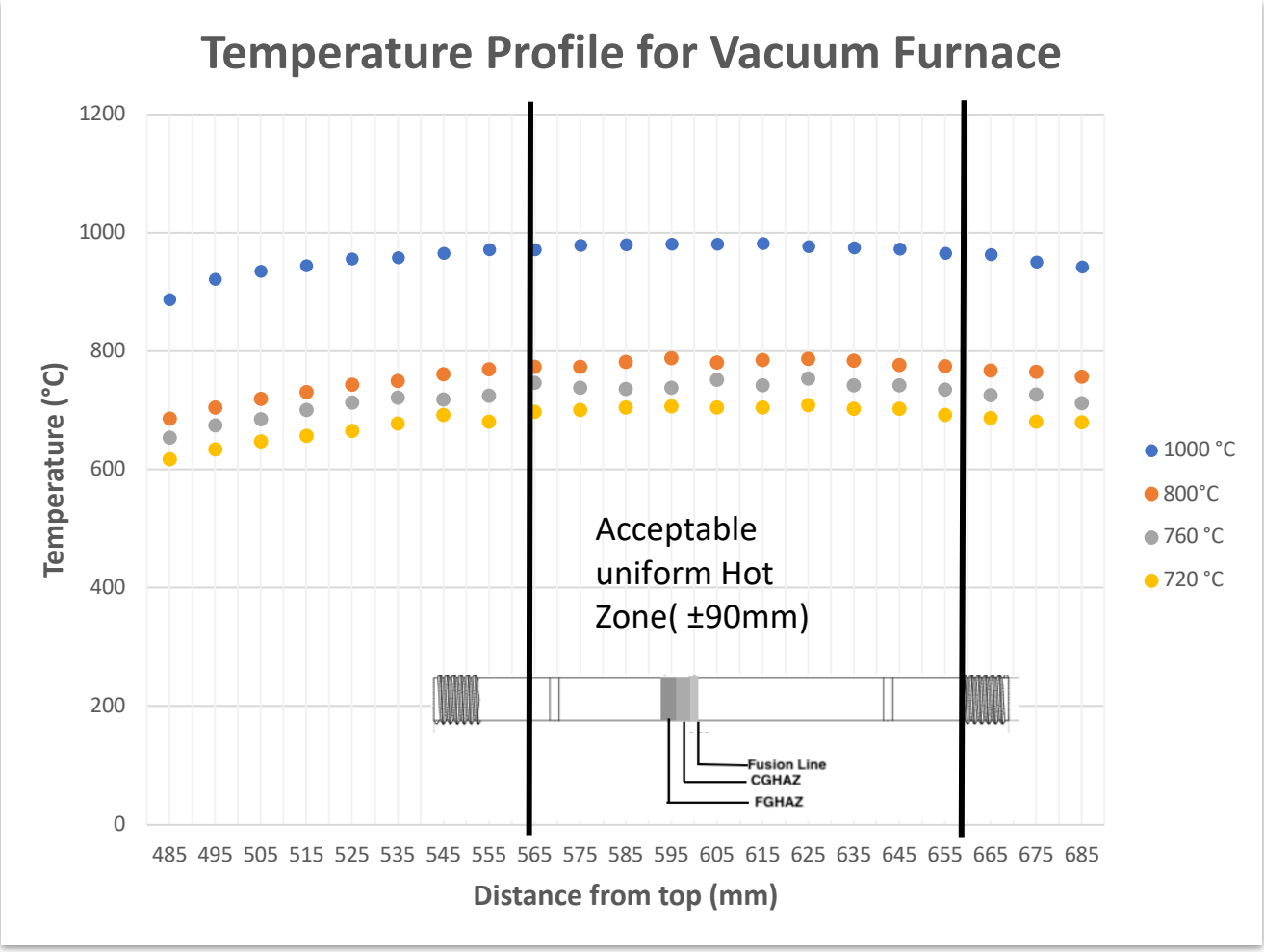

Figure 3.2: Vacuum furnace temperature profile

The furnace has a high temperature hot zone of ± 90 mm from 565 mm to 655 mm measured from the top of the furnace. It is important to ensure that during heat treatment, the gauge section of the specimen has its centre in the hot zone. The average temperature difference

between the thermocouple temperature and the furnace temperature was established to be 19°C in the hot zone.

Taking note of the deviation, temperature measurements were repeated at 820°C, 780°C and 740°C. Figure 3.*3* shows the temperature profile results. The temperature profiles were closer to the target temperatures for measurements taken at 820°C and 780°C.

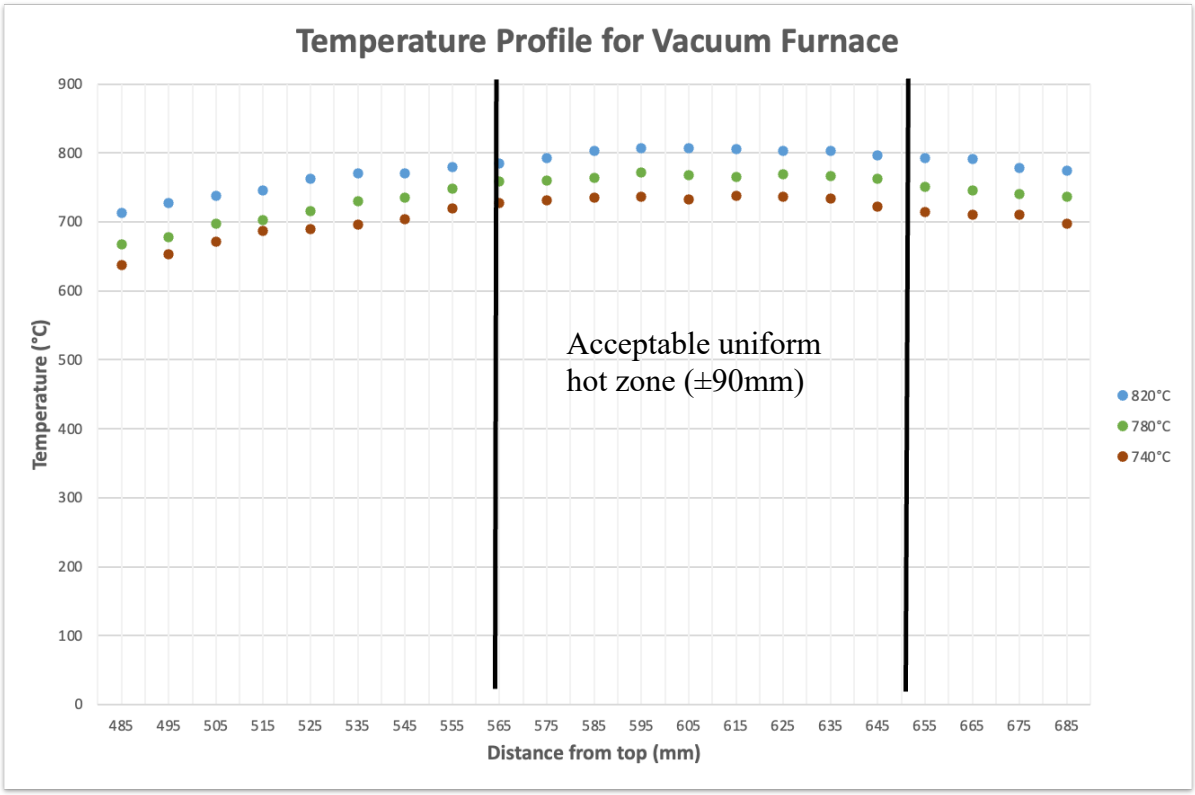

Figure 3.3: Temperature profiles including deviation

Figure 3.4 - Figure 3.*6* show the temperature profiles obtained for various furnace temperature settings. Heat treatments were designed to be conducted at target temperatures of 720°C, 760°C and 800°C. When the furnace temperature was set above the target temperature, the temperature profile in the hot zone was closer to the target temperature in comparison to measurements taken when the furnace temperature was set to the target temperature.

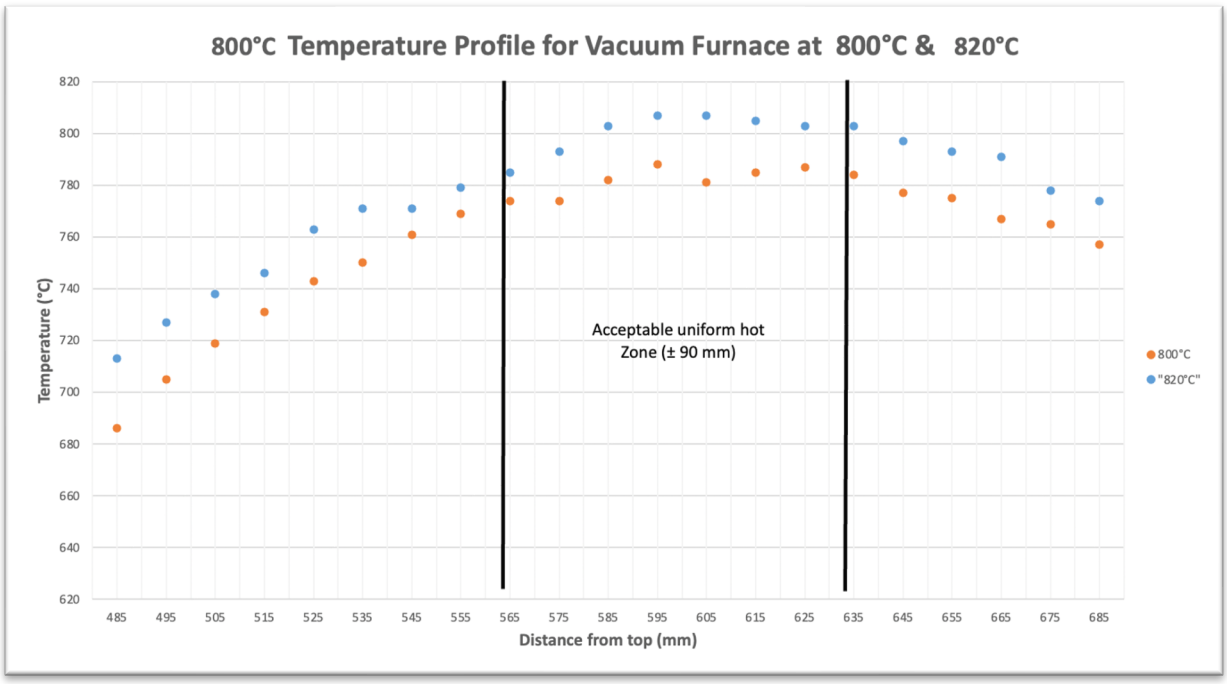

Figure 3.4: 800°C Vacuum furnace temperature profile at 820°C

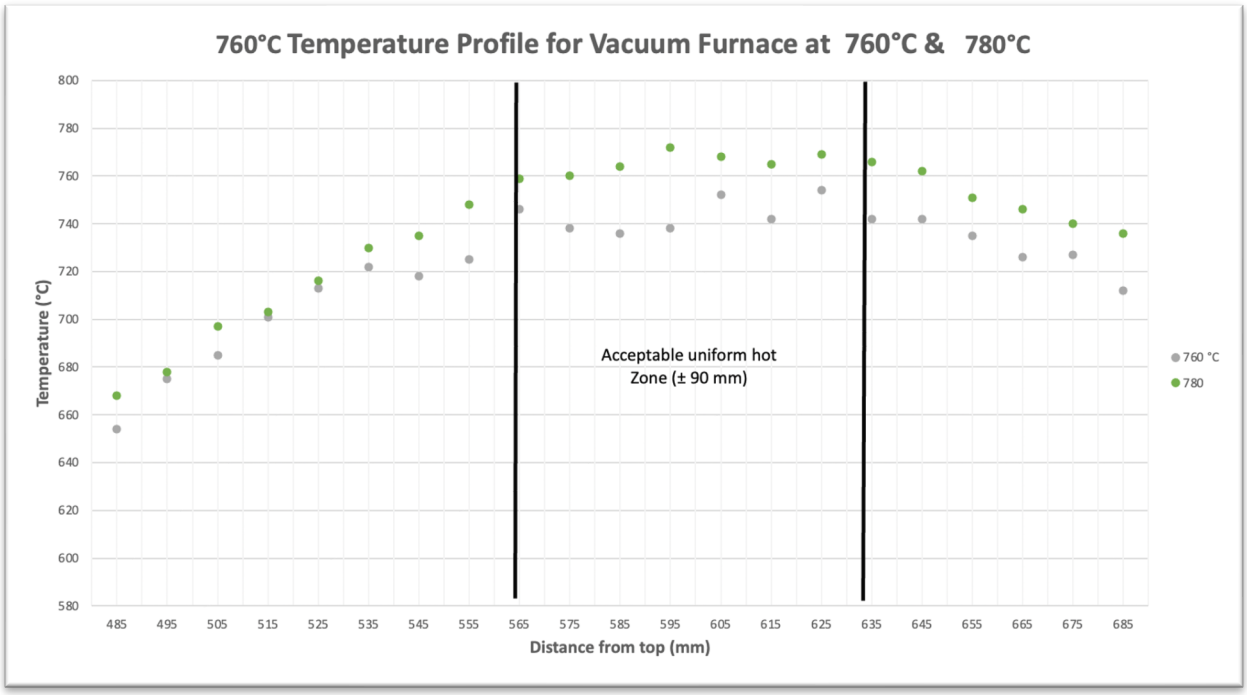

Figure 3.5: 760°C Vacuum furnace temperature profile at 780°C

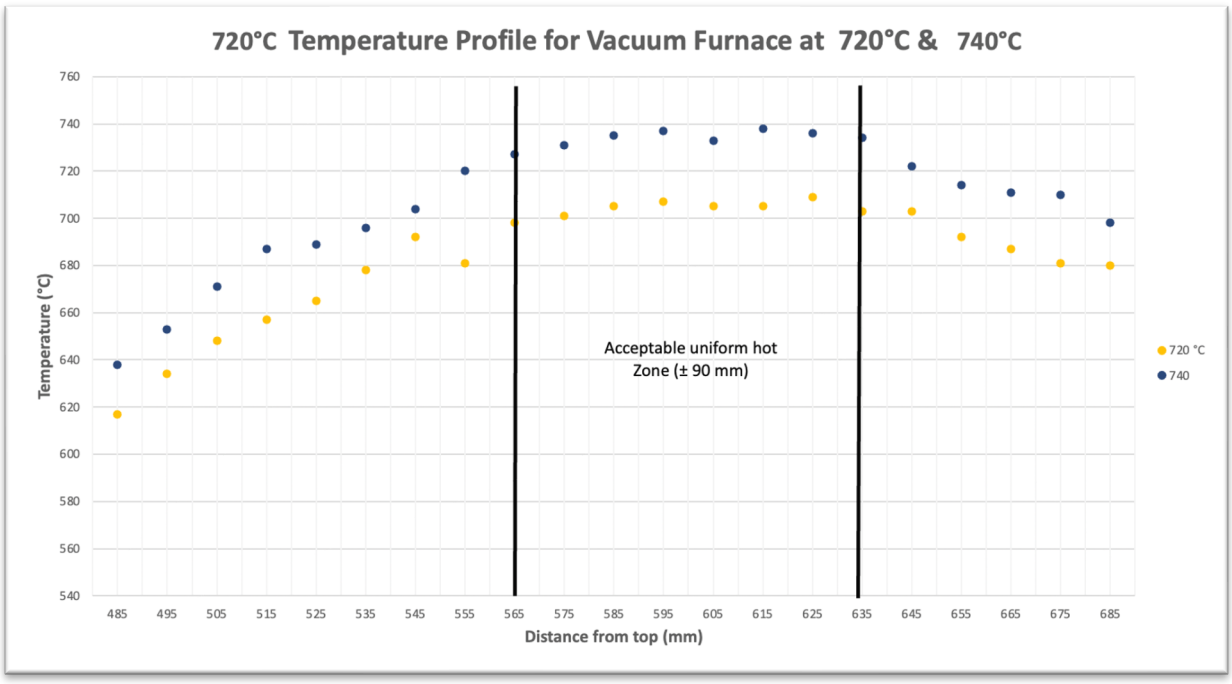

Figure 3.6: 720°C Vacuum furnace temperature profile at 740°C

The average temperature in the hot zone for measurements taken at 740°C was 731°C. This was higher than the target temperature of 720°C. The furnace temperature profile measurement at 740°C was repeated for the target temperature of 720°C with the furnace temperature set to 735°C. Figure 3.7 shows the temperature profile at 735°C. The average temperature in the hot zone was 721°C which was closer to the target heat treatment temperature of 720°C.

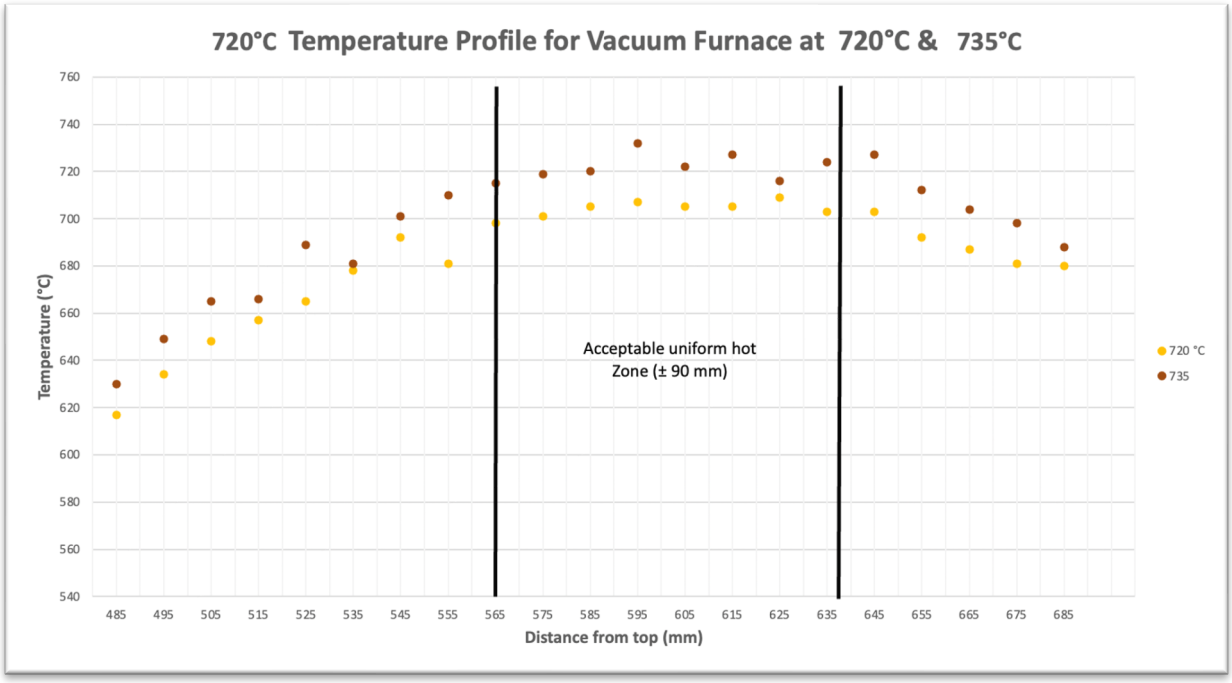

Figure 3.7: 720°C Vacuum furnace temperature profile at 735°C

In summary, a 90-100 mm hot zone was established in the vertical furnace within which the average temperature was close to the target heat treatment temperature by adjusting to a temperature above the target temperature. This adjustment was achieved by adding the established deviation to the initial target temperature. Table 3.*2* shows the furnace adjusted temperature, the average temperature in the hot zone and the target heat treatment temperature. This deviation observed were within acceptable range of ± 1-3 °C [34].

Table 3.2 : Vacuum furnace temperature measurements

Adjusted furnace temperature (°C)	Hot-zone average temp (°C)	Target temperature (°C)
820	798	800
780	763	760
735	721	720

3.2.2 Post weld heat treatments

Heat treatments were conducted at temperatures 720°C, 760°C and 800°C for two hours. All heat treatments were done under vacuum and at the end of the heat treatment, specimen were quenched in air. Deviations from standard practice can occur during field heat treatments. These include heat treatment excursions which occur where the temperature overshoots the specified heat treatment temperature then cools down to the required temperature.

When a temperature excursion occurs, causing the temperature to surpass the Ac1 point, a change happens in steel. This change involves the conversion of ferrite to austenite. As the steel cools down again, the austenite changes back into ferrite and possibly alpha ferrite. This sequence of transformations leads to a material that is softer and possesses reduced tensile strength properties compared to its original state. This entire process is closely related to the heat treatment of P91 steel and its phase diagram in Figure *2.4*. Heat treatments to study the effects of excursions on tensile properties of P91 weldments were done at 760°C for two hours with ten minute excursions to 820°C and 840°C.

Another form of deviation from standard practice is extended heat treatments where heat treatment time is prolonged. Heat treatments to study the effects of deviations from standard heat treatment practice were conducted at 760°C for 4 h and 6 h. Figure 3.8 shows the different heat treatments done according to the heat treatment matrix 1 in Table 3.1. Figure 3.9 a-d, shows heat treatments done according to heat treatment matrix 2 in Table 3.4.

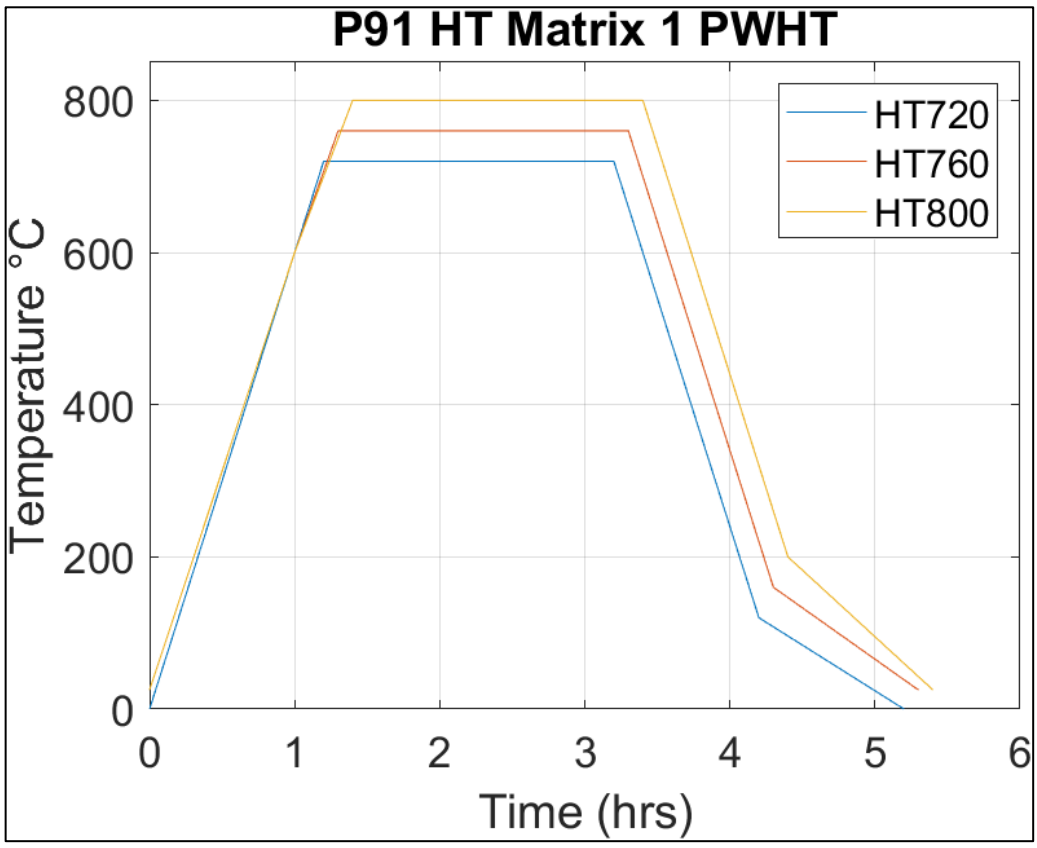

Figure 3.8: HT matrix 1 heat treatments

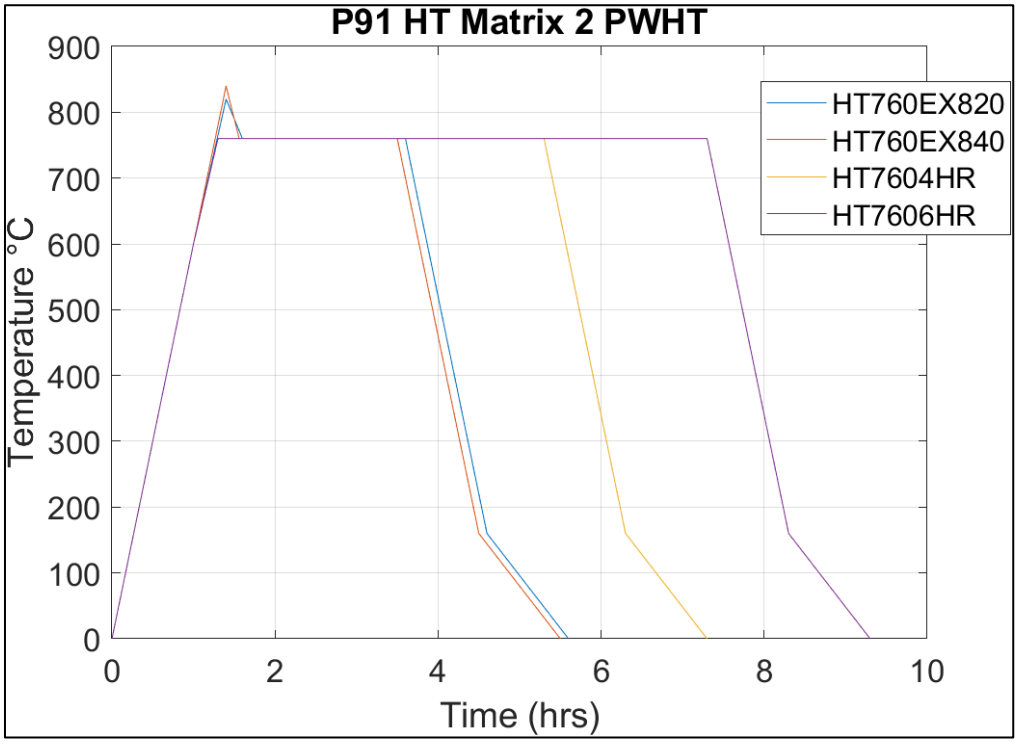

Figure 3.9: HT matrix 2 excursions and extended heat treatments

3.3 Tensile Testing method

Table 3.*3* shows the experimental validation matrix indicating the tests done on specimens. The matrix follows the work done by Singh [29] in the development of an experimental technique to measure the influence of temperature on the mechanical properties of weldments. A total of 12 specimen were tested at different temperatures. As-welded (AW) Specimen were be used for benchmark comparison.

Table 3.3: Experimental Validation Matrix

Specimen	No. of specimen	Strain rate (s^{-1})	Temperature (°C)
As-Welded	3	10^{-3} /s	Room temperature
			300
			535
HT720°C	3	10^{-3} /s	Room temperature
			300
			535
HT760°C	3	10^{-3} /s	Room temperature
			300
			535
HT800°C	3	10^{-3} /s	Room temperature
			300
			535

The temperatures shown in Table 3.3 were chosen based on the applications of the experimental technique in the work done by Singh [29]. The temperatures were chosen based on the intended applications of the developed technique on the steam penetration, turbine housing weld (THW) and loop pipe weld (LPW) [29]. The LPW had nominal operating conditions of 535°C and 16.1 MPa, whilst the THW had nominal operating conditions of 332°C and 4.1 MPa. Experiments in this work followed the same testing temperatures as well as a test at room temperature. The different test temperatures assisted in giving a clear indication on the effects of heat treatments on the mechanical properties of weldment.

The heat treatments shown in Table 3.1 occur under ideal standard conditions. However, in practice there can be deviations from standard PWHT practice. The deviations result in excursions during heat treatment process. We investigated the standard PWHT at 760°C 2h with extended dwell times to 4 and 6 hours. This situation could arise in practice if the PWHT process is left unattended for too long. Another consideration is given to the possibility of overheating the weld during the PWHT and then cooling back down to the standard 760°C and holding for 2 hours before cooling to room temperature. Cooling from the overheat temperature to 760°C should be at a cooling rate equivalent to the heating rate. It is therefore necessary to conduct additional heat treatments to investigate the effect of these deviations on the mechanical properties of P91 weldments. Table 3.4 shows the heat treatments done on specimens to study the effect of deviations.

Table 3.4: Heat treatment Matrix 2

Description	Thermal cycle	Specimen
Extended PWHT (4h)	Heat to 760°C and dwell for 4 hours	3
Extended PWHT (6h)	Heat to 760°C and dwell for 6 hours	3
Over-heat PWHT (820)	Heat to 820°C, dwell for 10 mins, cool to 760°C and dwell for 2 hours	3
Over-heat PWHT (840)	Heat to 840°C, dwell for 10 mins, cool to 760°C and dwell for 2 hours	3

3.4 Tensile specimen preparation

Machined tensile specimens were etched to reveal the weldment position on the specimen gauge length. Before etching, the gauge length of the specimen was polished by hand until a smooth surface was achieved. A 2% Nital solution deposited by a pipette was used to etch specimens for 10 minutes. The etching process was considered complete when the Nital solution turned cloudy. Etching of specimens revealed the weld metal, fusion lines and the HAZ.

Further inspection of the specimen under a light microscope would reveal a distinct weld and HAZ. The etched specimen was inspected under a Leica MZ 8 light microscope to measure the width of the weld and the HAZ. The position of the weld and HAZ in the gauge length was recorded for all specimens before testing.

3.5 Tensile specimen survey

To prepare specimens for experiments, measurements locating the gauge length, fusion zone width and fusion lines positions were taken. A vernier gauge was used to measure the gauge length and the position of the fusion lines relative to the left edge of the gauge length selected as the origin axis. Tensile test specimens were designed with a 70mm gauge length. The width of the fusion zone was measured under the Leica light microscope. Figure 3.*10* shows a specimen with measurements on the fusion zone.

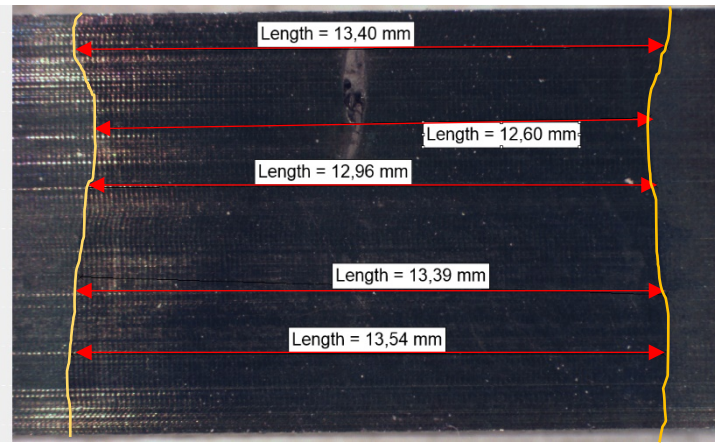

Figure 3.10:Measurement of fusion zone Width

After the specimens were surveyed, the gauge length was speckled in preparation for DIC. Speckle patterns were applied using VHT Flameproof ™ high temperature paint (white and black). The speckle pattern was applied 30 minutes before testing. Before speckling the gauge length was roughened using 80 grit sand paper. A uniform thin layer of white paint was sprayed first followed by speckle application using black paint. The speckles were achieved by placing the specimen under the spray mist allowing fine mist particles to be distributed on the gauge length. The speckle pattern was applied to match an average speckle diameter of approximately 0.09 mm [29]. Figure 3.*11* shows a speckled specimen before an experiment.

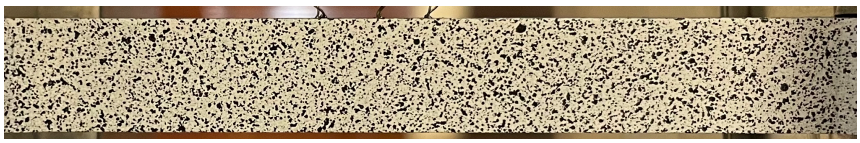

Figure 3.11: Speckled specimen

Figure 3.12 shows thermocouples welded on a specimen gauge length. After the speckle pattern was applied, thermocouples were spot welded at positions 30 mm, 35 mm and 40 mm. The control thermocouple was positioned at the centre of the specimen i.e., 35 mm. This placed the fusion line in the hot zone where the highest temperature is recorded on the specimen. In this Configuration the specimen would be designated TC1, TC2 and TC3 respectively according to positioning at 30 mm, 35 mm and 40 mm. The thermocouple in the centre of the specimen was set as the control thermocouple for each experiment.

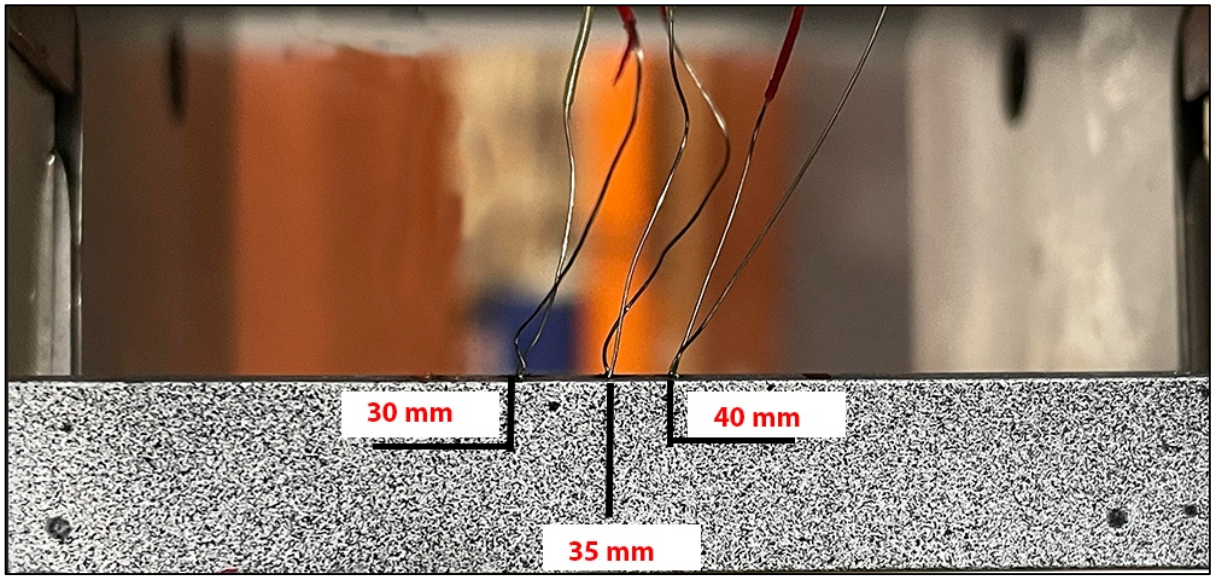

Figure 3.12: Gauge length and specimen positions

The speckle pattern was visually inspected, initially using visual judgement and then using Istra 4D DIC speckle pattern evaluation tools by changing image palettes in the Dantec DIC software tool bar drop down menu. Image palettes show contrast patterns which can be used to visually determine the quality of a speckle pattern.

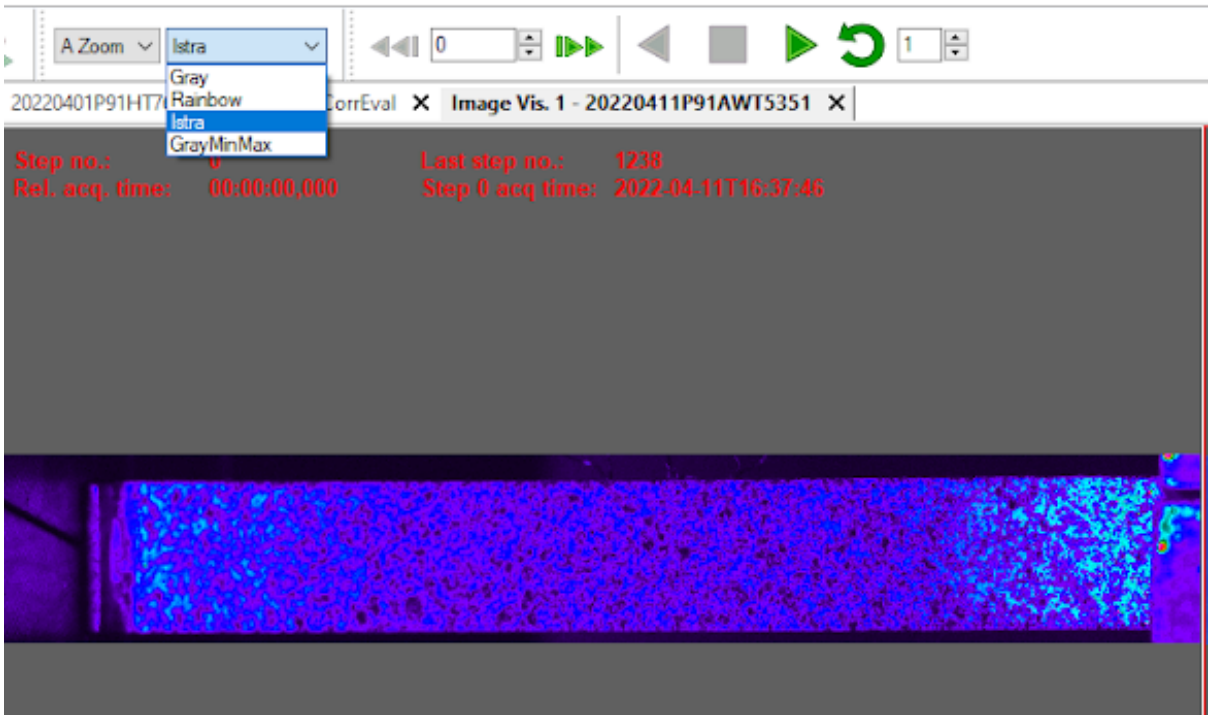

Figure 3.13: Istra image palettes

Figure 3.13 shows the Istra image palette selected in the drop-down toolbar menu, which shows maximum grey value pixels in blue and minimum in white. The dense contrast of maximum grey values and even distribution shown indicate that the speckle pattern can be tracked by the software during deformation . Other image palettes are available such as the GrayMinMax and Rainbow palette. The Istra palette was chosen because of ease of interpretation.

3.6 Tensile testing experimental set-up

Tensile tests were conducted on the Gleeble thermomechanical simulator machine. Figure 3.*14* shows a specimen mounted in the Gleeble machine. The Gleeble machine uses electrical resistance to heat specimen mounted between hydraulic grips in the Gleeble chamber. During tensile testing, a specimen was pulled apart by hydraulic grips. The specimen parameters such as the gauge length, width and height were entered into the Gleeble software before testing. The Gleeble machine produced load, stress, strain and temperature data for each step of the experiment as output. Figure 3.14 shows the tensile testing experimental set-up. In this instance, TC3 was in the centre of the specimen and thus was set as a control thermocouple for the experiment.

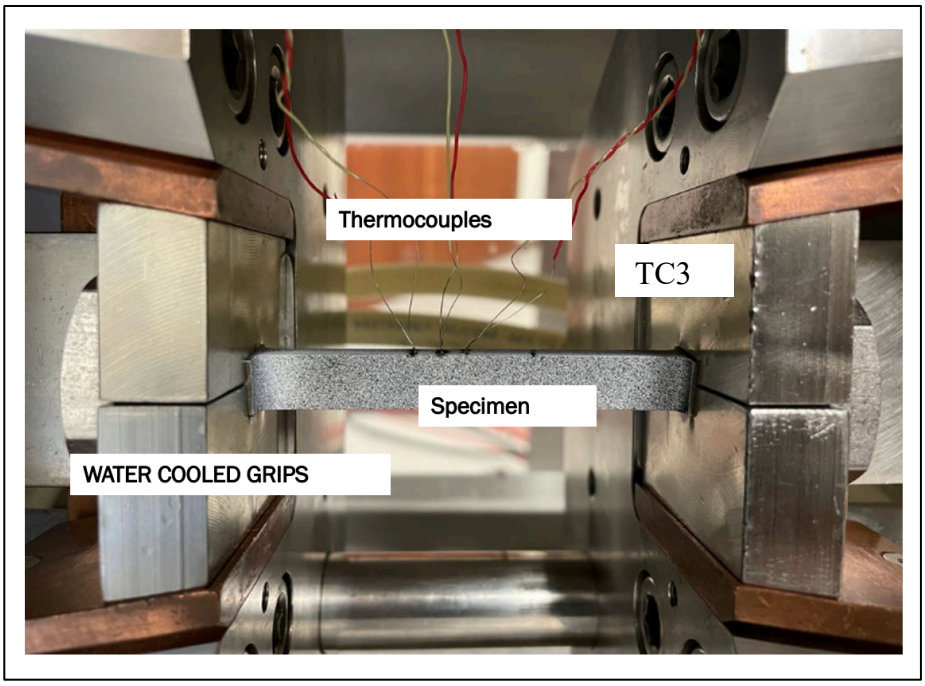

Figure 3.14: Mounted Gleeble specimen

The Gleeble loadcell force output was transferred to DIC as an analogue input utilising a National Instruments input output box. This allowed for synchronised measurement of the applied force during tensile testing on the Dantec Istra 4D DIC software eliminating the need to manually correlate Gleeble and DIC Data.

3.7 Experimental strain rate

Pandey et al. [35] conducted work to assess the effect of strain rate and notch geometry on tensile properties and fracture mechanism of creep strength enhanced ferritic (CSEF) P91 steel. The experiments were conducted at room temperature. It was observed that there is a continuous increase in tensile strength with increase in strain rate. For low strain (1.33×10^{-4}/s) and high strain rate (4×10^{-2}/s), the tensile strength was measured to be 688 MPa and 753 MPa, respectively. Hence, increase in strain rate from 1.33×10^{-4}/s to 4×10^{-2}/s resulted in a 9.4% increase in tensile strength value. The optimum value is obtained for the strain rate of 2.66×10^{-3}/s, as it gave the least % elongation and higher strength.

The optimum value used by Pandey et al. [35] falls within the range recommended by the standard for tensile testing. The standard test methods for tension testing of metallic materials ASTM E8 [36] recommends that for yield strength determination, a strain rate between 0.05 and 0.5 mm/mm/min i.e., 8×10^{-4} s^{-1} - 8×10^{-3} s^{-1} be used. A strain rate of 1×10^{-3} s^{-1} is applicable for a gauge length of 70 mm, which was the gauge length used for high temperature tensile tests in this work.

3.8 Localised strain measurement

Strain measurement values were determined with data from the Gleeble machine as well as from the DIC system. The Gleeble measures strain based on the stroke which indicates the displacement while pulling the specimen. The strain is calculated from the stroke and the gauge length specified in the program. The Dantec technologies DIC system measures point strain

using non-contact technology along the length of the specimen. A virtual strain gauge along the length of the specimen can be used to obtain engineering strain. Singh determined that a virtual strain gauge placed at the centre of the specimen gives the best strain measurement. [29].

To gain a better understanding of the effects of PWHT on mechanical properties of P91 weldments, it was necessary to obtain strain localisation across the weldments while tensile testing at different temperatures. Strain localization was obtained at yield stress (YS), ultimate tensile stress (UTS) and at a mid-point between YS and UTS. The yield stress was determined by the 0.2 % strain off-set method [36] and the UTS was determined by the position of maximum stress before onset of necking. The mid-point was established as the average of YS and UTS.

3.9 DIC Strain apparatus

Figure 3.15 shows the DIC strain apparatus set-up and a schematic diagram of the set-up. The DIC apparatus experimental set-up comprised of a 3D DIC rig with two cameras and an LED for illumination. The DIC rig was placed at a standoff distance of 1.5 m from the specimen. This allowed sufficient distance to give a high-resolution view of the speckled specimen and for opening and closing of the Gleeble window between experiments. The line of view of the cameras was adjusted to be perpendicular to the plane of the specimen.

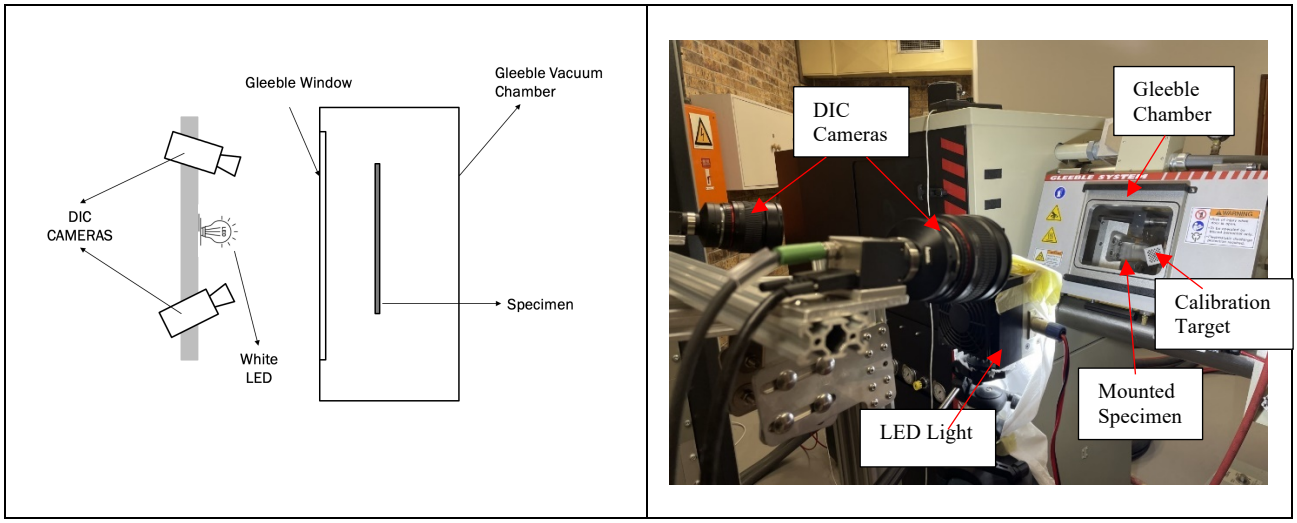

Figure 3.15: Experimental set-up and schematic diagram

Two DIC cameras were used to implement 3D DIC for spatial strain measurement. Lenses were attached to the cameras with a lens adapter to improve visibility of the specimen. A white LED was used to illuminate the specimen in the Gleeble chamber. Technical specifications for equipment used are listed in Table 3.5.

Table 3.5 : DIC Equipment Specifications

Item	Technical Specification	Quantity
Camera	Baumer USB 3.0 Camera VCXU-50M 5 Megapixel 2448 x 2048 pixel resolution 77 fps Sony IMX250	2
Lens	SAMYANG AF 35mm F1.4 FE	2
LED	100W White LED	1

Initial experiments were conducted with dummy specimens to familiarise with the experimental technique and correlate the Gleeble and the DIC data. Tensile test experiments were conducted on the Gleeble thermomechanical machine and the Dantec Systems Istra 4D DIC software was used for non-contact strain measurements.

The experiments with dummy specimens were done to familiarise with the equipment and compare DIC results to results from the Gleeble machine. The Gleeble machine program was set to deform the specimen for 4 mm applying a 2kN load, with load data recorded at a frequency of 10 Hz. The DIC software was also set to a frequency of 10 Hz. Setting the DIC and Gleeble to the same frequency reduced the discrepancy in data observed when the Gleeble is set at 20 Hz frequency, which showed plots indicating noisy data.

3.9.1 DIC calibration

DIC Calibration is a critical exercise in using DIC technology for non-contact strain measurement. The Gleeble chamber window was closed during DIC calibration. DIC calibration is done using a calibration target. Each target has its own identification (ID) and properties such as background and foreground colour, format and layout, serial number. The important properties of calibration targets are nominal grid square size , thickness and standard deviations of the square intersections. A 9 x 9 calibration target with a nominal square size of 4 mm was used to calibrate the DIC software. 4 mm represents nominal square size and 9x9 represents the number of squares on the target. During calibration, the calibration target was moved to different positions in the x,y planes and different angles to the z plane.

Calibration frames were recorded when the calibration target was fixed in one position. A new calibration was done before conducting experiments. For each calibration, a total of 10 calibration frames was recorded. Each frame captured the calibration target in a different position and identifies all intersections of grid squares. A target was successfully recognised if green circles were shown at the intersections of grid squares as shown in Figure 3.16 [37].

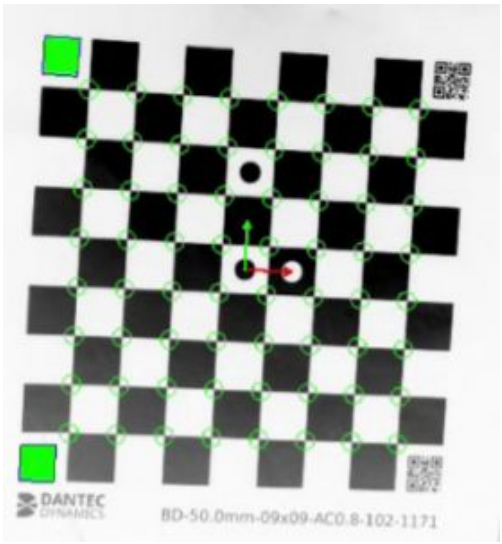

Figure 3.16: Successful recognition of a calibration target [37]

A calibration was successful when the residuum was below 0.5 on average a residuum of 0.1-0.12 was obtained for different calibrations. The residuum refers to the difference between the observed image deformation and the deformation predicted by a mathematical model. It was used to quantify the accuracy of the model and to determine whether additional iterations or refinements were needed to achieve a better fit between the model and the observed data. The calibration result was also checked for accuracy of stereo parameters as well as camera position parameters. Figure 3.*17* shows an illustration of 3D DIC stereo parameters.

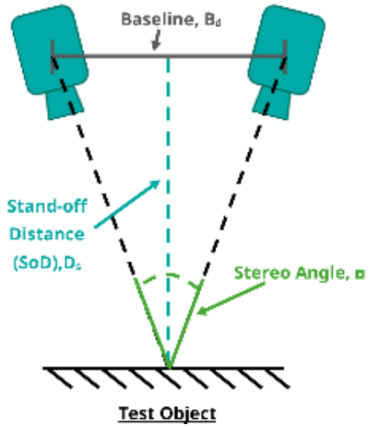

Figure 3.17: 3D DIC stereo camera parameters

The stereo parameters are the base line, standoff distance and the angle between the two cameras. The base line can be measured physically and compared to the DIC result. The stand-off distance was 1.5 m. A base line result of 433 - 436 mm was obtained during calibration. This was acceptable as it matched the measured baseline of 432 mm within less than 1% error. A stereo camera angle of 27.4 degrees was recorded. The camera position parameters were evaluated based on the principal focal point (x,y) result which was expected to match for both cameras with minimal deviation.

The calibration exercise was done each time before conducting experiments. Figure 3.18 shows a DIC calibration file output. The stereo parameters shown on the DIC calibration file were used to validate accuracy of the calibration.

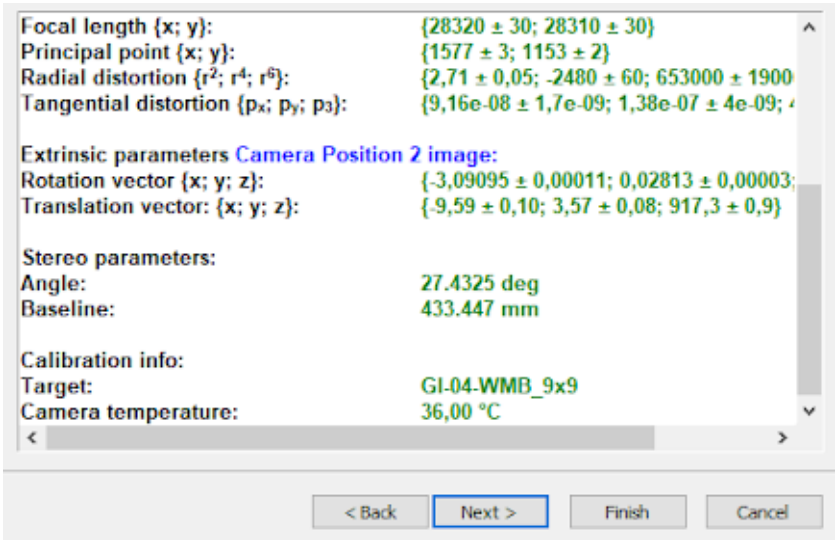

Figure 3.18: DIC Calibration File

3.9.2 Post processing of images and Facet Size Selection

Post processing of DIC images was done by the DANTEC Istra 4D software. To accurately evaluate DIC images it is important to select the appropriate evaluation parameters for the experiment. Facet size and grid spacing are two main settings that can affect the accuracy of measurement of strain localization. A facet covers a square of pixels assigned unique grey values. Each pixel represents a unique datapoint. Grid spacing is the distance between centres of two facets. Figure 3.19 shows a speckled specimen, 19 x 19 pixel facets with a grid spacing of 17 pixel.

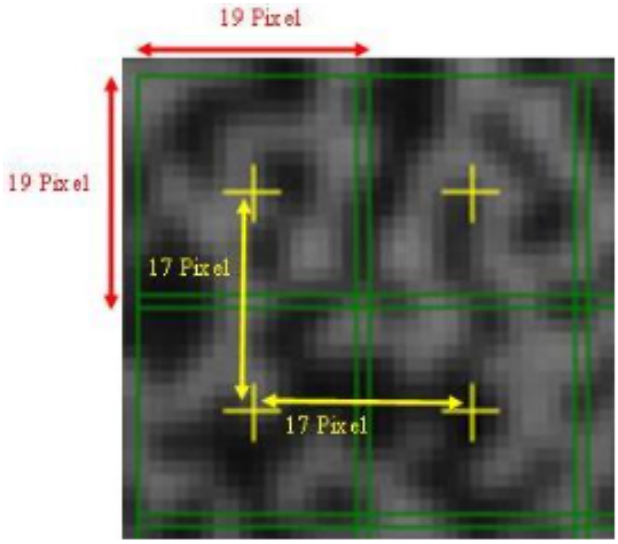

Figure 3.19: Facet size [38]

The facet size should be smaller than the size of the local strain area covered by the region of interest [38]. Grid spacing determines the distance between the centres of two adjacent facets. The smaller the grid spacing the more data points exist in the DIC evaluation. Large grid spacing values result in smoothening effect on data. Figure 3.*20* shows local strain plots with different grid spacing. The smoothing effect can be observed with an increase in grid spacing from 1 pixel to 50 pixels. Smoothing results in loss of localised strain data.

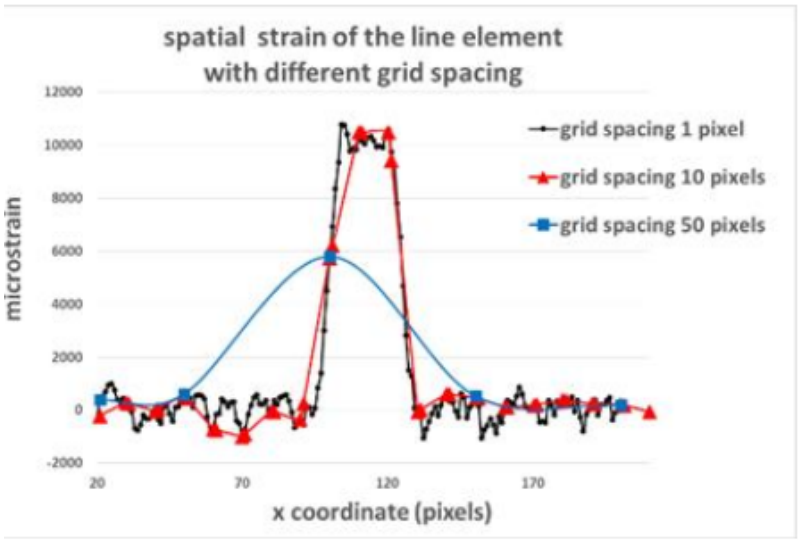

Figure 3.20: Grid spacing and smoothing effect [38]

The accuracy of different facet sizes was determined at 50% grid spacing. An evaluation of facet size versus displacement standard deviation was done. During this exercise, the facet size was changed and the standard deviation value resulting from each facet size at zero was recorded. Figure 3.21 shows a plot of standard deviation versus facet size from baseline test. Smaller facet sizes have a higher standard deviation which means there is a high standard deviation error. This is because of fewer datapoints, increasing the facet size increases the datapoints and results in a reduced error. However, it is important to ensure that the facet size is smaller than the size of the local strain area in cases of localised strain measurement. The determined local strain area on the tensile test specimens required in this work measured 323 x 456 pixels.

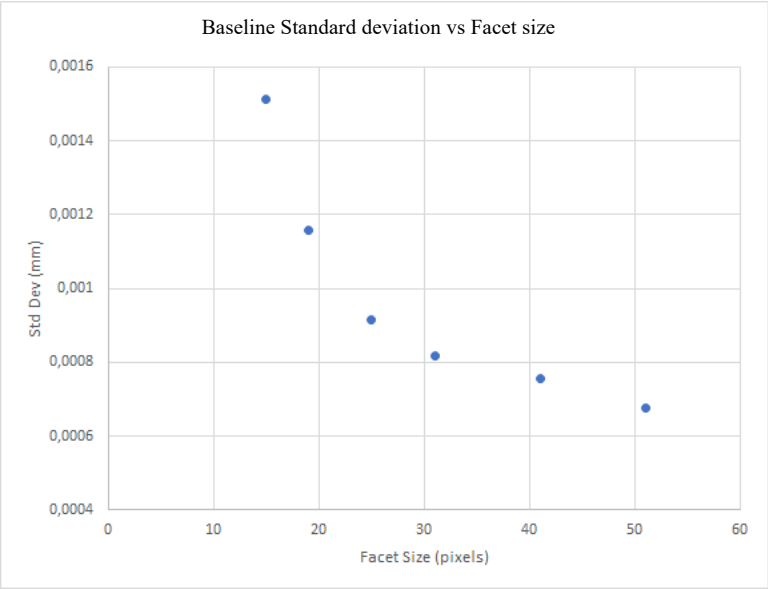

Figure 3.21: Baseline standard deviation vs facet size

A rigid body translation test was done to measure the difference of the recorded displacement on DIC. A rigid body translation test is where an object is moved from a point of origin to another known position in the same plane. An input displacement of 5mm was used for the rigid body translation test. The input displacement is the physical planar displacement of the specimen by the Gleeble machine. The mean displacement was recorded on the DIC and the difference was a subtraction of the recorded displacement from the input displacement. Figure 3.*22* shows the plot of difference versus facet size. The difference was defined as the difference between the recorded DIC displacement and the input displacement of 5mm.

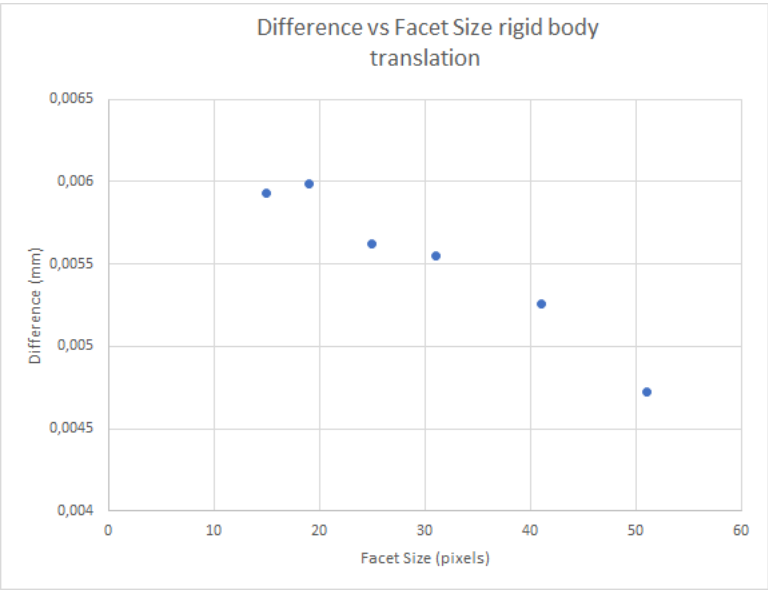

Figure 3.22: 5mm Translation Rigid body Test Difference from input displacement

The results show that there was improved accuracy with increased facet size. It was then important to determine the effect of different facet sizes on the strain localization data from a tensile test. Strain localization data for a tensile test was evaluated for different facet sizes.

Figure 3.*23* shows a plot of strain localisation data from a tensile test of as-welded P91 specimen at 300°C, at ultimate tensile stress.

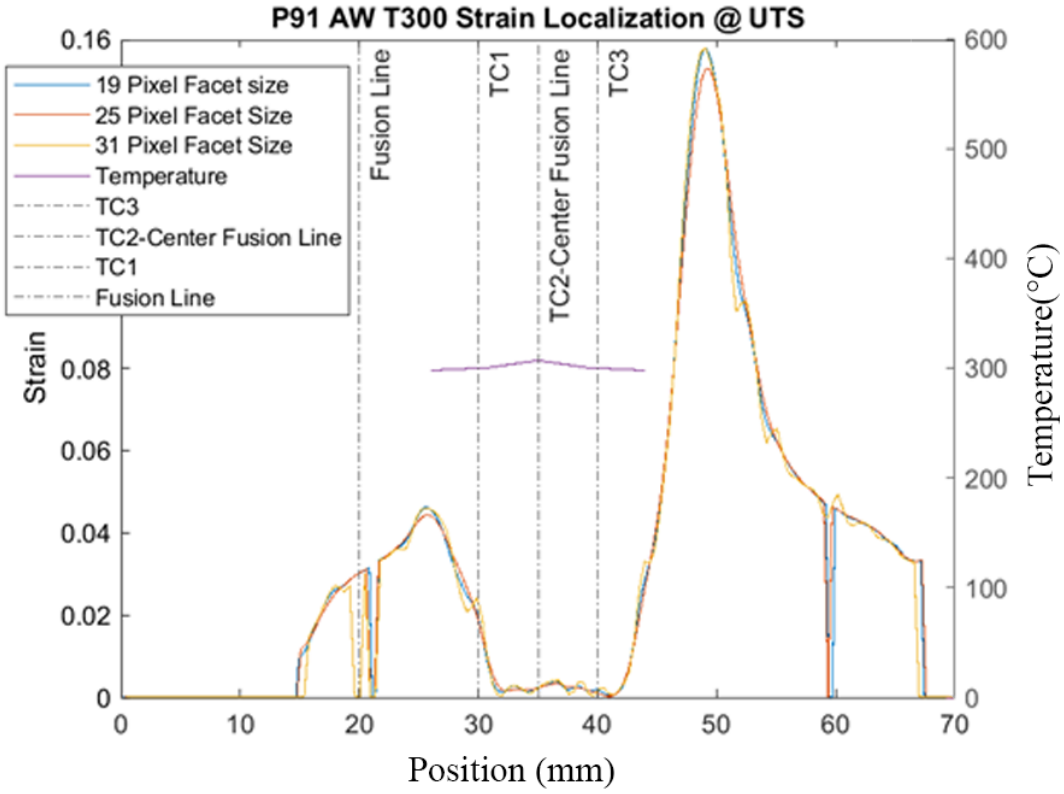

Figure 3.23: Strain localization data for different facet sizes of as-welded P91 Steel at 300 °C

Figure 3.23 shows that the results obtained were similar with minimal differences. A facet size of 19 pixels exhibited more displacement at UTS Localised strain peaks, this illustrated the smoothing effect of increasing facet size between 19 and 25. In Figure 3.23, a facet size of 31 pixels shows peaks matching a 19-pixel facet size, but more noise is visible in the plot due to increased number of data points. Figure 3.21 shows that a 31-pixel facet size had a lower standard deviation error than a 19-pixel facet size. In Figure 3.22, comparing 19 pixel facet size to 31 pixel facet size, the 31 pixel facet size had a smaller difference. Based on these observations, facet size of 31 pixels at 50% grid spacing (15 pixels) was deemed more appropriate DIC evaluation settings.

3.9.3 3D DIC Evaluation

Figure 3.*24* shows 3D DIC evaluation for a tensile test specimen. Figure 3.24 a shows a rectangular mask drawn on the gauge area marking the region of interest for evaluation. The gauge area measured 70 mm in length. Figure 3.24 b shows evaluation of x displacement from a mask on the gauge length at step 0. Figure 3.24 c-e were taken at the onset of necking.

These images show evaluation of x-y-z displacement from a completed DIC evaluation. For each image, the visualisation was changed to show x, y or z displacement. The color-coded scale on the right shows the displacement values. Figure *3.24* c shows x displacement, Figure *3.24* d shows the y displacement and Figure *3.24* e shows the z displacement (out of plane). The maximum x displacement was on the side of the specimen where the crosshead was moving pulling the specimen.

The maximum y and z displacement were in the area where necking occurred. DIC software used displacement to calculate spatial strain. The strain values for the virtual strain gauge were exported from DIC software as gauge strain in HDF5 file format. These strain values were used to plot localised strain maps.

a)

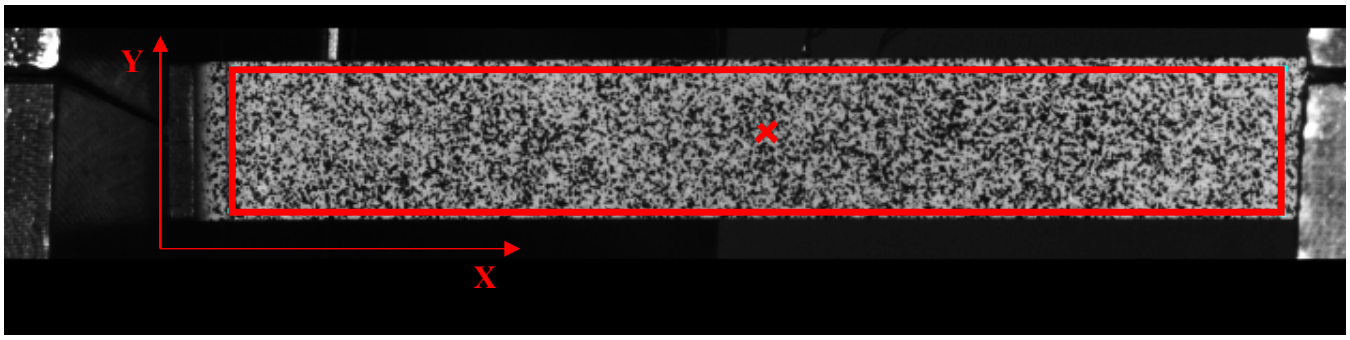

b)

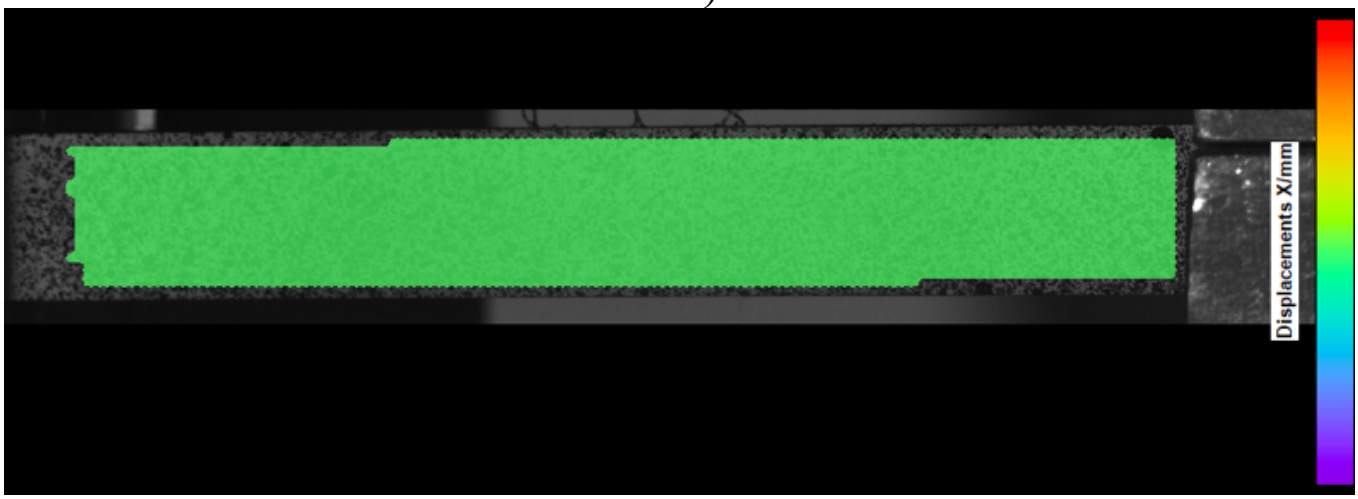

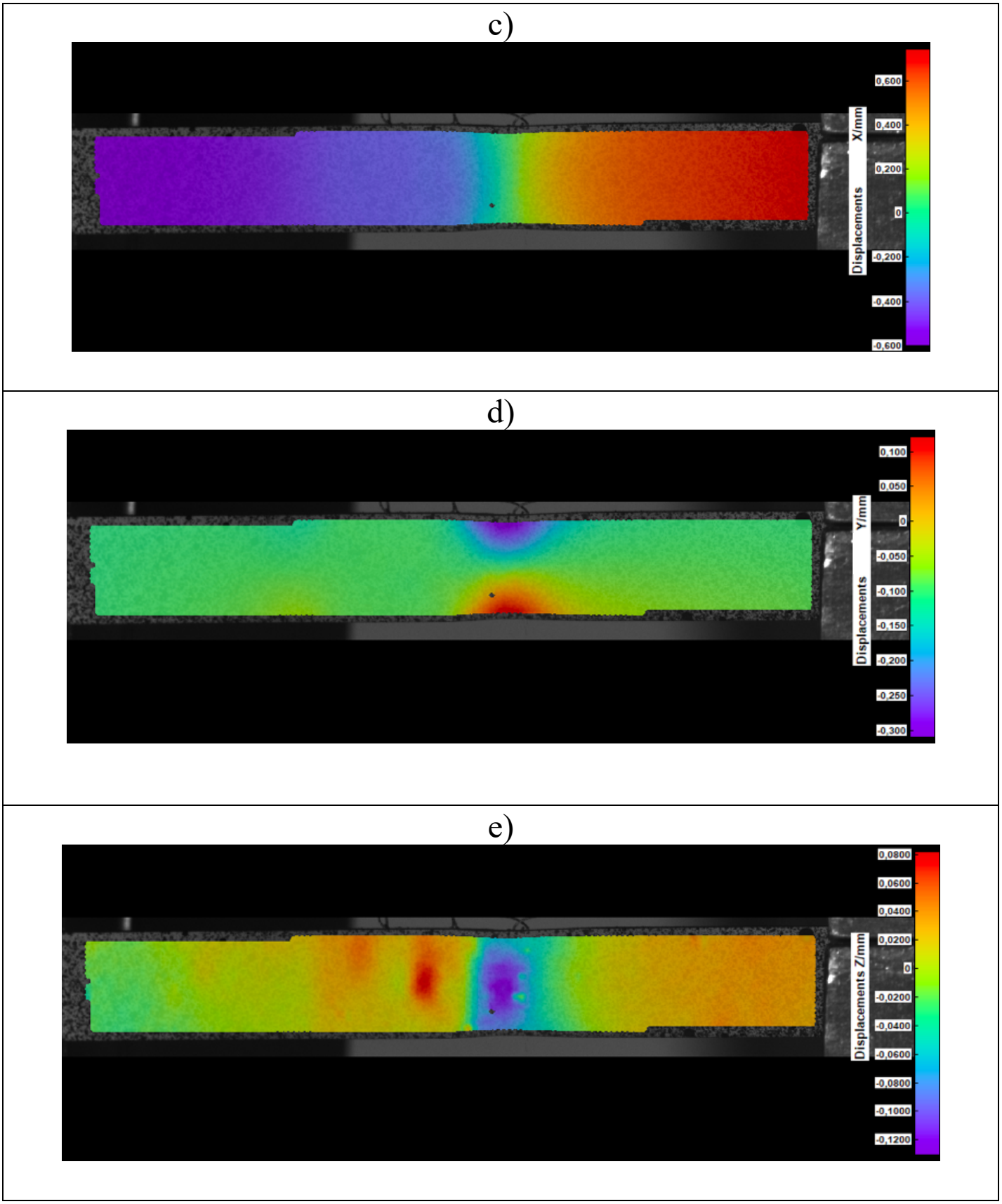

Figure 3.24 : DIC displacement visualization a) defined mask b) initial step c) x displacement d) y displacement e) z displacement

To align a localised strain map to a gauge length, a co-ordinate system was selected. The Dantec DIC system used a 2 point coordinate system where a red dot is used to select an arbitrary origin and a blue dot indicated the x direction of the coordinate system. The arbitrary origin was placed close to the far-left side of the DIC mask, within the mask. Figure 3.*25* a shows a defined mask with a marker in the centre with evaluated grid points. Figure 3.*25* b shows the 2 point coordinate system circular markers in red indicating the arbitrary origin and blue circle indicating the direction of the x-axis.

After an evaluation of DIC image data, experimental data was exported as HDF5 files. HDF5 files stored information in a hierarchical structure using a file directory structure. The information stored included displacement and strains in the x, y and z coordinates for each pixel on the specimen. These HDF5 files were processed in MATLAB to extract displacement and strain information from the specimen. Figure 3.*25* c shows a 3D surface plot of the processed HDF5 file output. It was apparent from the surface plot that there was out of plane movement. Therefore, considering planar strain values only would result in inaccurate strain measurement. Figure 3.*25* d shows a 2D surface plot in the x-y plane. A start and end point was selected on the plot represented by corresponding x,y,z values. Start points were selected for each evaluated experiment. These coordinates represented end points of a line along which localised strain map data were extracted for the specimen. 3D DIC recorded strain data in three different planes.

To obtain accurate longitudinal strain data, it was necessary to map the 3D strain data into planar strain. The MATLAB script utilised divided a line between the start and end points into several points on which small 2D planes were fitted, 3D strain data was mapped onto this 2D plane to give longitudinal strain. Figure 3.25 d, shows an illustration of a start and end point line divided into several points and fitted with 2D planes as shown in Figure 3.25 e. The number of planes and plane size fitted on a line was adjusted by user input. A plane size of 2 mm x 5 mm was used fitted on 65 on the line. This was repeated for each evaluated experiment to extract localised strain. Figure 3.25 f, shows a localised strain map between selected end points.

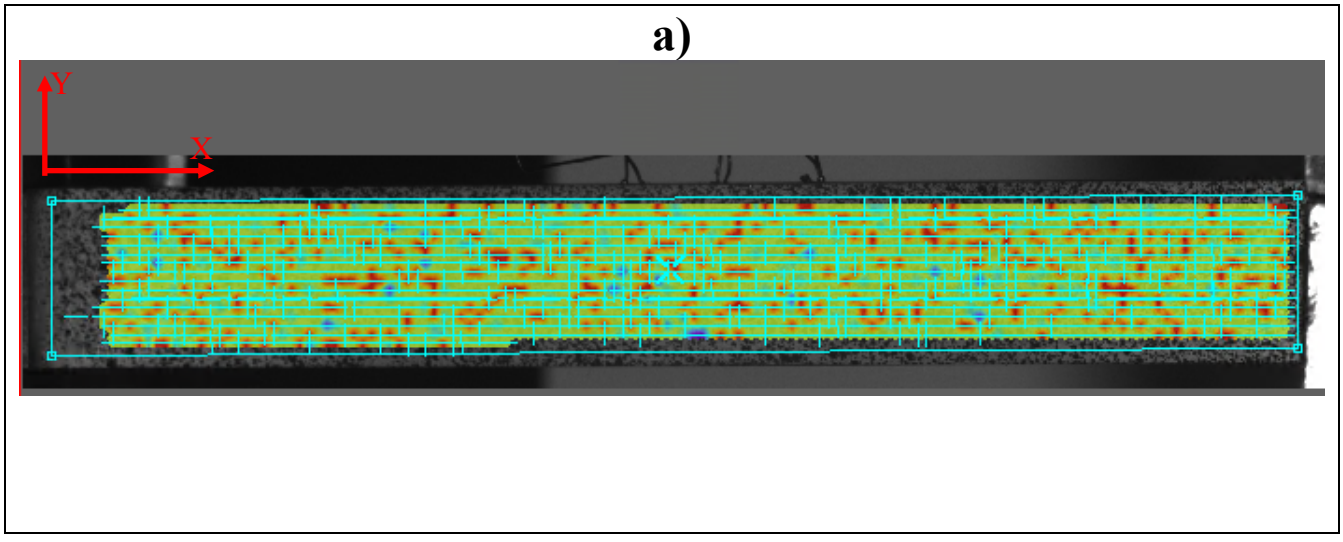

b)

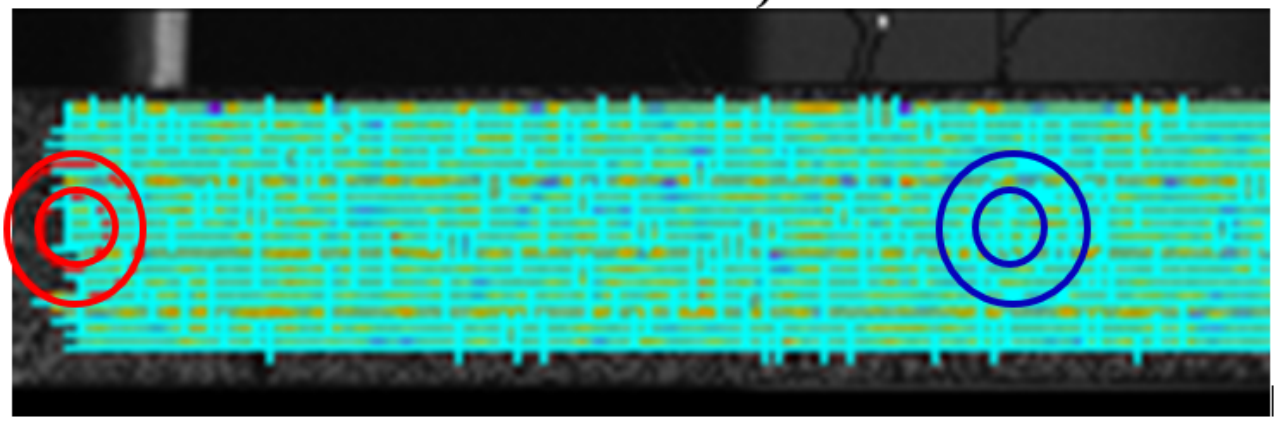

c)

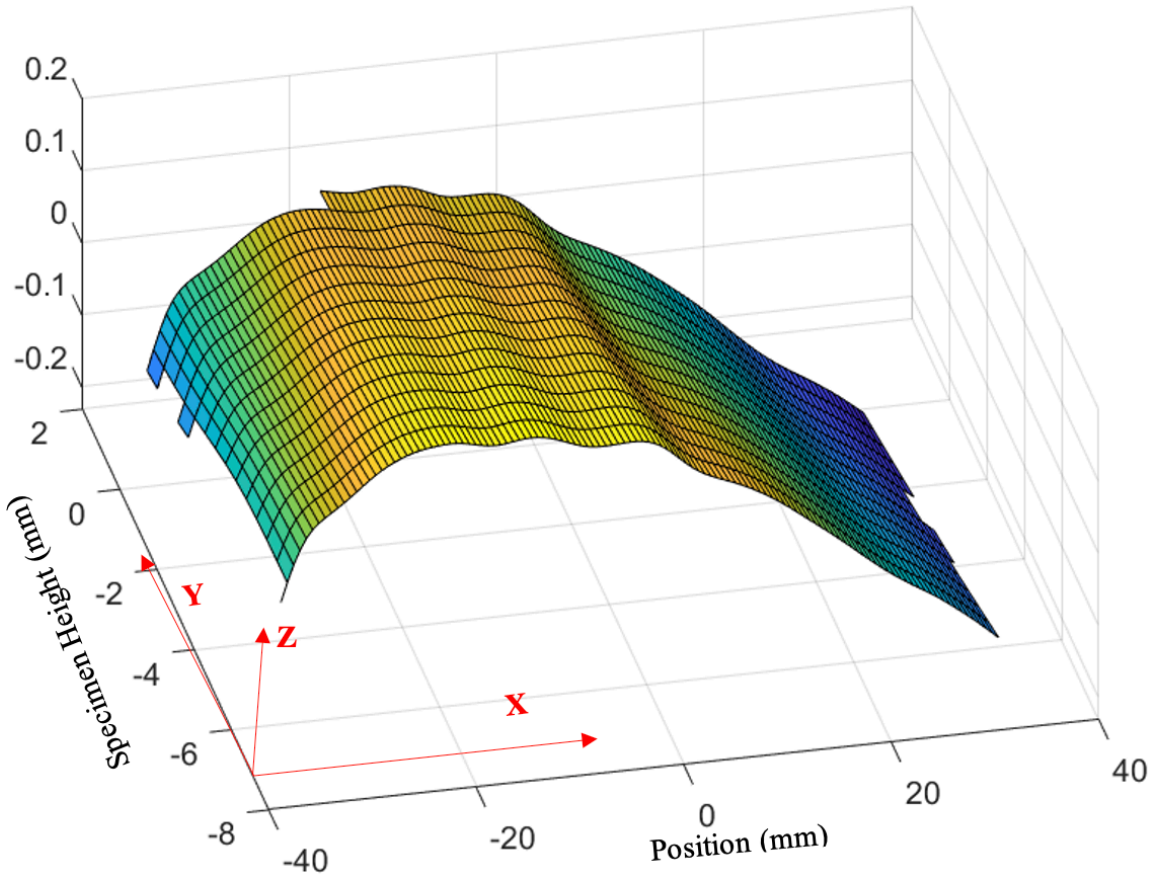
0.2
0.1
0
-0.1
-0.2
2
0
-2
-4
-6
-8
Specimen Height (mm)
Y
Z
X
-40
-20
0
20
40
Position (mm)

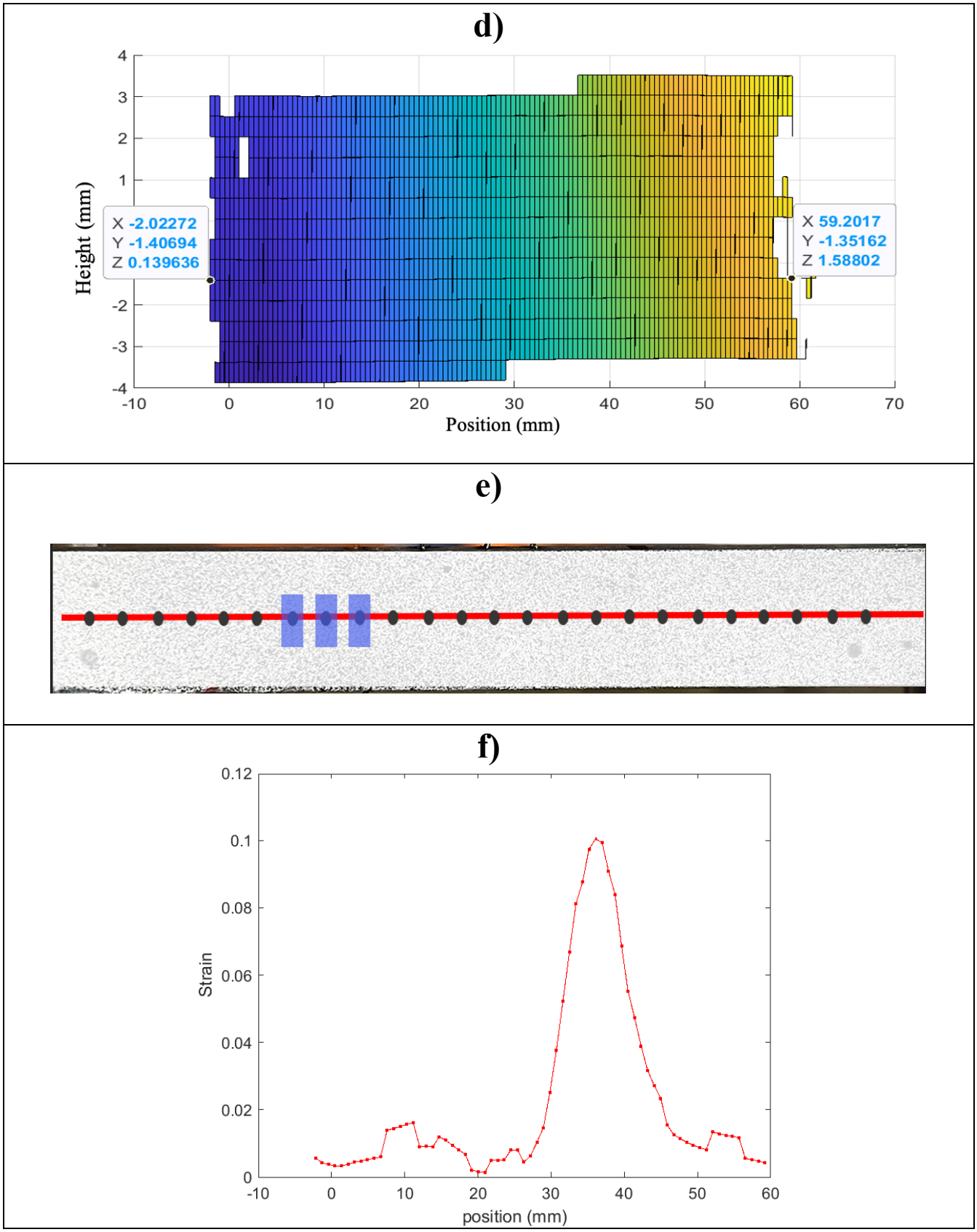

Figure 3.25: a) Evaluated DIC mask, b) DIC coordinate markers, c) 3D Surface map d) 2D surface plot with start and end point e) 2d planes f) localised strain map between end points

It is important to note that not all grid points in the mask in Figure 3.25 a are evaluated within the selected area covered by a blue rectangle. Grid points on the left edge and along edges of the mask are not evaluated. There is also no physical reference on this edge to assign an origin. To match the DIC strain map more accurately to the gauge length, the position of the origin was adjusted to align with the thermocouple at gauge centre position 35 mm as illustrated in Figure 3.26 a and b. Figure 3.26 c and d show the evaluated DIC mask and corresponding localised strain map based on the indicated start and end points in Figure 3.26 c.

a)

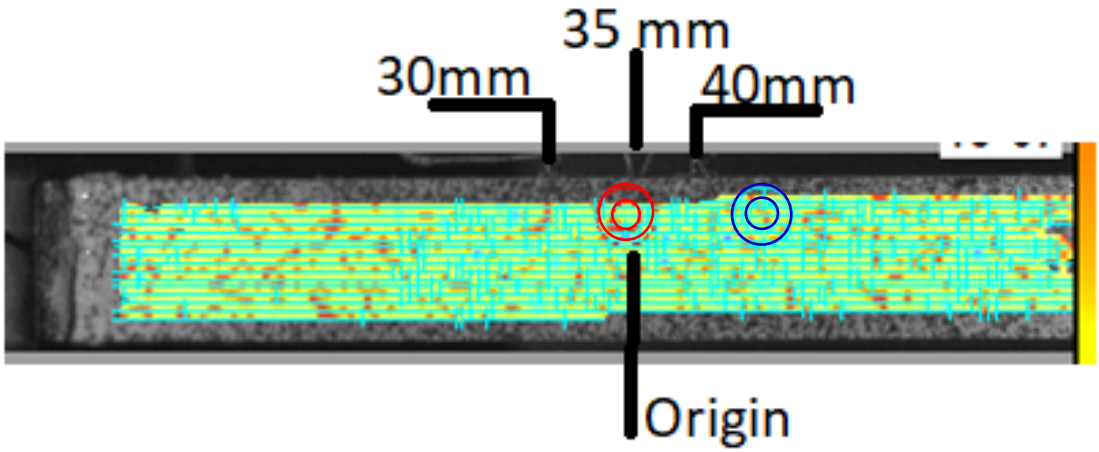

b)

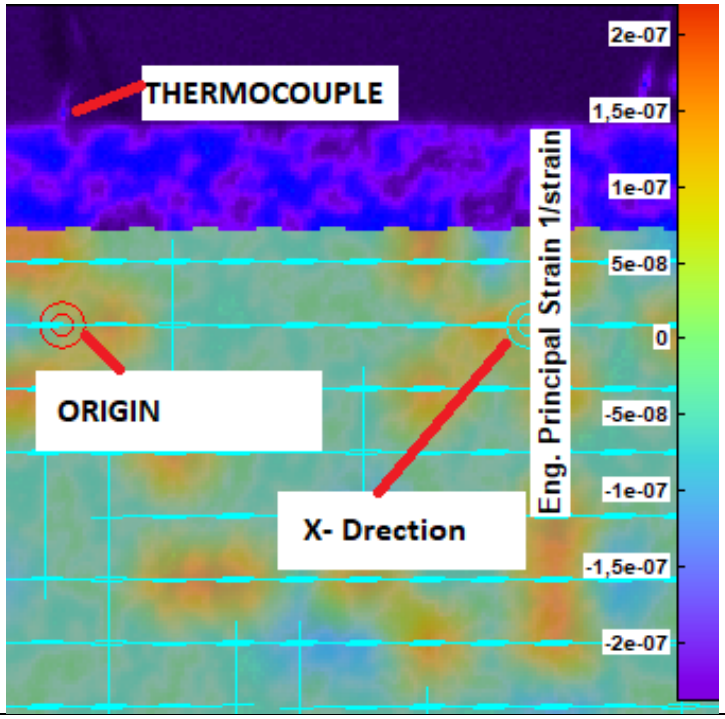

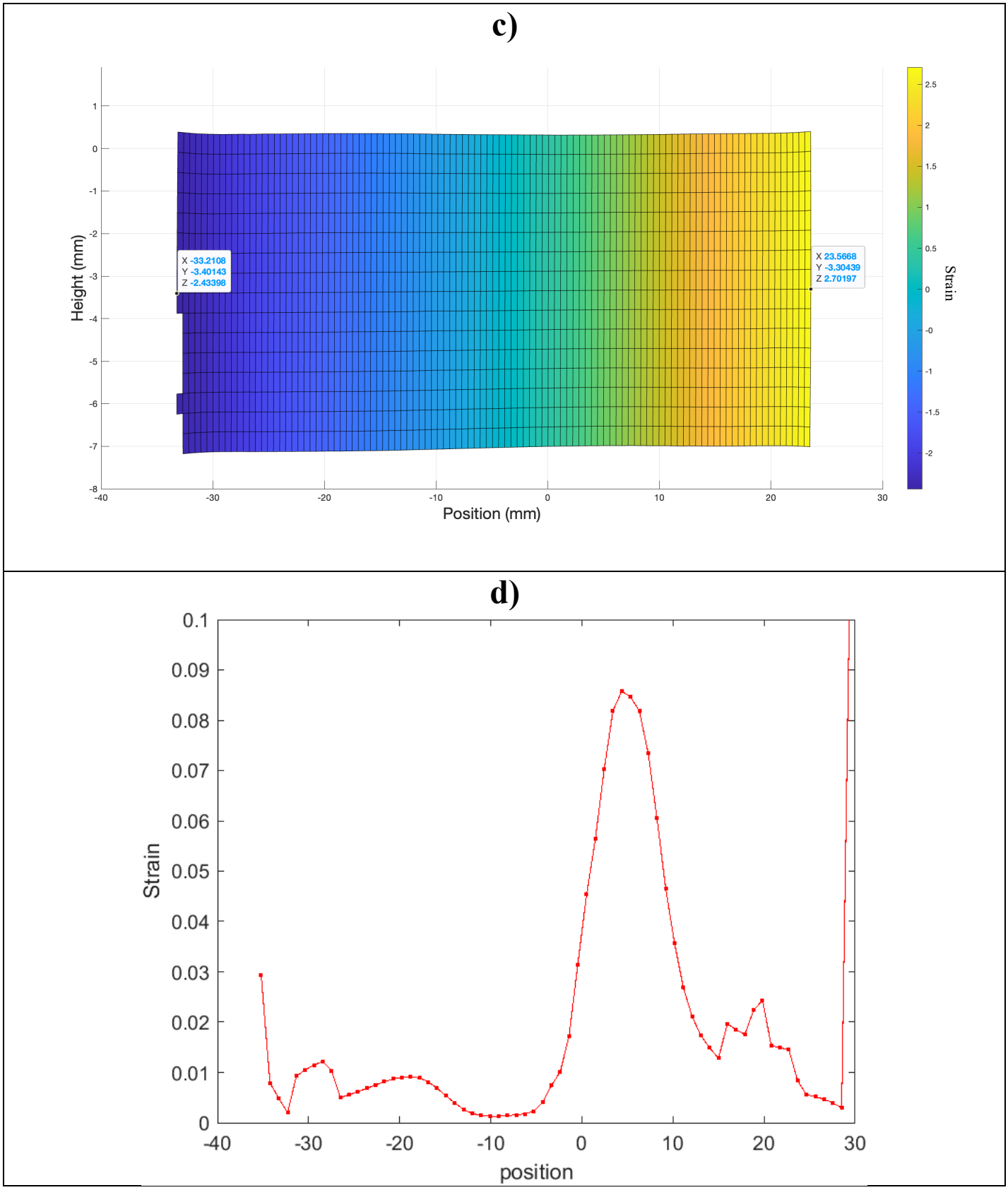

Figure 3.26: Aligning origin with thermocouples for accurate measurement a) Thermocouple and origin positions, b) co-ordinate axis, c) 2D surface plot start and end point, d) localised strain map between end points

This technique was more appropriate because the technique accurately extracts strain data for the region of interest i.e., the weldment which is in the centre of the specimen. All grid points on the DIC mask in this region were fully evaluated.

3.10 Temperature measurement

The Gleeble 3800 machine measures temperatures using K- type thermocouples attached to the specimens. Gleeble's standards specify a minimum of 2.5 mm spacing between thermocouple weld beads. Figure 3.*27* shows the placement of thermocouples in work done by Singh [29]. In Singh's work four thermocouples were placed on the specimen with TC1 at the centre of the gauge length. The control thermocouple TC2 was welded at the fusion line 5 mm away from TC1. TC3 was welded approximately 3mm from TC2. TC3 and TC4 were welded approximately 3 mm apart in compliance with the Gleeble standards.

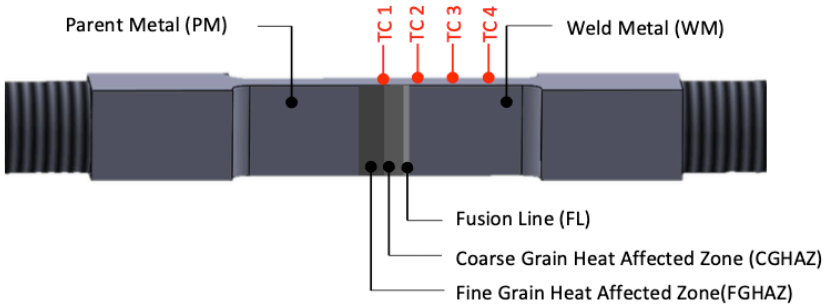

Figure 3.27 : Schematic diagram of a tensile specimen illustrating the placement of thermocouples [29]

In this work, three thermocouples, placed 5 mm apart were used with the control thermocouple TC2 was placed at the fusion line. TC1 and TC3 were placed 5mm away from TC2. This positioned the HAZ within the required temperature range of 535°C as the control thermocouple overshoots this temperature by ±10°C. The fusion line should then be placed in the centre of the specimen such that thermal symmetry can be achieved by the centre of the specimen. Figure 3.*28* shows a schematic diagram illustrating the placement of thermocouples.

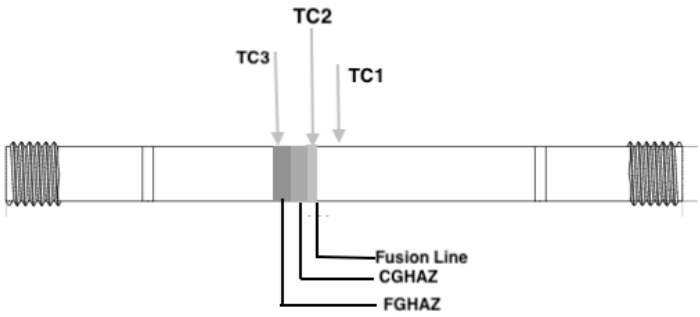

Figure 3.28: Schematic diagram of specimen illustrating placement of thermocouples

In addition to this, a thermal imaging camera was used to measure the temperature across the specimen. This allowed for temperature measurement across the entire specimen giving multiple points from which temperature readings were taken.

A thermal camera was used to record the temperature of the entire Region of Interest (ROI) on the specimen. The specimen was coated with a black paint on the side where temperature readings were recorded by the thermal imaging camera. This was also done by Singh [29] where an infrared radiometric camera was used. Obtaining temperature along the entire length was necessary for quantitative evaluation of the effect of temperature on strain localization on specific points of the specimen.

In some specimens, the fusion line did not coincide with the centre of the specimen. In these cases three thermocouples were connected from the centre of the specimen with a spacing of 5 mm between thermocouples. The thermocouples recorded temperatures T1, T2, T3 with T2 as the control at the fusion line and T3 being at the centre of the specimen.

A temperature profile on the specimen was obtained using a Telops infrared camera. The IR camera was positioned at the back of the Gleeble chamber. One side of the specimen's gauge length was painted black with a high temperature resistant VHT flameproof paint to improve surface emissivity so that the IR thermal camera recorded the surface temperature. The results were monitored and collected via the Reveal IR software. Figure 3.*29* shows a schematic diagram of the experimental set-up with the IR camera. The IR camera was later discarded. This is because there was a mismatch between the pixel resolutions of the IR camera data and the DIC data which made it impossible to match the temperature to pixels on the DIC data without compromising the integrity of the data. To avoid this complexity, the experimental set-up in Figure 3.*15* was adopted which employs a predetermined point-based temperature measurement.

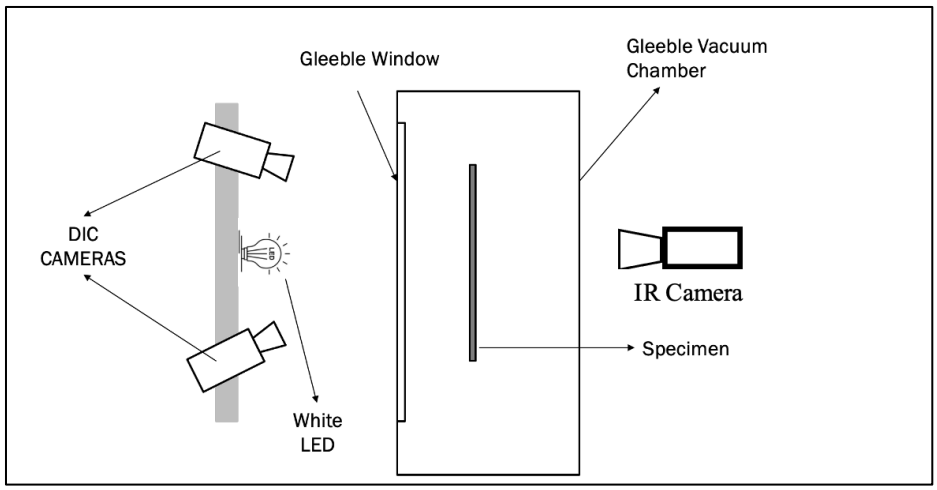

Figure 3.29: DIC Strain apparatus experimental set-up with IR camera

IR temperature recordings were done under the radiometric temperature setting. During the experiment the emissivity was set to 100% and the radiation factor was set at 75%. In playback mode, the values were set to be the same as during experiment. The temperature values indicated on the Gleeble for each point where thermocouples were attached to was used to calibrate the IR thermal camera. Figure 3.*30* shows an infrared image of the specimen at high temperature as seen on the Reveal IR software. Reveal IR software allows exporting of an ASCII file with temperature readings matrix for each pixel on the image. The exported data in the file was further be processed in excel.

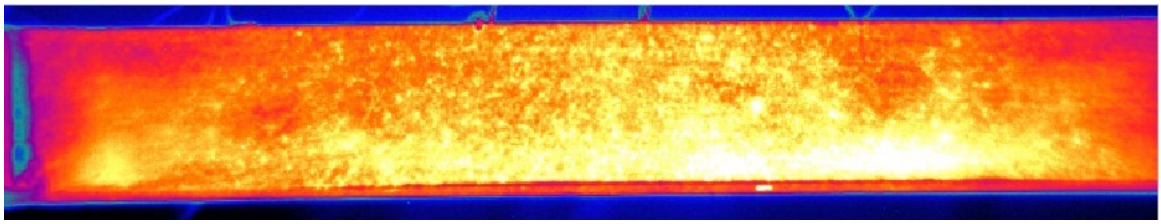

Figure 3.30: IR camera image showing temperature across the dummy specimen.

Figure 3.31 shows the parabolic temperature profile of the specimen. The temperature profile of the infrared camera matched the temperature profile recorded by thermocouples on the Gleeble machine. The specimen had a hot zone of 10 mm when thermocouples were placed 5 mm apart.

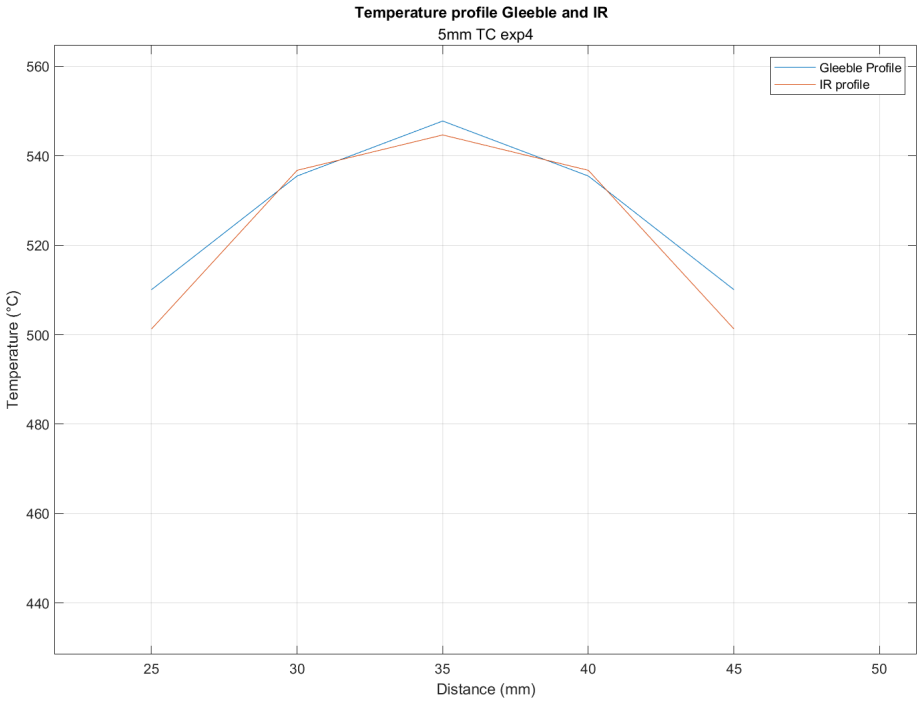

Figure 3.31: IR and Gleeble specimen temperature profile

3.11 Comparison of the DIC and Gleeble Data

Experiments were conducted to evaluate DIC as a suitable method to accurately measure the displacement of specimen under tensile testing on the Gleeble machine. Results from the Zwick tensile testing machine were used as a benchmark to compare results obtained from DIC strain measurements on the Gleeble machine. Figure 3.32 and Figure 3.33 show stress-strain curves from mild steel dummy specimen tensile tests. The DIC system used on the Zwick machine and Gleeble machine were from the same manufacturers, however they had two separate DIC set-ups. In Figure 3.*32*, the resulting stress strain curve from DIC output is compared to the Zwick machine output. The DIC stress strain curve is near ideal showing a very high elastic modulus. The difference in the DIC and Zwick results was attributed to the machine compliance phenomenon [29], the linear movement of the crosshead affected the overall result. Figure 3.*33* shows results from strain measurements using the video extensometer technique, which closely matched the results from the DIC.

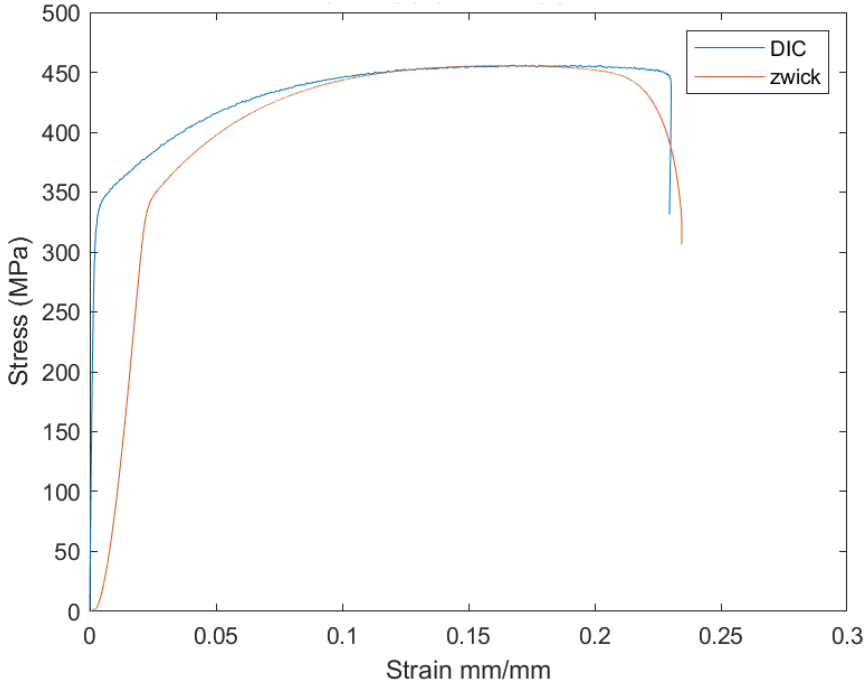

Figure 3.32: Mild steel dummy specimen ZWICK-DIC tensile test stress strain plot

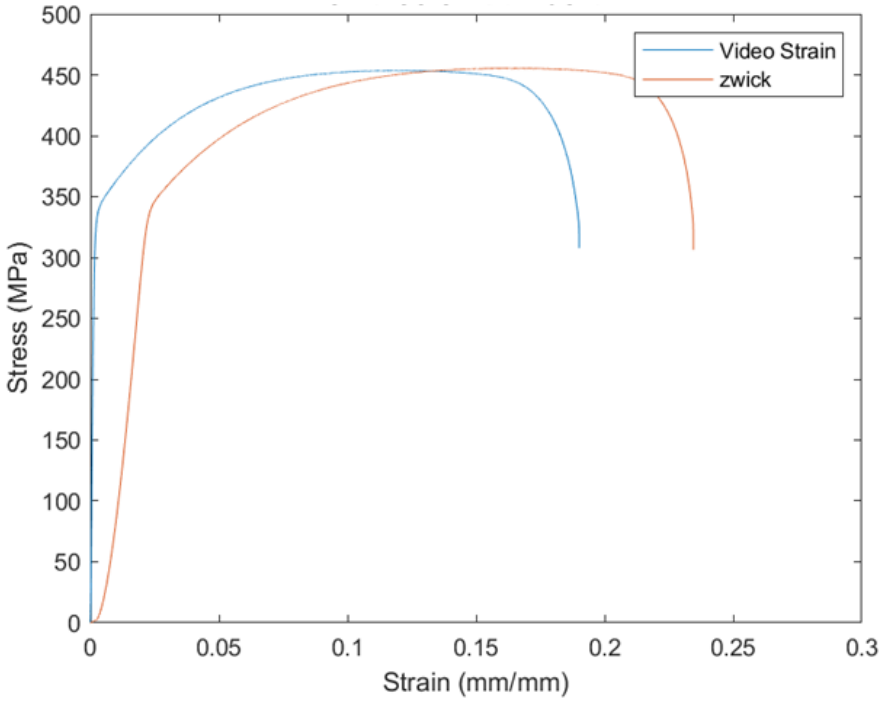

Figure 3.33: Mild steel dummy specimen Video Extensometer vs Zwick tensile test stress strain plot

Figure 3.34 shows a stress strain plot of P91 specimen tensile test on the Gleeble machine, from Gleeble and DIC data. This shows that the DIC technique was repeatable and could accurately record non-contact strain measurement on the Gleeble machine.

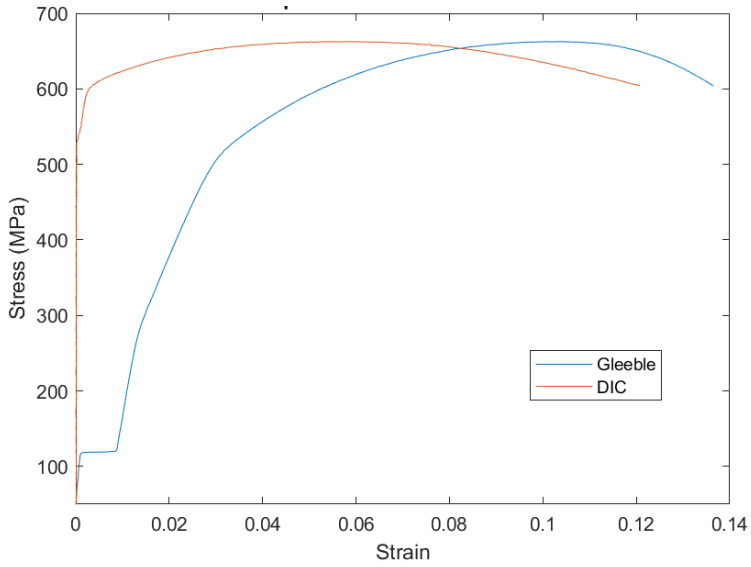

Figure 3.34: P91 DIC-Gleeble room temperature tensile tests stress strain plot

Figure 3.35 shows the strain time plots of the P91 tensile test at room temperature. The strain represents longitudinal strain of the specimen. Longitudinal strain measurements were determined by extracting data from both the Gleeble and the DIC system. The Gleeble strain measurements were determined by the relative movement of the stroke, while the longitudinal strain from the DIC system was found by tracking the movement of a virtual strain gauge line from one end of the gauge length to another, placed at the vertical centre of the specimen.

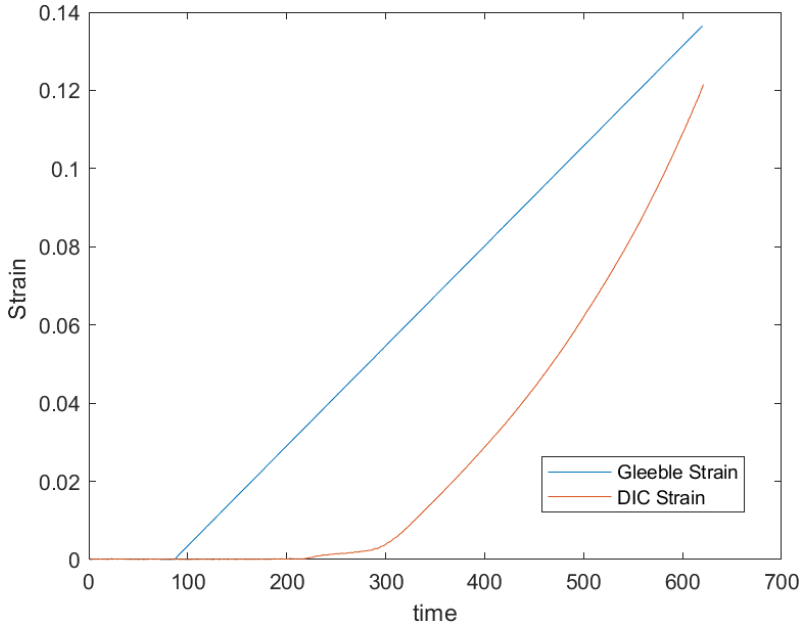

Figure 3.35: DIC-Gleeble global strain time curve

The Gleeble was programmed to extend the specimen at a constant strain rate of 51.5 x10^{-3}/s. The Gleeble strain was found to be a diagonal straight strain-time graph. Strain from the DIC system was measured by evaluating the relative displacement of pixels. Strain from the DIC system did not follow the same linear trend as the strain recorded by the Gleeble. The strain had an almost bilinear strain-time relationship. The strain data from the DIC was a more accurate gauge strain measurement because the artificial strain due to the influences of non-specimen displacement in the grips of the grips machine was not included.

3.12 Hardness tests

Vickers hardness tests were conducted in accordance with test method ASTM E384, standard test method for micro-indentation hardness of materials. For pipes with wall thickness 0.200 in. [5.1 mm] or over; either the Brinell or Rockwell hardness test method must be used. When Brinell hardness testing is used, a 10-mm ball with 3000, 1500, or 500-kg load shall be used at the option of the supplier or user [39].

Hardness testing was performed to compare the mechanical properties of all heat treatment conditions before tensile testing and to approximate the weld zones on specimen. Singh [29] utilised the hardness test to validate the length and location of the heat affected zone in weldments. The Vickers microhardness tests were performed using a Dura Scan EMCO tester along the transverse direction of the welds on small rectangular specimens of dimensions of 28mm x 10mm x 10mm. Hardness test specimens with similar dimensions were prepared from different specimens as shown in Table 3.*6*.

Table 3.6: Hardness test matrix

Heat treatment temperature	**Number of specimens**
As-welded	1
720°C	1
760°C	1
800°C	1

In the experimental work done by Singh [29] all specimens were ground and polished using a one-micron water based diamond suspension prior to hardness testing to produce a smooth surface finish. All tests were conducted at intervals of 0.3 millimetres, using a constant load of 300 g ($HV_{0.3}$).

Hardness tests were conducted at room temperature. Five heat treatment conditions were selected for hardness tests. The selected heat treatments for hardness testing are AW, HT760-2Hr, HT800-2Hr, HT760-6Hr, HT760EX840. HT720-2Hr, HT760-4Hr and HT760EX820 were left out because these were intermediate conditions. Hardness tests were done to accurately locate the HAZ, measure HAZ width and identify different weld zones.

The first set of hardness tests was done at a macro scale with a spacing of 1mm between indentations on the Zwick Roell hardness tester. Indentations were made with a 10kgf load. The first indentation had a diagonals measuring 290 μm, based on that a spacing of 900 μm was allowed between indents. The weld is assumed to be symmetrical, so indentations were done on only one side of the weld.

To further distinguish between different weld zones in the HAZ i.e., ICHAZ, FGHAZ, CGHAZ, FZ, microhardness tests were done at room temperature with a 300gf load on a Highwood HVDM3 micro hardness tester. The indentations had a diagonals of 49 μm, a spacing of 150μm was allowed in between indents. Hardness measurements were taken from the base metal up into the weld metal mostly covering the HAZ.

3.13 Microscopy Analysis

Understanding microstructure includes comprehending the compounds or phases present in the material. Microscopic analysis is important to relate material property to mechanical properties. Pandey et al. [2] conducted SEM, EDS spectra and line mapping on P91 specimens. This helped confirm the precipitates present at PAGBs based on chemical composition and compare heat treatments microstructural compositions. Wang and Li [18] created an EBSD phase map that shows microstructural phase composition and precipitate density of the FGHAZ of P91 specimen subjected to creep test after PWHT.

The strengthening mechanism for P91 is solid solution strengthening and precipitate hardening. This is a function of precipitates present in the microstructure on PAGBS and intragranular. Characterising the precipitates within the microstructure can help relate tensile strength properties of the HAZ, WM (Weld metal) and BM to the microstructural composition. The study also aimed to validate the weld zone locations as approximated by the hardness tests. It was therefore important to analyse microstructural phase compositions as a function of heat treatment.

A set of specimens was set aside for microscopic analysis. Five heat treatment conditions were selected. Specimens AW, HT760HR2, HT800HR2, HT760HR6 and HT760EX840 were selected for microstructural investigation. Specimens HT720HR2, HT760HR4 and HT760EX820 were left out because these were intermediate conditions. The etching procedure mentioned Section 3.4, was followed in preparing specimen for microscopic analysis. Specimens were investigated using light microscopy followed by scanning electron microscopy (SEM). Specimens were mounted on stubs for the SEM microscope.

Samples for microstructural analysis were cut from heat treated specimens with dimensions of 20 x 10 x 4 mm. To facilitate easier handling during grinding and polishing, samples were hot mounted in an acrylic ClaroFast SEM acrylic resin. The grinding involved three different grades of Struers waterproof silicon carbide paper, namely 800, 1200 and 2400 grit. Samples were carefully inspected under a light microscope at regular intervals during the grinding process. The inspection process consisted of rinsing the sample with ethanol and drying it with a hairdryer; this was done to remove any impurities such as silicon carbide which might have embedded into the sample during the grinding process. Thereafter, the samples were inspected under a Leica MZ 8 light microscope.

Before a finer grit grinding paper could be used, the sample was inspected under a light microscope and ensured to be scratch free and all small scratches were in the same direction. The polishing process entailed the use of a Struers Tegramin-25 automatic polisher. Both Struers DAC and NAP polishing pads, each with a different micron polishing grain, was used. Each pad, along with its corresponding water-based diamond suspension, was used in a specific sequence for a specified period of time, as detailed in the polishing procedure in Table 3.7.

Table 3.7 : Polishing procedure

Polishing Pad	Lubricant	Duration (minutes)
DAC	Dia-Duo-2 (3µm)	5
NAP	Dia-Duo-2(1µm)	5
NAP	Water	5

After grinding and polishing processes were completed, each sample was thoroughly cleaned in an ultrasonic ethanol bath. A 2 % Nital solution was used for chemical etching. Specimens were placed on a flat, dry surface, and a pipette deposited 2% Nital over the sample's surface. Specimens were etched for 10 minutes. Once the sample's surface became cloudy, the etching process was deemed complete, and the excess Nital was flushed away with ethanol. Samples were dried once more before microscopy. Two microscopes were used for SEM imaging. A Tescan MIRA SEM and a Nova NanoSEM. EDX analysis was done on the Nova NanoSEM. On the Nova NanoSEM magnification of 5,000x was used to capture low magnification images and 10,000x was used for higher magnification.

EDX was used to obtain spectrums of P91 microstructure in order to characterise the microstructure composition. The size of these precipitates in P91 microstructure, ranges from 100 to 200 nm for $M_{23}C_6$ carbides and from 20 to 50 nm for MX precipitates [10]. The setting for the SEM should allow for sufficient penetration volume in order to get accurate topographical analysis of P91 microstructure.

The region of interaction between the solid and the beam is known as the interaction volume [40]. The resulting excitation volume is a hemispherical to pear-shaped region with the neck of the pear at the specimen surface.

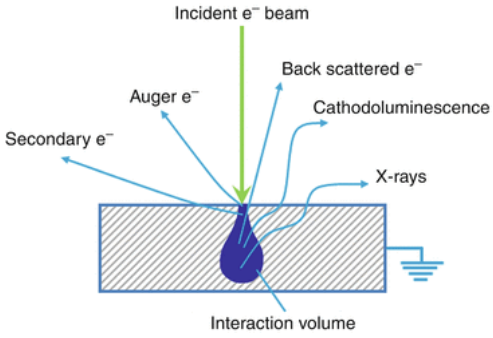

Figure 3.36: SEM interaction volume schematic diagram [40]

The depth of electron penetration of an electron beam and the volume of the specimen with which it interacts are a function of its angle of incidence, the magnitude of its current, the accelerating voltage, and the average atomic number (Z) of the sample.

The depth of penetration depth and width of the specimen were calculated for different excitation voltages. This determines the depth at which information obtained from EDX analysis. Table 3.*8* shows calculated specimen interaction volume parameters. These were calculated according to equations shown below:

$$Penetration\ depth = \frac{0.1 * {E_0}^{1.5}}{\rho} \quad \text{.....3-1} \quad [41]$$

$$Width = \frac{0.077 * {E_0}^{1.5}}{\rho} \quad \text{.....3-2} [41]$$

where E_0 is the excitation voltage and ρ is the material density in grams per cubic centimetres. The material density of P91 steel is 7.77 g/cm^3 [42].

Table 3.8: P91 Specimen interaction volume parameters

Excitation Voltage (keV)	Penetration Depth (µm)	Width (µm)
10	0.41	0.31
15	0.75	0.58
20	1.16	0.89
25	1.62	1.25
30	2.13	1.64

EDX analysis on SEM has physical limitations to the size of precipitates that can be reliably measured. The primary acceleration voltage should be 3x the energy of the X-rays that will be excited [40]. The Kα X-ray energy for Fe is 6.4keV. This means that the energy of the primary beam should be at least 18-20keV. This corresponds to a penetration depth of 1.62 micron which is greater than the maximum precipitate size of 200nm. Exciting at lower voltages results in reduced reliability. At this voltage the electron beam penetration depth exceeds precipitate thickness. As a result, the EDS spectra does not only contain information from the precipitate but information from below the precipitate which reduces reliability of the results. Analysis was limited to analysing effects of heat treatment on the microstructure without analysis into the composition.

4. Results and Discussion

Welding of P91 steel results in a heterogeneous microstructure in the weldment. This results in varying mechanical properties across the weldment. PWHT is done on welds to alleviate the effects of welding and create a homogeneous microstructure and mechanical properties in weldments. The HAZ has undergone microstructural change because of weld thermal cycles. Specimen were initially etched to reveal the HAZ. Room temperature hardness tests were done on etched specimen to establish an accurate approximate location of the HAZ. After obtaining the approximate location of the HAZ, microhardness tests were conducted to accurately locate the HAZ and further characterise it, identifying different zones and their respective widths

Tensile tests were conducted to analyse the tensile behaviour of P91 weldments by measuring the mechanical strength. Welded P91 specimens were subjected to different heat treatments and tensile tests were conducted according to experimental matrices 1 and 2, in Table 3.1 and Table 3.4 respectively. Temperature measurement was achieved through the use of K-type thermocouples, spot welded on the specimen. The thermocouple in the centre of the 70mm specimen gauge length at 35mm was set as the control thermocouple. The maximum temperature across the specimen occurs at the control thermocouple.

3D DIC was used to track specimen deformation and measure full-field strain. Experimental data was further analysed in MATLAB. Full-field localised macrostrain and tensile test plots were produced from experimental data. Full field localised strain maps show strain progression across the specimen gauge length. Three steps were selected for extraction of localised strain maps i.e., yield strength (YS), middle point (mid-point), Ultimate tensile strength (UTS). The middle point step was identified as the step with stress equal to the average of the YS and UTS. 0.2% offset strain method was used to obtain yield strength. Hardness tests were done to accurately locate the HAZ and fusion line. This allowed the weldment to be categorised into weld metal (WM), base metal (BM), and heat affected zone (HAZ). These locations were used to extract location specific mechanical properties in the weldment. Microhardness tests were done to further categorise the HAZ into distinct zones. HAZ localised strain maps were also obtained at YS, mid-point and UTS. HAZ localised strain maps show strain progression in the HAZ.

4.1 Hardness tests

Five heat treatment conditions were selected for hardness tests, eliminating intermediate heat treatment conditions. The hardness test results helped interpret the outcome of the localised strain maps in Section 4.4 Localised Strain Maps by supporting the relationship between hardness and strain localisation for the room temperature tensile tests, or linking strain localisation with the highest temperature location on the tensile specimen gauge. Figure 4.1 shows the weld hardness distribution at room temperature for different heat treatment conditions.

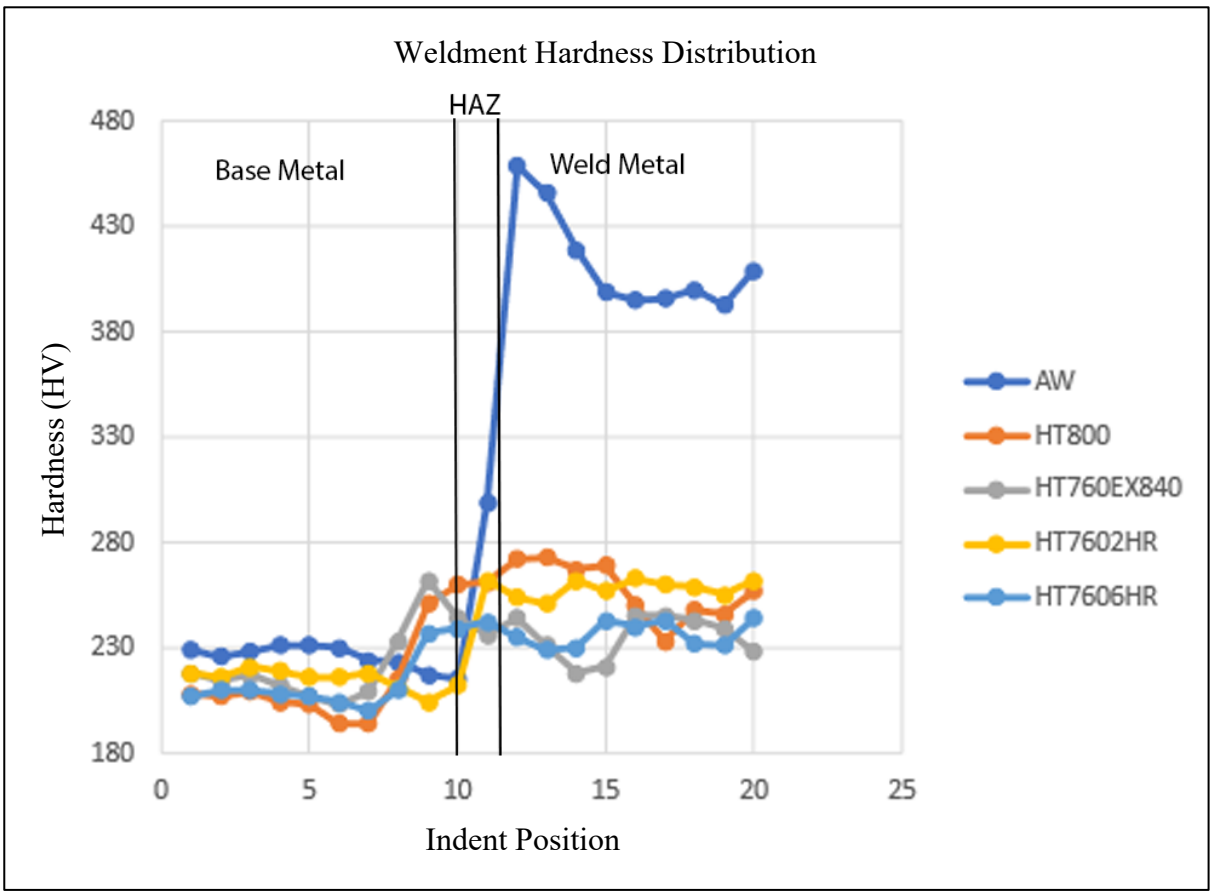

Figure 4.1: Weld hardness Distribution

Figure 4.*2* a-e shows the weld hardness distribution for specimen subjected to different heat treatments and the approximate location of the HAZ in each specimen. The hardness data and visible HAZ revealed after etching were used to approximate the location and width of the HAZ.

a)

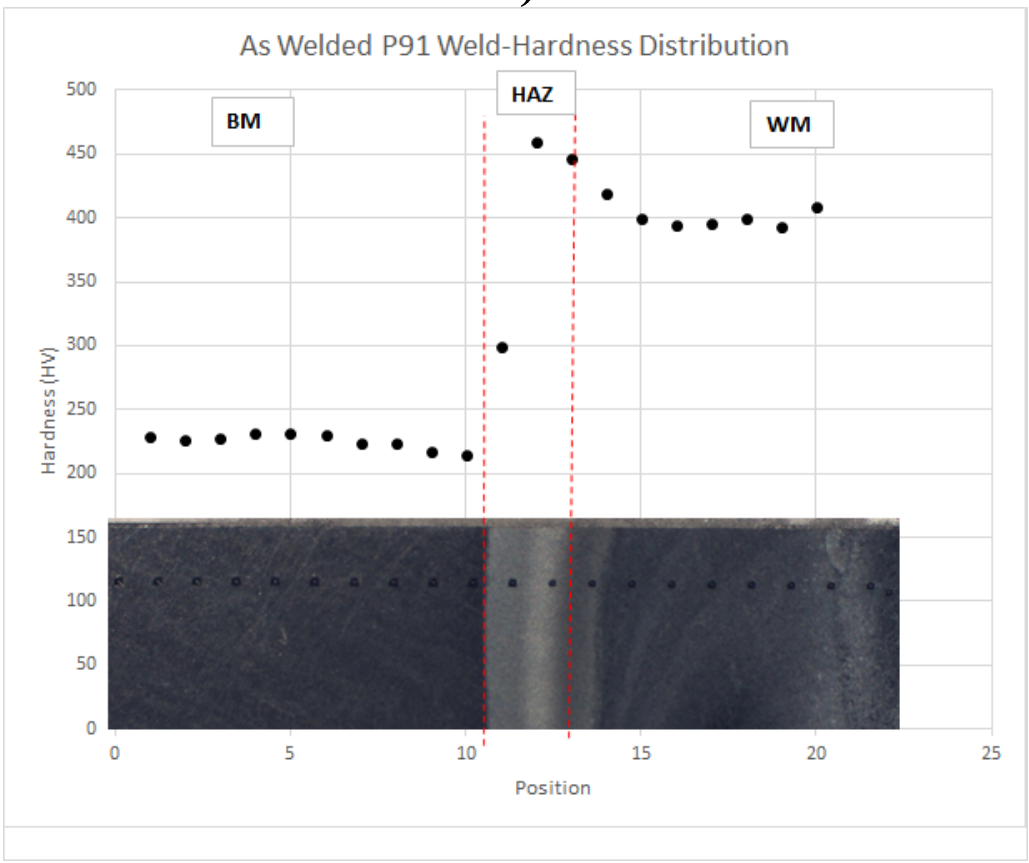
As Welded P91 Weld-Hardness Distribution
BM
HAZ
WM
Hardness (HV)
Position
0
50
100
150
200
250
300
350
400
450
500
0
5
10
15
20
25

b)

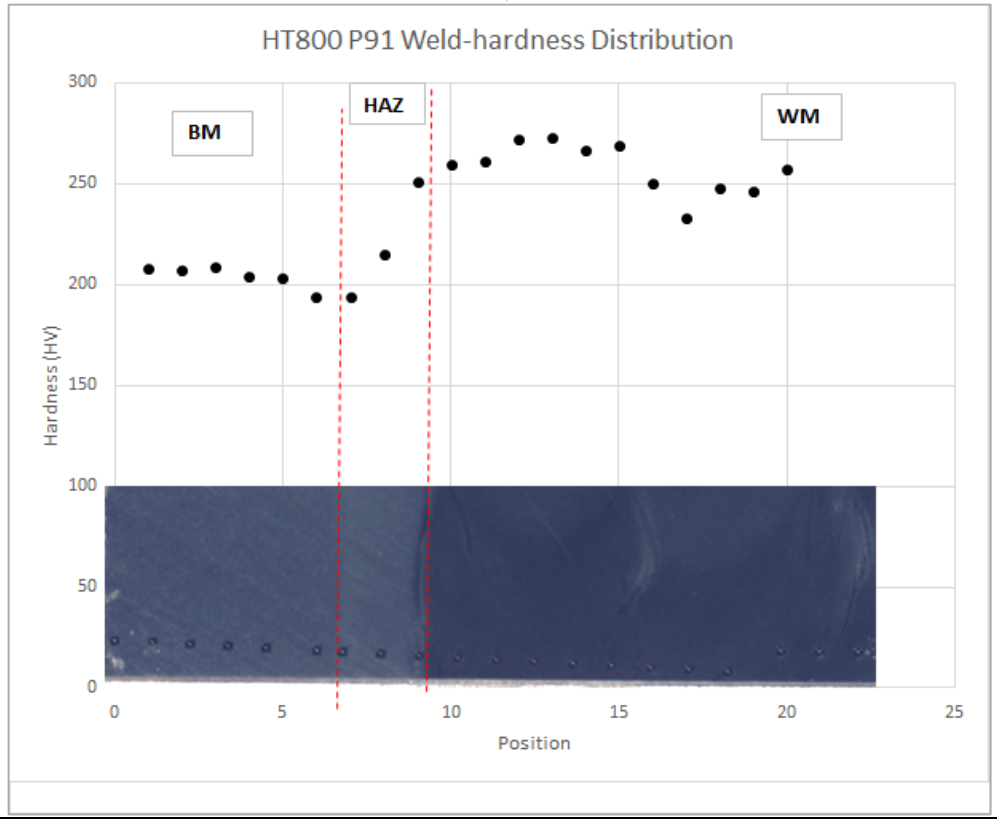
HT800 P91 Weld-hardness Distribution
BM
HAZ
WM
Hardness (HV)
Position
0
50
100
150
200
250
300
0
5
10
15
20
25

c)

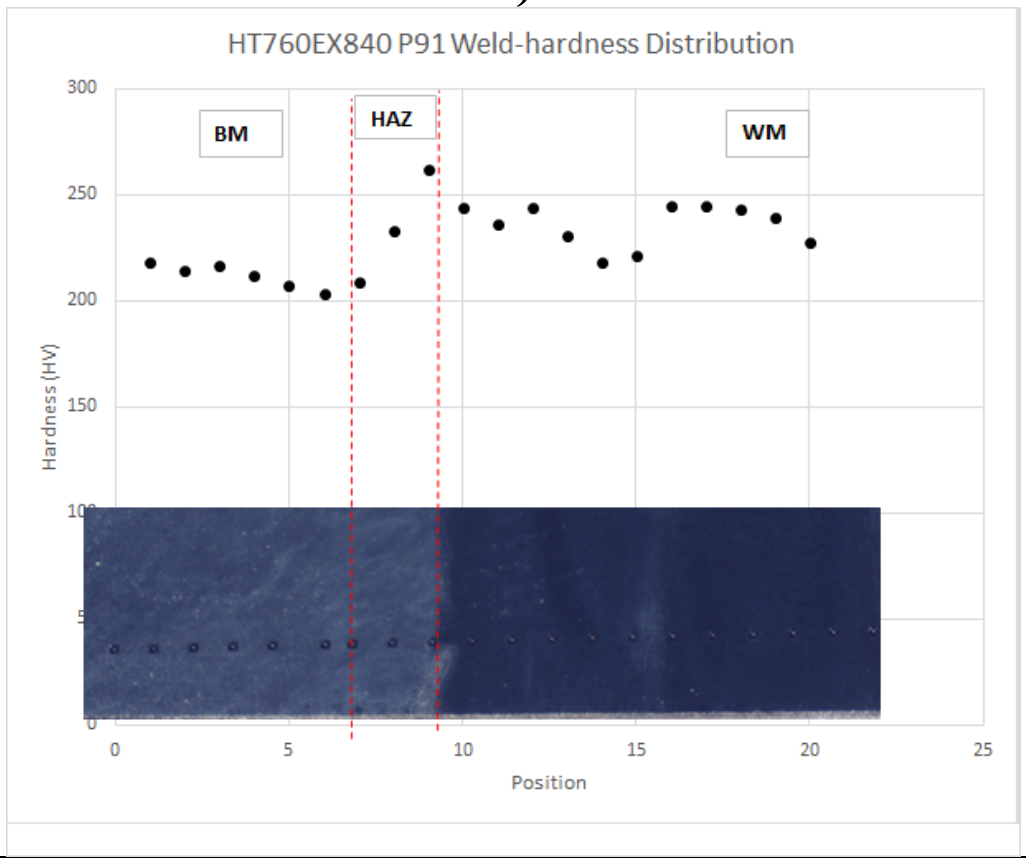
HT760EX840 P91 Weld-hardness Distribution
BM
HAZ
WM
Hardness (HV)
Position
300
250
200
150
0
0
5
10
15
20
25

d)

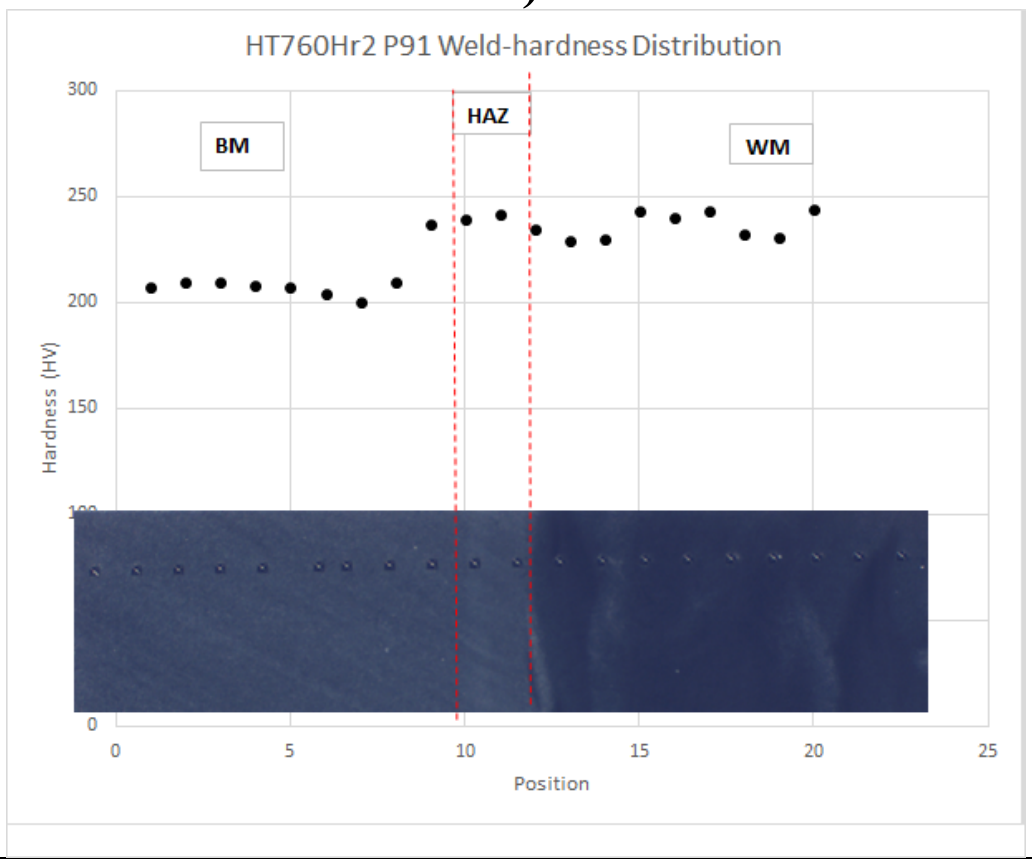
HT760Hr2 P91 Weld-hardness Distribution
BM
HAZ
WM
Hardness (HV)
Position
300
250
200
150
0
0
5
10
15
20
25

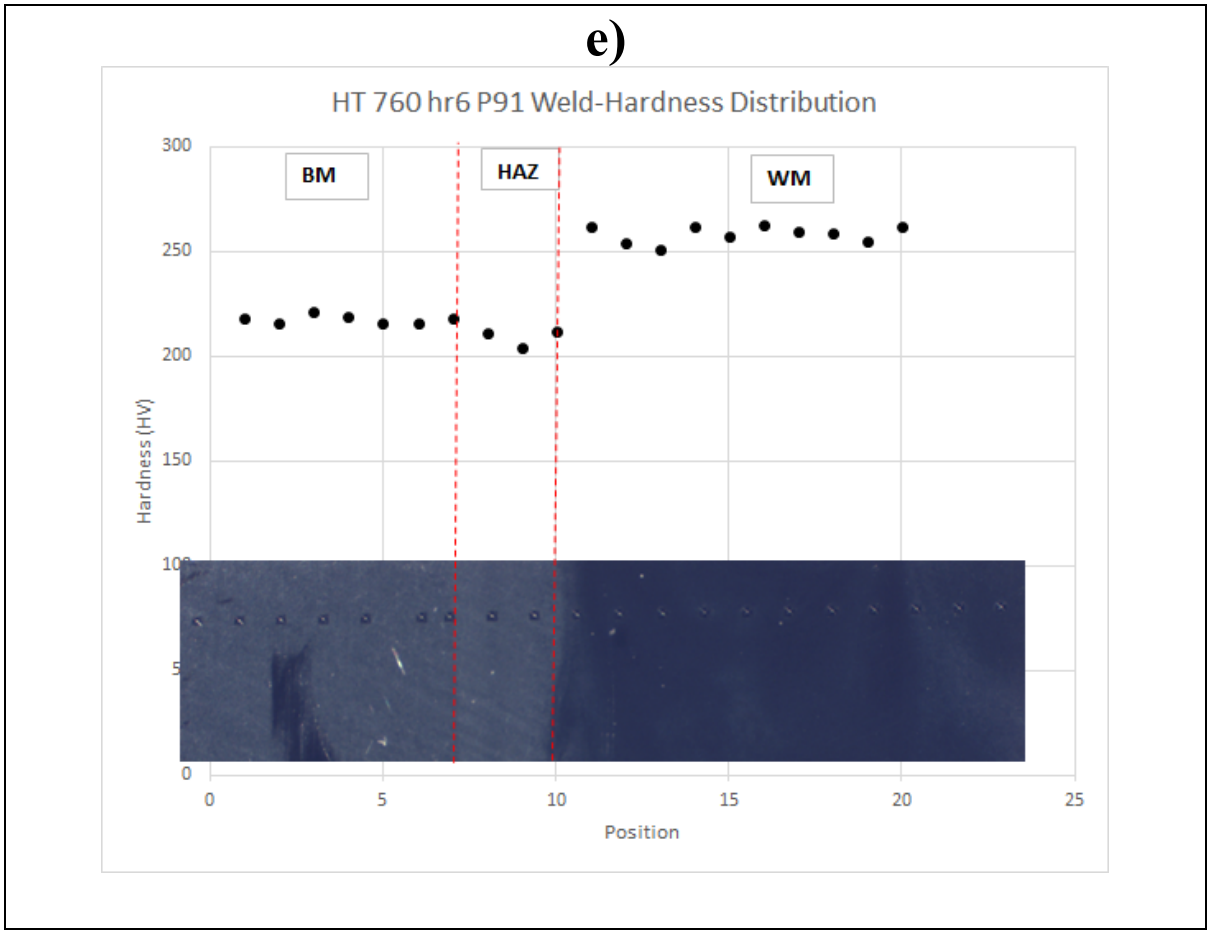

Figure 4.2: Specimen weldment hardness distribution

The non-uniform hardness across the weldment showed the presence of heterogeneous material properties. Heat treatment resulted in reduced hardness significantly in the weld metal. The reduction in material hardness was also observed in the base metal. Further reduction in hardness occurred in the base metal as heat treatment temperature was increased. Comparing all heat treatment conditions, the lowest hardness value was obtained in the base metal at the edge of the HAZ.

The position with lowest hardness varied at different heat treatment temperature. The hardness data indicated that as the heat treatment temperature increased, the location of lowest hardness migrated from the edge of the HAZ where the microstructure was over tempered, into the parent metal. This correlates to the observation that the peak strain location moves further into the base metal from the fusion line with increased heat treatment temperatures based on room temperature tensile tests.

4.2 Microhardness tests

To further characterise the HAZ, microhardness tests were done. Figure 4.*3* shows the identified locations of distinct zones in the HAZ i.e., ICHAZ, FGHAZ, CGHAZ. The as-welded condition was used to approximate the HAZ zones starting from the fusion line to the base metal. This separation was based on increments when hardness values increased to another range. This was based on the assumption that the HAZ was uniform for all specimens as welding conditions were the same.

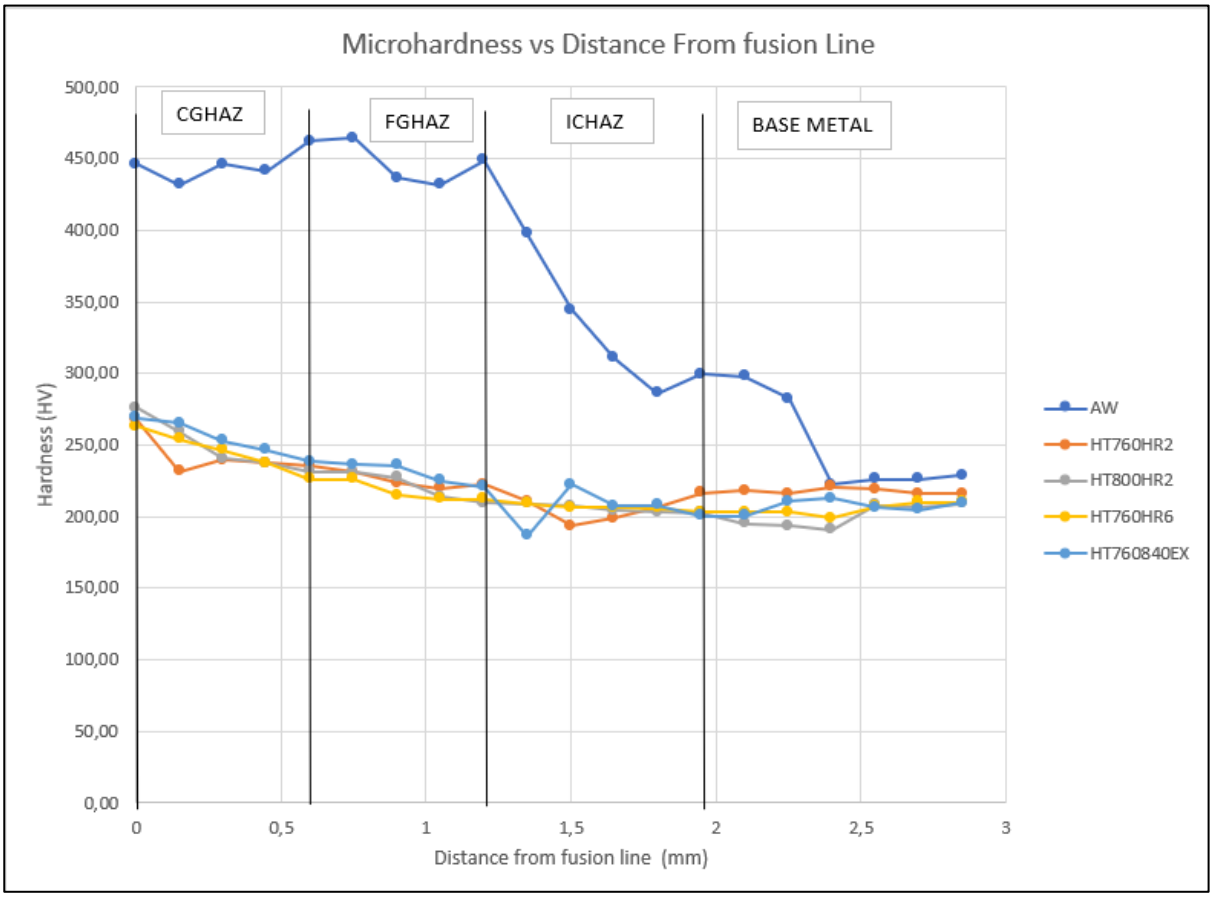

Figure 4.3 : HAZ weld zone hardness characterization

Hardness data shows an increase in hardness as we moving towards the fusion line. The average width of the HAZ measured was 2 mm with a standard deviation of ± 0.1. Table 4.1 shows the minimum and maximum microhardness values obtained in the weldment. The maximum HV value was the hardness at the fusion line i.e., fusion zone, the minimum HV value was the hardness value in the ICHAZ at the edge of the heat affected zone. The hardness values in the HAZ were similar for all tempering heat treatment conditions with minimal variances. The average hardness for all tempered specimens had a maximum of 270 BHN with a standard deviation of ± 7 and minimum of 193 BHN with a standard deviation of ± 5.

Table 4.1: HAZ hardness values

	AW	HT760HR2	HT760HR6	HT800HR2	HT760840EX
MIN (HV)	223	194	199	191	187
MAX (HV)	465	268	263	280	269
HAZ Width (mm)	1.8	1.95	2.1	1.8	2.1

Figure 4.4 a-e, shows the microhardness test profiles and HAZ width in each specimen and images of the etched weldment.

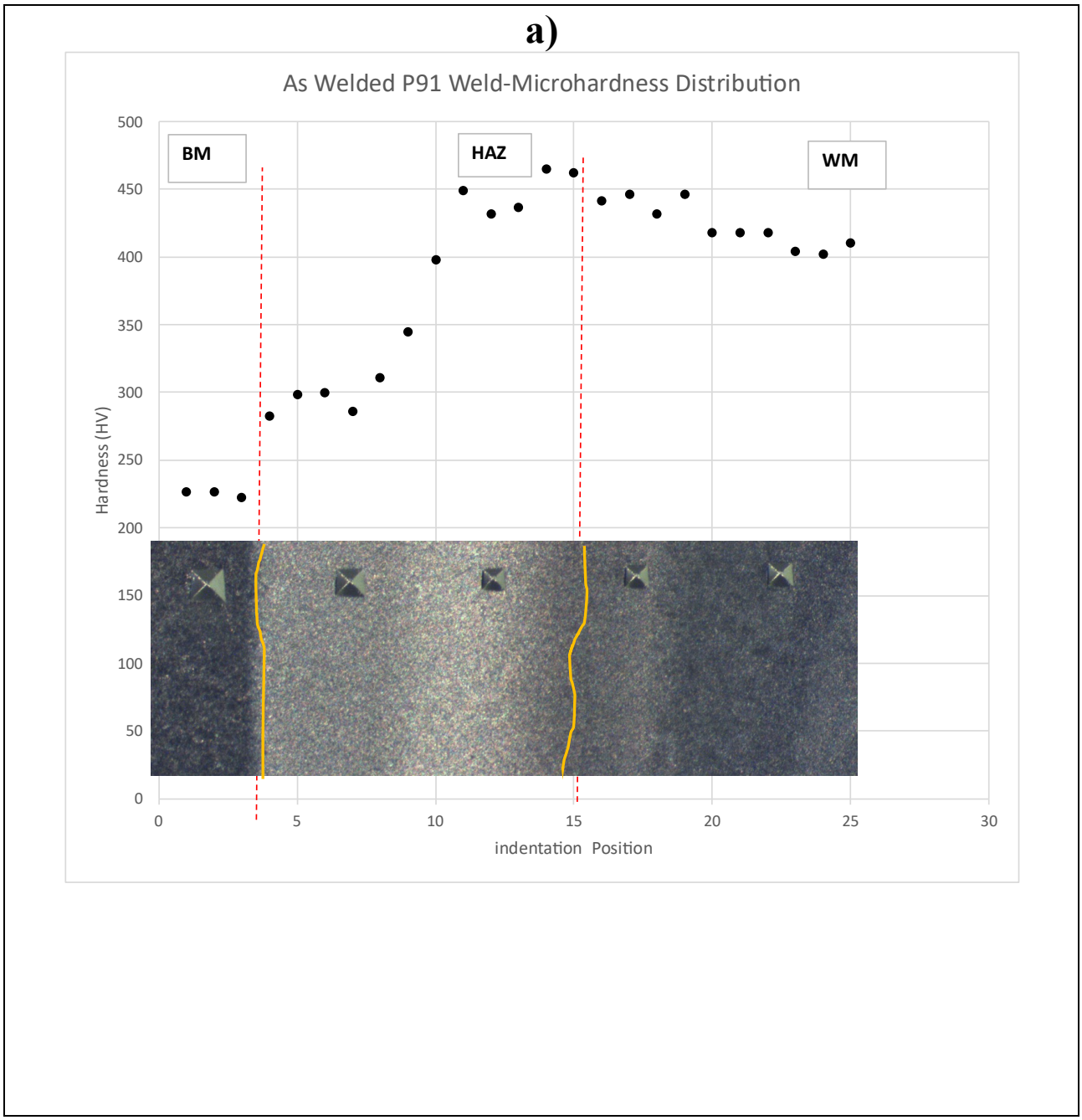

b)

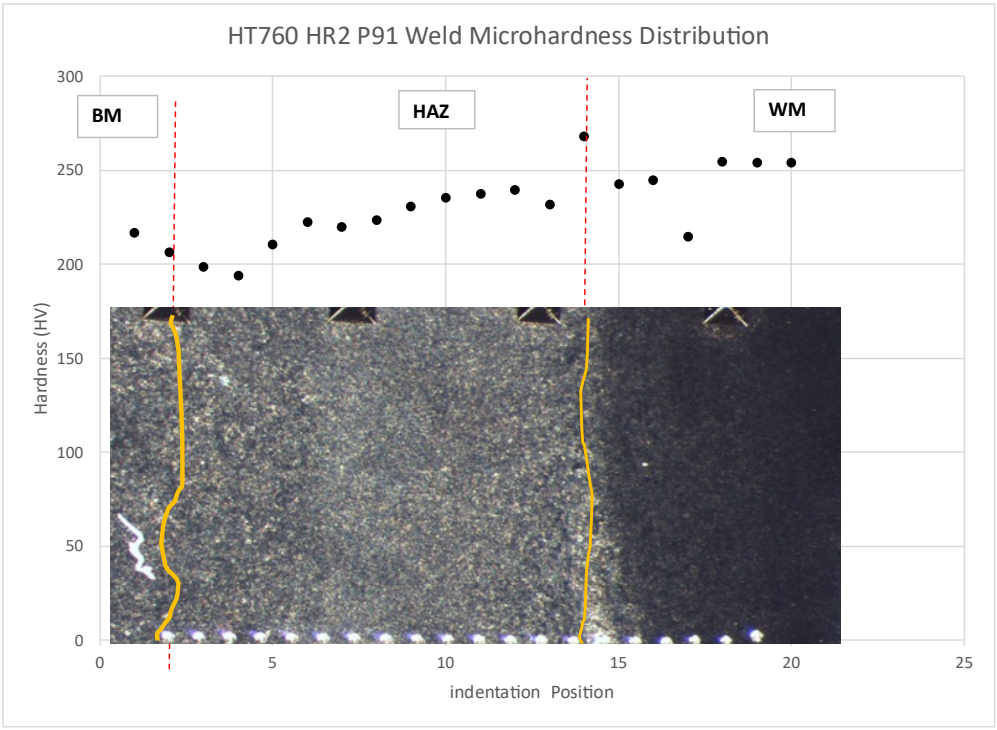
HT760 HR2 P91 Weld Microhardness Distribution
BM
HAZ
WM
Hardness (HV)
indentation Position
0
50
100
150
200
250
300
0
5
10
15
20
25

c)

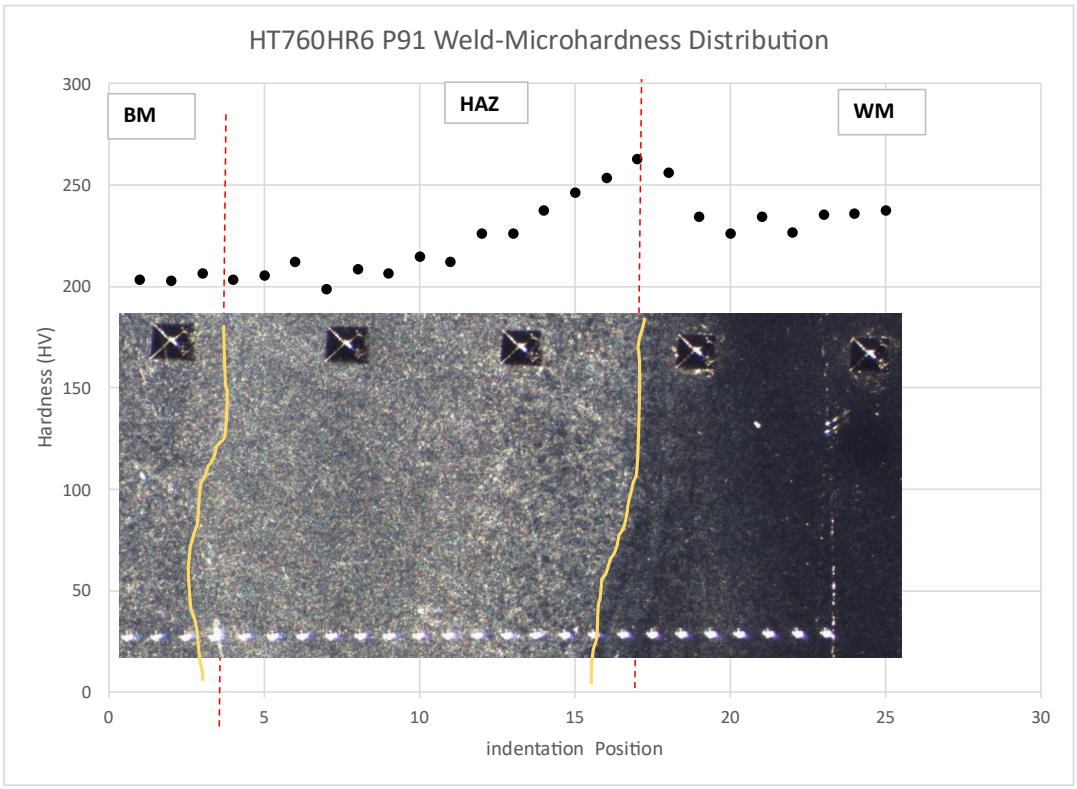
HT760HR6 P91 Weld-Microhardness Distribution
BM
HAZ
WM
Hardness (HV)
indentation Position
0
50
100
150
200
250
300
0
5
10
15
20
25
30

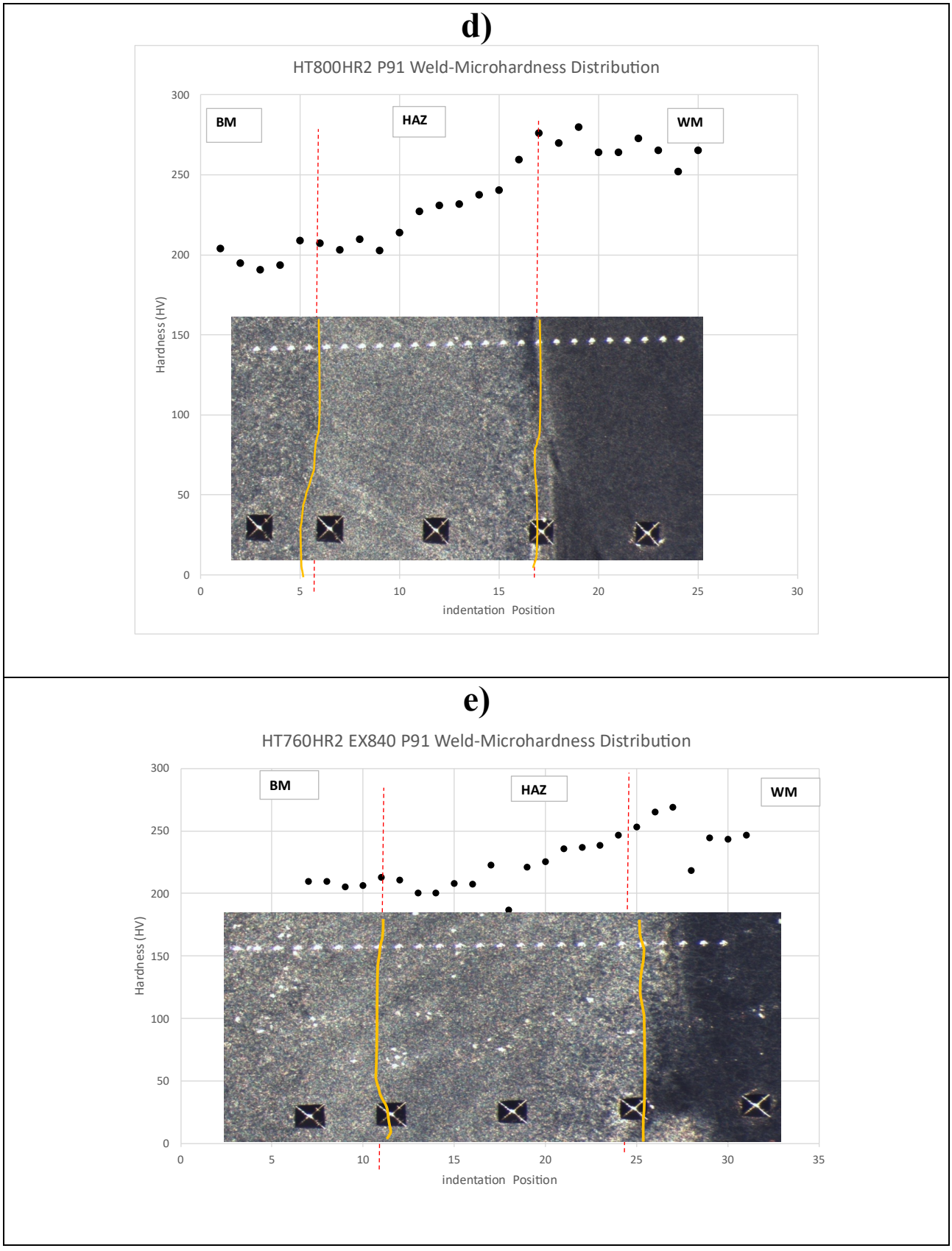

Figure 4.4 : Specimen microhardness test profiles: a) As-welded, b) HT760 HR2, c) HT760 HR6, d) HT800 HR2, e) HT760HR2 EX840

4.3 Tensile Tests

Figure 4.5 shows plots from tensile test experiments. Tensile tests were done for to experimental matrixes 1 and 2. Pandey et al. [4] observed that tempering heat treatments resulted in reduced material strength and increased ductility. This is because the tempered microstructure has a lower dislocation density, dispersed second phase precipitates and consequently less resistance to plastic deformation. Tensile test results obtained matched these expectations establishing that material strength is a function of heat treatment.

Figure 4.5 d shows the tensile properties of tests done in experimental matrix 2 where there were deviations from standard practice which resulted in degradation of tensile strength properties. P91 exhibited lower yield strength as the temperature during an excursion increased. This was also observable as heat treatment time was extended at 760°C to 6 hours (HT760-6Hr), showing that there was no benefit in extended heat treatment times for P91 steel. Figure 4.5 e, shows a comparison of different heat treatment times at 760°C. There was no significant difference in yield strength (YS) and ultimate tensile strength (UTS) for heat treatment at 760°C for 2 hours (HT760-2Hr) and 4 hours (HT760-4Hr), it would suffice to say the yield strength was approximately the same for the two heat treatment conditions. HT760-4Hr had a higher UTS than HT760-2Hr, however HT760-2Hr specimens were more resistant to plastic deformation as they experienced UTS after the HT760-4Hr specimens.

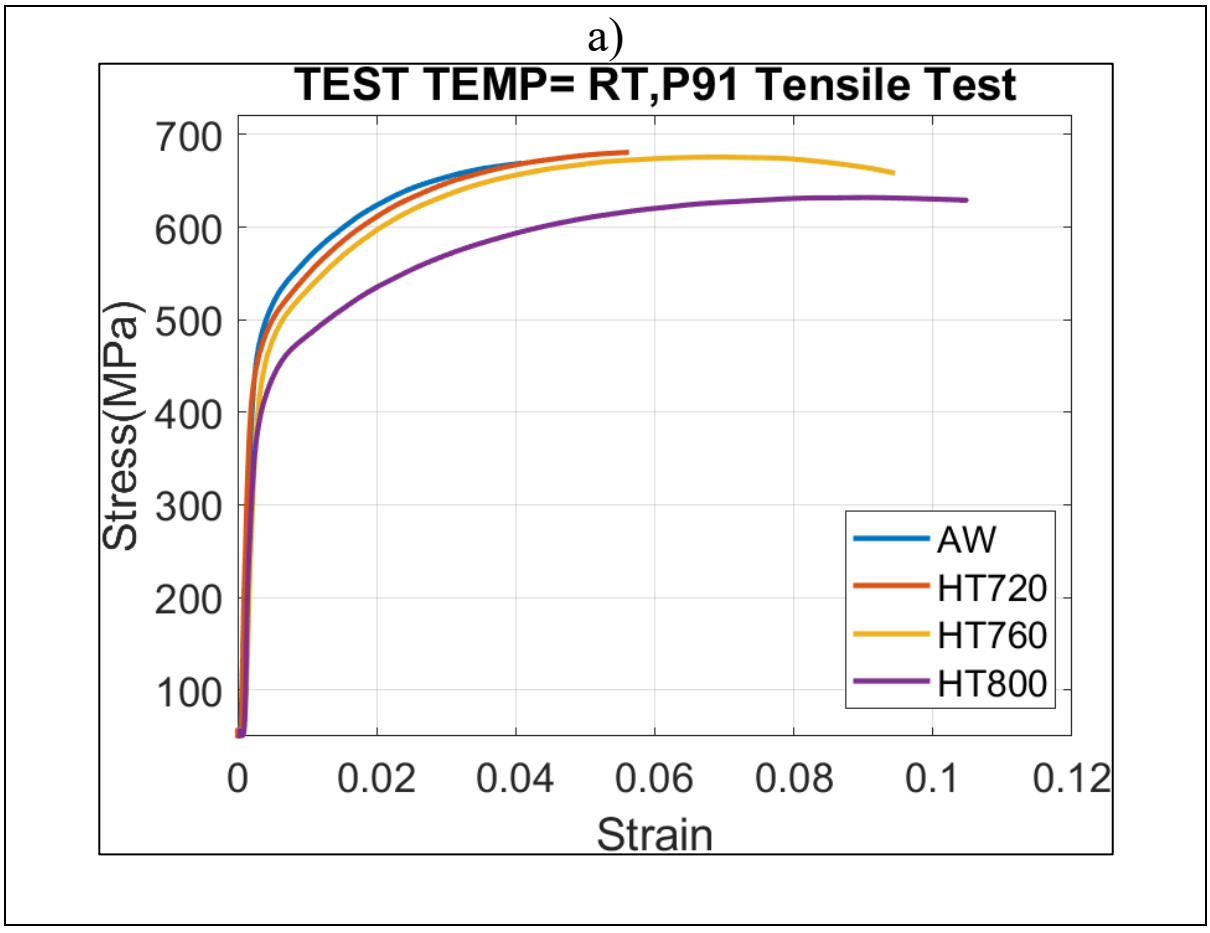

b)

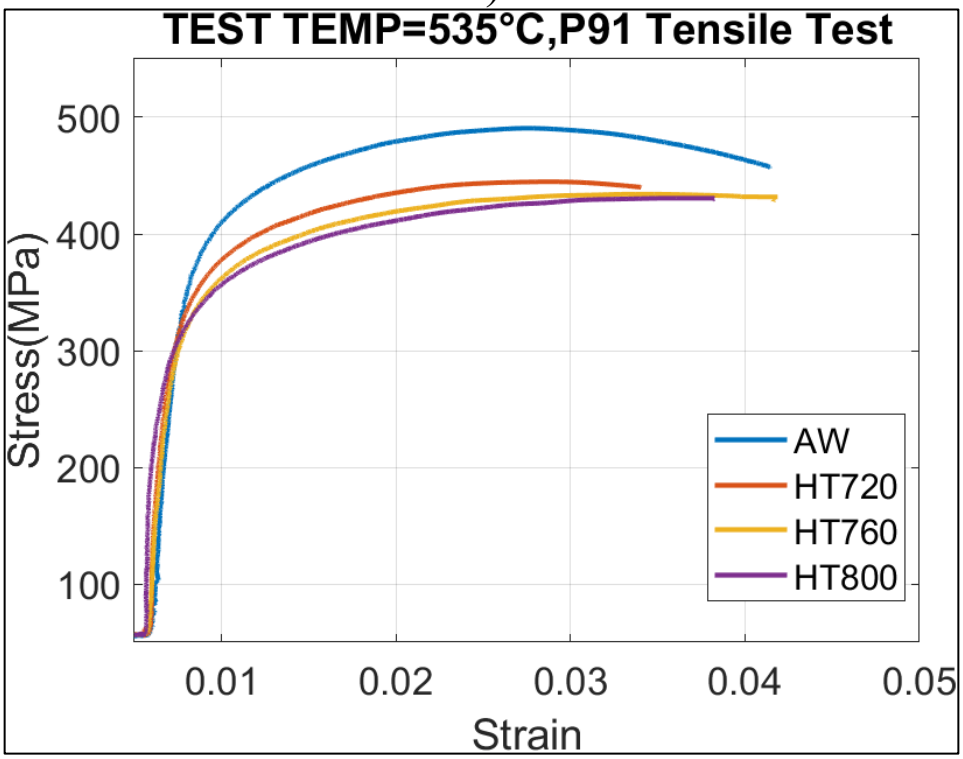
TEST TEMP=535°C,P91 Tensile Test
Stress(MPa)
500
400
300
200
100
0.01
0.02
0.03
0.04
0.05
Strain
AW
HT720
HT760
HT800

c)

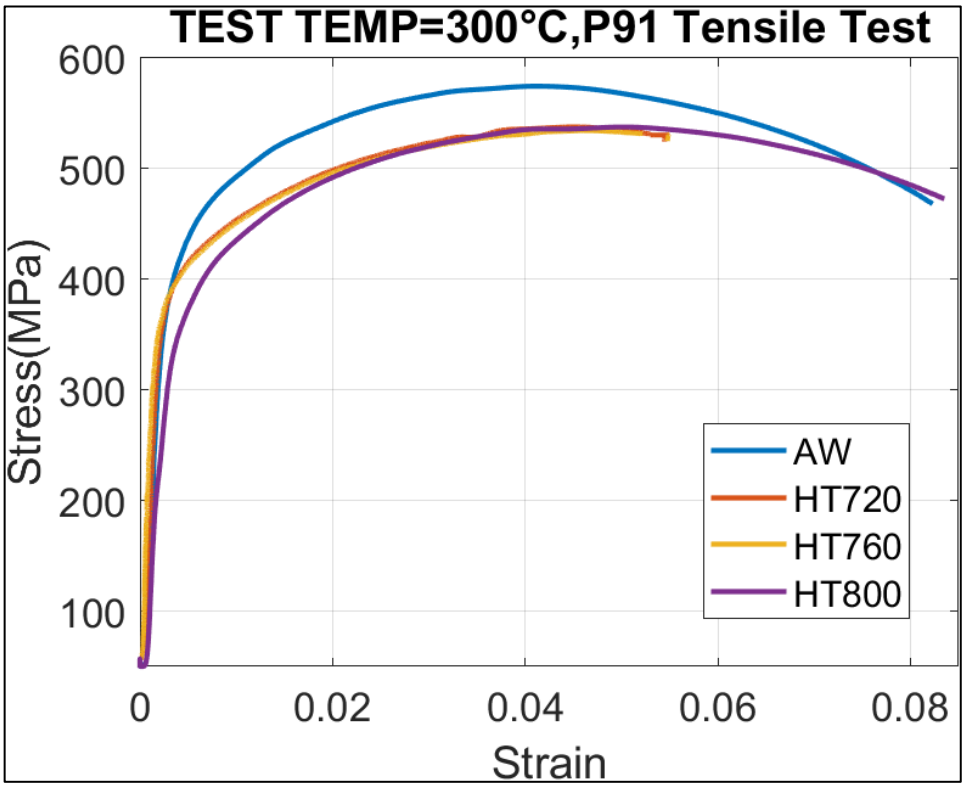
TEST TEMP=300°C,P91 Tensile Test
Stress(MPa)
600
500
400
300
200
100
0
0.02
0.04
0.06
0.08
Strain
AW
HT720
HT760
HT800

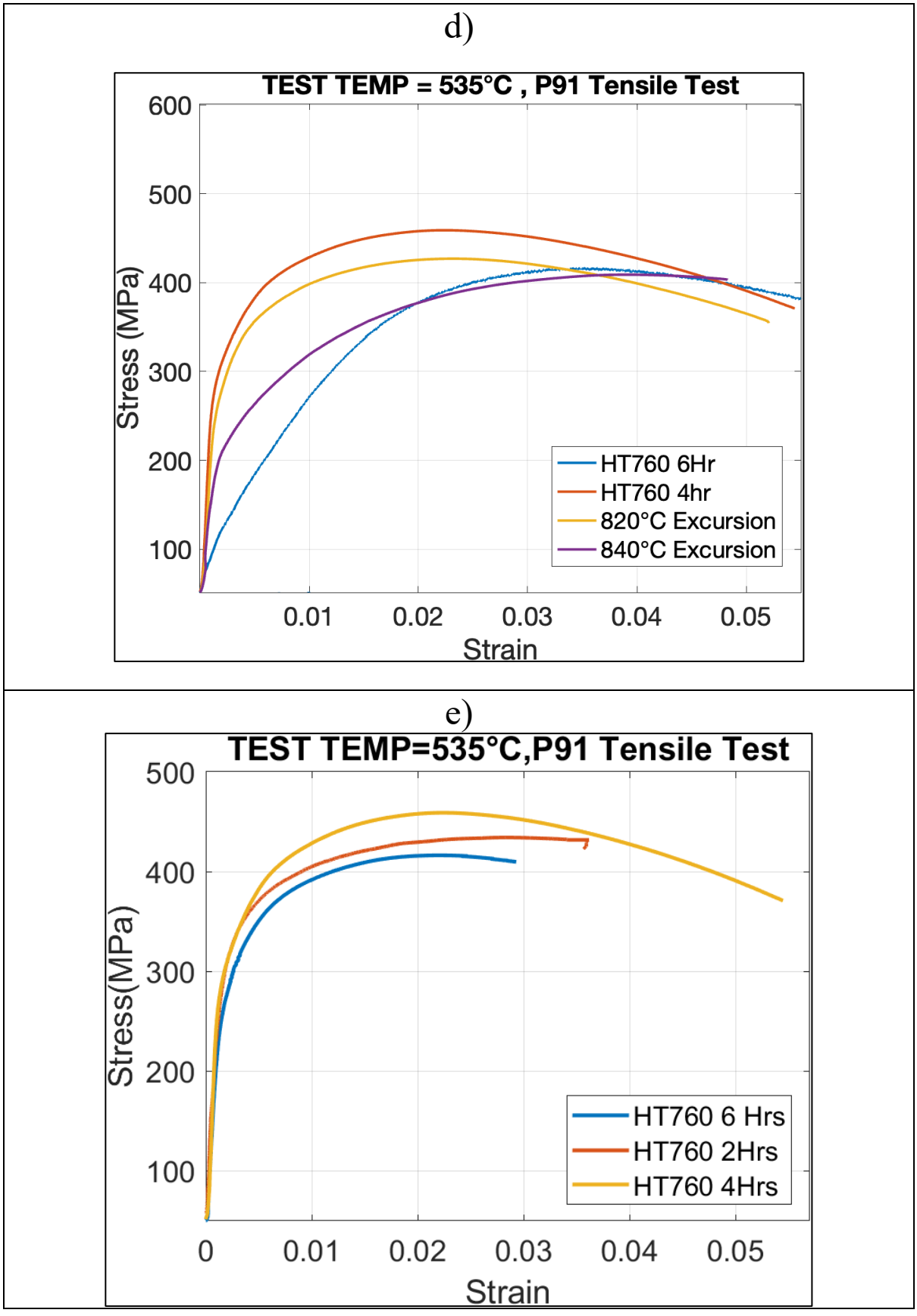

Figure 4.5 : P91 Tensile Tests a) Rom temperature, b) T535, c) T300, d) T535 Excursions, e) HT760 comparison

Table 4.2-Table 4.4 show the tensile properties of P91 for experimental matrixes 1 and 2. The strain hardening ratio was calculated as the ratio of the UTS to yield strength [1]. Figure 4.6 shows a plot constructed from data in table 4.3. Table 4.3 shows the average tensile properties based on three tests as recommended in the standard for tensile testing [36][1] on determining mechanical properties. The plot in Figure 4.6 illustrates the effect of increased heat treatment temperature on tensile properties. Tensile tests at 535°C show a 30% reduction in YS and UTS compared to tests at room temperature. The YS and UTS were therefore established as a function of heat treatment condition and test temperature. The YS was obtained using 0.2% offset method in MATLAB and the UTS was taken to be the point of maximum stress from the tensile test data. At this point, there were not enough data from the tensile properties of P91 steel to explain the difference in mechanical behaviour of P91 weldments. It was therefore necessary to further investigate the development of localised strain in the specimen as a function of heat treatment and test temperature.

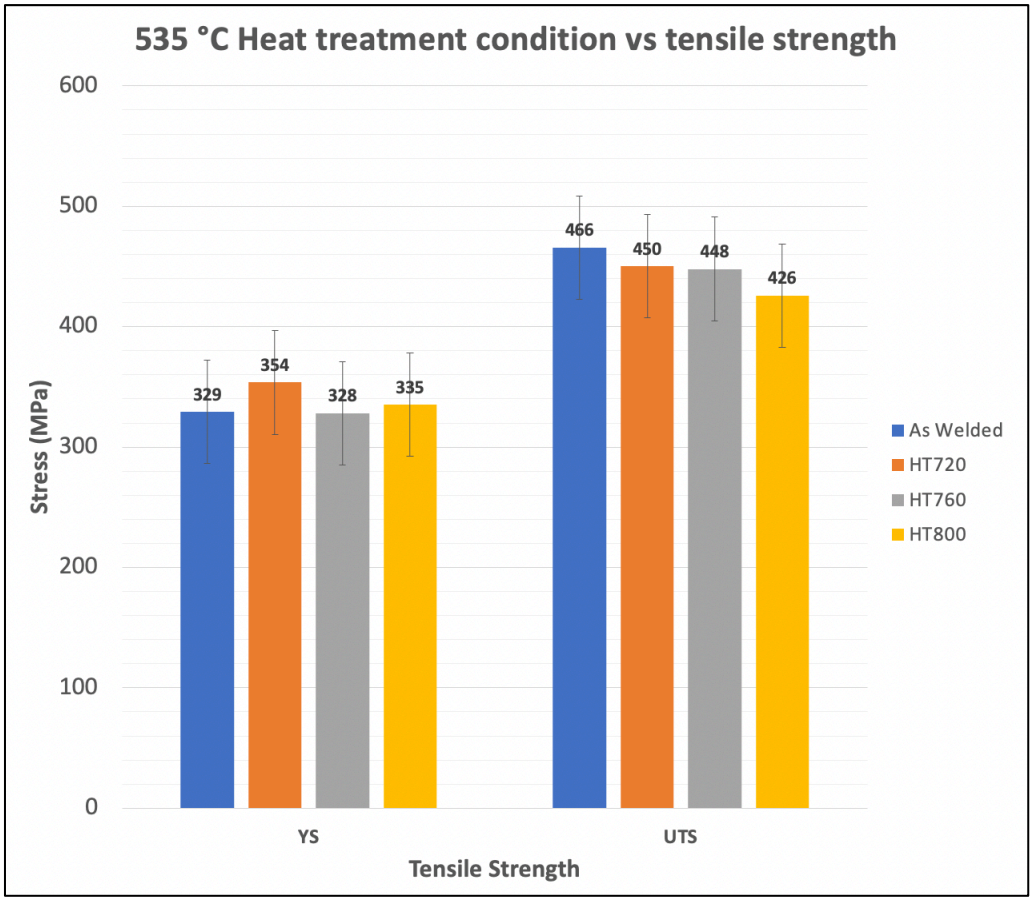

Figure 4.6 : Heat treatment condition YS and UTS by tensile strength 535°C

Table 4.2 : P91 Tensile properties at room temperature

Room Temperature			
Heat Treatment Condition	**YS (MPa)**	**UTS (MPa)**	**Strain Hardening Ratio**
HT 800 2h	404	631	1.6
HT760 2h	458	675	1.5
HT 720 2h	474	683	1.4
As-Welded	506	673	1.3
Mean	461	666	1
Standard Deviation	43	23	0.1

Table 4.3: Matrix 1 Average P91 Tensile Properties at 535°C

535 °C Tensile Tests			
Heat Treatment Condition	**YS (MPa)**	**UTS (MPa)**	**Strain Hardening Ratio**
As-Welded	329	466	1.4
HT720	354	450	1.3
HT760	328	434	1.4
HT800	335	436	1.3
Mean	337	447	1
Standard Deviation	12	15	0.1

Table 4.4: Matrix 2 P91 Tensile Properties at 535°C

535 °C			
Heat Treatment Condition	**YS (MPa)**	**UTS (MPa)**	**Strain Hardening Ratio**
HT 760 EX840	`207	416	2.0
HT 760 EX820	256	422	1.6
HT760 6h	310	416	1.3
HT 760 4h	335	459	1.4
Mean	300	428	2
Standard Deviation	40	21	0.3

Pandey et al. [4] suggested that the extended heat treatment time does not improve material strength. The tensile properties for heat treatment condition HT760-4Hr were similar to that of HT760-2Hr. Figure 4.7 shows a plot of tensile properties of different heat treatment conditions of P91 HT760 at 535°C for experimental matrix 2. Heat treatment beyond 4 hours resulted in degradation of tensile properties. There was no significant benefit in extended heat treatment beyond 2 hours. HT760-4Hr had a yield strength of 335 MPa while HT760-2Hr had a yield strength of 327 MPa for tensile tests at 535°C. At UTS HT760-4Hr had 2.3 % elongation while HT760-2Hr had a 3.3 % elongation indicating a difference of 1%. The small increase in ductility and tensile strength properties from 2 h to 4 h heat treatments was not sufficient to justify the additional time and costs associated with this practice. The increase in tensile strength in HT760-4Hr also resulted in degradation of ductile properties compared to HT760-2Hr.

Room temperature tests and have a mean YS of 461 MPa and UTS of 666 MPa. A standard deviation of 43 MPa YS and 23 MPa UTS suggested that these values have a relatively large amount of variability from the mean. This was also observed in heat treatments where there was a deviation from standard practice with a standard deviation of 40 MPa YS and 21 MPa UTS . At room temperature there was a standard deviation of 12 MPa YS and 15 MPa UTS which showed that values are generally close to the mean. The smaller the standard deviation, the less spread out the data points are from the mean, indicating lower variability in the dataset.

The average strain hardening ratio at room temperature and 535°C was 1 with a standard deviation of 0.1. The strain hardening ratio data suggests that the material behaves consistently with minimal variability. However, where there are deviations from standard practice and extended heat treatments, the material's behaviour becomes more variable, as indicated by the larger standard deviation. The standard deviation values help quantify the spread of the data points around the mean, providing insight into the consistency and variability of the material's response under different conditions.

Excursions during heat treatments resulted in significantly reduced material yield strength. Specimens subjected to heat treatment excursions had yield strength 207 MPa and 256 MPa for 10-minute excursions to 840°C and 820°C respectively. During an excursion the whole specimen was subjected to temperatures occurring in the HAZ during welding. It would be an ideal if monolithic specimens could be created to represent each of the HAZ microstructures. However, the excursion cannot re-produce the effects imparted in the HAZ during weld thermal cycles in the entire specimen because it is almost impossible to reproduce the complex weld thermal cycles.

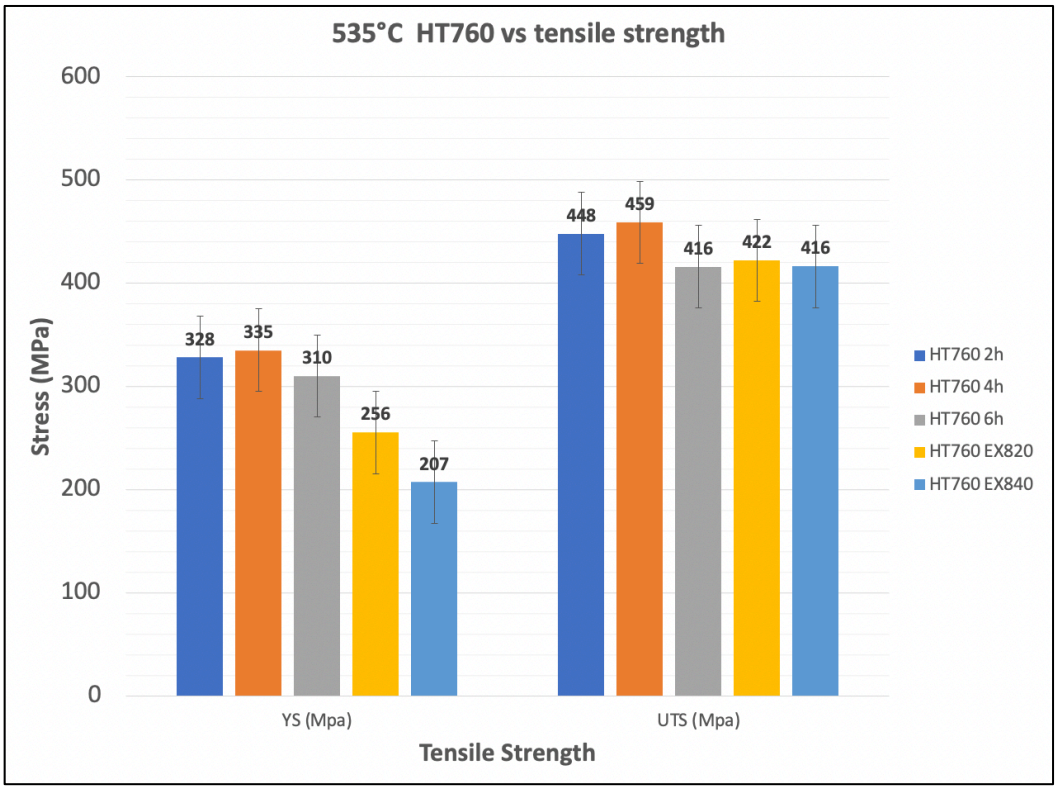

Figure 4.7: A Comparison of Standard HT to Experimental Matrix 2 Tensile properties at 535°C

4.4 Localised Strain Maps

Localised strain maps illustrate the distribution of macroscopic strain in a specimen during tensile testing. The localised strain map was captured along a line on the specimen, defined by a start and end on the evaluated DIC mask. These localised strain maps serve to identify and visualise the point of maximum strain localisation. A localised strain peak occurred at the point of maximum strain localisation, this is the point where the maximum localised strain value occurs on a strain map. Therefore, the peak strain location occurred in a region of high strain on the specimen. The point of peak strain coincides with the point most susceptible to failure. Localised strain maps were obtained at YS, UTS and an intermediate middle point (mid-point) an average of YS and UTS. HAZ Localised strain maps were obtained for selected heat treatment conditions i.e., AW, HT760, HT800, HT760EX840. The HAZ localised strain maps show the progression of localised strain in the HAZ.

Localised strain maps showed that strain peaks occurred in two areas on both sides of the weld. One peak was higher than the other, the strain peaks were not a mirror image of the other and there was no symmetry in material properties about the center of the weld metal. This can be attributed to material properties and was also influenced by the non-uniform parabolic temperature profile across the specimen. Localised strain maps compare the localised strain in each specimen for each test temperature. This comparison added to the understanding of the relationship between test temperature, heat treatment condition and tensile properties.

4.4.1 Room Temperature Localised Strain Maps

In Figure 4.8, the weld metal (WM) is the region between two fusion lines, i.e., center-FL1 and a corresponding FL2 line for each HT condition. At room temperature specimens subjected to different heat treatment conditions exhibited varying localised strain maps. The variations were attributed to changes in material properties resulting from heat treatment. Figure 4.8 a-c, shows plots of localised strain maps at room temperature. Localised strain maps were obtained at YS, mid-point and UTS. Compared to other heat treatment conditions, HT800 exhibits increased localised strain in the weld metal, which suggested a reduced resistance to localised plastic deformation due to over-tempering. This, in turn, results in a distribution of the load to the weld metal as a result of reduced to resistance to deformation in the weld metal.

At UTS the highest values of peak localised strain in the necked region were recorded for the AW and HT800 conditions. A combination of low tensile strength and highly stressed matrix resulted in high strain localisation in HT800 specimen due to over-tempering. Lower values of peak localised strain were recorded in HT720 and HT760 conditions at UTS. These specimens exhibited improved resistance to localised plastic deformation because of heat treatment, establishing that resistance to localised plastic deformation increased with an increase in heat treatment temperature until HT760. At room temperature, peak localised strain occured in the base metal for all HT conditions. The location of peak localised strain at room temperature was further from the fusion line for HT760, which had the lowest value of peak localised strain compared to other heat treatment conditions.

In Figure 4.8, the WM had lowest values of localised strain. This indicated that there was resistance to localised plastic deformation and strain localisation in the weld metal at room temperature. In the WM, the Localised strain remained low at UTS, mid-point and YS. Resistance to localised plastic deformation in the weld metal decreased as heat treatment

temperature was increased and there is load distribution into the weld metal because of microstructure homogenisation and effects of over tempering for temperatures above 760°C.

The HAZ in specimen tested at room temperature had a width of 2 mm and was assumed to be uniform in all specimens because the pipe from which specimens were extracted, experienced the same thermal cycle during welding. The average WM width for specimen used for room temperature tensile tests was 20 mm and varied in each specimen. This was because specimen are extracted at different positions in the pipe cross section. The control thermocouple was set at TC2 for all experiments at room temperature.

Figure 4.9 a-c shows HAZ localised strain maps at YS, mid-point and UTS. HAZ Localised strain increases from the fusion line at position zero into the base metal. AW and HT800 specimens had higher localised strain in the HAZ compared to HT720 and HT760. Comparing the HAZ localised strain maps to the HAZ hardness plots in Figure 4.3, higher values of localised strain were recorded in weld zones with low hardness and decreased towards weld zones with high hardness. Therefore, in the localised strain was an inverse linear function of weld zone hardness. This was due to resistance to deformation in areas of high hardness.

Table 4.*5* shows the peak localised strain values in specimens at room temperature at UTS. AW and HT800 specimen had the highest peak strain values. HT720 and HT760 had lower peak localised strain values at UTS. AW and HT800 specimens were more susceptible to fail before HT760 and HT720 specimens during room temperature tensile testing because of the higher localised strain values recorded at UTS.

Table 4.5 : Room Temperature Peak strain at UTS

Specimen	**% Peak Localised Strain**	**Location**
As-Welded	12.8	BM
HT720	11.4	BM
HT760	11.3	BM
HT800	13.74	BM

Based on experimental results obtained at room temperature, strain localisation was established as a function of heat treatment condition. In the HAZ, strain localisation was an inverse function of hardness at room temperature due to resistance of plastic deformation in regions of high hardness. Heat treatment improved material resistance to localised plastic deformation at room temperatures which consequently improved ductile properties of specimen at room temperature.

a)

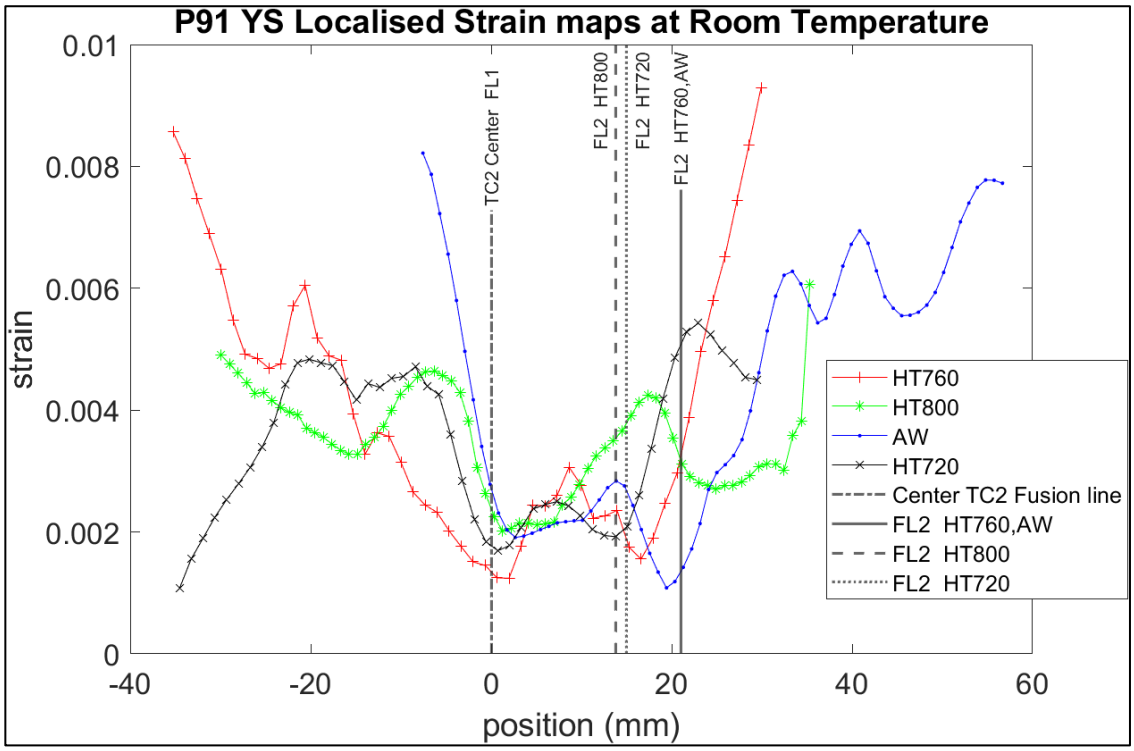
P91 YS Localised Strain maps at Room Temperature
strain
position (mm)
TC2 Center FL1
FL2 HT800
FL2 HT720
FL2 HT760,AW
HT760
HT800
AW
HT720
Center TC2 Fusion line
FL2 HT760,AW
FL2 HT800
FL2 HT720

b)

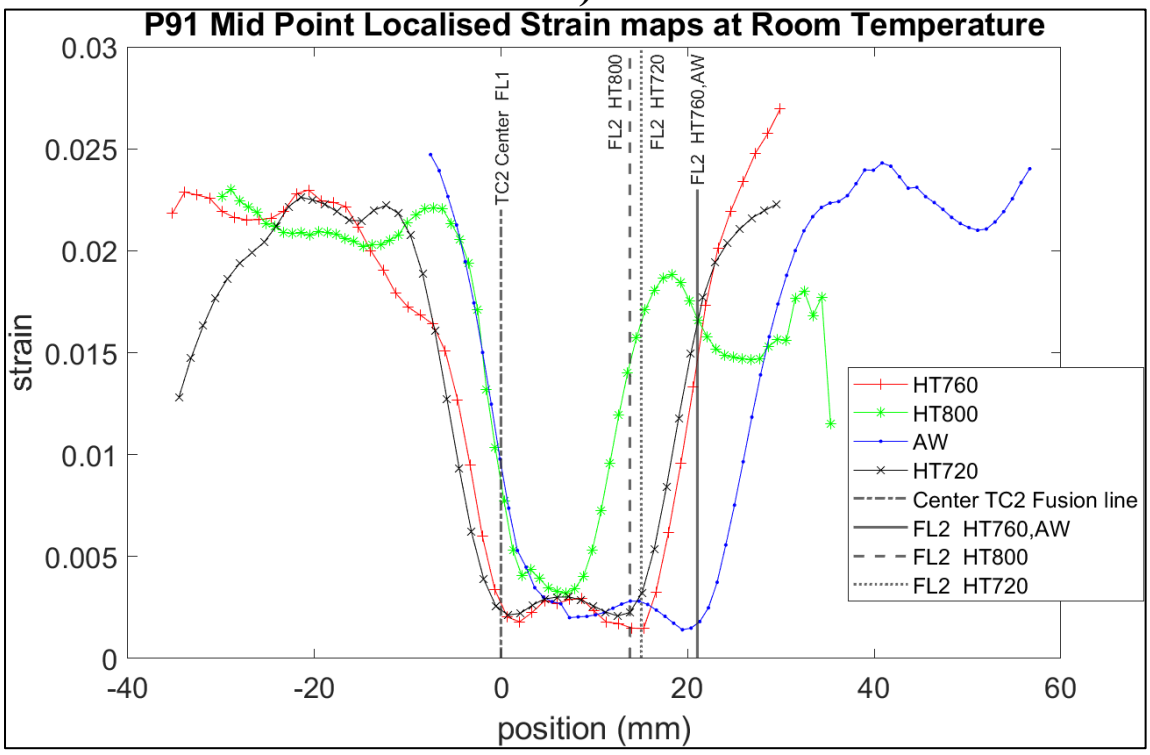
P91 Mid Point Localised Strain maps at Room Temperature
strain
position (mm)
TC2 Center FL1
FL2 HT800
FL2 HT720
FL2 HT760,AW
HT760
HT800
AW
HT720
Center TC2 Fusion line
FL2 HT760,AW
FL2 HT800
FL2 HT720

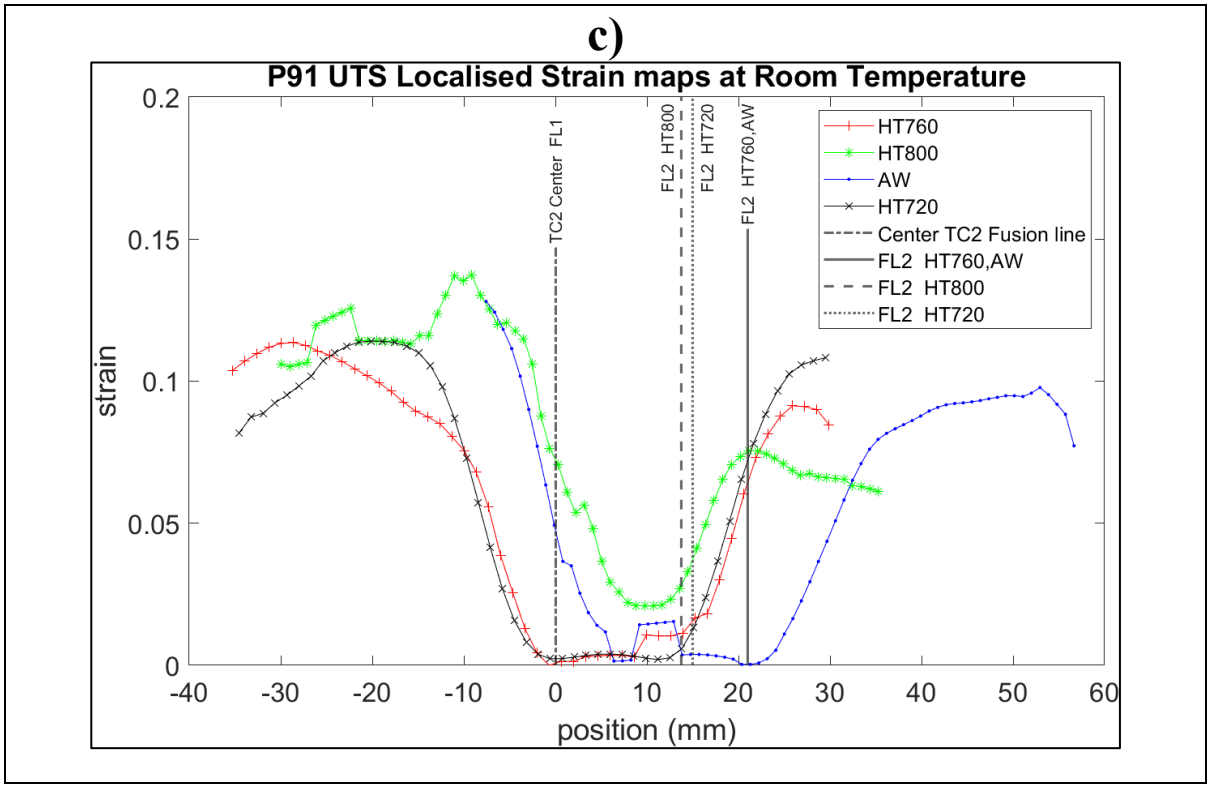

Figure 4.8: P91 Room Temperature localised strain maps a) YS, b) Middle Point, c) UTS

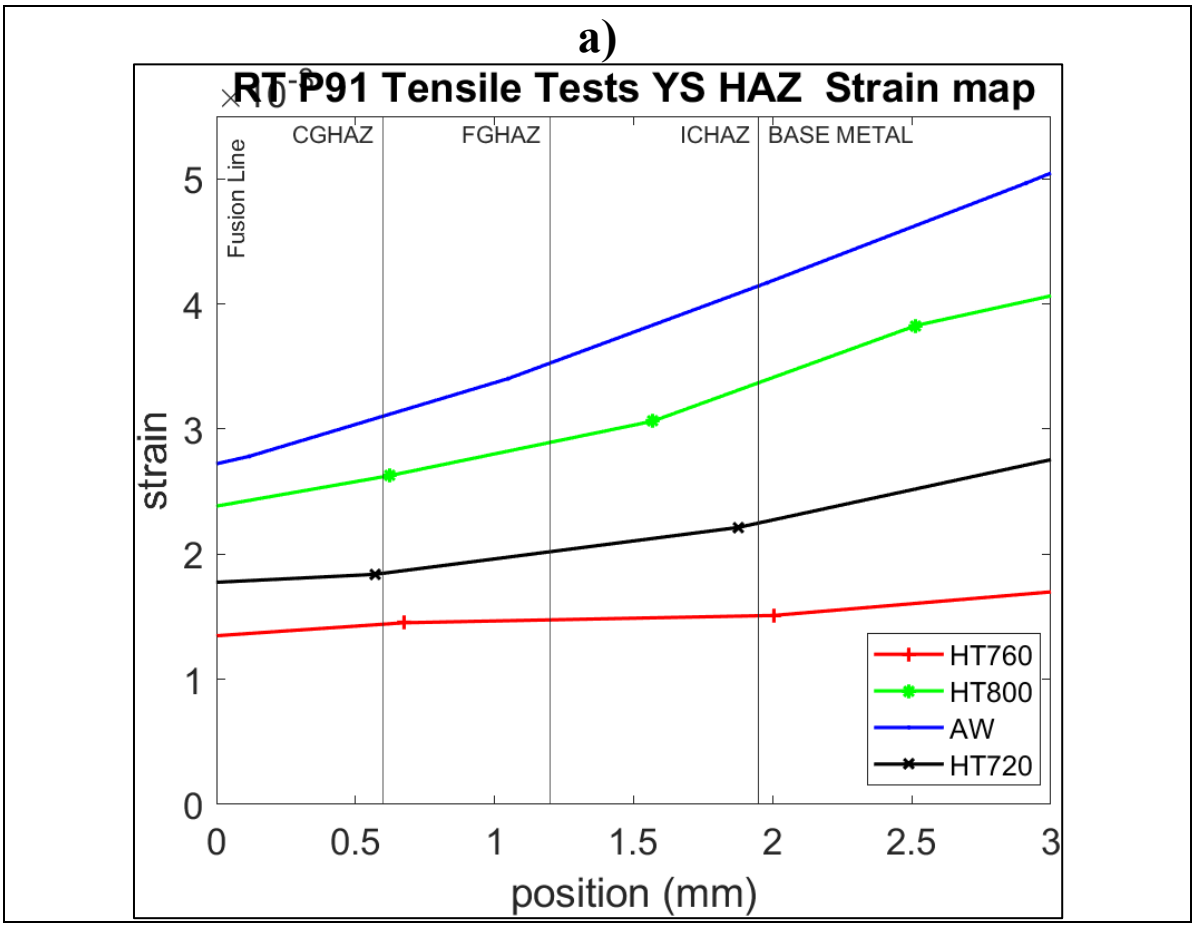

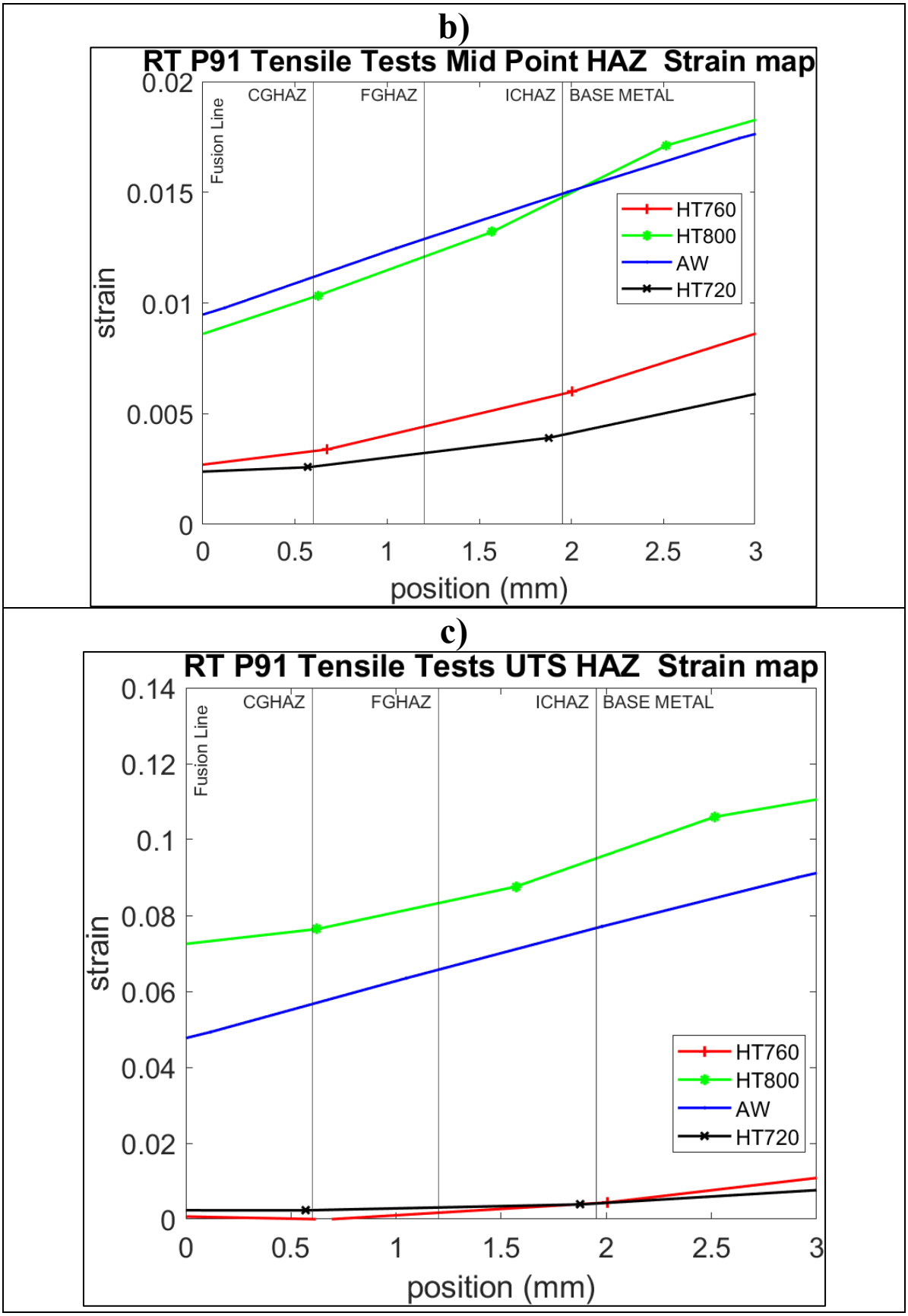

Figure 4.9: P91 HAZ Room Temperature localised strain maps a)HAZ YS, b)HAZ Mid-Point, c)HAZ UTS

a)

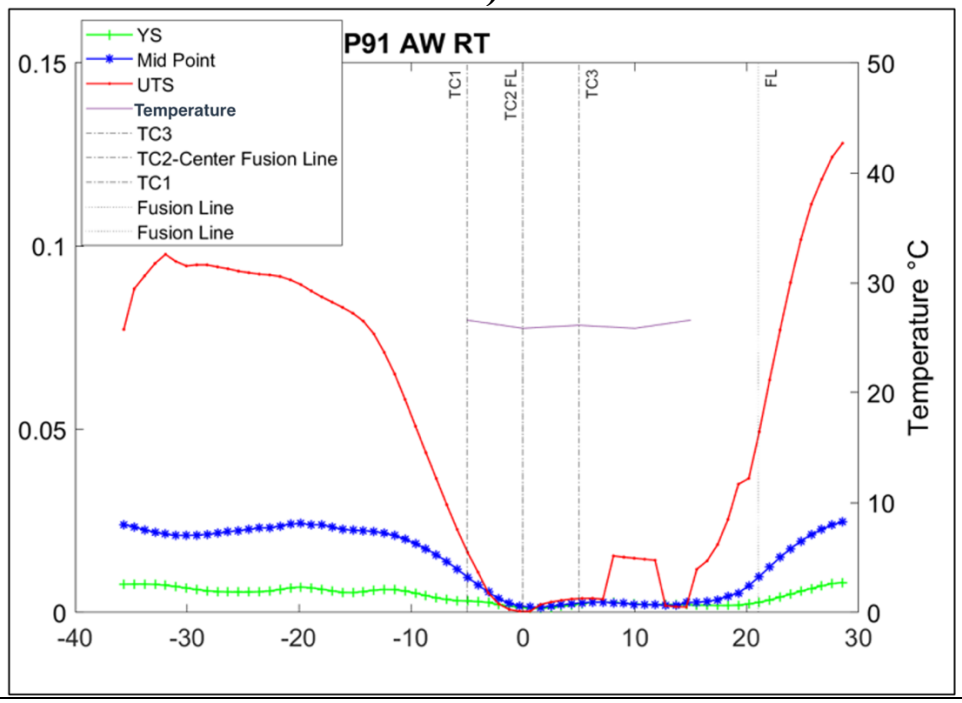
P91 AW RT
YS
Mid Point
UTS
Temperature
TC3
TC2-Center Fusion Line
TC1
Fusion Line
Fusion Line
TC1
TC2 FL
TC3
FL
0.15
0.1
0.05
0
50
40
30
20
10
0
Temperature °C
-40
-30
-20
-10
0
10
20
30

b)

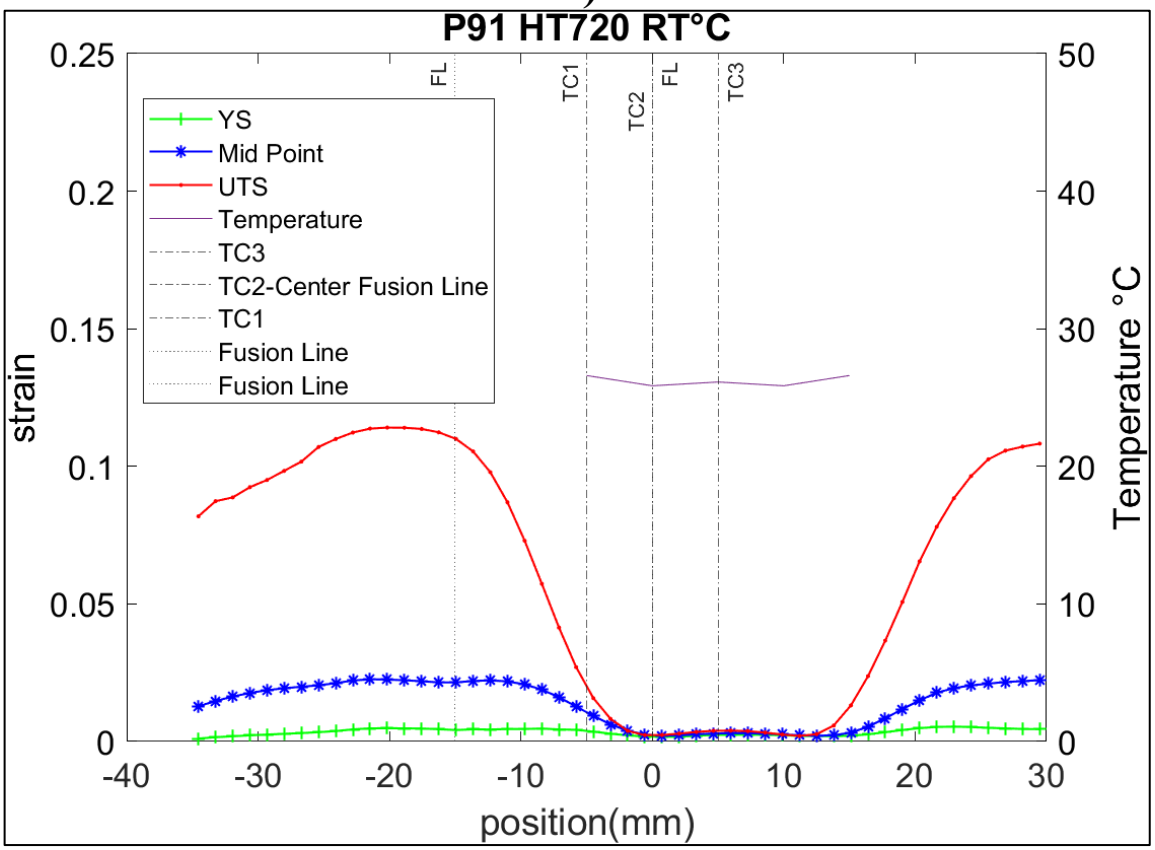
P91 HT720 RT°C
FL
TC1
TC2
FL
TC3
YS
Mid Point
UTS
Temperature
TC3
TC2-Center Fusion Line
TC1
Fusion Line
Fusion Line
strain
0.25
0.2
0.15
0.1
0.05
0
50
40
30
20
10
0
Temperature °C
-40
-30
-20
-10
0
10
20
30
position(mm)

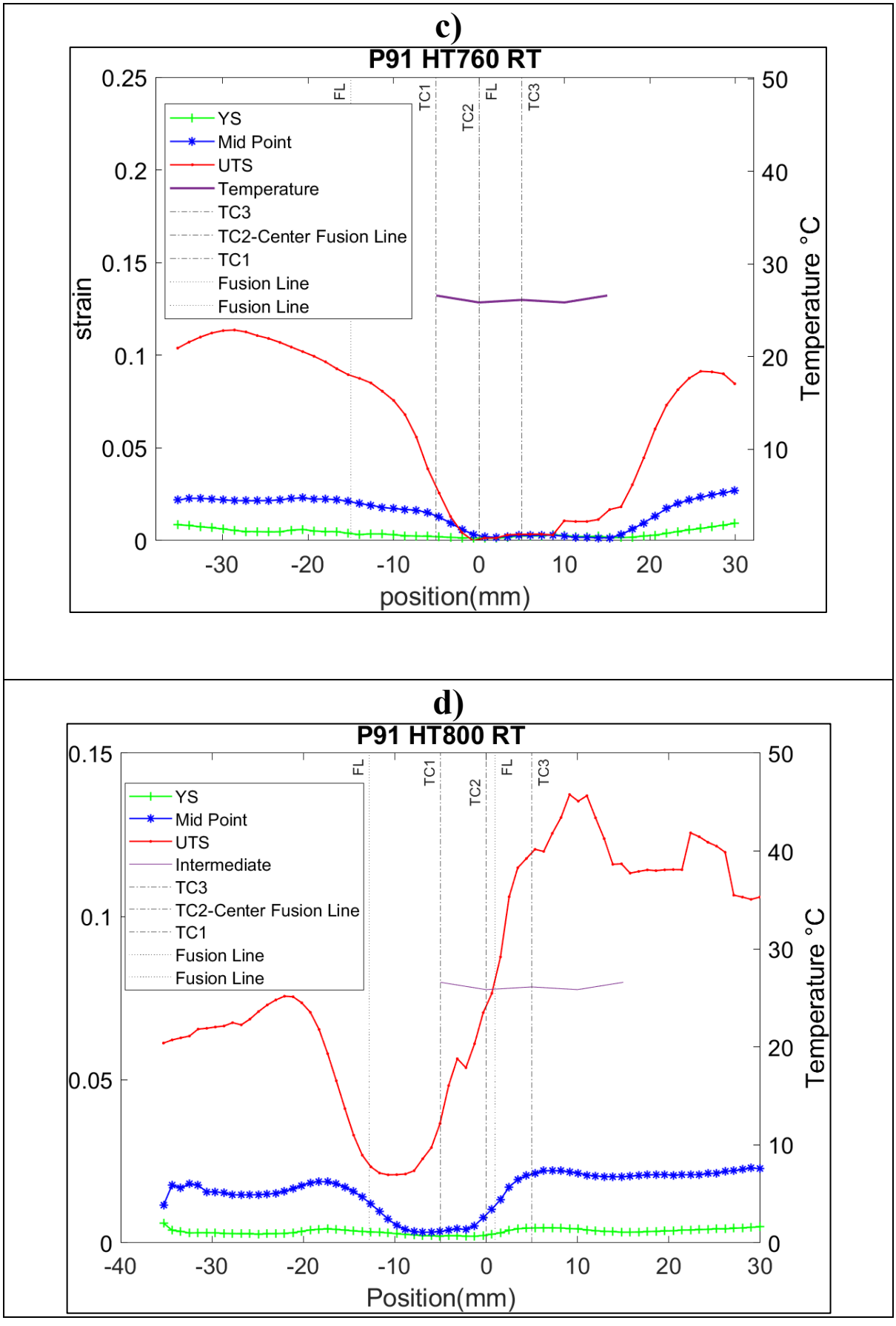

Figure 4.10: RT Individual experiment localised Strain maps a)AW b)HT720 c)HT760 d)HT800

4.4.2 300 °C Localised Strain Maps

300°C is an intermediate test temperature that can add to understanding the relationship between peak strain location, heat treatment condition and test temperature. Figure 4.11 a-c shows plots of localised strain maps at 300°C. Localised strain maps were obtained at YS, mid-point and UTS. At this elevated test temperature, the load bearing was distributed from adjacent BM into the WM for all HT conditions. Based on the localised strain maps obtained at 300°C in Figure 4.11, a wider portion of the WM experiences increased localised strain compared to room temperature localised strain maps. However, the WM remained the region experiencing the lowest localised strain across the specimens.

This indicates that test temperature influences the distribution of localised strain in the specimen. Elevated test temperature led to reduction in resistance to localised plastic deformation in the WM which was a region of high hardness because localised strain maps at higher temperatures showed increased deformation in the WM compared to room temperature. Table 4.6 shows the maximum localised strain obtained in each specimen at UTS. The highest localised strain in the necked region was observed in the AW condition. The value of the peak localised strain in the AW specimen was almost double that of the peak localised strain in all other HT conditions. This indicates that the AW condition was more susceptible to failure at elevated temperatures compared to other HT conditions. This also demonstrated that heat treatment improved the microstructural properties of P91, resulting in high resistance to localised plastic deformation at elevated temperatures and lower localised strain values. Materials with high resistance to localised plastic deformation generally had low levels of Localised strain. This means that the material can resist deformation even when subjected to a high load. On the other hand, materials with low resistance to localised plastic deformation exhibited high levels of Localised strain and could fail or break under load.

Table 4.6: 300°C Peak strain at UTS

Specimen	% Peak Localised Strain	Location
As-welded	20.3	BM
HT720	10.6	BM
HT760	10.7	BM
HT800	12.9	BM

Figure 4.12 a-c shows HAZ localised strain maps at YS, mid-point and UTS. These plots show the progression of localised strain in the HAZ from YS to UTS. Localised strain increases from the fusion line at position zero into the adjacent base metal. At UTS, AW HAZ experiences the higher localised strain with a steep gradient compared to other HT conditions. This further established the improved resistance to localised plastic deformation at elevated temperatures in HT760, HT720 and HT800 heat treatment conditions compared to the AW condition.

Figure 4.13 a-d shows localised strain maps and temperature profiles for each experiment. The control thermocouple was set at TC2 centre thermocouple for all experiments at 300°C. The location of peak strain was a function of PWHT, which influenced the strength of the metal, and test temperature because it occurred in the peak temperature region of the test specimen.

a)

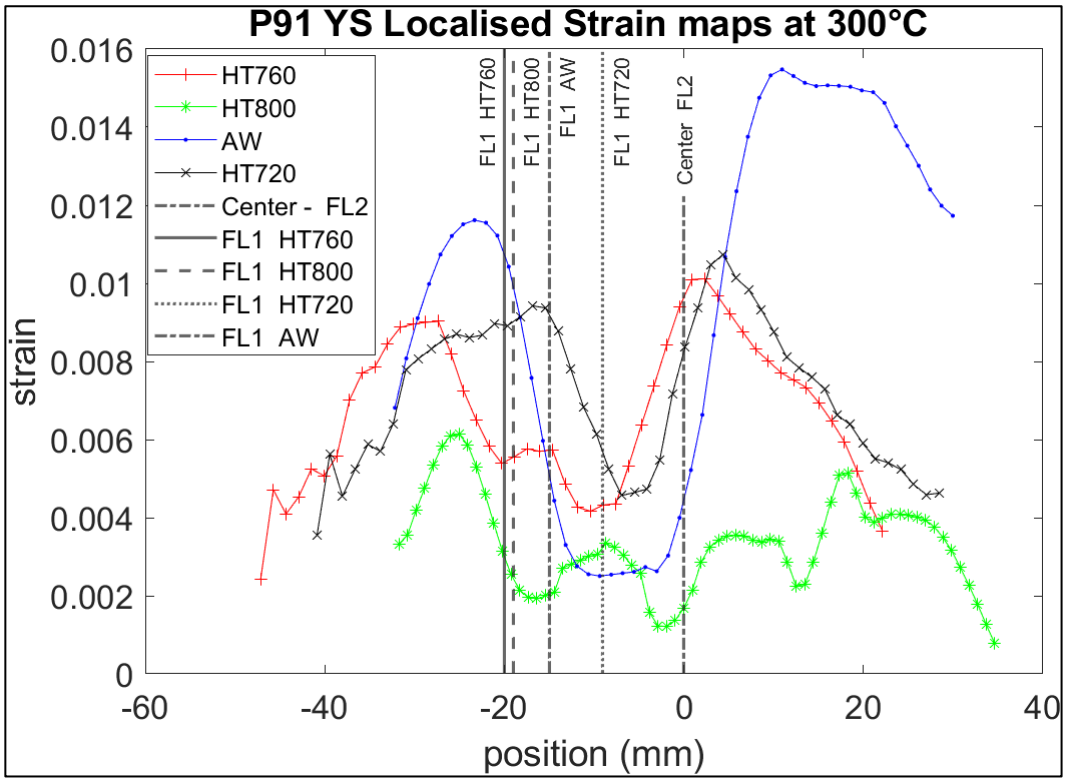
P91 YS Localised Strain maps at 300°C
strain
position (mm)
HT760
HT800
AW
HT720
Center - FL2
FL1 HT760
FL1 HT800
FL1 HT720
FL1 AW
FL1 HT760
FL1 HT800
FL1 AW
FL1 HT720
Center FL2

b)

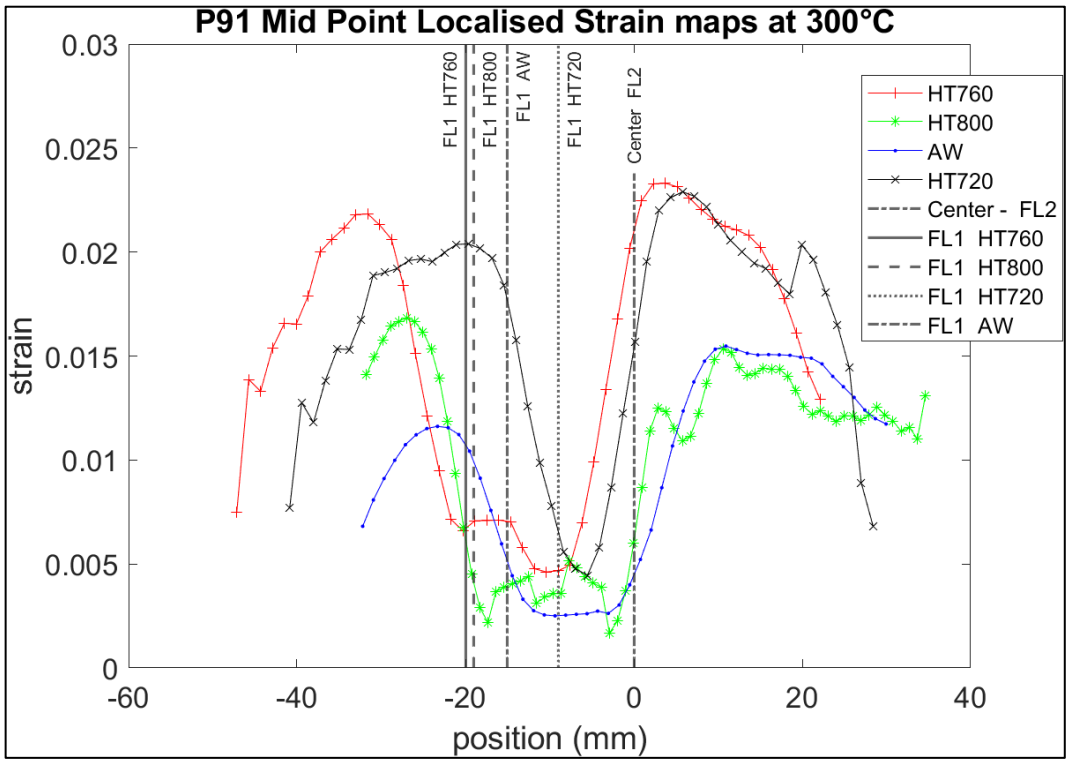
P91 Mid Point Localised Strain maps at 300°C
strain
position (mm)
HT760
HT800
AW
HT720
Center - FL2
FL1 HT760
FL1 HT800
FL1 HT720
FL1 AW
FL1 HT760
FL1 HT800
FL1 AW
FL1 HT720
Center FL2

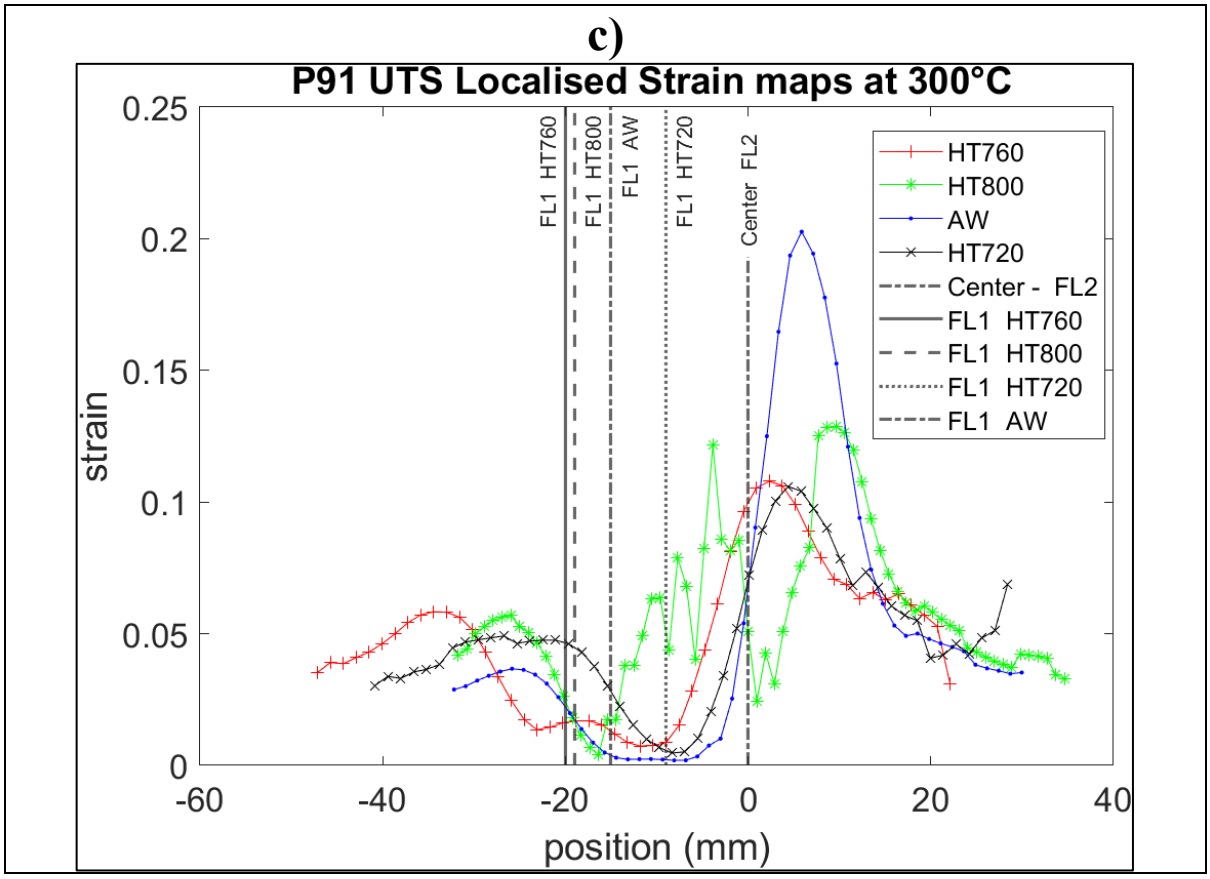

Figure 4.11: 300°C P91 Localised Strain Maps a) YS b) Mid-Point c) UTS

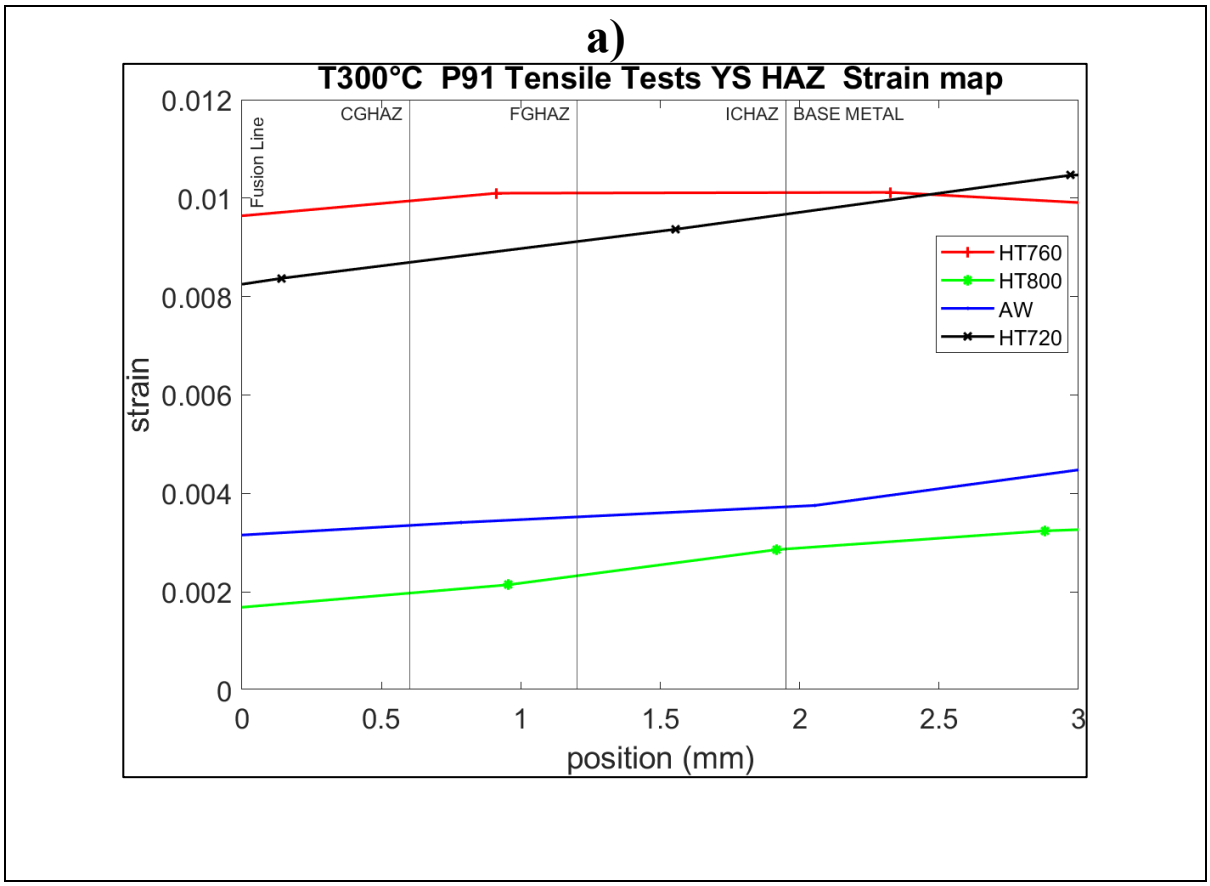

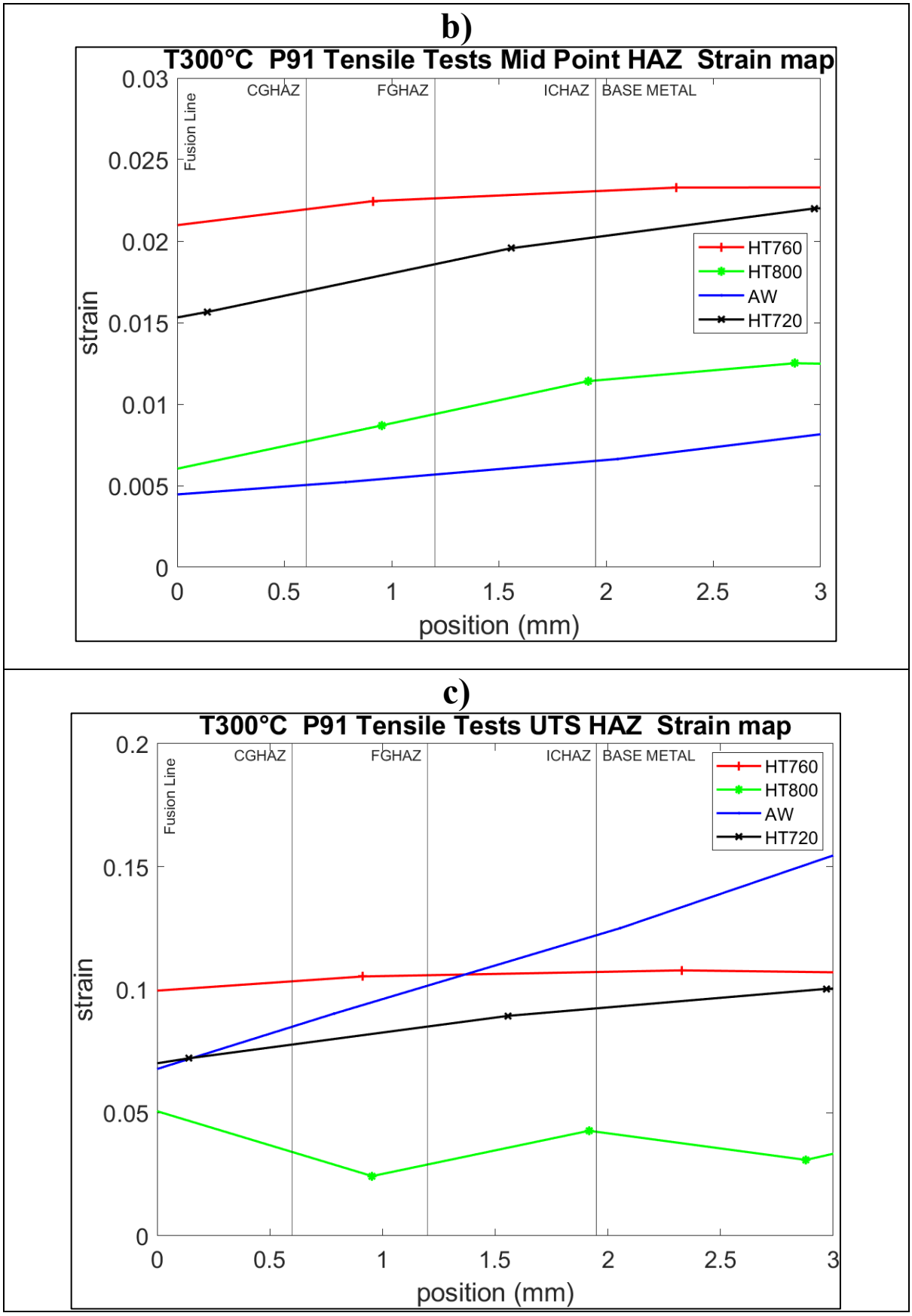

Figure 4.12: 300°C P91 HAZ Localised strain maps a)HAZ YS b)HAZ Mid-Point c)HAZ UTS

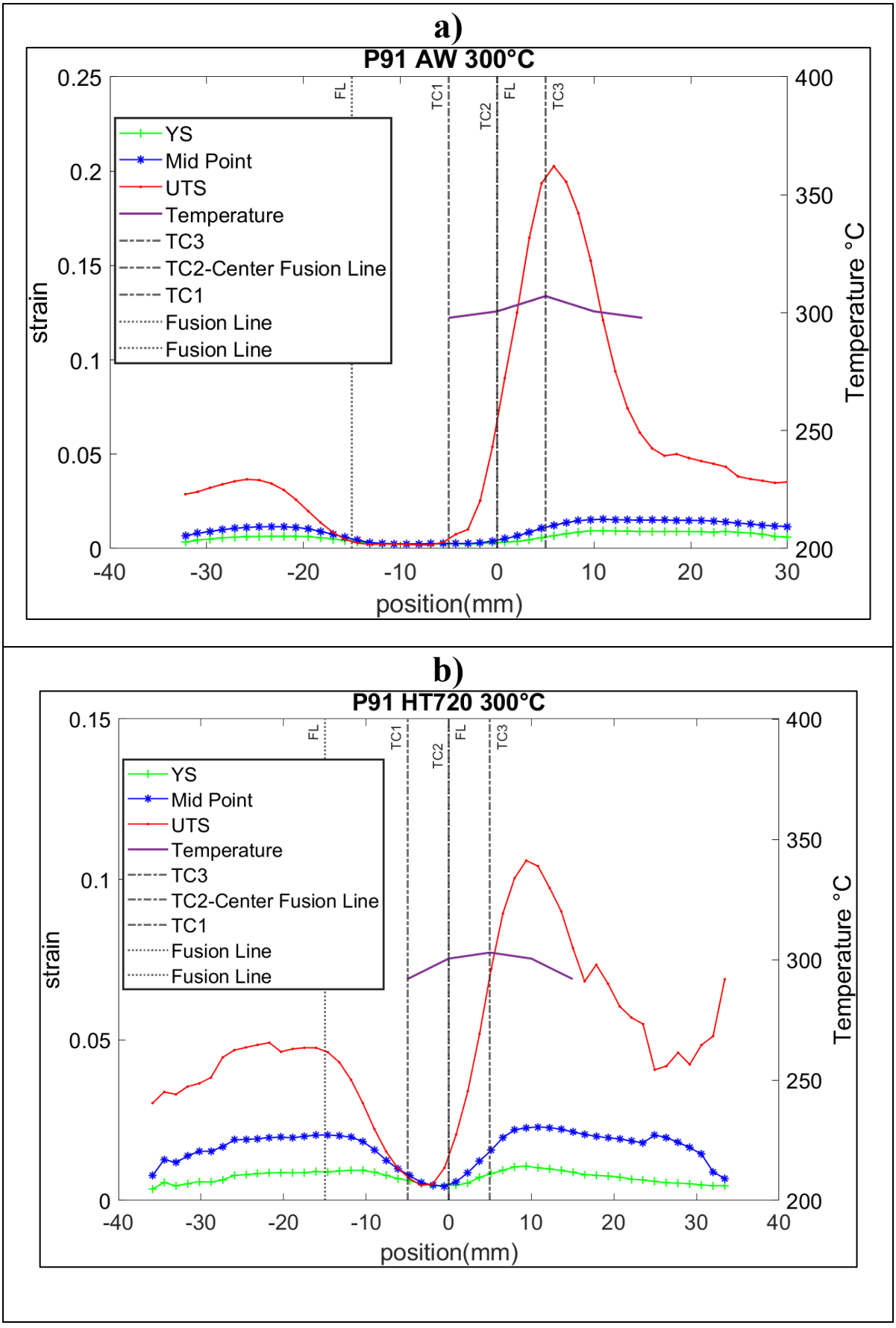
a)
P91 AW 300°C
YS
Mid Point
UTS
Temperature
TC3
TC2-Center Fusion Line
TC1
Fusion Line
Fusion Line
FL
TC1
TC2
FL
TC3
strain
Temperature °C
position(mm)
b)
P91 HT720 300°C
YS
Mid Point
UTS
Temperature
TC3
TC2-Center Fusion Line
TC1
Fusion Line
Fusion Line
FL
TC1
TC2
FL
TC3
strain
Temperature °C
position(mm)

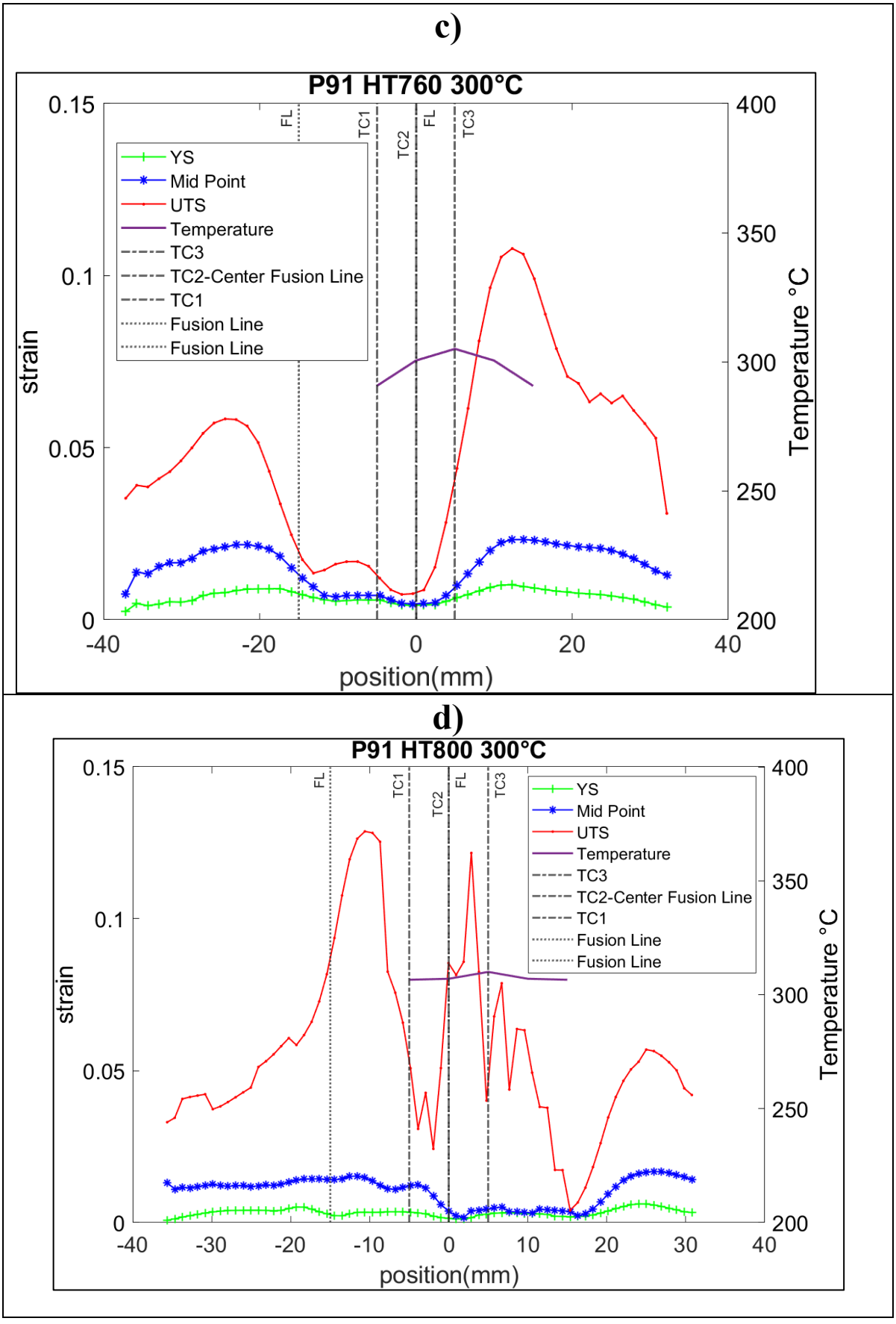

Figure 4.13: HT300 individual experiment localised strain maps a)AW d)HT720 c)HT760 d)HT800

4.4.3 535°C Localised Strain Maps

The 535°C tensile tests simulated power plant operating temperature to which P91 weldments are exposed. The control thermocouple was set at TC3 for all the experiments at 535°C. Figure 4.15c shows a comparison of localised strain at UTS for tensile tests at 535°C. Comparing the tensile tests in Figure 4.5 at 535°C, specimen reached UTS between 1.5-3% strain, at 300°C specimen reached UTS between 4-5% strain and at room temperature specimen reached UTS between 4-8%. This indicated reduced material resistance to plastic deformation at elevated test temperatures.

Table 4.7 shows the maximum localised strain obtained in specimen at 535°C at UTS. The peak localised strain decreased with increasing heat treatment temperature up to HT760, showing that even at elevated temperatures the effect of increase in resistance to localised plastic deformation due to heat treatment was maintained. However, in comparison to other test temperatures, UTS occurred at lower strains due to a lower work hardening ability of P91 at 535°C. A material with a lower work hardening is more susceptible to Localised plastic deformation and failure. Due to low work hardening ability when subjected to plastic deformation, the material could increase its resistance to further deformation. HT760 specimens had the lowest peak localised strain at UTS, this showed increased resistance to localised plastic deformation for heat treatment condition HT760. HT720, AW and HT800 specimens were more susceptible to fail before HT760 specimens during high temperature tensile testing as they experienced higher localised strain. HT720 specimens experience partial tempering. AW and HT800 specimens had a high resistance to localised plastic deformation which results in higher localised strain values.

Table 4.7: 535 °C Peak strain at UTS

Specimen	Peak Localised Strain %	Location
As-Welded	8.6	BM
HT720	8.4	BM
HT760	7.5	HAZ/OBM
HT800	9.5	BM

Figure 4.14 shows a plot comparing the localised peak strain at room temperature, 300°C and at 535°C. 300°C is an intermediate test temperature. At all test temperatures the peak localised strain at UTS decreased with increased in heat treatment temperature, except for HT800. This resulted in an improvement in material resistance to localised plastic deformation as HT temperature increased. However, tensile tests showed that it did not necessarily translate to increased strength properties. Tensile tests showed that heat treatment resulted in reduction in yield strength which reduced the materials resistance to the onset of plastic deformation. For all HT conditions, the peak localised strain decreased with increased test temperature. This indicated a relationship between localised strain, resistance to plastic deformation and test temperature. The trend also helped understand the effect of heat treatment on specimen as it became more defined as test temperature increased. HT760 had the lowest peak strain at 535°C indicating that this heat treatment had the highest resistance to localised plastic deformation at 535°C.

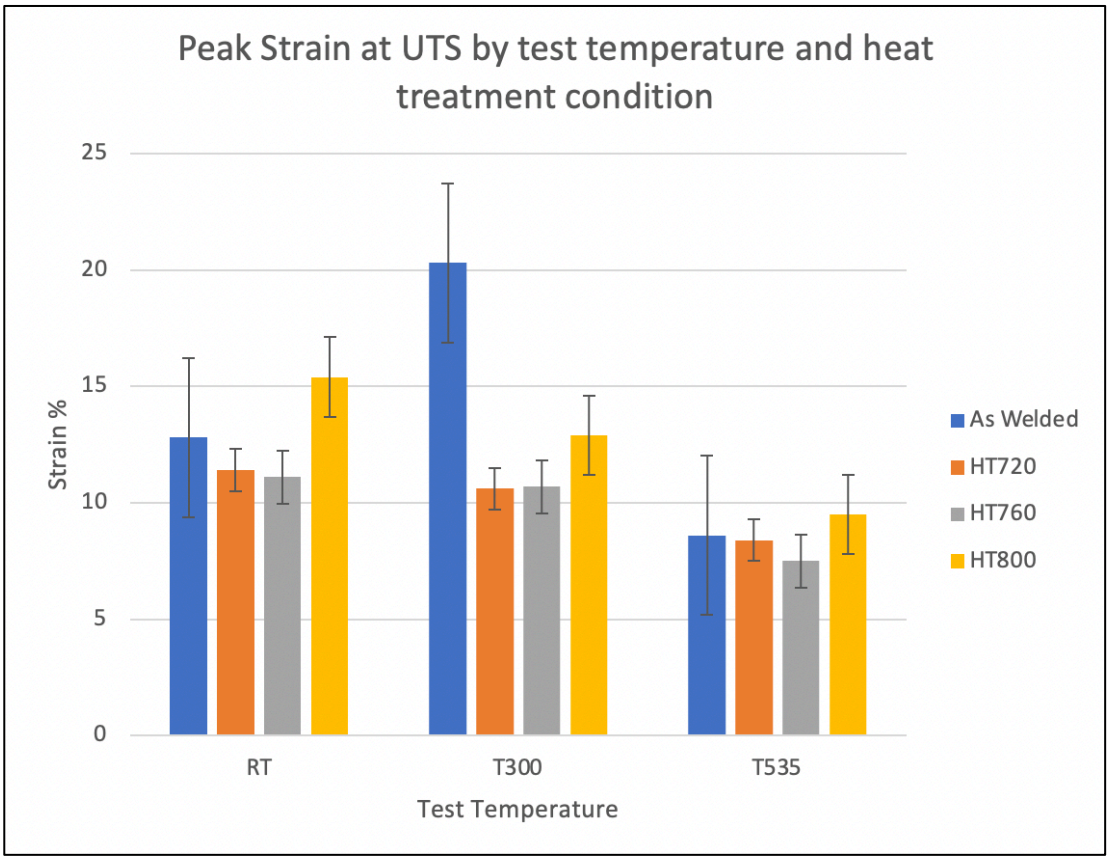

Figure 4.14: UTS Peak Localised strain comparison

Figure 4.17 a-d showed localised strain maps for tensile tests done at 535°C for each experiment and Figure 4.17 e shows localised strain map for a monolithic specimen. Strain maps were taken at YS, mid-point UTS. In all instances, the peak localised stain occurred within the 10 mm hot zone except for HT720. AW and HT720 WM experienced minimal strain compared to the base metal adjacent to the weld. HT800 and HT760 WM experienced more strain due to distribution of load bearing into the WM because of homogenisation due to heat treatment. Figure 4.16 a-c shows the HAZ localised strain maps. At 535°C AW experienced the least strain in the HAZ compared to other HT conditions. Heterogeneous weldment microstructure properties in AW specimen favoured strain localisation in the BM. Homogenised weldment microstructure properties due to heat treatment allowed for load distribution across the specimen resulting in higher strain in the HAZ for other specimens. At UTS the maximum localised strain for HT760, HT800 and AW were almost equal. The location of peak strain was a function of heat treatment, material strength and test temperature, however it did not always occur in the region with the highest temperature which coincides with the centre of the specimen

a)

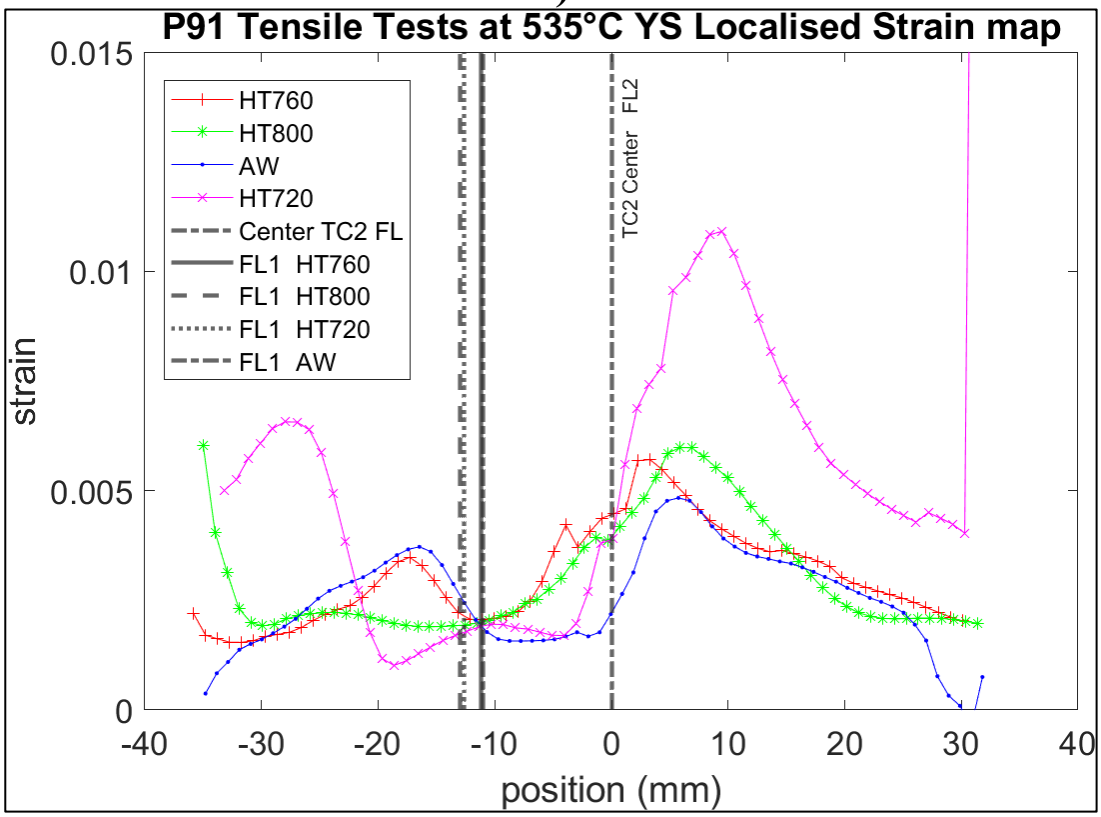
P91 Tensile Tests at 535°C YS Localised Strain map
HT760
HT800
AW
HT720
Center TC2 FL
FL1 HT760
FL1 HT800
FL1 HT720
FL1 AW
TC2 Center FL2
strain
position (mm)
0.015
0.01
0.005
0
-40
-30
-20
-10
0
10
20
30
40

b)

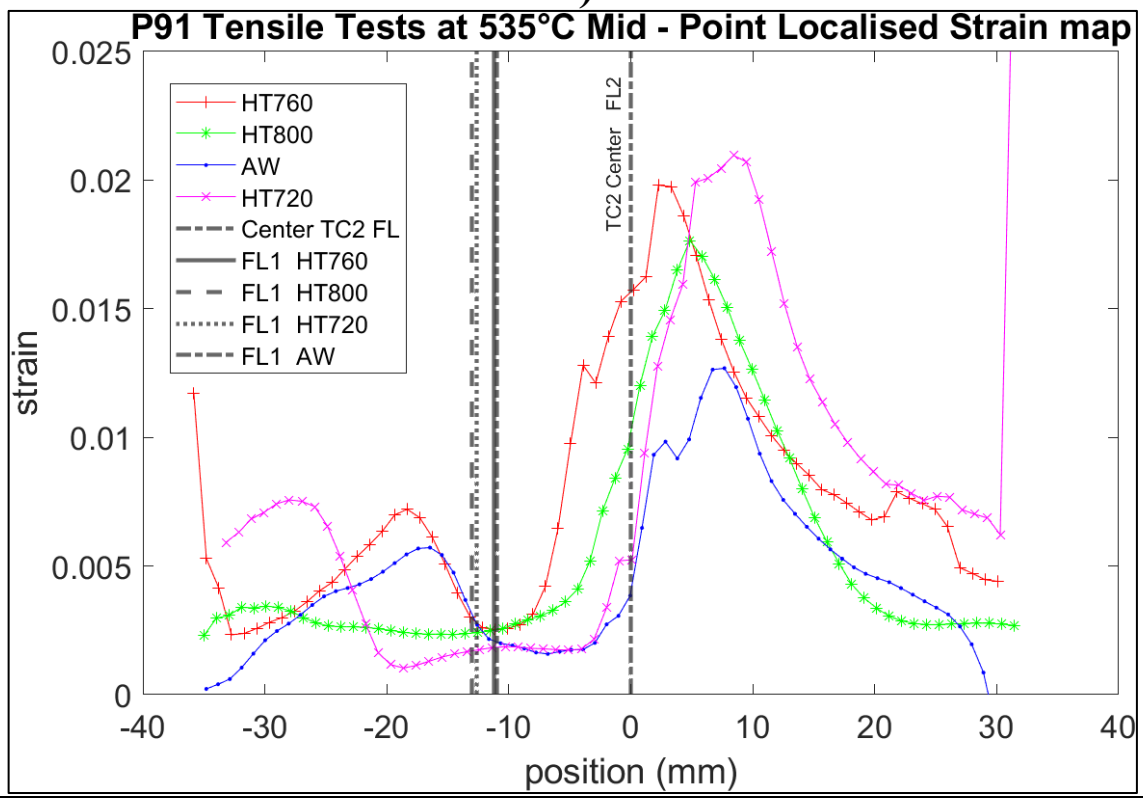
P91 Tensile Tests at 535°C Mid - Point Localised Strain map
HT760
HT800
AW
HT720
Center TC2 FL
FL1 HT760
FL1 HT800
FL1 HT720
FL1 AW
TC2 Center FL2
strain
position (mm)
0.025
0.02
0.015
0.01
0.005
0
-40
-30
-20
-10
0
10
20
30
40

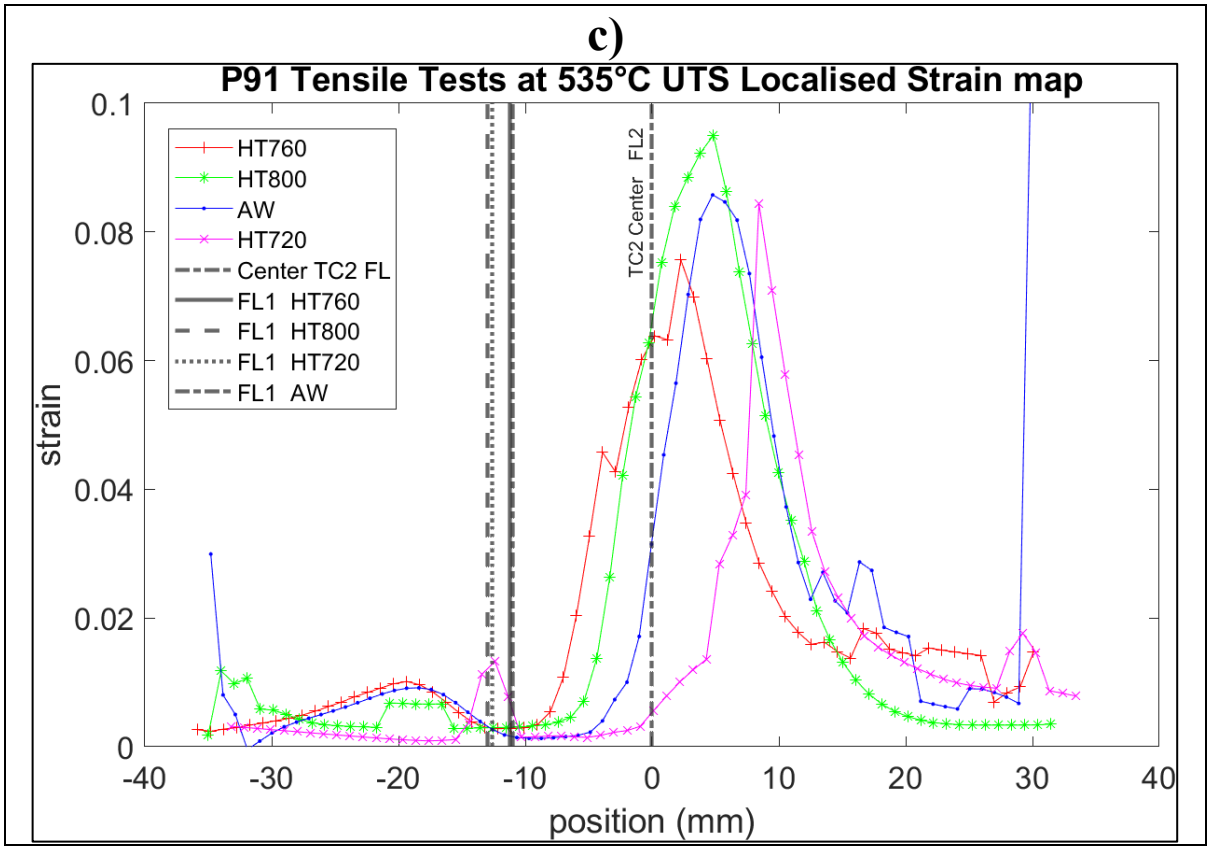

Figure 4.15: 535°C P91 Localised Strain Maps a) YS, b) Middle Point, c) UTS

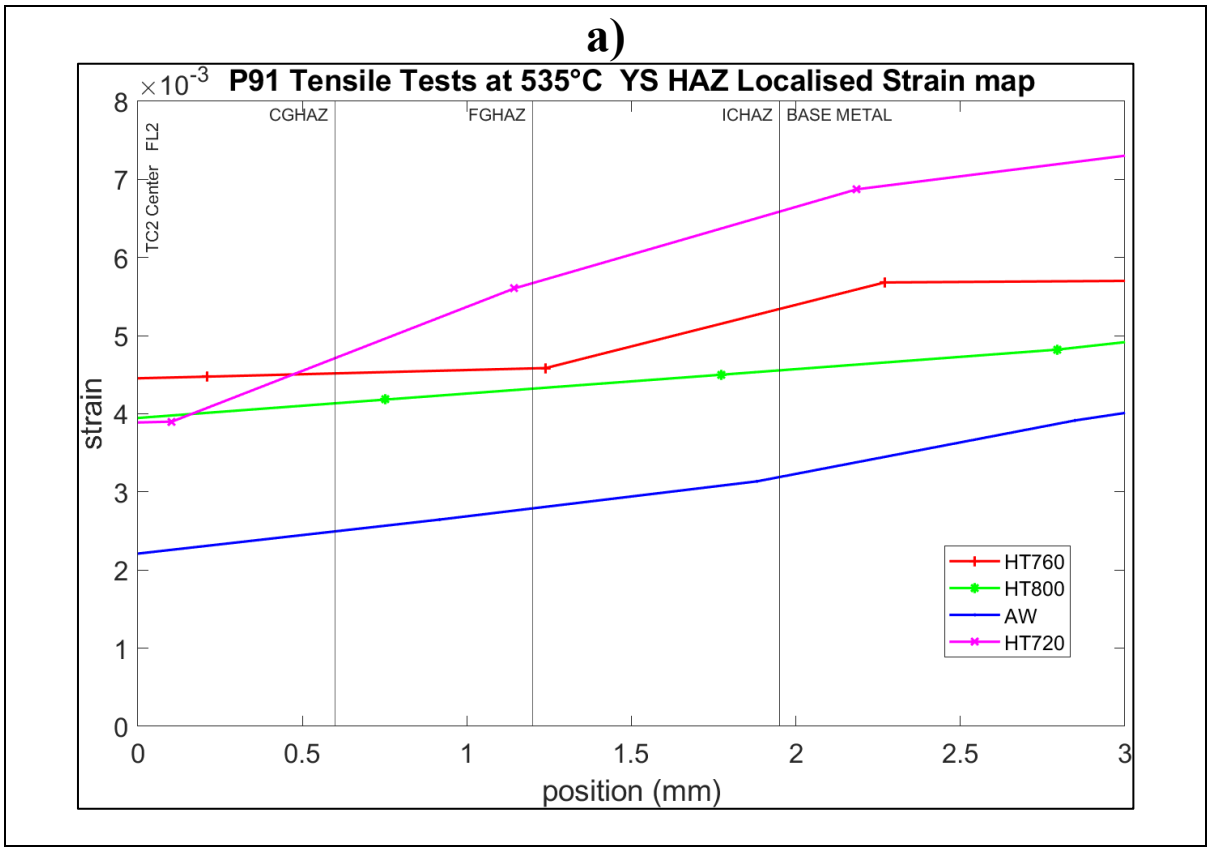

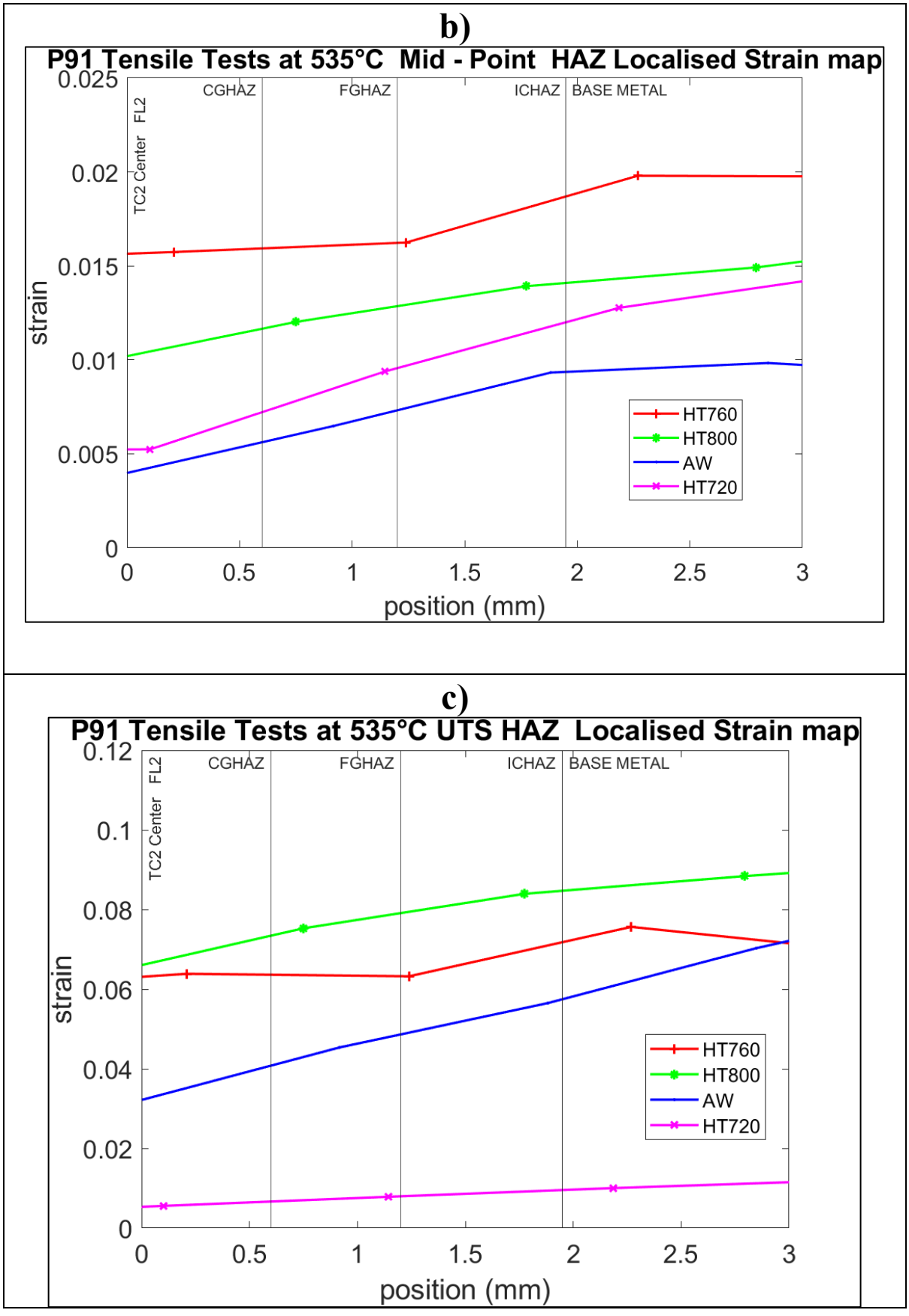

Figure 4.16: 535°C P91 HAZ Localised Strain Maps a) HAZ YS, b) HAZ Middle Point, c) HAZ UTS

a)

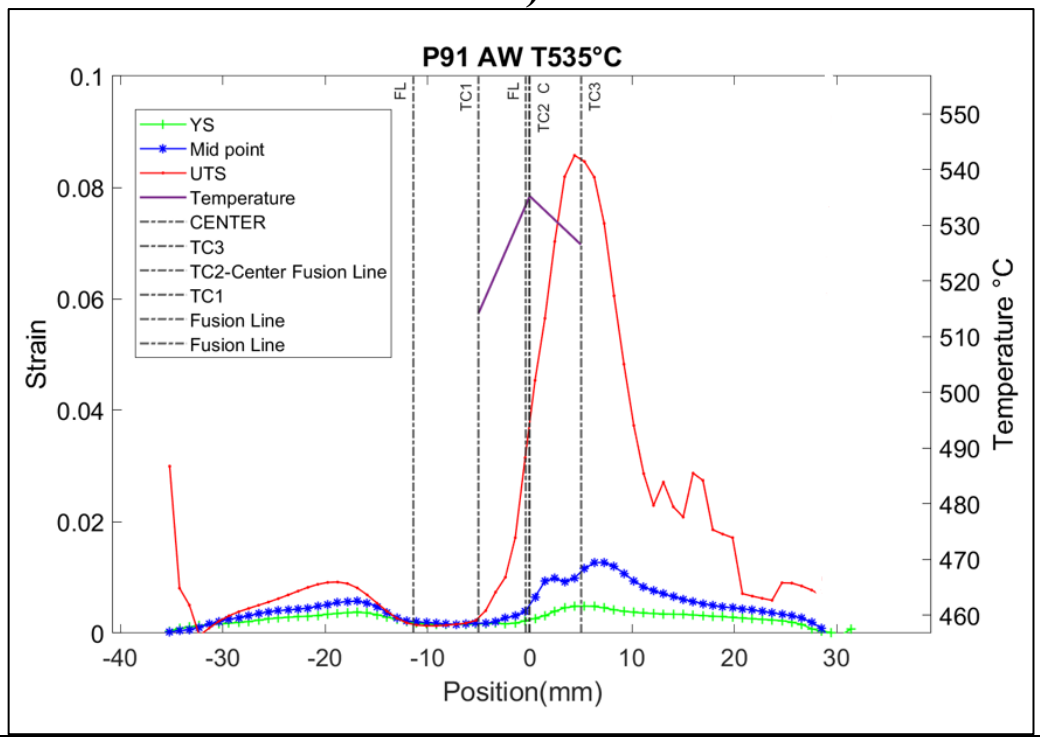
P91 AW T535°C
YS
Mid point
UTS
Temperature
CENTER
TC3
TC2-Center Fusion Line
TC1
Fusion Line
Fusion Line
FL
TC1
FL
TC2 C
TC3
Strain
Temperature °C
Position(mm)

b)

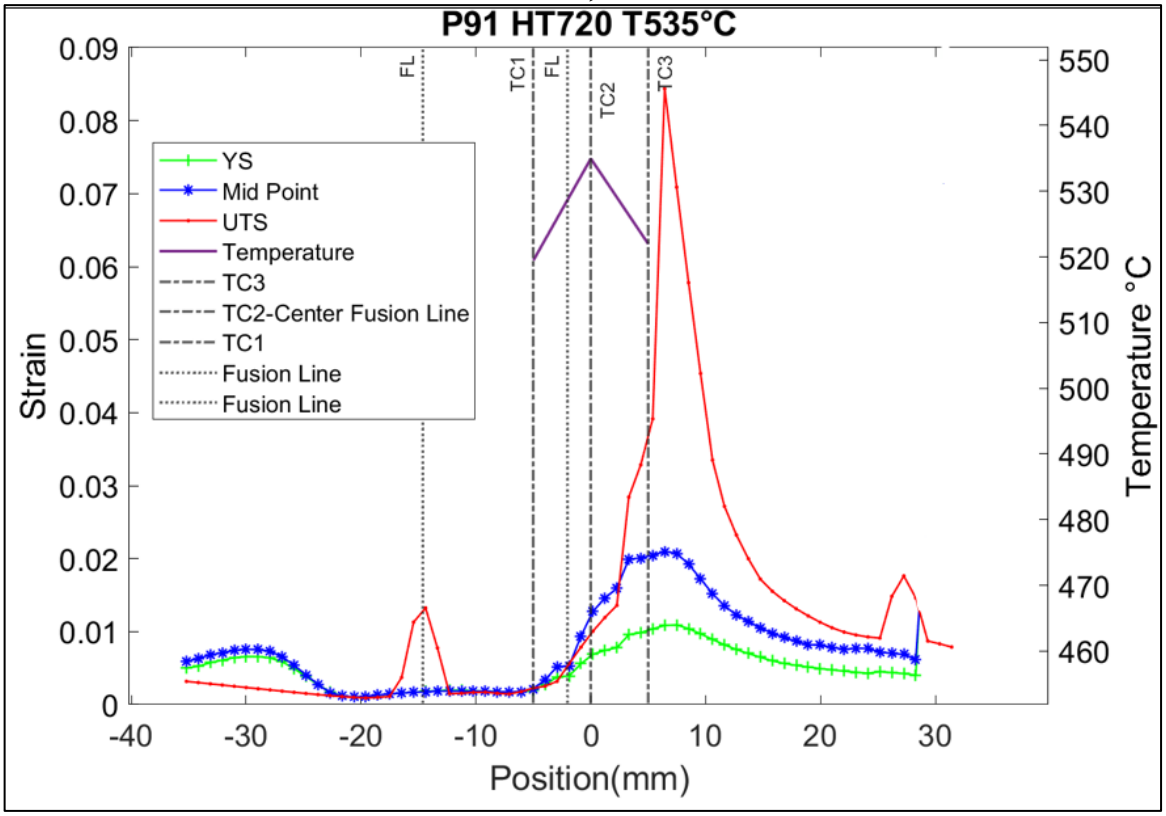
P91 HT720 T535°C
YS
Mid Point
UTS
Temperature
TC3
TC2-Center Fusion Line
TC1
Fusion Line
Fusion Line
FL
TC1
FL
TC2
TC3
Strain
Temperature °C
Position(mm)

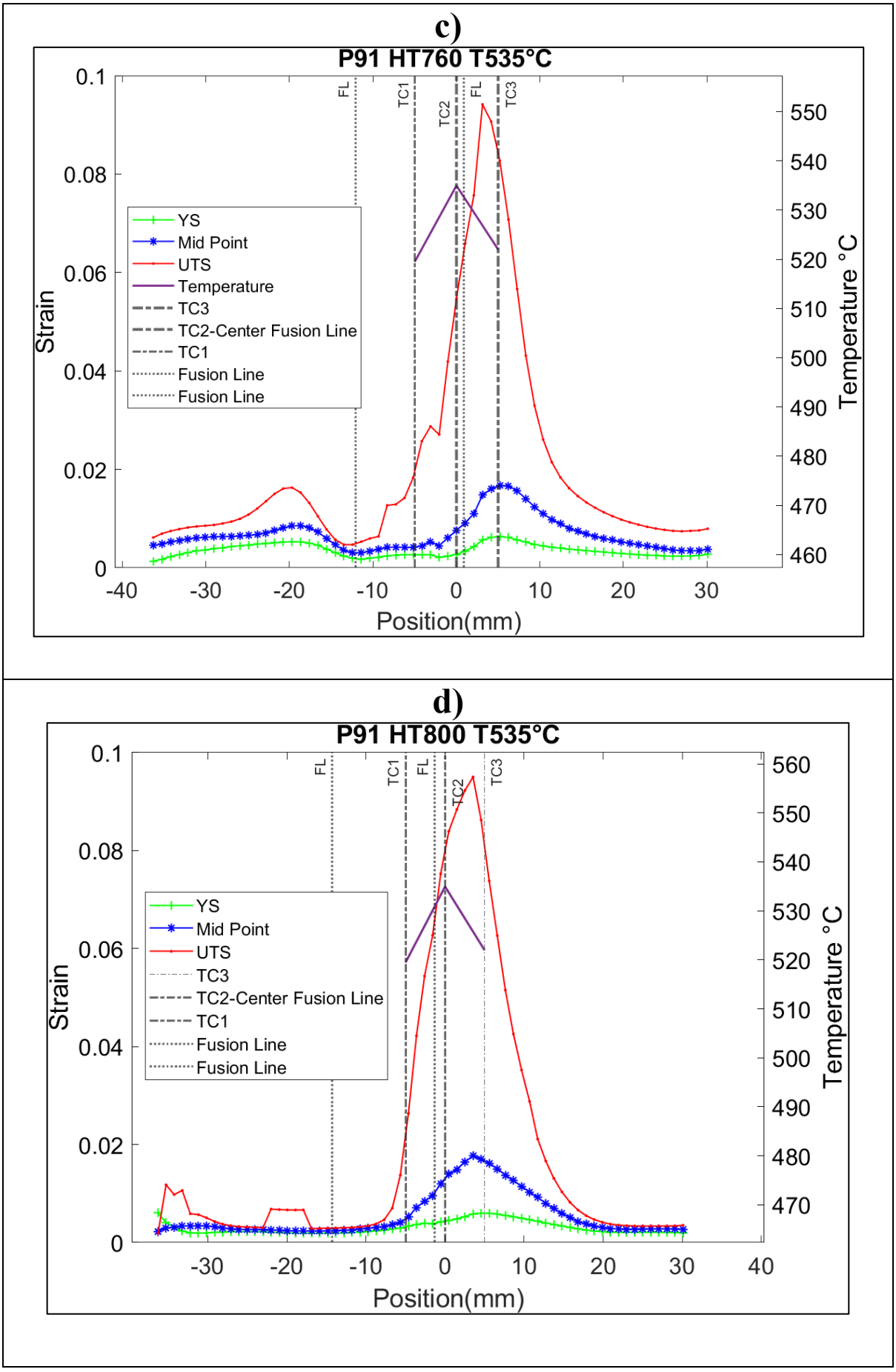
c)
P91 HT760 T535°C
Strain
Temperature °C
Position(mm)
FL
TC1
TC2
FL
TC3
YS
Mid Point
UTS
Temperature
TC3
TC2-Center Fusion Line
TC1
Fusion Line
Fusion Line
d)
P91 HT800 T535°C
Strain
Temperature °C
Position(mm)
FL
TC1
FL
TC2
TC3
YS
Mid Point
UTS
TC3
TC2-Center Fusion Line
TC1
Fusion Line
Fusion Line

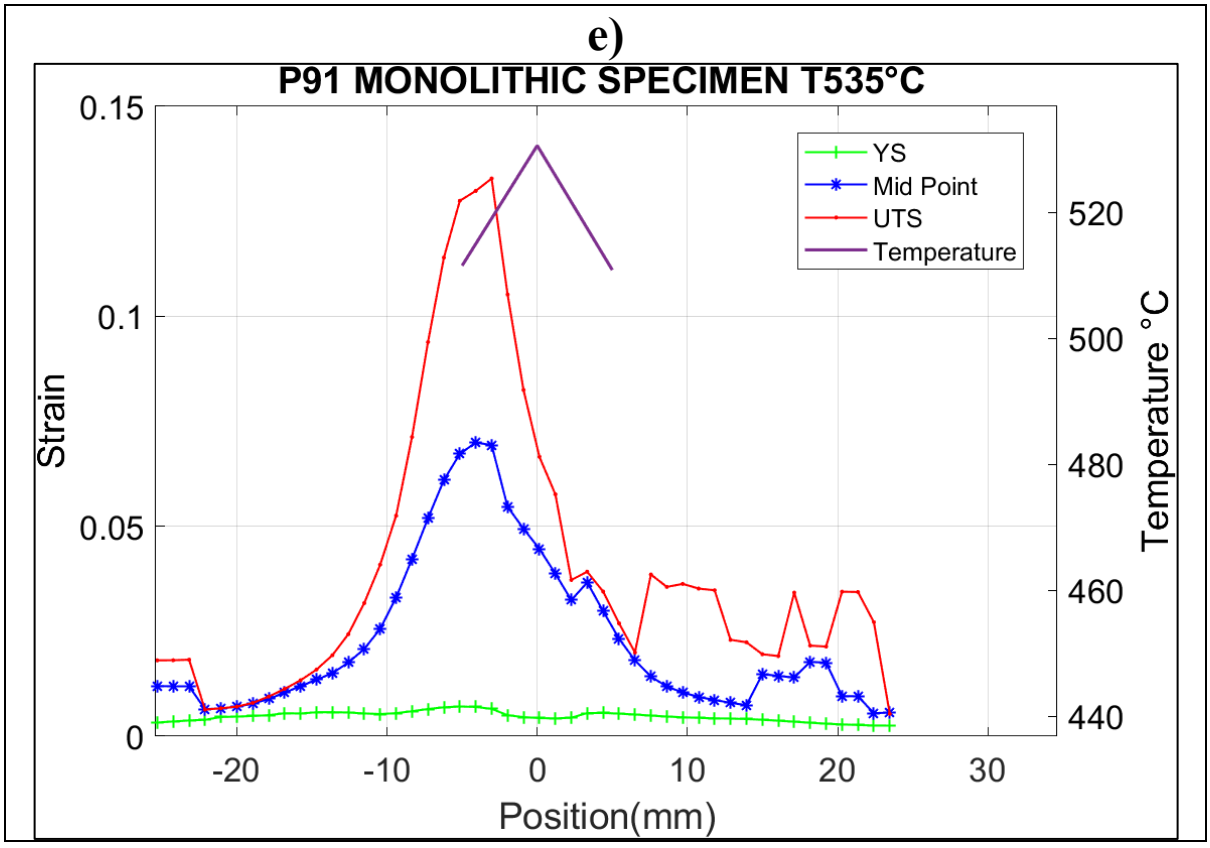

Figure 4.17: 535°C P91 Individual experiment localised strain maps a)AW b)HT720 c)HT760 d)HT800 e)Monolithic specimen

4.4.4 Excursions and Extended heat treatments

Figure 4.18 a-d shows localised strain maps for experimental matrix 2 tensile tests. Experimental matrix 2 heat treatment conditions represent deviations from standard practice that can occur during field heat treatments. These heat treatments simulated extended field heat treatments and excursions during heat treatments. The control thermocouple was set at TC2 for all experiments. All tensile tests were done at 535°C. Table 4.8 shows a comparison of peak strain at UTS for different HT760 heat treatments. Specimens subjected to excursions and extended heat treatments showed higher Localised strain peaks. Deviations from standard heat treatment resulted in reduced resistance to Localised plastic deformation at 535°C in HT760 specimens.

Figure 4.*19* a-c shows a comparison of localised strain at YS, Mid-point and UTS. At UTS the location of peak strain in HT760 and HT760EX840 occurred in the edge of the HAZ in the over tempered base metal (OBM) in the hot zone. HT760EX820 had localised strain that closely matched the profile of HT760EX840 at YS, Mid-point and UTS. Tensile tests in Figure 4.*5* show that the overall effect of deviating from standard heat treatment practice was reduced material strength resulting in lower YS and UTS properties.

Figure 4.20 a-c shows HAZ localised strain maps. Due to heterogeneous mechanical properties in the weldment, the progression of strain in the HAZ was not a direct reflection of the magnitude strain localisation in the specimen. HT760 4H had the lowest strain in the HAZ at UTS but recorded highest value of localised strain in the specimen at UTS. Strain localisation

in the HAZ was therefore a function of material properties in the HAZ and was not a representation of overall material behaviour.

Table 4.8: 535 °C Peak strain at UTS

Specimen	Peak localised strain %	Location
HT760 EX 820	9.4	BM
HT760 EX 840	9.4	OBM
HT760 4H	9.9	BM
HT760 6H	8.3	BM
HT760 2H	7.5	OBM

a)

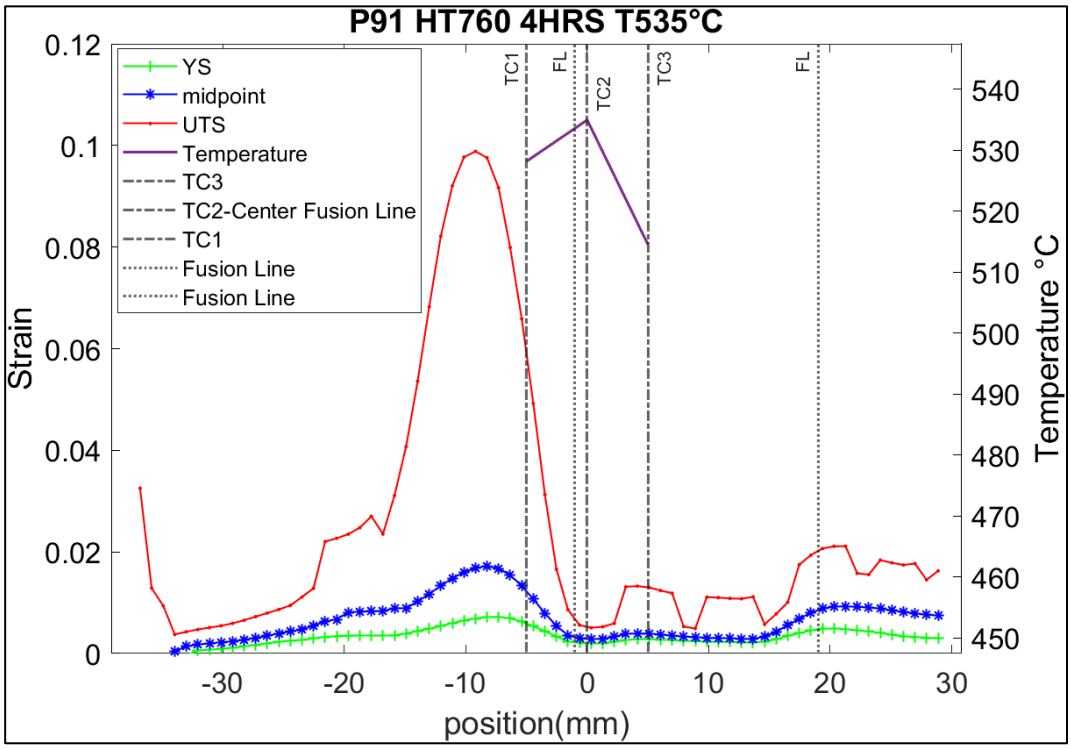

b)

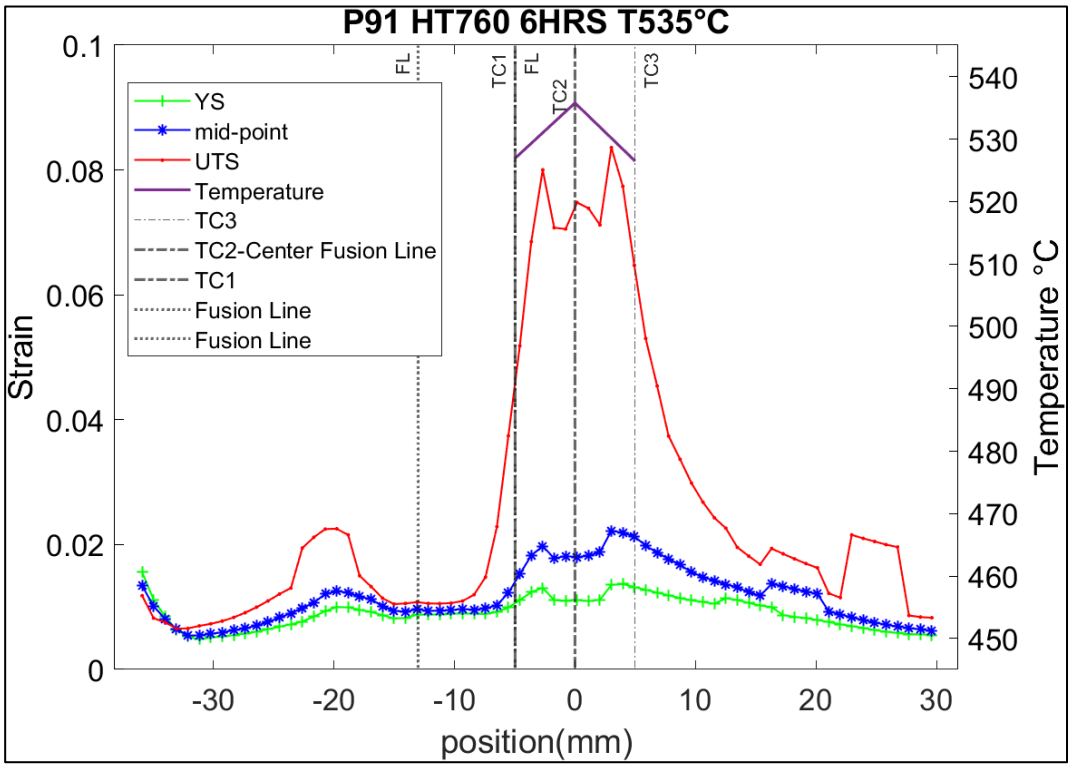
P91 HT760 6HRS T535°C
Strain
Temperature °C
position(mm)
YS
mid-point
UTS
Temperature
TC3
TC2-Center Fusion Line
TC1
Fusion Line
Fusion Line
FL
TC1
FL
TC2
TC3

c)

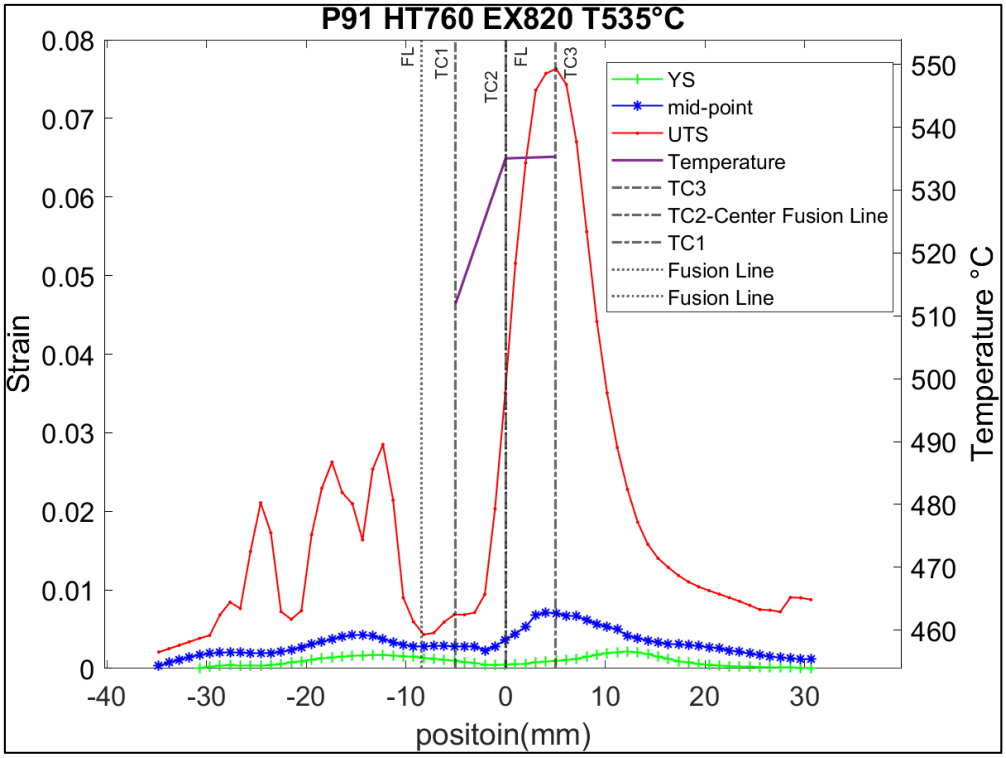
P91 HT760 EX820 T535°C
Strain
Temperature °C
positoin(mm)
YS
mid-point
UTS
Temperature
TC3
TC2-Center Fusion Line
TC1
Fusion Line
Fusion Line
FL
TC1
TC2
FL
TC3

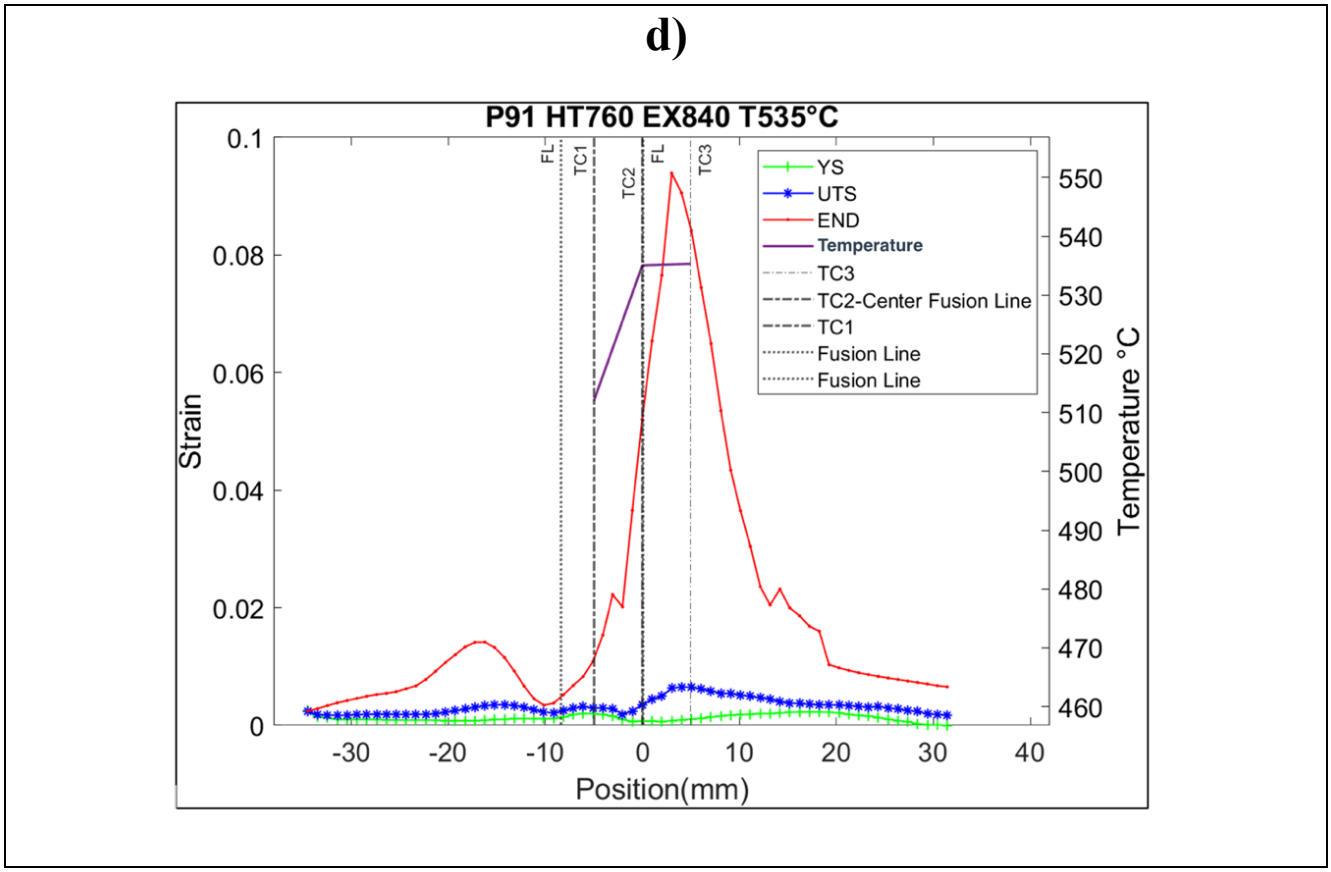

Figure 4.18: 535°C P91 Ext PWHT and excursion individual experiment localised strain maps a)HT740 HR4 b)HT760 HR6 c)HT760 EX820 d)HT760 EX840

a)

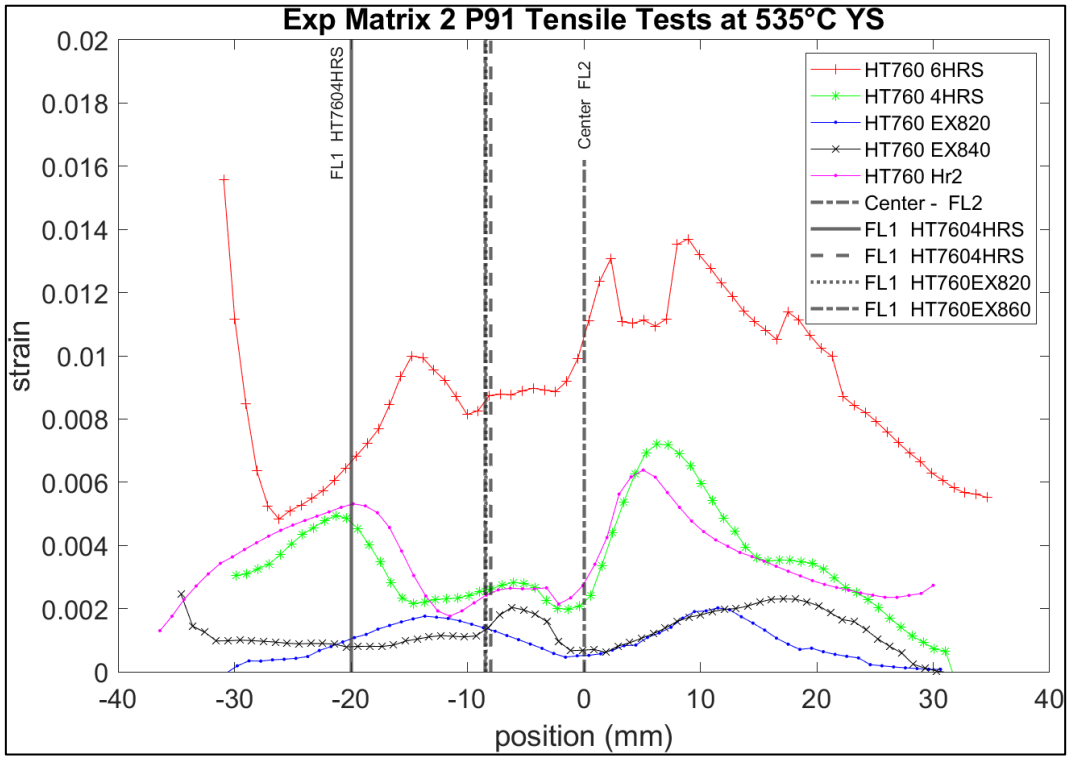
Exp Matrix 2 P91 Tensile Tests at 535°C YS
strain
position (mm)
FL1 HT7604HRS
Center FL2
HT760 6HRS
HT760 4HRS
HT760 EX820
HT760 EX840
HT760 Hr2
Center - FL2
FL1 HT7604HRS
FL1 HT7604HRS
FL1 HT760EX820
FL1 HT760EX860

b)

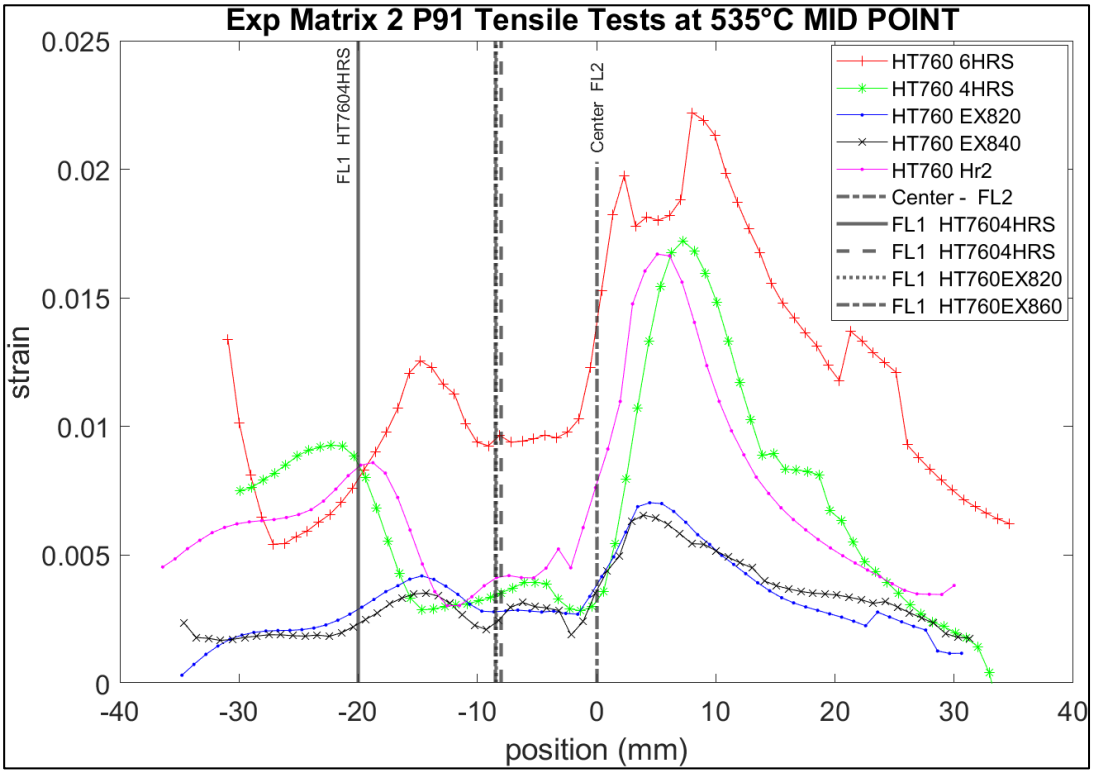
Exp Matrix 2 P91 Tensile Tests at 535°C MID POINT
strain
position (mm)
FL1 HT7604HRS
Center FL2
HT760 6HRS
HT760 4HRS
HT760 EX820
HT760 EX840
HT760 Hr2
Center - FL2
FL1 HT7604HRS
FL1 HT7604HRS
FL1 HT760EX820
FL1 HT760EX860

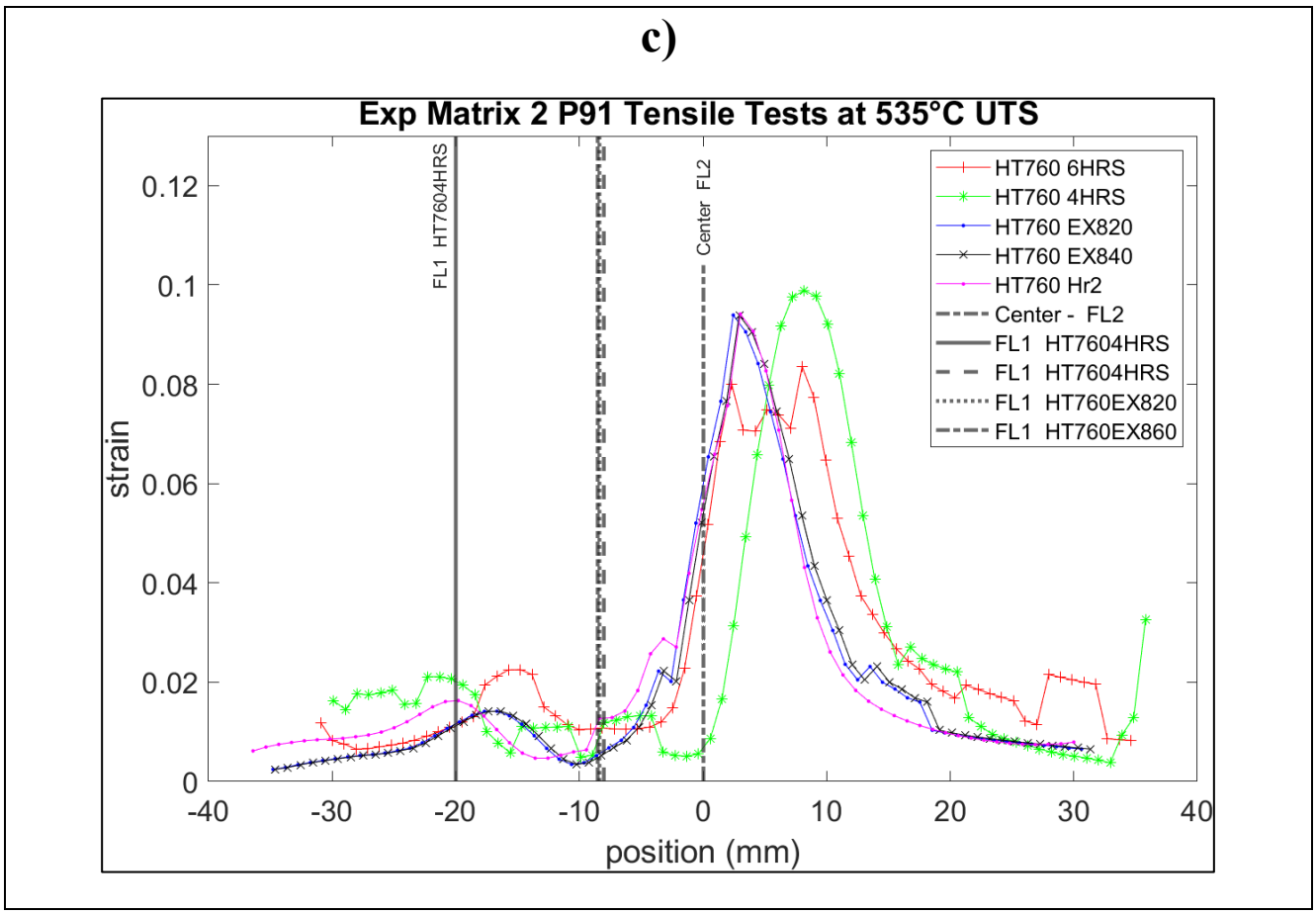

Figure 4.19: P91 535°C Ext PWHT and excursion localised strain maps a) YS, b) Middle Point, c) UTS

a)

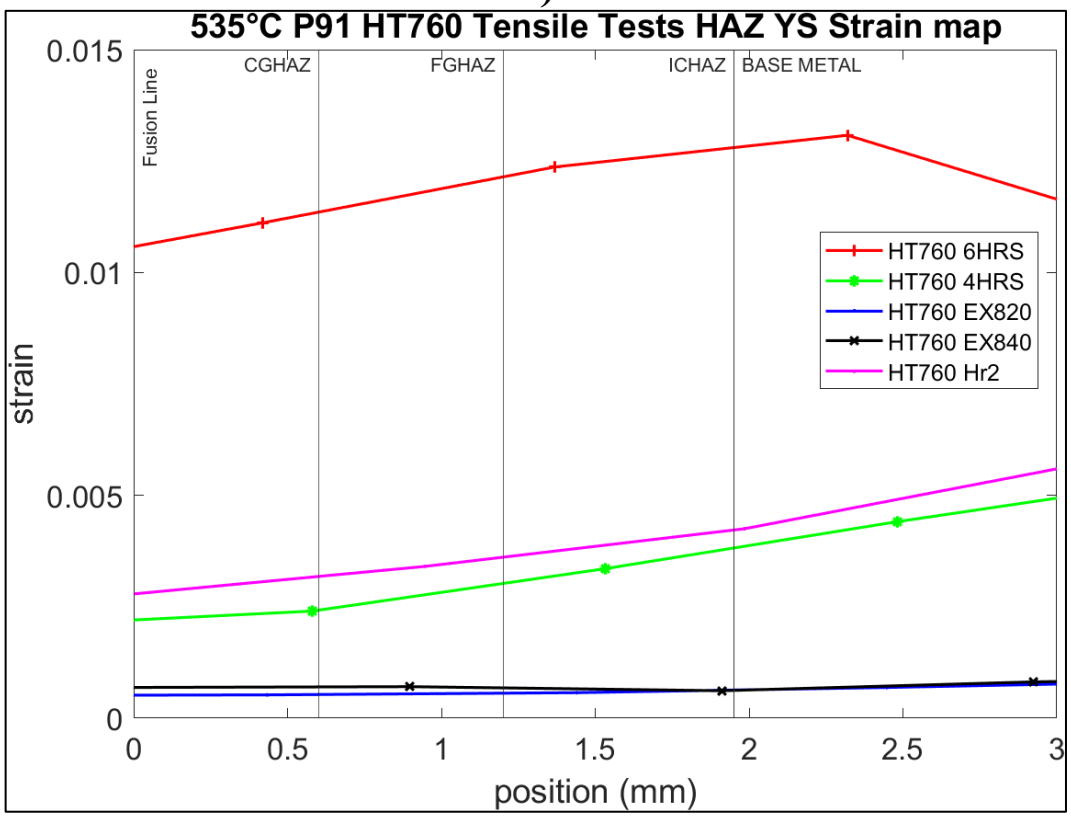
535°C P91 HT760 Tensile Tests HAZ YS Strain map
CGHAZ
FGHAZ
ICHAZ
BASE METAL
Fusion Line
HT760 6HRS
HT760 4HRS
HT760 EX820
HT760 EX840
HT760 Hr2
strain
position (mm)
0.015
0.01
0.005
0
0
0.5
1
1.5
2
2.5
3

b)

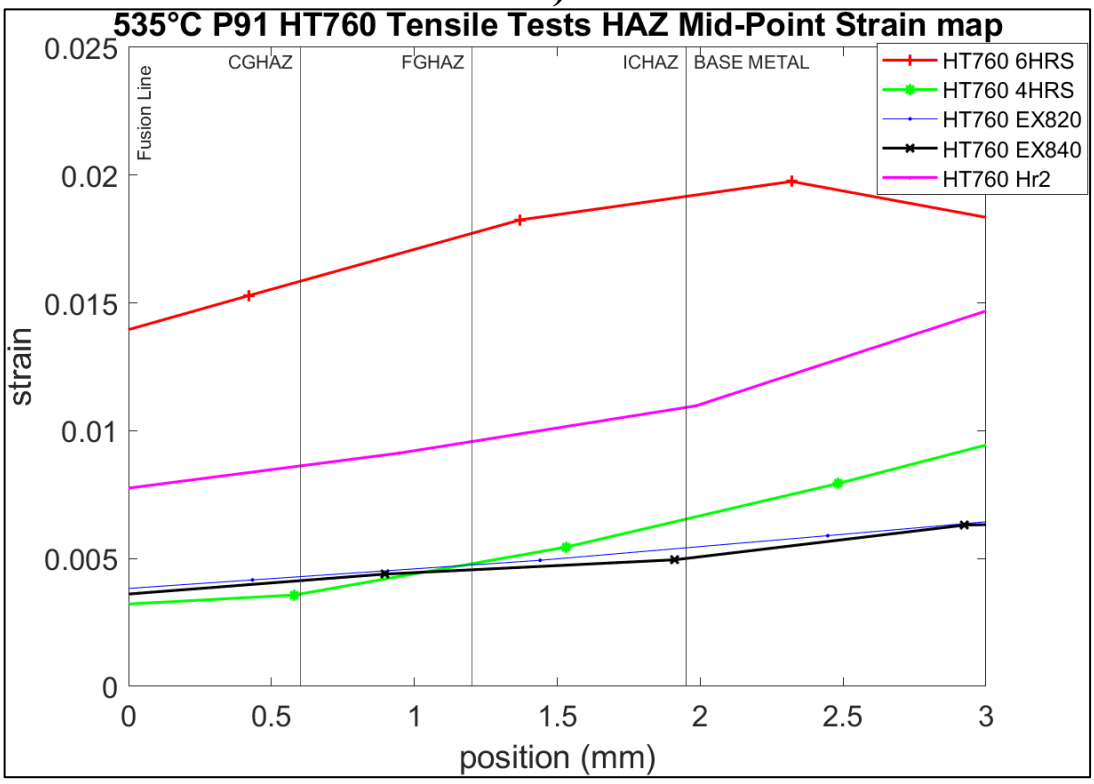
535°C P91 HT760 Tensile Tests HAZ Mid-Point Strain map
CGHAZ
FGHAZ
ICHAZ
BASE METAL
Fusion Line
HT760 6HRS
HT760 4HRS
HT760 EX820
HT760 EX840
HT760 Hr2
strain
position (mm)
0.025
0.02
0.015
0.01
0.005
0
0
0.5
1
1.5
2
2.5
3

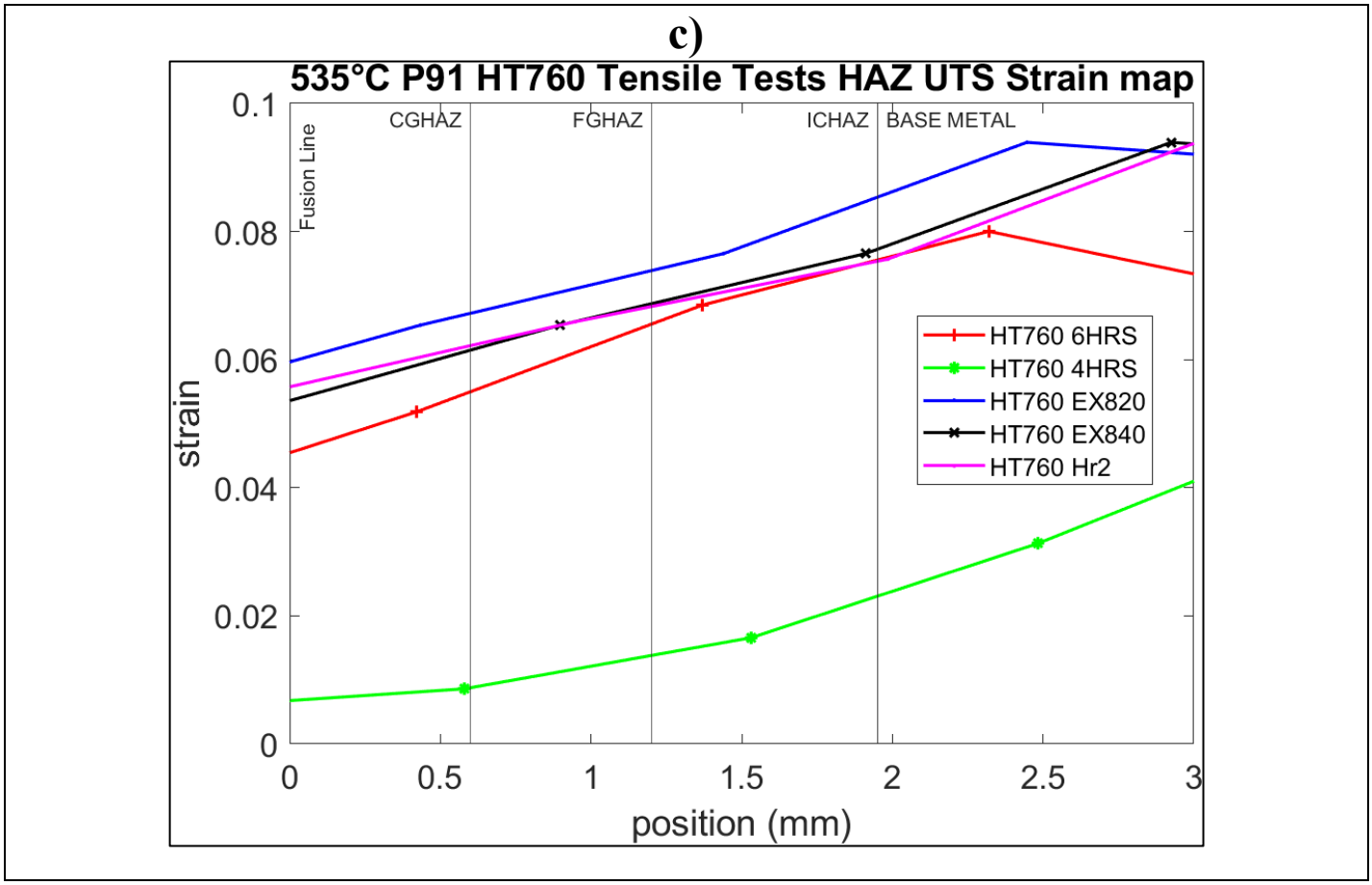

Figure 4.20: 535°C P91 Ext PWHT and excursion HAZ localised strain maps and excursion strain maps a) HAZ YS, b) HAZ Middle Point, c) HAZ UTS

4.5 Peak Strain Location

Welding results in heterogeneous mechanical properties in the weldment. When subjected to stress, the heterogeneous mechanical properties result in non-uniform material response to mechanical and thermal loads. Specimens are subjected to tensile stress and compressive stresses due to thermal expansion [26]. Strain localization occurs due to non-uniform material response. Accurately predicting the location of failure in weldments is essential for maintenance as it reduces the cost and time to do maintenance. Non-Destructive testing (NDT) techniques used to assess material condition in service can obtain data from a width as small as 10 mm. The location most susceptible to failure coincides with the point where peak strain occurs.

4.5.1 Peak strain location relative to the Fusion line

Figure 4.*21* shows the location of peak strain relative to the fusion line. Heat treatment condition and test temperature affected the location of peak strain relative to the fusion line. For all heat treatment conditions, the location of peak strain shifted from the base metal towards the HAZ as the test temperature increased. Tests at room temperature showed peak strain occurring in the base metal for all heat treatment conditions. At room temperature the effect of PWHT on location of peak strain was that it moved further into the base metal relative to the fusion line compared to the As-welded condition. This indicated improved microstructure homogeneity in the base metal because of heat treatment.

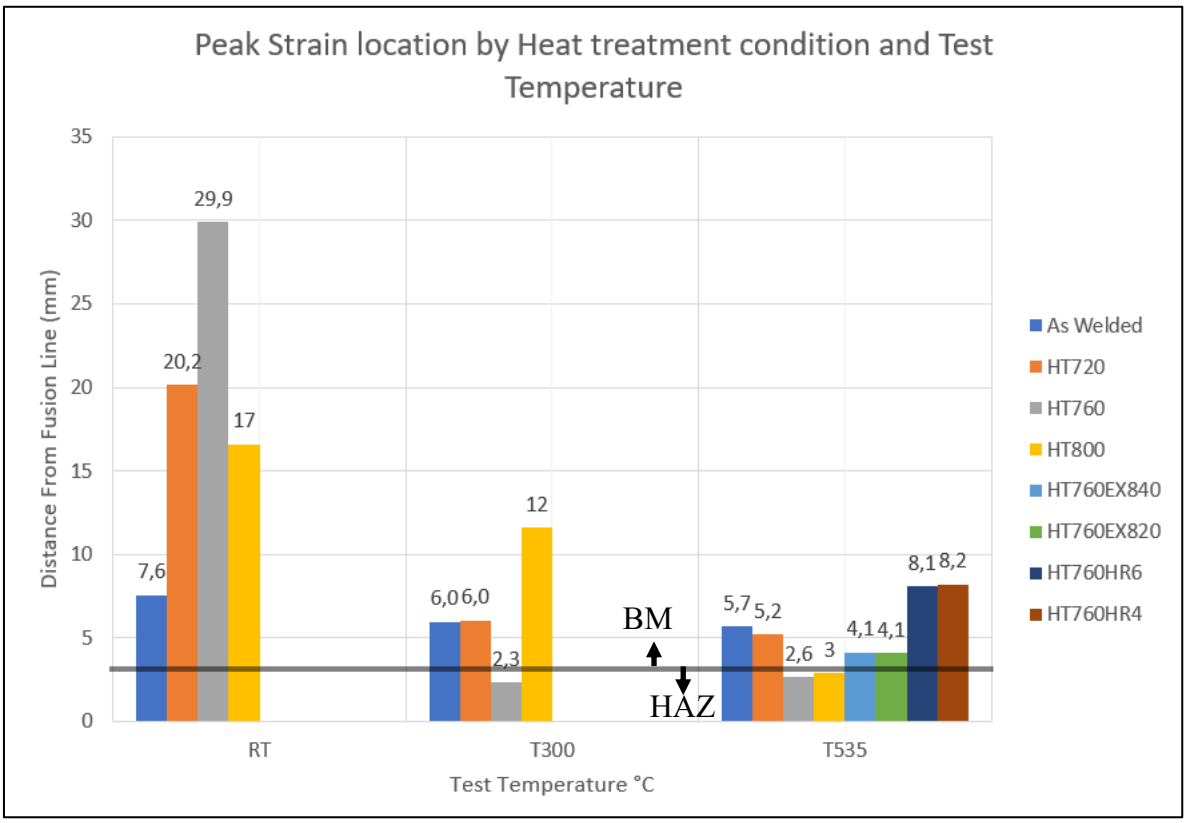

Figure 4.21 : Peak Strain Location by test temperature and HT Condition

At T535 heat treatments at HT760 and HT800 peak strain location was closer to fusion line compared to HT720 and As-Welded conditions. There was no significant change in the location of peak strain for HT760, HT720 and As-welded heat treatment conditions at T535 and T300. Increased in tensile test temperature moved the peak strain localisation closer to the fusion line for all test conditions. Repeatability experiments are necessary to improve confidence in results. Tensile tests in Section 4.1, Figure 4.5 d show that heat treatment excursions and extended heat treatments resulted in reduced material strength. Due to weakened base metal, heat treatment conditions HT760HR4, HT760HR6, HT760EX840 and HT760EX840 resulted in the peak strain location moving further into the base metal relative to the fusion line.

The location of peak strain for all heat treatment conditions at T535 was between 2mm - 10mm from the fusion line, giving a width of 10 mm from the fusion line which can be detected using NDT equipment with a width of 10 mm. The fusion line was located in the hot zone which is a maximum temperature region on the specimen. The movement of the location of peak strain along the tensile specimen gauge length was influenced by test temperature and material resistance to deformation.

4.5.2 Repeatability study

Experiments were repeated to obtain confidence in experimental results and experimental technique. Three heat treatment conditions i.e. As-welded, HT760, HT800 and HT760EX840 were selected for repeat experiments due to material limitation. Experiments were conducted

under the same conditions. Figure 4.*22* shows the experimental results comparing the initial experiment to repeat experiments. For each experiment, the localised strain plot shows an identical trend, this reinforced confidence in the experimental technique showing the capability to reproduce similar results for the same material.

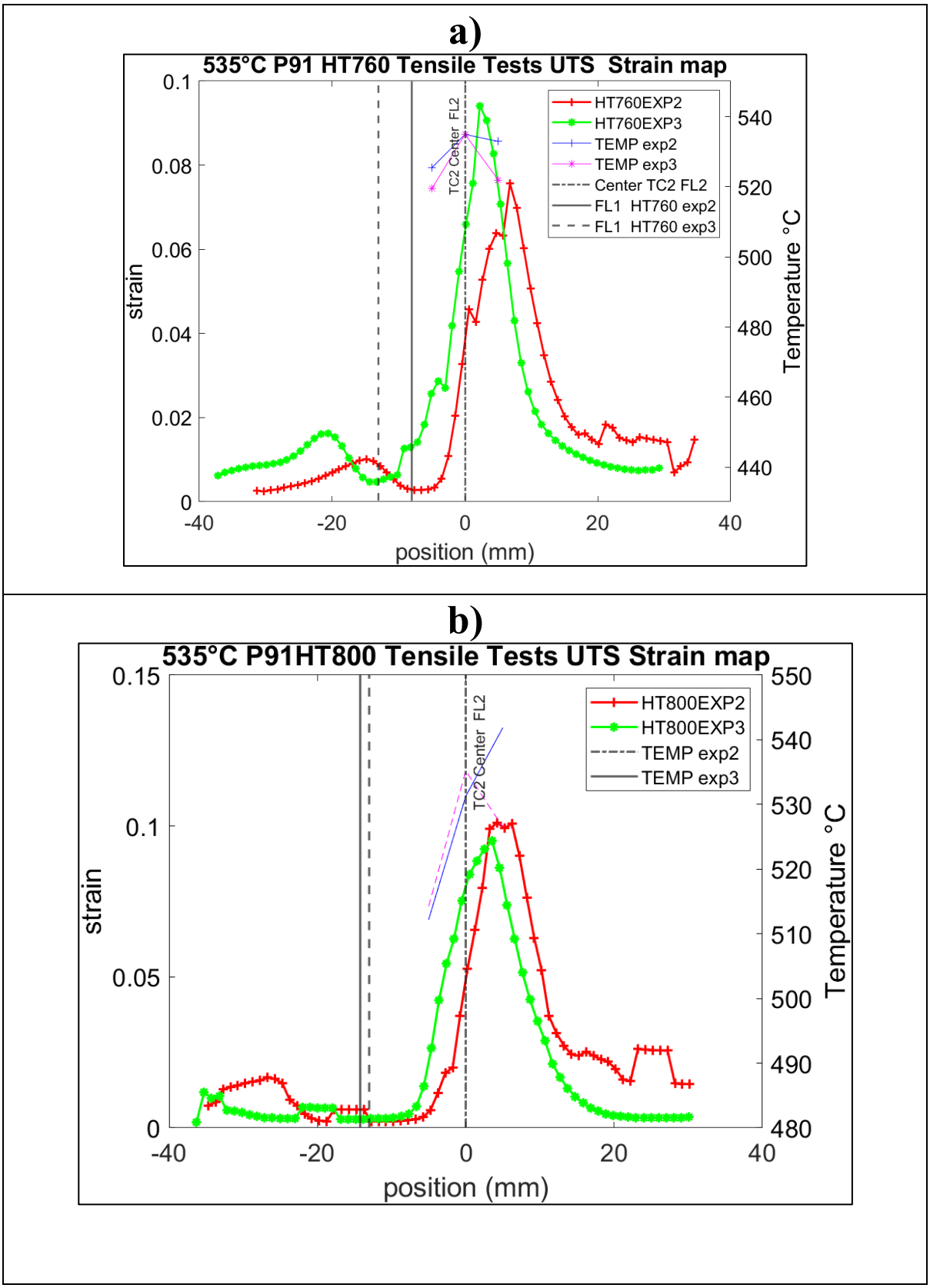

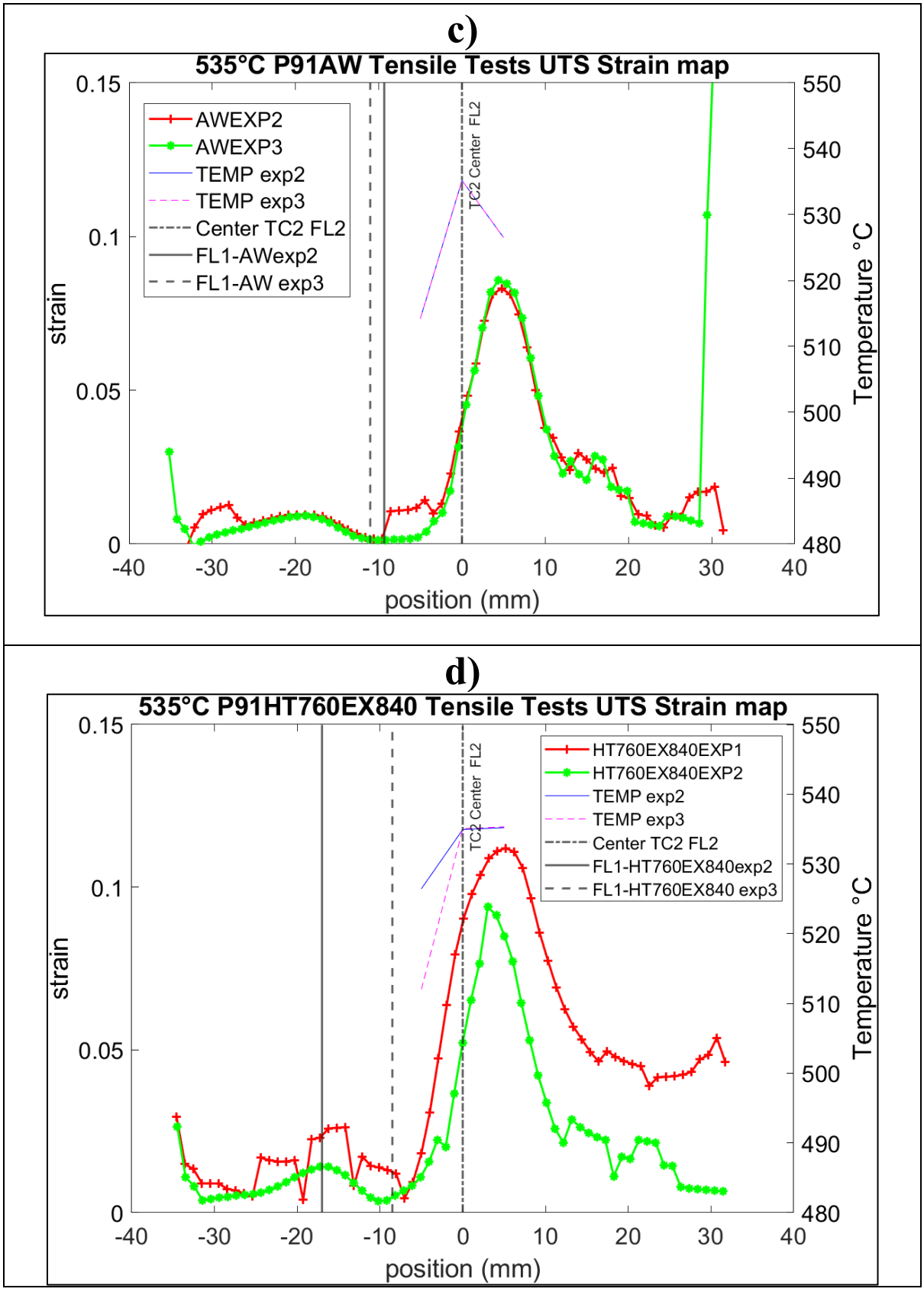

Figure 4.22: Repeatability study of P91 localised strain map at 535 °C

4.6 Superimposed Hardness and Strain Localisation

Figure 4.23 shows superimposed room temperature HAZ localised strain maps and microhardness tests for heat treatment conditions HT760, AW and HT800. Hardness tests on heat treated specimens showed minimal difference for HT760 and HT800. AW heat treatment condition had the highest hardness at room in the HAZ as well as in the base metal. UTS HAZ localised strain maps showed that hardness was directly related to resistance to localised plastic deformation. For the AW condition, as hardness decreased the resistance to localised plastic deformation decreased. Low resistance to localised plastic deformation made the material more susceptible to localised strain consequently localised strain increases as hardness decreased.

HT800 and HT760 heat treatment had similar hardness values and profiles. However, there was a significant difference in strain localization in the specimens. HT760 showed increased resistance to localised plastic deformation compared to HT800. This difference can be attributed to the microstructural differences in the two specimens.

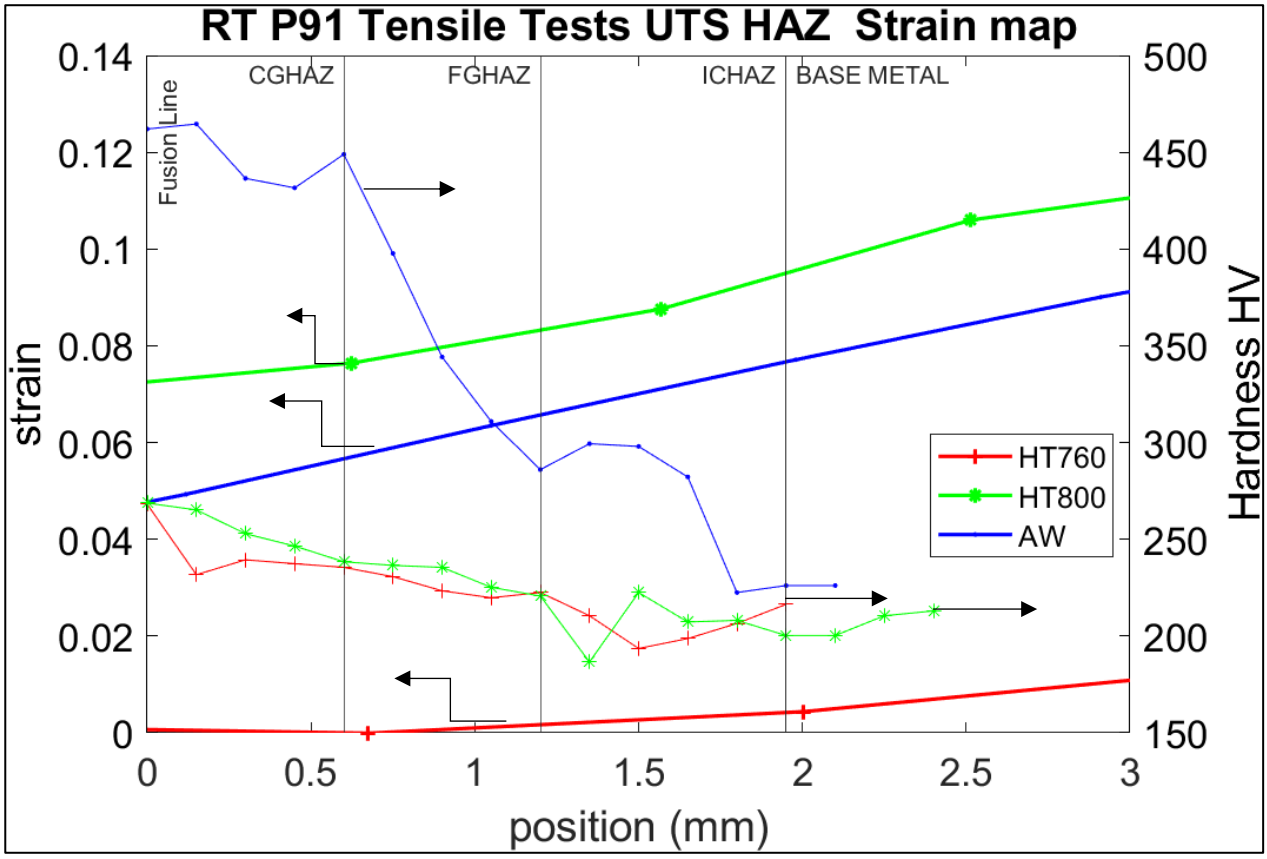

Figure 4.23: Superimposed Room Temperature Hardness and UTS Localised strain maps.(Arrows show the relevant vertical axis)

Investigating room temperature tensile test localised strain maps in Figure 4.8 c and hardness tests in Figure 4.1, AW and HT800 had the highest localised strain which occurred in the base metal. In the base metal region of strain localisation, Figure 4.1 shows that HT800 has the lowest average hardness value 204 HV while AW had the highest 229 HV and HT760 had an average hardness value of 218 HV. HT800 had the highest accumulation of localised strain in the base metal compared to HT720 and HT760. This indicated that low hardness reduced a

material's resistance to localised plastic deformation consequently resulting in high localised strain, extending the phenomenon observed in the HAZ. The AW condition experienced higher localised strain compared to HT760 despite having higher hardness. This showed the effects of PWHT in improving material resistance to localised plastic deformation through homogenisation and tempering of the microstructure.

Material hardness is generally related to resistance to localised plastic deformation because harder materials tend to have stronger bonds between their constituent atoms, making it more difficult for them to deform. However, hardness alone does not necessarily dictate a material's resistance to localised plastic deformation. Other factors such as ductility, toughness, test temperature and microstructure, also play important roles. Harder materials are often more brittle and can be more prone to strain localization, as was the case with the AW condition. On the other hand, materials with a lower hardness but higher ductility can deform more uniformly and be less prone to strain localization.

5. Experimental limitations and recommendations

Experimental limitations affect the degree of resolution at which experimental data can be analysed. Limitations were identified while working with the DIC, Gleeble, hardness and microscopy. To understand the effects of PWHT of P91 weldment tensile behaviour, it would be important to understand the effects of PWHT on the factors contributing to the tensile properties of the material. These would be the strengthening mechanisms of P91 steel which are precipitate hardening and solid solution strengthening. An analysis of the precipitates present in the microstructure after different heat treatments would help answer this question. This would be possible if the chemical composition of precipitates could be obtained such that they can be classified as MX or $M_{23}C_6$ precipitates and their density in the microstructure analysed for different heat treatment conditions. This can be achieved using SEM and EDX as well as simultaneous EDX and EBSD. There was no capacity to perform simultaneous EDS and EBSD. The penetration depth of the electron beam during SEM analysis exceeded the required depth to accurately obtain spectra for precipitates. As a result, it was not possible to conduct the analysis. Other microscopy techniques, such as TEM, could be adopted; however, this was beyond the scope of this work.

A significant limitation of Dantec DIC Istra 4D software is that it does not include temperature measurement. Data analysis from DIC software was done using virtual strain gauges on the specimen. These strain gauges can be a point, line or a polygon drawn over an area. The output was given as a matrix with pixels in the strain gauge, each pixel in the matrix had corresponding values for that point on the selected parameter being measured e.g., displacement, strain. Since there was no temperature measurement on the DIC software, external temperature measurement tools need to be adopted. In the case of IR thermal camera, the temperature measurement data was exported as a matrix with pixels equivalent to the specimen area. Each pixel had a corresponding temperature measurement value for that point on the specimen, but the temperature matrix did not match the DIC matrix. This is because the DIC and IR software were created differently, and the export parameters could not change. As a result, temperature measurement was limited to Gleeble 3800D thermocouples.

The resolution in small area measurement of the DIC software depends on evaluation parameters. The evaluation parameters used in this work gave a resolution of 430 micron per facet, which is nearly half a millimetre. This limited the number of points in HAZ weld zones from which localised strain properties could be obtained since the HAZ is only 2 mm. The robust technique for DIC data extraction applied divided a given length into points. The number of points can be controlled to allow for extraction of DIC data on any point on the input length. This improved the resolution of data that could be extracted. The input length can be controlled by reference marks on the gauge length. This level of control improves the resolution of data extraction and reduces limitations due to resolution since data can be extracted at any point.

Dantec DIC software did not allow onscreen measurement. The drawn lines or polygons were not translated to metric measurements within the software. It would be helpful when drawing a virtual strain gauge over an area of interest to be able to calibrate the software for metric measurements, such that there would be confidence that the input parameters were correct. A conversion of the DIC matrix to metric measurements was performed with IntelliJ image processing software. This introduced additional error during the processing of results and may affected their accuracy.

The evaluated DIC matrix did not cover the entire region covered by the DIC mask. This introduced an ambiguity in terms of assigning an origin for accurate interpretation of data. To improve the accuracy of Dantec DIC evaluation there needs to have measured and marked physical references placed on the specimens that can be referenced as origins during evaluation. Ideally in the centre of the region of interest. To accommodate for these references the speckle pattern need not cover the ROI end to end. Figure 5.1 illustrates an ideal tensile test specimen speckle pattern and reference marks configuration.

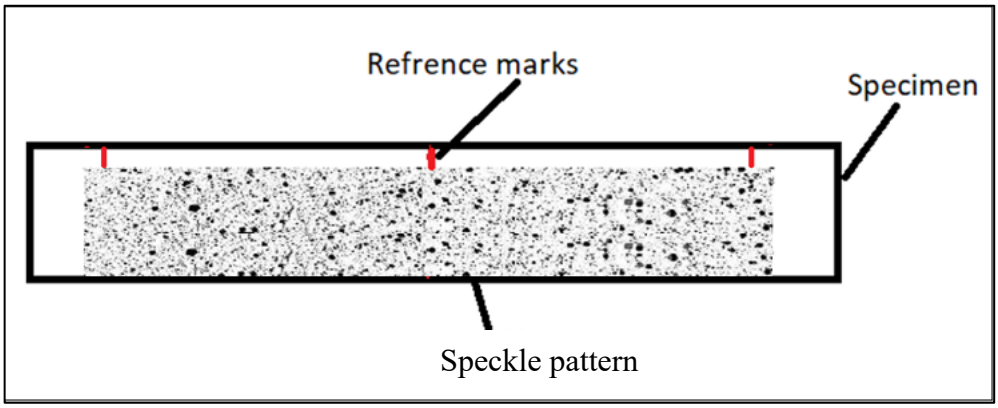

Figure 5.1: Ideal DIC evaluation specimen preparation

The Gleeble thermomechanical machine was used for high temperature tensile testing. Strain measured included movement of the jaws which could not be accounted for. A comparison of DIC and Gleeble strain in Section 3.11 shows a linear strain curve compared to an exponential curve obtained in DIC. The strain measurements on the Gleeble machine were not accurate due to the machine compliance phenomena also reported by Signh [29] which defined as the nonlinear displacement within the loading system which arises from the nonlinearity associated with the many connections and/or linkages present within the loading system [32]. The strain measurements on the gleeble machine include the displacement of the gleeble jaws.

Hardness values were calculated by measuring the length of indentation diagonals. On the ZwickRoel hardness tester, calculation of hardness values was automated using software developed at UCT Centre of Materials. This was achieved by visually identifying and manually placing markers on four corners of the indentation, then the software reported the hardness value. This visual identification and manual placement of markers introduces a source of human error which may affect accuracy of hardness values. The microhardness tester employed manual measurement of indentations. Vertical lines were adjusted under a microscope to the edges of the indentation then the length was measured. The manual adjustment introduced a source of error, which may have affected results.

6. Conclusions

The influence of post weld heat treatment on the tensile behaviour of P91 weldments was investigated experimentally. The technique adopted was an improvement of the initial experimental technique developed by Singh [29]. Localised strain maps were obtained for elevated temperature tensile tests. The methodology for tracking strain localisation was well established. It was established that strain localization was a function of test temperature as the peak localised strain occurred within the hot zone. However, the non-uniform temperature profile made it difficult to reliably identify the extent to which strain localisation is influenced by heat treatment and material property. The set out objectives included:

i) **Sensitivity of tensile strength (across the composite weldment) to the microstructural state that evolves during different PWHT**.

The Ac_1 temperature for material used in this work is 800°C. Heat treatments below this temperature subject the material to tempering. There was a limit to the extent to which tempering resulted improved tensile strength of P91 weldments. The recommended tempering temperature is 760°C for 2 hours.

At room temperature, PWHT resulted in reduced resistance to deformation. PWHT conditions exhibited lower yield strength and UTS compared to the AW condition. This material behaviour was also observed in tensile strength properties at 300°C and 535°C. Over tempering beyond the recommended HT760 results in diminished tensile properties as observed in the HT800 condition.

At elevated temperatures, specimens subjected to PWHT also showed lower yield strength and UTS compared to the AW condition indicating that PWHT lowered the material's resistance to the onset of plastic deformation. A comparison of specimens subjected to excursions and extended heat treatments for PWHT condition HT760 showed that excursions resulted in poor tensile properties with very low YS and UTS compared to the recommended PWHT HT760. Specimen subjected to tempering for four hours at 760°C indicate that there was little difference in tensile strength compared to specimen subjected to the recommended PWHT to suggest any benefit of extended heat treatment. Tempering for 6 hours resulted in reduced resistance to plastic deformation exhibiting a lower YS and UTS compared to HT760 and HT760 HT4. Specimens subjected to excursions and over tempering in post weld heat treatments exhibited diminished tensile properties compared to the recommended PWHT.

These changes in tensile properties were due to changes in the microstructural state because of PWHT. Extended tempering resulted in spheroide of carbides which reduced the solid solution strengthening and precipitate hardening mechanism leading to easier formation of voids in the microstructural matrix during high temperature tensile testing and premature failure. The identification of changing tensile behaviour across weldments as function of PWHT contributed to understanding the metallurgical risk associated with deviations in PWHT field practices.

ii) Tensile behavior of the different zones within the cross-weld specimen.

The tensile behavior of different zones was analysed using Localised strain maps and hardness plots. The cross-weld specimen comprised of the weld metal (WM), base metal (BM) and the

heat affected zone (HAZ). The HAZ comprises of four distinct weld zones i.e., fusion zone (FZ), course grained heat affected zone (CGHAZ), fine grained heat affected zone (FGHAZ) and intercritical heat affected zone (ICHAZ). HAZ localised strain had an inverse linear function of weld zone hardness in the HAZ from the fusion line to the ICHAZ. This was due to resistance to localised plastic deformation in areas of high hardness. Hardness in the HAZ increased from the ICHAZ towards the fusion line and was highest in the weld metal. Strain progression in the HAZ was not a direct reflection of strain localisation in the base metal due to heterogeneous material properties.

There was high resistance to localised plastic deformation in the weld metal at room temperature. Microstructure homogenisation that occurred because of heat treatment resulted in WM tempering reducing resistance to localised plastic deformation in the WM. This resulted in extension of deformation into the weld metal. Resistance to localised plastic deformation in the WM decreases at elevated test temperatures for all PWHT conditions.

The base metal had lower hardness compared to the WM and HAZ from room temperature hardness tests. At room temperature, tensile tests localised strain maps showed that the peak strain localization occurred in the base metal. Due to low hardness, the BM had reduced resistance to localised plastic deformation compared to the HAZ and WM. The difference in tensile behaviour of weld zones was due to tempering which resulted in finely dispersed second phase particles and reduced dislocation density in the microstructure.

iii) The effect of PWHT and tensile test temperature on strain localization.

At room temperature the peak localised strain occurred in the base metal (BM) for all PWHT conditions. The peak localised strain migrated further into the BM with increased PWHT temperature i.e., HT720, HT760. PWHT improved microstructure homogeneity and the materials' resistance to localised plastic deformation. Over tempering resulted in a reduction in resistance to localised plastic deformation, which resulted in accumulation of high localised strain as shown in the HT800 PWHT condition. Based on experimental results obtained at room temperature, strain localisation was established as a function of heat treatment condition.

In the HAZ, strain localisation was an inverse function of hardness at room temperature due to resistance of plastic deformation in regions of high hardness. Heat treatment improved material resistance to plastic deformation at room temperature which consequently improved ductile properties of specimen at room temperature.

It was established that strain localization was also a function of test temperature as the peak localised strain occurred within the hot zone at elevated temperature. The non-uniform temperature profile was difficult to reliably identify the extent to which strain localisation was influenced by heat treatment. Increased test temperatures cause a lower resistance to localised plastic deformation which results in strain localisation. In this work the peak localised strain shifted towards the fusion line, into the hot zone as test temperature was increased, thus strain localisation was dependent on test temperature which lowered material's resistance to localised plastic deformation resulting in accumulation of localised strain.

Deviations from standard heat treatment can occur during field heat treatment, these include extended time heat treatments and temperature excursions during heat treatment. These deviations from standard heat treatment practice at HT760 resulted in a higher level of localised strain occurring in the specimens subjected to the same amount of deformation compared to

standard heat treatment. Consequently, deviations from standard practice resulted in poor material tensile properties.

Factors affecting peak strain location and thus the location most susceptible to failure were established as heat treatment condition, test temperature and resulting microstructure. Further quantitative microstructural study is recommended to establish the major factor controlling strain localisation between temperature and microstructure.

iv) Evaluate the test technique to optimise the acquisition and interpretation of tensile data for accurate strain localization (a function of temperature) measurement in composite cross-weld specimen.

Experimental limitations can limit the resolution of data interpretation. A key drawback of DIC software was its lack of non-contact temperature measurement. This led to adoption of an IR camera with a different data post-processing software. Combining the data sets from the different software proved to be futile due to the different dimensions of the data sets which would compromise the data quality if transformed to match by mapping the IR temperature matrix on the DIC strain matrix. For obtaining localised strain, the resolution to which DIC could be evaluated limited the number of points in a small area for which strain measurements could be obtained. The Dantec Istra 4D DIC software did not transform polygons and lines drawn on specimen to metric measurements. This reduces the confidence in the input parameters such as the measured gauge length or area over which strain localisation maps were obtained.

A more robust technique is recommended to optimise the acquisition and interpretation of tensile data for accurate strain localization measurement in composite cross-weld specimens. In this method, position reference markers are strategically placed along the specimen's gauge length. These markers as essential origin references within the analysed DIC mask, contributing to the precision of strain measurements. The technique used in this work did not use markers as references, instead, welded thermocouples were used as reference marks within an accuracy of 1 mm. This was sufficient for accurate data acquisition but can be improved by adding reference markers on the specimen.

References

[1] Norman E Dowling and Stephen L. Kampe, *Mechanical Behavior of Materials*, vol. 4, no. 12. 2013. [Online]. Available: https://www.pearson.com/en-us/subject-catalog/p/mechanical-behavior-of-materials/P200000003452/9780137524594?tab=accessibility

[2] C. Pandey, M. M. Mahapatra, P. Kumar, S. Kumar, and S. Sirohi, "Effect of post weld heat treatments on microstructure evolution and type IV cracking behavior of the P91 steel welds joint," *J Mater Process Technol*, vol. 266, pp. 140–154, Apr. 2019, doi: 10.1016/j.jmatprotec.2018.10.024.

[3] H. Li and D. Mitchell, "Microstructural characterization of P91 steel in the virgin, service exposed and post-service re-normalized conditions," *Steel Res Int*, vol. 84, no. 12, pp. 1302–1308, Dec. 2013, doi: 10.1002/SRIN.201300055.

[4] C. Pandey, M. M. Mahapatra, P. Kumar, and N. Saini, "Some studies on P91 steel and their weldments," *Journal of Alloys and Compounds*, vol. 743. Elsevier Ltd, pp. 332–364, Apr. 30, 2018. doi: 10.1016/j.jallcom.2018.01.120.

[5] J. G. Thakare, C. Pandey, A. Gupta, P. K. Taraphdar, and M. M. Mahapatra, "Role of the heterogeneity in microstructure on the mechanical performance of the Autogenous Gas Tungsten Arc (GTA) welded dissimilar joint of F/M P91 and SS304L steel," *Fusion Engineering and Design*, vol. 168, p. 112616, Jul. 2021, doi: 10.1016/J.FUSENGDES.2021.112616.

[6] C. Middleton, J. Brear, R. Munson, and R. Viswanathan, "Assessment of the risk of type IV cracking in welds to header, pipework and turbine components constructed from the advanced ferritic 9% and 12% chromium steels," *Proceedings of the 3rd Conference on Advances in Material Technology for Fossil Power Plants*, no. April 2001, pp. 69–78, 2001, Accessed: Oct. 09, 2023. [Online]. Available: https://www.researchgate.net/profile/John-Brear/publication/288128785_An_assessment_of_the_risk_of_type_IV_cracking_in_welds_to_header_pipework_and_turbine_components_constructed_from_the_advanced_ferritic_9_and_12_chromium_steel/links/575bd93308aed8846212be37/An-assessment-of-the-risk-of-type-IV-cracking-in-welds-to-header-pipework-and-turbine-components-constructed-from-the-advanced-ferritic-9-and-12-chromium-steel.pdf

[7] EPRI, *The Grade 91 Steel Handbook 2013*. 2013.

[8] "ASTM A335 / ASME SA335 P91 Alloy Steel Seamless Pipes, P91 Alloy Steel SMLS Pipes." Accessed: Apr. 10, 2020. [Online]. Available: http://www.amardeepsteel.com/astm-a335-p91-alloy-steel-seamless-pipes.html

[9] Panait Clara, W. Bendick, Gourgues-Lorenzon, Anne-Françoise, and J. Besson, "Study of the microstructure of the grade 91 steel after more than 100.000h of creep exposure at 600°C," *International Journal of Pressure Vessels and Piping*, vol. 87, pp. 326–335, 2010, doi: 10.1016/j.ijpvp.2010.03.017ï.

[10] J. Vivas, C. Capdevila, J. A. Jimenez, M. Benito-Alfonso, and D. San-Martin, "Effect of ausforming temperature on the microstructure of G91 steel," *Metals (Basel)*, vol. 7, no. 7, 2017, doi: 10.3390/met7070236.

[11] J. D. Walker, "Heat Transfer Analysis of Localized Heat-Treatment for Grade 91 Steel," 2017, Accessed: Oct. 05, 2023. [Online]. Available: https://api.semanticscholar.org/CorpusID:136315262

[12] P. Doubell, M. E. J. Bezuidenhout, R. D. Knutsen, and J. Westraadt, "Investigating effects of variations in heat treatment parameters on performance of CSEF welds,"

Advances in Materials Technology for Fossil Power Plants - Proceedings from the 8th International Conference, pp. 1182–1193, 2016.
[13] L. Li, R. Wright, and S. Lesica, "Effect of Post-Weld Heat Treatment on Creep Rupture Properties of Grade 91 Steel Heavy Section Welds," *U.S. Department of Energy*, no. 09, 2012.
[14] "What is type IV cracking, and how is it detected? - TWI." Accessed: Apr. 22, 2020. [Online]. Available: https://www.twi-global.com/technical-knowledge/faqs/faq-what-is-type-iv-cracking-and-how-is-it-detected
[15] EPRI, "Creep Strength–Enhanced Ferritic (CSEF) Steel Welding Guide," 2011.
[16] EPRI, "Best Practice Guideline for Well-Engineered Weld Repair of Grade 91 Steel," p. 124, 2014.
[17] L. Chen and K. Yamashita, "Effects of PWHT temperature on mechanical properties of high-cr ferritic heat-resistant steel Weld metals," *Welding in the World*, vol. 56, no. 1–2, pp. 81–91, 2012, doi: 10.1007/BF03321150.
[18] Y. Wang and L. Li, "Microstructure Evolution of Fine-Grained Heat-Affected Zone in Type IV Failure of P91 Welds Microstructure and creep behaviour of heat affected zone in Grade 91 steel weldments View project Diffusion Bonding of Dissimilar Alloys View project," 201AD.
[19] B. Silwal, L. Li, A. Deceuster, and B. Griffiths, "Effect of Postweld Heat Treatment on the Toughness of Heat-Affected Zone for Grade 91 Steel," *Welding Research*, vol. 92, no. March, pp. 80–87, 2013.
[20] "What is the Holloman-Jaffe parameter? - TWI." Accessed: Aug. 12, 2020. [Online]. Available: https://www.twi-global.com/technical-knowledge/faqs/faq-what-is-the-holloman-jaffe-parameter
[21] EPRI, "Guide to grade 91 use temperature limits due to steam oxidation and exfoliation," *Eskom Power Plant Engineering Institute*, no. August, 2017.
[22] ASTM Standard E21, "Standard Test Methods for Elevated Temperature Tension Tests of Metallic Materials," *ASTM Book of Standards*, vol. i, pp. 1–8, 2009, doi: 10.1520/E0021-17E01.2.
[23] M. van Rooyen, T. H. Becker, J. E. Westraadt, and G. Marx, "Measurement of creep deformation of ex-service 12% Cr steel using digital image correlation," *Journal of Strain Analysis for Engineering Design*, vol. 55, no. 3–4, pp. 71–85, 2020, doi: 10.1177/0309324720904517.
[24] R. Curry, R. D. Knutsen, and K. Singh, "Mapping high temperature strain localisation in steel weldments using digital image correlation," in *Advances in Engineering Materials, Structures and Systems: Innovations, Mechanics and Applications*, no. Dic, CRC Press, 2019, pp. 383–387. doi: 10.1201/9780429426506-67.
[25] Y. A. Cengel, *Thermodynamics An engineering Approach*. McGraw-Hill Education - Europe, 2005. doi: 9780071250849.
[26] M. van Rooyen and T. H. Becker, "High-temperature tensile property measurements using digital image correlation over a non-uniform temperature field," *Journal of Strain Analysis for Engineering Design*, vol. 53, no. 3, pp. 117–129, Apr. 2018, doi: 10.1177/0309324717752029.
[27] A. Ruiz-Moreno, P. Hähner, F. Fumagalli, V. Haiblikova, M. Conte, and N. Randall, "Stress−strain curves and derived mechanical parameters of P91 steel from spherical nanoindentation at a range of temperatures," *Matererial & Design*, vol. 194, p. 108950, Sep. 2020, doi: 10.1016/J.MATDES.2020.108950.
[28] Q. Zheng, N. Mashiwa, and T. Furushima, "Evaluation of large plastic deformation for metals by a non-contacting technique using digital image correlation with laser speckles," *Mater Des*, vol. 191, p. 108626, 2020, doi: 10.1016/j.matdes.2020.108626.

[29] K. Singh, “The Development of an Experimental Technique to Measure the Influence of Temperature on the Mechanical Properties of Weldments,” *M.S Thesis University of Cape Town*, 2018.
[30] “2D-/3D Stereo DIC Digitital Image Correlation.” Accessed: Jun. 18, 2020. [Online]. Available: https://www.lavision.de/en/applications/materials-testing/stereo-dic/
[31] L. Yang, “Measure Strain Distribution Using Digital Image Correlation (DIC) for Tensile Tests Final Report,” 2010. Accessed: Dec. 07, 2020. [Online]. Available: https://www.a-sp.org/wp-content/uploads/2020/08/Measurement-of-Strain-Distribution-Using-Digital-Image-Correlation.pdf
[32] S. R. Kalidindi, A. Abusafieh, and E. El-Danaf, “Accurate characterization of machine compliance for simple compression testing,” *Exp Mech*, vol. 37, no. 2, pp. 210–215, 1997, doi: 10.1007/BF02317861.
[33] “Hardness Testing: Rockwell / Brinell / Vickers Scales and Applicability to Stamped Sheet Steel Parts | The Future is Forming.” Accessed: Mar. 09, 2020. [Online]. Available: https://thefutureisforming.wordpress.com/2012/06/26/hardness-testing-rockwell-brinell-vickers-scales-and-applicability-to-stamped-sheet-steel-parts/
[34] P. Sherwin, “Temperature Control in Heat Treating,” *Steel Heat Treating Technologies*, pp. 152–169, Dec. 2014, doi: 10.31399/ASM.HB.V04B.A0005925.
[35] C. Pandey, M. M. Mahapatra, P. Kumar, and N. Saini, “Effect of strain rate and notch geometry on tensile properties and fracture mechanism of creep strength enhanced ferritic P91 steel,” *Journal of Nuclear Materials*, vol. 498, pp. 176–186, Jan. 2018, doi: 10.1016/j.jnucmat.2017.10.037.
[36] ASTM E8, “ASTM E8/E8M standard test methods for tension testing of metallic materials 1,” *Annual Book of ASTM Standards 4*, no. C, pp. 1–27, 2010, doi: 10.1520/E0008.
[37] Dantec Dynamics, “Calibration Targets - Dantec Dynamics.” Accessed: Aug. 31, 2023. [Online]. Available: https://www.dantecdynamics.com/components/calibration-targets/
[38] Dantec Dynamics, “Evaluation Settings-Influence of Facet size and Grid spacing for DIC evaluations.”
[39] ASTM335, “Standard Specification for Seamless Ferritic Alloy-Steel Pipe for High-Temperature,” *Society*, no. October 2002, pp. 1–11, 2003, doi: 10.1520/A0335_A0335M-22.
[40] C. Ni, “Scanning Electron Microscopy (SEM),” *Encyclopedia of Tribology*, pp. 2977–2982, 2013, doi: 10.1007/978-0-387-92897-5_1217.
[41] P. J. Potts, *A Handbook of Silicate Rock Analysis*. Dordrecht: Springer Netherlands, 1987. doi: 10.1007/978-94-015-3988-3.
[42] “T91 / P91 Steel.” Accessed: Aug. 22, 2022. [Online]. Available: http://www.metalspiping.com/t91-p91-steel.html